INAUGURAL-DISSERTATION
zur
Erlangung der Doktorwürde
der
Naturwissenschaftlich-Mathematischen
Gesamtfakultät
der
Ruprecht-Karls-Universität
Heidelberg

vorgelegt von

Dipl.-Phys. Thomas Nunnemann
aus Mainz

Tag der mündlichen Prüfung: 11.2.1999

Measurement of Leading Neutron Production in Deep–Inelastic *ep* Scattering at HERA

Gutachter: Prof. Dr. Bogdan Povh
Prof. Dr. Jürgen von Krogh

Bestimmung der Produktion vorwärts gestreuter Neutronen in tiefinelastischer *ep*-Streuung bei HERA

Beim H1 Experiment am HERA Beschleuniger wurden Neutronen, die unter einem kleinen Winkel ($0\,\mathrm{mrad} \leq \theta \lesssim 0.6\,\mathrm{mrad}$) in tiefinelastischer Streuung produziert wurden, nachgewiesen. Dazu wurde ein Kleinwinkel-Kalorimeter benutzt, welches 1996 eingebaut wurde. Vorgestellt wird die Messung des semi-inklusiven Wirkungsquerschnittes $\mathrm{d}\sigma(ep \to enX)/(\mathrm{d}x\mathrm{d}Q^2\mathrm{d}E')$ für die Produktion von Neutronen mit einem Transversalimpuls $p_T \leq 200\,\mathrm{MeV}$ im kinematischen Bereich von $2\,\mathrm{GeV}^2 \leq Q^2 \leq 50\,\mathrm{GeV}^2$, $6\cdot10^{-5} \leq x \leq 6\cdot10^{-3}$ und $160\,\mathrm{GeV} \leq E' \leq E_p$, wobei E' die Energie des Neutrons und $E_p = 820\,\mathrm{GeV}$ die des Protonstrahles bezeichnen. Verschiedene Produktionsmechanismen werden dem Ergebnis gegenübergestellt und ihre Vorhersagen überprüft. Die Neutronen-Daten werden mit einer ähnlichen Messung der Produktion von führenden Protonen verglichen. Für Energiebruchteile $0.7 \leq E'/E_p \leq 0.9$ stimmen beide semi-inklusive Wirkungsquerschnitte mit einem Regge-Modell überein, welches die Produktion von führenden Baryonen durch Pion-, Pomeron- und Reggeonaustausch beschreibt. Die Messung des Wirkungsquerschnittes für die Produktion von Neutronen ermöglicht die erste Abschätzung der Pion-Strukturfunktion bei kleinen Werten der Bjorkenvariable x.

Measurement of Leading Neutron Production in Deep–Inelastic *ep* Scattering at HERA

Deep–inelastic scattering events with a leading neutron have been observed by the H1 experiment at HERA using a forward neutron calorimeter. The calorimeter has been installed in 1996 and covers scattering angles between 0 mrad and $\lesssim 0.6\,\mathrm{mrad}$. For the first time at HERA, the semi–inclusive cross section $\mathrm{d}\sigma(ep \to enX)/(\mathrm{d}x\mathrm{d}Q^2\mathrm{d}E')$ for the production of leading neutrons with transverse momenta $p_T \leq 200\,\mathrm{MeV}$ has been measured in the kinematic region $2\,\mathrm{GeV}^2 \leq Q^2 \leq 50\,\mathrm{GeV}^2$, $6\cdot10^{-5} \leq x \leq 6\cdot10^{-3}$ and neutron energy $160\,\mathrm{GeV} \leq E' \leq E_p$, where $E_p = 820\,\mathrm{GeV}$ is the proton beam energy. The data are used to test different production models. The neutron data are compared to a similar measurement of leading proton production. For fractional energies $0.7 \leq E'/E_p \leq 0.9$, both semi–inclusive cross sections can be described by a Regge model of leading baryon production which consists of pion, pomeron and reggeon exchanges. The leading neutron data are used to estimate for the first time the structure function of the pion at small Bjorken–x.

Animadverti jam ante aliquot annos quàm multa, ineunte aetate, falsa pro veris admiserim, & quàm dubia sint quaecunque istis postea superextruxi, ac proinde funditus omnia semel in vitâ esse evertenda [...]

Several years have now elapsed since I first became aware that I had accepted, even from my youth, many false opinions for true, and that consequently what I afterward based on such principles was highly doubtful; and from that time I was convinced of the necessity of undertaking once in my life to rid myself of all the opinions I had adopted [...]

René Descartes, *Meditationes De Prima Philosophia*, 1641, Meditatio I.1,
English Translation by John Veitch, 1901.

Contents

Introduction

Revealing the structure of matter is one of the key issues in modern physics. The construction of systems, e. g. galaxies, solid states or elementary particles, gives information about the underlying physical forces and laws. Whereas in the macroscopic world the structure can be often seen directly with the naked eye, in the microscopic world of subatomic and subnuclear particles, most of the information is obtained by means of scattering experiments with highly energetic beams.

At the HERA accelerator, the structure of the proton is probed using high–energy beams of electrons and protons. The process of deep–inelastic scattering of the electron off the proton allows to study the partonic structure of the nucleon. The proton, as we understand it nowadays, is composed of quarks, antiquarks and gluons, which are assumed to be point–like objects. After many experiments, which started in the late 1960's, the structure of the proton can be parameterized in terms of parton distribution functions, which give the probability of finding an (anti–)quark or gluon with a certain momentum fraction inside the proton. Are these partons homogeneously and independently distributed over the full size of the proton or are there correlations between the different type of components? Hadronic correlations in the proton in form of virtual pions are believed to play a very important dynamical role in the nucleon structure, e. g. within the time allowed by the uncertainty principle, the proton might fluctuate into a state consisting of a pion and a neutron. Consequentially the question arises, is it possible to probe the structure of the pion inside the proton? Numerous theoretical works have suggested, that the production of highly energetic, forward neutrons in deep–inelastic *ep* scattering is sensitive to the structure of the pion. The produced neutron tags the virtual pion, which is probed by the exchanged photon.

In order to study neutron production, a *Forward Neutron Calorimeter* was installed in the H1 experiment at the *ep* collider HERA in the beginning of 1996. The calorimeter is located inside the HERA tunnel, approximately 100 m away from the central part of the H1 detector. This position allows to measure forward neutrons which are produced with very small scattering angles.

This work will focus on the measurement of the semi–inclusive production cross section of leading neutrons in deep–inelastic *ep* scattering using data obtained with the H1 detector in 1996. It is organized as follows: Chapter 1 gives an overview over the theory of semi–inclusive deep–inelastic scattering and discusses the pion exchange mechanism and alternative approaches for the production of leading neutrons. The HERA collider and the H1 detector are briefly described in Chapter 2. The construction of the forward neutron calorimeter is covered in Chapter 3, where special focus is put on the acceptance, calibration and resolution of the detector. The cross section measurement is presented in Chapter 4: The event selection and reconstruction, in particular the determination of the neutron's energy spectrum, are discussed in detail. In the last Chapter the result of this cross section measurement is presented and compared to the predictions of Monte Carlo simulations, which are based on different production mechanisms.

The neutron data are compared to a similar analysis of leading proton production. For high energies of the leading neutron or proton, both data sets can be described by a Regge Model of leading baryon production, which consists of pion, reggeon and pomeron exchanges. The leading neutron data are used to estimate for the first time the structure function of the pion at small Bjorken–x.

Chapter 1

Deep–Inelastic Scattering with a Leading Baryon

High energy scattering experiments of leptons on protons have a long and successful tradition in resolving the internal structure of the proton. Starting in the 1960's the measurement of elastic electron–proton scattering was used to determine the electromagnetic form–factor of the proton, which is directly related to the charge distribution and the magnetic moment of the proton.

In the late sixties, deep–inelastic scattering events, where the scattered electron looses a large amount of energy, were observed at the *Stanford Linear Accelerator Center* (SLAC). The experiments done at SLAC revealed, that the structure function of the proton only depends on the scaling variable x, and shows nearly no dependence on the four–momentum transfer Q^2 between the electron and the proton target [Blo69, Bre69]. This famous scaling behaviour had been predicted by Bjorken already in 1967 [Bjo67]. The *Quark Parton Model* (QPM), which was formulated by Feynman, gave an intuitive explanation for the observation of scaling [Fey69]. The scaling variable x was interpreted as the fractional momentum of the struck, point–like partons which were identified with the spin 1/2 quarks. Further experimental and theoretical progress showed that the proton does not consist only of quarks (valence and sea quarks) but that approximately half of the proton's momentum is carried by gluons, which in the framework of *Quantum Chromodynamics* (QCD) are identified as the carrier of the strong interaction. Due to the fact that the strong force between two partons is growing with increasing distance (the so called *confinement*), long range correlations between the quarks and gluons inside the proton are prominent and can lead to the formation of colourless hadronic fluctuations inside the proton.

Scattering processes on a long range scale, e. g. extended objects, are typically characterized by little transfer of transverse momentum. In *Regge* theory the scattering off a colourless hadronic fluctuation is described by the exchange of this colour–singlet object leaving the remainder of the target in a non–excited state, mostly a proton or a neutron.

The H1 and ZEUS experiment at the *ep* collider HERA discovered *large rapidity gap* events [ZEU93, H1C94], in which no particles are produced in the forward direction except a low mass state, presumably a high–energy proton, which escapes through the beam pipe undetected in the central detector. These events are usually interpreted

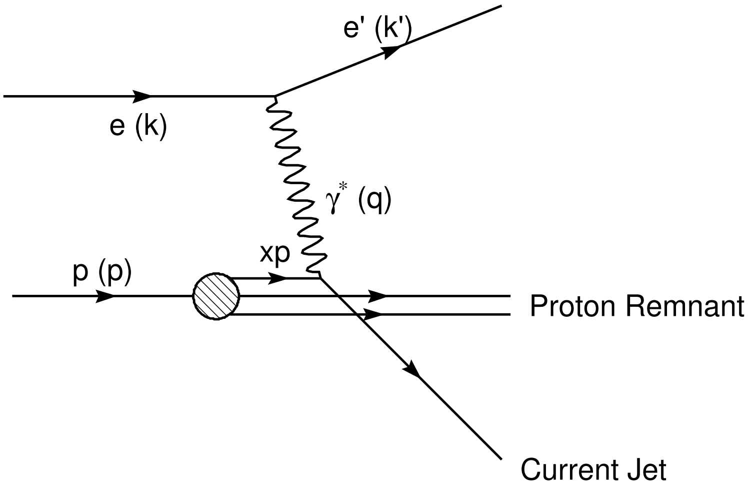

Figure 1.1: Schematic representation of inclusive deep–inelastic scattering in the QPM. The electron (e) interacts via an exchanged photon (γ^*) with a parton inside the proton (p). In the infinite momentum frame, xp can be identified with the initial momentum of the struck quark.

in terms of *pomeron* exchange [H1C95a, H1C97b, ZEU95, ZEU98]. The pomeron is a virtual particle which carries the quantum number of the vacuum and does not exist as a free particle. Also mesonic fluctuations inside the proton contribute to the total observed cross section. The most prominent contribution is the pion, since it is the lightest hadron.

Having these fluctuations, the deep–inelastic scattering process can take place on a parton of the virtual pion inside the proton rather than on a parton, which belongs to the "bare" proton. The pion might be probed by the exchanged photon offering the possibility of measuring the pion structure function in deep–inelastic *ep* scattering at HERA.

1.1 Inclusive Deep–Inelastic Scattering

Nowadays inclusive deep–inelastic scattering (DIS) is extensively studied at the HERA *ep* collider. In the Quark Parton Model, this reaction can be understood as the elastic scattering of the electron with a quark belonging to the proton. The distributions of the partons inside the proton can be determined by measuring only the energy and the scattering angle of the outgoing electron. Therefore this kind of measurement is called inclusive. At HERA one has the possibility of detecting in addition the hadronic final state, providing a more accurate determination of the kinematic variables.

1.1.1 Kinematics of Inclusive DIS

The deep–inelastic scattering reaction is sketched in Figure 1.1. Neglecting the contribution of the weak interaction, the scattering of the electron off the proton is, to lowest order, mediated by the exchange of a virtual photon. The struck parton hadronizes into the *current jet*, whereas the rest of the target proton constitutes the *proton remnant.*

The kinematics of this process can be naturally described in the four–dimensional *Minkowski* space. The following notation is of common use[1]:

k, k'	four–momentum of the incoming and outgoing electron,
E_e, E'_e	energy of the electron before and after the scattering process[2],
p	four–momentum of the proton in the initial state,
E_p	energy of the incoming proton[2],
m_e, m_p	masses of the electron and proton respectively,
P	sum of the four–momenta of the hadronic final state,
$q = k - k'$	four–momentum of the virtual photon,
θ_e	scattering angle of the electron[2,3],
$s = (k+p)^2$	squared centre–of–mass energy of the proton–electron system,
$W^2 = (q+p)^2$	squared centre–of–mass energy of the photon–proton system.

At fixed centre–of–mass energy $\sqrt{s}$, the inclusive event kinematics are completely defined by two of the following three Lorentz invariant variables:

$$\begin{aligned} Q^2 &= -q^2 = -(k-k')^2 \ , \\ x &= \frac{Q^2}{2p\cdot q} \ , \\ y &= \frac{p\cdot q}{p\cdot k} \ , \end{aligned} \tag{1.1}$$

which are related by $Q^2 = sxy$, if mass terms are neglected. In the HERA laboratory frame, the invariant variables can be expressed in terms of the beam energies and the kinematic quantities of the scattered electron:

$$\begin{aligned} s &= 4E_eE_p \ , \\ Q^2 &= 4E_eE'_e\cos^2\frac{\theta_e}{2} \ , \\ y &= 1-\frac{E'_e}{E_e}\sin^2\frac{\theta_e}{2} \ . \end{aligned} \tag{1.2}$$

The equations are exact only to lowest order, e. g. in the absence of initial or final state radiation (see Section 4.7).

The quantities Q^2, x and y can be intuitively illustrated. *Heisenberg's* uncertainty principle relates Q^2, the virtuality of the exchanged photon, to the minimal distance, which can be resolved by the photon: $\hbar/\sqrt{Q^2}$. Thus, with increasing Q^2 smaller distances within the proton can be probed. In a frame where the momentum of the proton is much larger than its mass (*infinite momentum frame*), the scaling variable x can be interpreted as the fraction of the proton momentum carried by the struck quark. In the proton rest frame, $y = (E_e - E'_e)/E_e$, which can be illustrated as the part of the energy, which is transferred by the photon. Therefore, y is called “inelasticity”.

---

[1] In this work, a system of natural units is used, whereby $\hbar = c = 1$.

[2] Quantities defined in the laboratory frame.

[3] In the HERA convention, scattering angles are defined with respect to the proton beam direction.

1.1.2 The Structure of the Proton

For not too high Q^2 ($Q^2 \ll m^2_{Z^0}$), the contribution of the weak interaction to the deep–inelastic scattering process can be neglected. In this region of Q^2 the double–differential cross section can be parameterized by two structure functions F_1 and F_2 [4]:

$$\begin{aligned} \frac{\mathrm{d}^2\sigma^{ep}}{\mathrm{d}x\,\mathrm{d}Q^2} &= \frac{4\pi\alpha^2}{x\,Q^4}\left[xy^2F_1(x,Q^2) + (1-y)F_2(x,Q^2)\right] \\ &= \frac{4\pi\alpha^2}{x\,Q^4}\left[1 - y + \frac{y^2}{2[1+R(x,Q^2)]}\right]F_2(x,Q^2)\ , \end{aligned} \tag{1.3}$$

where α is the electromagnetic coupling constant and $R = (F_2 - 2xF_1)/(2xF_1)$ is the ratio between the absorption cross sections for longitudinally and transversely polarized virtual photons. The expectation of the QPM is, that R vanishes for spin 1/2 partons (*Callan–Gross* relation [Cal69]). QCD predicts deviations from zero, which is in accordance with recent measurements [Tao96, NMC97, Yu98].

In the Quark Parton Model the structure function F_2 is expected to be independent of Q^2 and can be related to the parton momentum distributions $f_i(x)$:

$$F_2(x) = \sum_{i=q_j,\bar{q}_j} e_i^2 x f_i(x)\ , \tag{1.4}$$

where the sum is over the quarks and antiquarks, and e_i is their electric charge.

1.1.3 QCD Evolution and the Violation of Scaling

In the QPM the normalization of the parton distribution functions $f_i(x)$ is constrained by the momentum sum rule:

$$\sum_i \int_0^1 \mathrm{d}x\, x f_i(x) = 1\ . \tag{1.5}$$

Measurements made in the seventies demonstrated that this sum rule is not fulfilled: Quarks and antiquarks can only account for approximately half the proton momentum. The experiments also showed that the scaling behaviour is only true for $x \approx 0.2$. Outside this x region F_2 depends on Q^2: the scaling hypothesis is violated. These deviations from the predictions of the QPM are explained by Quantum Chromodynamics.

QCD is the field theory of the strong interaction. Quarks, which carry a colour charge, interact by the exchange of a gluon. Since also the gluons have a colour charge, they interact with each other as well as with quarks. The self–coupling of the gluon field creates an anti–screening effect leading to a logarithmic decrease of the strong coupling constant $\alpha_s(Q^2)$ with increasing Q^2. Since $\alpha_s(Q^2) \to 0$ for $Q^2 \to \infty$, the quarks appear to be free at very large Q^2. This property is called *asymptotic freedom.* For low values of Q^2, $\alpha_s(Q^2)$ is large: The partons are confined in hadrons.

QCD gives an intuitive interpretation of the violation of the scaling behaviour. As the virtuality Q^2, with which the proton is probed by the photon, increases, finer

---

[4] A derivation of this formula can be found in numerous textbooks, e. g. [Rob90, Nac90, Per87, Pov95]

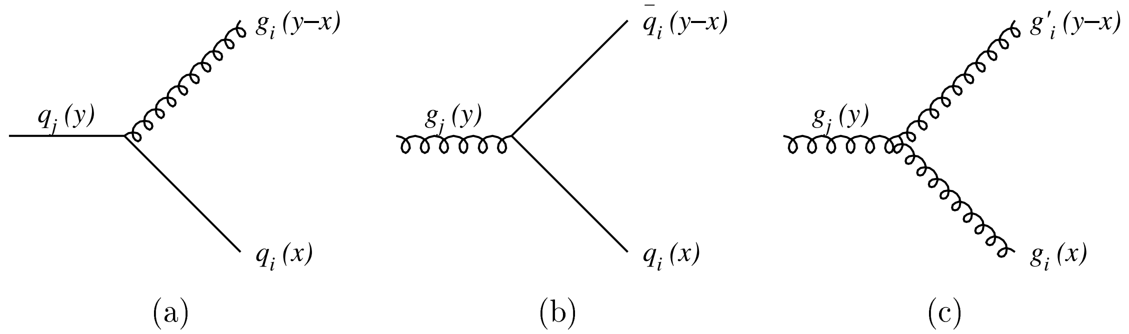

Figure 1.2: Vertices relevant to parton splitting functions: (a) Quark–gluon vertex determining P_{qq} and P_{gq}; (b) Annihilation vertex which induces P_{qg}; (c) Three gluon vertex determining P_{gg}.

structures within the proton are resolved. A quark, which is seen at a certain $Q^2 = Q_0^2$, might have radiated a gluon, when it is probed at a higher $Q^2 > Q_0^2$. The quark has lost momentum. With increasing Q^2 more and more splitting processes occur. Thus, as Q^2 increases, the quark density at low x grows and the probability to find a quark at large x decreases.

This physical picture can be quantitatively expressed by perturbative Quantum Chromodynamics (pQCD): For sufficiently small values of the strong coupling constant, solutions to QCD may be expanded in a perturbation series of powers of $\alpha_s(Q^2)$.

In pQCD the (anti–)quark ($q_i(x)$, $\bar{q}_i(x)$) and gluon ($g(x)$) distributions evolve as a function of Q^2. The dynamics of this evolution is described by the DGLAP equations (Dokshitzer, Gribov, Lipatov, Altarelli, Parisi) [Gri72, Dok77, Alt77], which are given in leading order (LO) by

$$\begin{aligned}\frac{\mathrm{d}q_i(x,Q^2)}{\mathrm{d}\ln Q^2} &= \frac{\alpha_s(Q^2)}{2\pi}\int_x^1 \frac{\mathrm{d}y}{y}\left[\sum_j q_j(y,Q^2)P_{q_iq_j}\left(\frac{x}{y}\right) + g(y,Q^2)P_{q_ig}\left(\frac{x}{y}\right)\right] \qquad (1.6)\\ \frac{\mathrm{d}g(x,Q^2)}{\mathrm{d}\ln Q^2} &= \frac{\alpha_s(Q^2)}{2\pi}\int_x^1 \frac{\mathrm{d}y}{y}\left[\sum_j q_j(y,Q^2)P_{gq_j}\left(\frac{x}{y}\right) + g(y,Q^2)P_{gg}\left(\frac{x}{y}\right)\right]\ .\end{aligned}$$

The splitting functions $P_{ba}(x/y)$ denote the probability for a parton a with fractional proton momentum y radiating a parton b, which has a fractional momentum $x < y$. The relevant LO vertices, which determine the splitting functions, are shown in Figure 1.2.

The DGLAP formalism permits, parton distributions, which are assumed to be known for all x at a certain Q_0^2, to be predicted for all x at larger $Q^2 > Q_0^2$. However, the equations cannot predict the x behaviour of the structure function.

In leading order[5] pQCD the structure function F_2 is like in the case of the QPM closely connected to the quark and antiquark distribution functions:

$$F_2(x,Q^2) = \sum_i e_i^2 x\left[q_i(x,Q^2) + \bar{q}_i(x,Q^2)\right]\ , \qquad (1.7)$$

---

[5] In the DIS regularization scheme, Eq. 1.7 is valid to all orders.

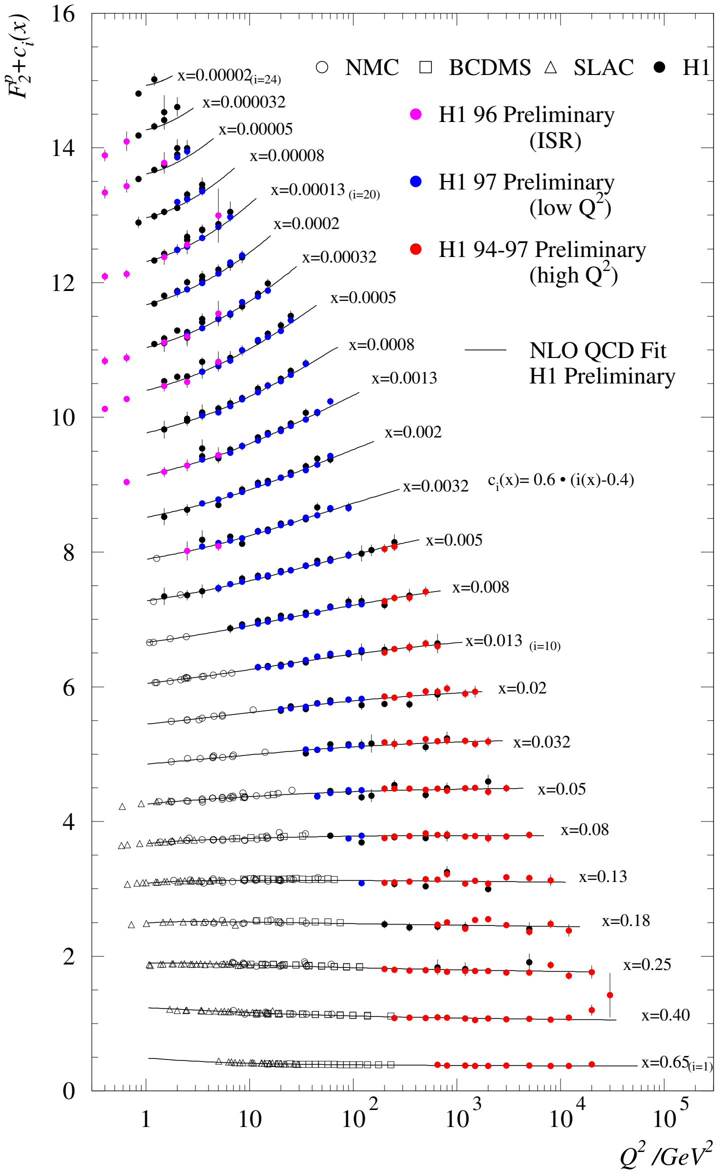

Figure 1.3: Measurement of the structure function $F_2(x, Q^2)$ as a function of Q^2 at different values of x. The figure combines data from H1 [H1C96b, H1C98a], NMC [NMC95], BCDMS [Ben89] and SLAC [Whi92].

where the sum is over the different quark flavours. In next–to–leading order (NLO) in the commonly used $\overline{\mathrm{MS}}$ regularization scheme[6], F_2 is also directly related to the gluon density.

The high centre–of–mass energy at HERA allows one to measure the proton structure function in a wide kinematic region not explored by the preceding fixed–target experiments. Q^2 ranges from $\sim 1\,\mathrm{GeV}^2$ to $\sim 10,000\,\mathrm{GeV}^2$, and x values of approximately 10^{-5} can be reached at small Q^2. Figure 1.3 shows the measurement of $F_2(x, Q^2)$ made by the H1 collaboration together with the data from previous fixed–target experiments.

---

[6] The modified minimal subtraction scheme, e. g. see [Rob90].

1.2 Semi–Inclusive DIS with a Leading Baryon

In a semi–inclusive measurement, the properties of an additional final state particle besides the scattered electron are determined. In part of the DIS events a high–energy baryon (most likely a proton or neutron) is produced with a very small scattering angle. These very forward baryons are subsequentially referred to as leading particles.

The kinematics of the semi–inclusive process $ep \to eNX$, where N denotes a leading nucleon, can be intuitively described in the particle–exchange picture. The proton exchanges a virtual particle which interacts with the electron, whereas the rest of the proton composing the leading baryon acts as “spectator” (see Figure 1.4). The definition of the kinematics is however general and does not depend on the underlying physical model.

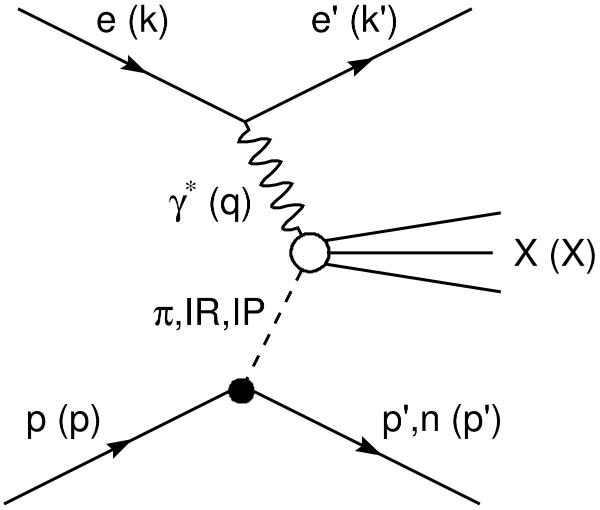

Figure 1.4: Production of a leading proton or neutron in the particle–exchange picture. A pion, reggeon or pomeron is exchanged.

The four–momentum, energy, mass and transverse momentum of the leading baryon is denoted by p', E', m_N and p_T respectively. Besides the two inclusive kinematic variables (e. g. x, Q^2) the kinematics of the semi–inclusive process are described by two additional variables[7]. A Lorentz invariant choice of the kinematic variables is

$$\begin{aligned} z &= 1 - x_{\mathbb{P}} = 1 - \frac{q \cdot (p - p')}{q \cdot p} \simeq \frac{E'}{E_p} \,, \\ t &= (p - p')^2 \simeq -\frac{p_T^2}{z} - (1 - z)\left(\frac{m_N^2}{z} - m_p^2\right) \,. \end{aligned} \tag{1.8}$$

For $p_T \ll \sqrt{p'^2}$, which is in general true for tiny scattering angles, z is equivalent to the fractional energy of the leading baryon. $x_{\mathbb{P}}$ can be identified with the fractional

---

[7] The angle between the electron and baryon scattering plane is not considered here.

momentum of the exchanged object. t, which is always a negative quantity, corresponds to the four–momentum transferred between the proton and the final state baryon. In the particle–exchange picture t can be identified with the squared four–momentum of the exchanged particle. Another useful variable is

$$\beta = \frac{Q^2}{2q \cdot (p - p')} = \frac{x}{1-z} \ , \tag{1.9}$$

which can be interpreted as the Bjorken variable of the exchanged particle.

The mass of the central hadronic system X is related to the variable z, since

$$M_X^2 = (q + p - p')^2 = (1-z)(W^2 + Q^2 - m_p^2) + t - Q^2 \simeq (1-z)W^2 - zQ^2 \ . \tag{1.10}$$

In analogy to the inclusive proton structure function F_2, the four–fold differential cross section for baryon production can be parameterized by a semi–inclusive structure function, $F_2^{LB(4)}$, defined by

$$\frac{\mathrm{d}^4\sigma(ep \to eNX)}{\mathrm{d}x\,\mathrm{d}Q^2\,\mathrm{d}z\,\mathrm{d}t} = \frac{4\pi\alpha^2}{x\,Q^4}\left[1 - y + \frac{y^2}{2[1 + R(x, Q^2, z, t)]}\right] F_2^{LB(4)}(x, Q^2, z, t) \ . \tag{1.11}$$

Since $\beta = x/(1-z)$ this equation can be rewritten with respect to β:

$$\frac{\mathrm{d}^4\sigma(ep \to eNX)}{\mathrm{d}\beta\,\mathrm{d}Q^2\,\mathrm{d}z\,\mathrm{d}t} = \frac{4\pi\alpha^2}{\beta\,Q^4}\left[1 - y + \frac{y^2}{2[1 + R(\beta, Q^2, z, t)]}\right] F_2^{LB(4)}(\beta, Q^2, z, t) \ . \tag{1.12}$$

The structure function $F_2^{LB(4)}$ is denoted by $F_2^{LP(4)}$ and $F_2^{LN(4)}$ for the semi–inclusive processes which have final state protons and neutrons respectively.

1.3 Hadron–Hadron Interactions

In hadronic interactions the appropriate QCD scale is given by the momentum transferred. For large momentum transfer, which is referred to as hard interaction, the strong coupling constant is small, which allows one to apply pQCD. However, the bulk of the hadronic interactions take place at low momentum transfer, where a perturbative calculation is not possible due to large $\alpha_s(Q^2)$. In this non–perturbative regime, one has to rely on phenomenological approaches. Regge theory provides a powerful apparatus being able to describe soft hadronic cross sections.

1.3.1 Regge Theory in a Nutshell

Since the postulation of the pion by Yukawa in 1935 [Yuk35], the interaction between hadrons, in particular nucleons, has been attempted to be described by meson exchange models. In the One–Pion–Exchange (OPE) model (see [Dre61]) the scattering amplitude corresponds to the exchange of a particle with fixed angular momentum. The Regge theory of potential scattering [Reg59] provides a further development of this concept. The angular momentum is treated as a continuous complex variable and the scattering amplitude is associated with the exchange of a Regge trajectory of composite particles. This formalism permits to avoid divergences which are present in the OPE model. Detailed and comprehensive reviews of Regge theory can be found in, for example, [Col84, Kai79, Alb81, Gou83]. Here only some relevant results are briefly summarized.

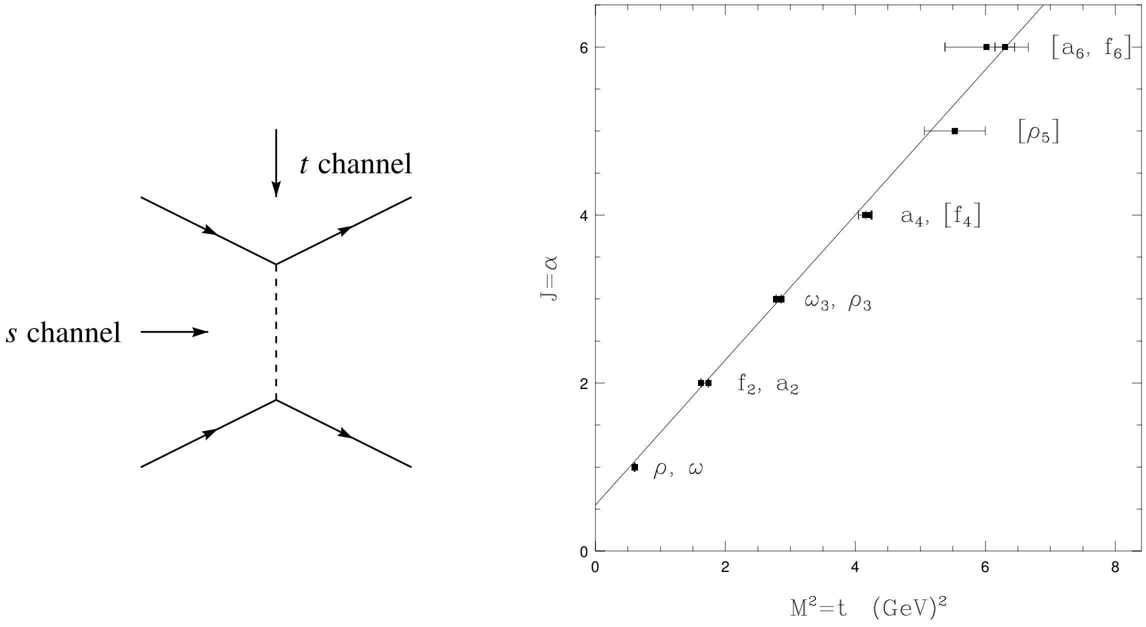

(a) (b)

Figure 1.5: (a) Diagrammatic representation of a generalized s and t channel process. (b) Reggeon trajectory. Shown is the spin of the resonances as a function of their squared mass, which is identified as t (from [Lan94]).

The Regge Trajectory

The Regge trajectory is represented by a linear function in t:

$$\alpha(t) = \alpha_0 + \alpha' \cdot t \;, \tag{1.13}$$

where α_0 and α' are referred to as intercept and slope (shrinkage) parameter. One distinguishes two regions of t. For $t < 0$ (s channel process), the trajectory is exchanged between the two scattering hadrons. In the t channel process ($t > 0$), t can be related to the squared mass of the channel resonances, which occur at integer (meson trajectory) or half integer (baryon trajectory) values of $\alpha(t)$, which correspond to the spin of the resonances.

A single trajectory is characterized by a definite set of quantum numbers (isospin I, parity P, charge–conjugation C). In elastic scattering the ρ, ω, a_2 and f_2 trajectories are degenerate, so that they can be combined in a single *reggeon* trajectory as demonstrated in Figure 1.5b. The most important trajectories are:

- pomeron ($\mathbb{P}$), $\alpha_{\mathbb{P}}(t) \simeq 1.08 + 0.25\,\mathrm{GeV}^2 \cdot t$, $I^{PC} = 0^{++}$;
- reggeon ($\mathbb{R}$), $\alpha_{\mathbb{R}}(t) \simeq 0.5 + 0.9\,\mathrm{GeV}^2 \cdot t$;
- pion (π), $\alpha_{\pi}(t) \simeq 0 + 1\,\mathrm{GeV}^2 \cdot t$, $I^{PC} = 0^{-+}$ (π^0).

The pomeron trajectory has the quantum numbers of the vacuum. Its intercept has been determined on the basis of total cross section measurements for pp and $p\bar{p}$ scattering [Don92]. The slope parameter results from an analysis of the elastic scattering data [Don86].

Elastic Cross Sections of Hadronic Interactions

In the asymptotic limit of $s \to \infty$ and $t/s \to 0$, the contribution of a Regge trajectory $\alpha_k(t)$ to the amplitude $A_k^{ij}(s,t)$ of the elastic scattering process $ij \to ij$ is

$$A_k^{ij}(s,t) \sim \hat{\beta}(t) \left(\frac{s}{s_0}\right)^{\alpha_k(t)} , \tag{1.14}$$

where $\hat{\beta}(t)$ is the function specifying the coupling of the trajectory to the external particles, and $s_0 \approx 1\,\mathrm{GeV}^2$ is the hadron mass scale. The differential elastic cross section can then be expressed as

$$\frac{\mathrm{d}\sigma_{el}^{ij}}{\mathrm{d}t} \sim \frac{1}{s^2}\left|A_k^{ij}(s,t)\right|^2 \sim F(t)\left(\frac{s}{s_0}\right)^{2[\alpha_k(t)-1]} . \tag{1.15}$$

Generalizing the findings to the case of the exchange of several trajectories k, the differential cross section for the elastic reaction $ij \to ij$ is given by[8]

$$\frac{\mathrm{d}\sigma_{el}^{ij}}{\mathrm{d}t} = \sum_k \frac{\beta_{ik}^2(t)\beta_{jk}^2(t)}{16\pi}\left(\frac{s}{s_0}\right)^{2[\alpha_k(t)-1]} , \tag{1.16}$$

where $\beta_{ik}(t)$, $\beta_{jk}(t)$ are form–factors parameterizing the coupling of the trajectory $\alpha_k(t)$ to the particles i and j respectively.

In the region $|t| \lesssim 1\,\mathrm{GeV}^2$ the form–factors can be well approximated by an exponential:

$$\beta_{ik}(t) \simeq \beta_{ik}(0)e^{B_{ik}t} . \tag{1.17}$$

For large centre–of–mass energies $\sqrt{s}$ the differential cross section is dominated by pomeron exchange. Due to the linearity of the trajectory (see Equation 1.13) the cross section can be written as

$$\frac{\mathrm{d}\sigma_{el}^{ij}}{\mathrm{d}t} \propto \left(\frac{s}{s_0}\right)^{2[\alpha_{I\!P}(0)-1]} e^{b(s)t} , \tag{1.18}$$

where

$$b(s) = b_0 + 2\alpha'_{I\!P}\ln(s/s_0) . \tag{1.19}$$

With increasing s the forward peak of the cross section ($t \to 0$) becomes sharper, since the slope b is growing. This is commonly called *shrinkage*.

Total Cross Sections of Hadronic Interactions

The total cross section is closely related to the forward elastic scattering amplitude via the *Optical Theorem* (see Figure 1.6):

$$\sigma_T^{ij} \sim \frac{1}{s}\,\mathrm{Im}A_k^{ij}(s,t=0) \sim s^{\alpha_k(0)-1} . \tag{1.20}$$

---

[8] The notation of [Gou83] is used.

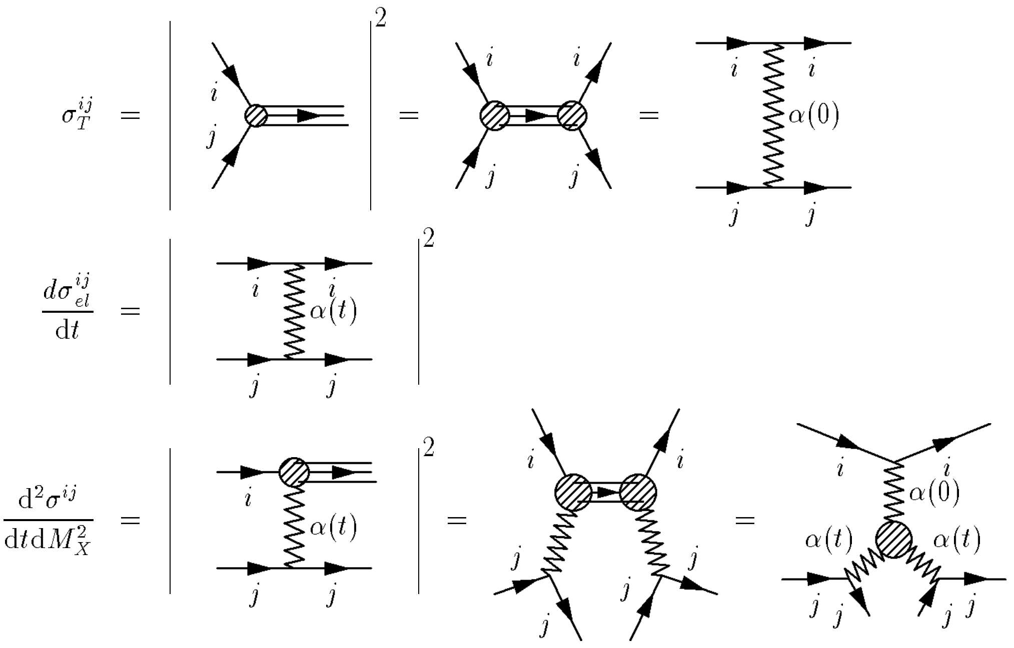

Figure 1.6: Regge diagrams for the total cross section, for elastic scattering and for single dissociation. The sketch for the total cross section σ_T^{ij} illustrates the optical theorem.

The generalization to the case of several exchanged trajectories yields

$$\sigma_T^{ij} = \sum_k \beta_{ik}(0)\beta_{jk}(0)s^{\alpha_k(0)-1} \ . \tag{1.21}$$

Donnachie and Landshoff showed that the total cross section of any hadronic reaction (including photoproduction $\gamma p \to X$) can be fitted to the form [Don92]

$$\sigma_T^{ij}(s) = X_{\mathbb{P}} s^{\alpha_{\mathbb{P}}(0)-1} + Y_{\mathbb{R}} s^{\alpha_{\mathbb{R}}(0)-1} \ , \tag{1.22}$$

with the normalizations $X_{\mathbb{P}}$ and $Y_{\mathbb{R}}$ for the pomeron and reggeon contribution respectively. The quantity of $X_{\mathbb{P}}$ is the same for reactions, where one particle has been replaced by its antiparticle, e. g. pp and $\bar{p}p$, leading to a convergence of both cross sections at high centre–of–mass energies. This is in agreement with a prediction from quantum field theory, known as the Pomerančuk theorem [Pom58], that the cross sections should become the same for particle and antiparticle at infinite high energies.

Cross Section of Single Dissociation

The cross section of the process $ij \to Xj$, in which the particle i dissociates into the system X with invariant mass M_X, is given by (compare Figure 1.6) [Gou83]

$$\frac{d^2\sigma^{ij}}{dt\,dM_X^2} = \sum_{k,l} \frac{\beta_{ik}(0)\beta_{jl}^2(t)g_{kll}(t)}{16\pi s^2}\left(\frac{s}{M_X^2}\right)^{2\alpha_l(t)} \left(M_X^2\right)^{\alpha_k(0)} \ , \tag{1.23}$$

where g_{kll} denotes the couplings between the trajectories. In the case of diffractive dissociation, where $M_X^2 \ll s$, the pomeron dominates the cross section, so that

$$\begin{aligned}\frac{\mathrm{d}^2\sigma_D^{ij}}{\mathrm{d}t\,\mathrm{d}M_X^2} &= \frac{\beta_{i\mathbb{P}}(0)\beta_{j\mathbb{P}}^2(t)g_{\mathbb{P}\mathbb{P}\mathbb{P}}(t)}{16\pi s^2}\left(\frac{s}{M_X^2}\right)^{2\alpha_{\mathbb{P}}(t)}\left(M_X^2\right)^{\alpha_{\mathbb{P}}(0)} \qquad (1.24)\\ &\propto s^{2[\alpha_{\mathbb{P}}(0)-1]}\left(M_X^2\right)^{-\alpha_{\mathbb{P}}(0)}\exp\left[b_D(s,M_X^2)t\right] ,\end{aligned}$$

where the last proportionality is valid in the limit of small $|t|$, where the couplings can be approximated by an exponential. The slope parameter b_D is

$$b_D(s,M_X^2) = b_{D,0} + 2\alpha'_{\mathbb{P}}\ln\left(\frac{s}{M_X^2}\right) , \qquad (1.25)$$

giving a logarithmic shrinkage in s/M_X^2. The t dependence of the cross section parameterization in Equation 1.24 was experimentally verified in various reactions [Coo81].

1.4 Regge Phenomenology in DIS

If factorization holds, the semi–inclusive DIS reaction $ep \to eNX$ can be split into a soft and hard part (compare [Ing85]). The non–perturbative dynamics at the proton vertex is described by a factor $f_{\mathcal{P}/p}(z,t)$, which parameterizes the flux of the particle[9] $\mathcal{P}$ in the proton. The hard deep–inelastic interaction occurs between the electron and the exchanged particle. The four–fold differential cross section for nucleon production can therefore be expressed by

$$\begin{aligned}\frac{\mathrm{d}^4\sigma(ep\to eNX)}{\mathrm{d}x\,\mathrm{d}Q^2\,\mathrm{d}z\,\mathrm{d}t} &= \sum_{\mathcal{P}} f_{\mathcal{P}/p}(z,t)\frac{\mathrm{d}\sigma^{e\mathcal{P}}}{\mathrm{d}x\,\mathrm{d}Q^2} \qquad (1.26)\\ &= \sum_{\mathcal{P}} f_{\mathcal{P}/p}(z,t)\frac{4\pi\alpha^2}{x\,Q^4}\left[1-y+\frac{y^2}{2(1+R)}\right]F_2^{\mathcal{P}}(\beta,Q^2) ,\end{aligned}$$

where $F_2^{\mathcal{P}}$ is the structure function of the exchanged particle. Comparing this expression with Equation 1.12, one obtains for the semi–inclusive structure function

$$F_2^{LB(4)}(\beta,Q^2,z,t) = \sum_{\mathcal{P}} f_{\mathcal{P}/p}(z,t)F_2^{\mathcal{P}}(\beta,Q^2) . \qquad (1.27)$$

The flux factors $f_{\mathcal{P}/p}$ can be parameterized by means of Regge phenomenology. Consider the reaction $Ap \to XN$. Since the fractional energy z of the leading nucleon N is related to M_X^2 by $z \simeq 1 - M_X^2/s$ (compare Equation 1.10)[10], Equation 1.23 can be rewritten with respect to z and t:

$$\begin{aligned}\frac{\mathrm{d}^2\sigma^{Ap\to XN}}{\mathrm{d}t\,\mathrm{d}z} &\simeq -s\frac{\mathrm{d}^2\sigma^{Ap\to XN}}{\mathrm{d}t\,\mathrm{d}M_X^2} \qquad (1.28)\\ &\simeq -\sum_{k,\mathcal{P}}\frac{\beta_{Ak}(0)\beta_{p\mathcal{P}}^2(t)g_{k\mathcal{P}\mathcal{P}}(t)}{16\pi}(1-z)^{1-2\alpha_{\mathcal{P}}(t)}\left[(1-z)s\right]^{\alpha_k(0)-1} .\end{aligned}$$

---

[9] The trajectories are identified with the corresponding particles.

[10] s is the squ. centre–of–mass energy of the Ap system, which in DIS ($A = \gamma^*$) corresponds to W^2.

This expression can be splitted into flux factors $f_{\mathcal{P}/p}$ and the Ak cross sections σ^{Ak}:

$$\frac{\mathrm{d}^2\sigma^{Ap\to XN}}{\mathrm{d}t\,\mathrm{d}z} = \sum_{\mathcal{P}} \left[\sum_k \sigma^{Ak}\left([1-z]s\right) \right] f_{\mathcal{P}/p}(z,t) \ , \tag{1.29}$$

with

$$\begin{aligned} f_{\mathcal{P}/p}(z,t) &\propto \beta^2_{p\mathcal{P}}(t)\,(1-z)^{1-2\alpha_{\mathcal{P}}(t)} \ , &(1.30)\\ \sigma^{Ak}\left([1-z]s\right) &\propto \beta_{Ak}(0)\ [(1-z)s]^{\alpha_k(0)-1} \ . &(1.31)\end{aligned}$$

It should be emphasized, that the z shape of the flux factor is controlled by the trajectory $\alpha(t)$ of the exchanged particle. The pomeron flux factor strongly rises with increasing z. For $z \gg 0.9$, pomeron exchange is the dominant contribution to the reaction $Ap \to Xp$. At fixed t the pion flux factor increases with decreasing z. Thus, pion exchange becomes an important production mechanism for the process $Ap \to XN$ at intermediate values of z $(0.6 \lesssim z \lesssim 0.9)$.

In Section 5.7 it will be demonstrated that for $z \geq 0.7$ the deep–inelastic production of leading protons and neutrons with small transverse momentum can be described by Regge phenomenology. Neutron production, which demands charge exchange, is dominated by pion exchange, whereas the observed proton cross section requires pion, reggeon and pomeron exchange.

1.5 DIS on a Virtual Pion

Pion exchange is believed to play a significant role in semi–inclusive hadronic interactions [Pum73]. As demonstrated in the previous section, its contribution to the cross section of the reaction $Ap \to XN$ can be parameterized by means of an universal flux factor. Thus, the question arises, if the proton itself, i. e. its structure function, comprises contributions of virtual pions. In the following section experimental indications for the pion content of the proton are briefly discussed.

1.5.1 The Pion Content of the Proton

Assuming isospin invariance the parton distribution functions of the neutron $q_n(x,Q^2)$ are directly related to the proton quark densities $q_p(x,Q^2)$:

$$u_n = d_p,\ d_n = u_p,\ \bar{u}_n = \bar{d}_p,\ \bar{d}_n = \bar{u}_p,\ s_n = s_p,\ \text{and etc.}$$

Thus, the difference between the proton and neutron structure function, expressed in terms of valence and sea quark distributions in the proton, is given by

$$F_2^p(x,Q^2) - F_2^n(x,Q^2) = \frac{1}{3}x[u_v(x,Q^2) - d_v(x,Q^2)] + \frac{2}{3}x[\bar{u}(x,Q^2) - \bar{d}(x,Q^2)] \ . \tag{1.32}$$

Integrating this equation over x and considering, that the integrated valence quark distributions have to fulfil the sum rules

$$\int_0^1 \mathrm{d}x\, u_v(x,Q^2) = 2 \ , \quad \int_0^1 \mathrm{d}x\, d_v(x,Q^2) = 1 \ , \tag{1.33}$$

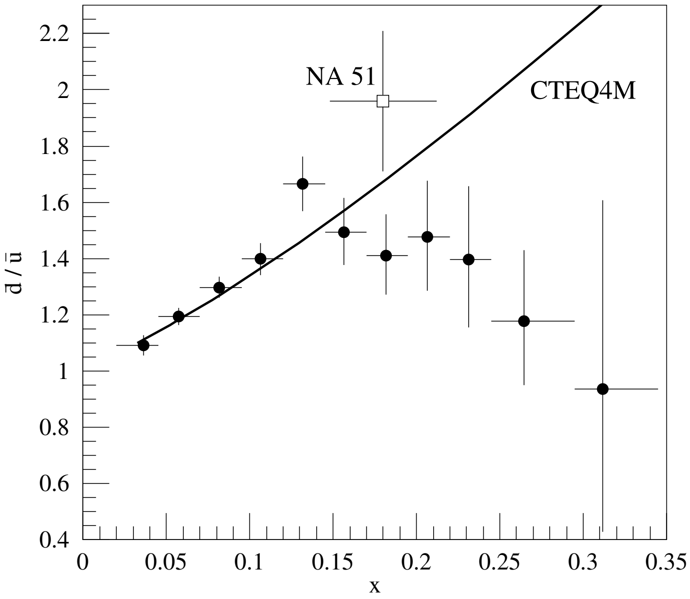

Figure 1.7: The ratio of $\bar{d}/\bar{u}$ in the proton as a function of x, obtained by the E866/NuSea Collaboration. The data are compared to the CTEQ4M parameterization of the proton parton distributions [Lai97]. Also plotted is the result from NA51 (from [E866-98]).

one obtains

$$I_G = \int_0^1 \mathrm{d}x \, \frac{1}{x} \left[F_2^p(x,Q^2) - F_2^n(x,Q^2) \right] = \frac{1}{3} + \frac{2}{3} \int_0^1 \left[\bar{u}(x,Q^2) - \bar{d}(x,Q^2) \right] . \tag{1.34}$$

If the sea is flavour symmetric, $\bar{u} = \bar{d}$, the integral over the sea distribution vanishes, yielding the *Gottfried* sum rule [Got67]:

$$I_G = \frac{1}{3} . \tag{1.35}$$

Measurements of deep–inelastic scattering of muons on hydrogen and deuterium by the NMC Collaboration revealed a significant and large violation of the Gottfried sum rule [NMC91, NMC94]. Extrapolating the measurement of $F_2^p - F_2^n$, obtained in the region $0.004 \leq x \leq 0.8$, to the full range in x, they evaluated the integral I_G [NMC94]:

$$I_G = 0.235 \pm 0.026 . \tag{1.36}$$

The violation of the flavour symmetry of the sea has been confirmed in semi–inclusive DIS [HER98] and in dimuon production in Drell–Yan processes [NA51-94, E866-98]. Figure 1.7 shows the recent measurement of the $\bar{d}/\bar{u}$ ratio in the range $0.020 < x < 0.345$, obtained by the E866/NuSea Collaboration [E866-98].

It has been shown that perturbative mechanisms or effects due to the finite quark mass cannot account for the observed large violation of the Gottfried sum rule [Kum98]. The pion cloud model, however, can provide an explanation for the origin of the asymmetry of the flavour sea [Tho83, Hol96a, Kum98]. The pion fluctuates in multi–particle

Fock states within the time allowed by the uncertainty principle. The predominant fluctuations are the πN states due to the low mass of the associated particles. The physical proton can be approximated by the following superposition[11]:

$$|p>_{phys} \simeq (1-a)|p>_{bare} + a\left(\frac{1}{3}|\pi^0 p> + \frac{2}{3}|\pi^+ n>\right) \ . \tag{1.37}$$

The contribution of $|\pi^+ n>$ is twice the one of $|\pi^0 p>$ due to the different Clebsch–Gordon coefficients. Looking at the quark content of the fluctuations, one recognizes immediately that $\bar{d}$ is favoured over $\bar{u}$.

The E866/NuSea Collaboration has demonstrated that their measurement of the light antiquark flavour asymmetry in the nucleon sea is in good agreement with the virtual pion model [E866-98a].

It is interesting to note, that also the inclusive proton structure function can be successfully described by a model, in which the sea partons mainly arise from pionic fluctuations [Edi98].

1.5.2 Pion Exchange in DIS

The experimental results indicate, that the cloud of virtual pions contained in the proton are an important source of the sea quarks. Since deep–inelastic *ep* scattering at low x probes the sea of partons inside the proton, one hopes to obtain information about the structure of the pion at HERA, provided evidence for the virtual pion is experimentally observed [Hol94, Lev95, Kop96].

Already in 1972 Sullivan pointed out, that π^+ exchange plays an important role for the deep–inelastic electro–production of neutrons [Sul72]. Since the production of a neutron requires the exchange of charge for the transition $p \to n$, neutral trajectories ($\mathbb{P}$, f_2, ω) cannot contribute to the cross section via the process sketched in Figure 1.4. It has been shown, that for $0.7 \lesssim z \lesssim 0.9$ and $|t| \lesssim 0.25\,\mathrm{GeV}^2$ neutrons are predominantly produced by pion exchange [Kop96]. Thus, in this kinematic region, the measurement of the semi–inclusive structure function $F_2^{LN(4)}$, as defined in Equation 1.12, might probe the pion content, since Equation 1.27 now simplifies to

$$F_2^{LN(4)}(\beta, Q^2, z, t) \simeq f_{\pi^+/p}(z,t) F_2^{\pi}(x, Q^2) \ . \tag{1.38}$$

Provided the flux factor $f_{\pi^+/p}$ is known, the measurement allows to extract the pion structure function F_2^{π}. The pion flux factor has been constrained using hadron–hadron data [Hol94, Hol96] [12]. In the light–cone representation it is given as a function of z and p_T by [Hol94]

$$f_{\pi^+/p}(z, p_T) = \frac{2}{3}\frac{3}{4\pi}\frac{g^2_{p\pi N}}{4\pi}\frac{[(1-z)^2 m_n^2 + p_T^2]}{z^2(1-z)\left[m_n^2 - M^2_{\pi n}(z, p_T^2)\right]^2}|F(z, p_T^2)|^2 \ , \tag{1.39}$$

where m_n is the mass of the neutron and the non–perturbative strong coupling constant is known from low–energy physics: $g^2_{p\pi N}/(4\pi) = 13.6$ [Tim91]. $M_{\pi n}$ is the invariant

---

[11] Some models also include $\pi\Delta$ fluctuations.

[12] For more details see Section 3.5.1.

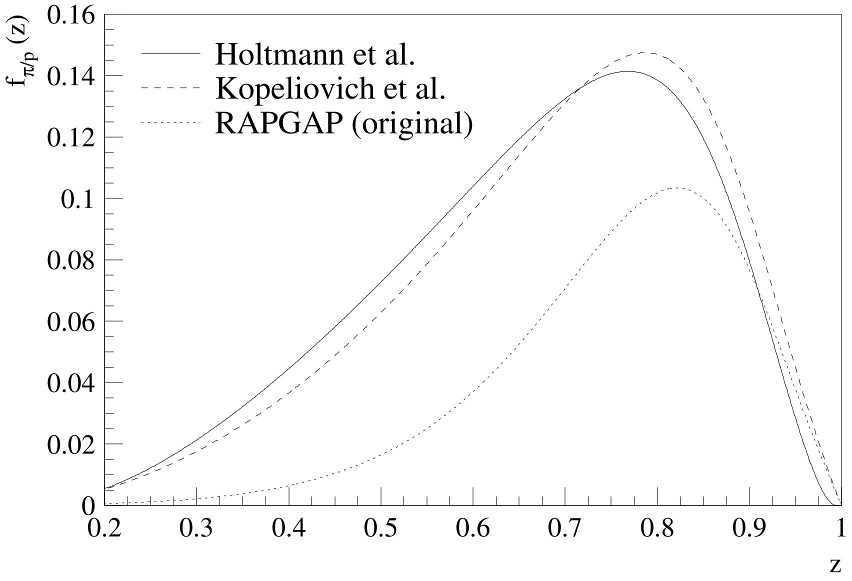

Figure 1.8: The pion flux factor $f_{\pi^+/p}$ integrated over the region $0 \leq p_T \leq 200\,\mathrm{MeV}$. Shown is the parameterization of Holtmann et al. [Hol94] compared to the one by Kopeliovich et al. [Kop96]. The flux–factor, which is implemented in the original version of the RAPGAP generator, has a much lower magnitude.

mass of the intermediate two–body pion–neutron Fock state

$$M^2_{\pi n}(z, p_T^2) = \frac{m_n^2 + p_T^2}{z} + \frac{m_\pi^2 + p_T^2}{1-z} \; . \tag{1.40}$$

The vertex light–cone form factor $F(z, p_T^2)$ is parameterized as [Zol92, Hol96]

$$F(z, p_T^2) = \exp\left[-\frac{R^2_{\pi n}}{2}(M^2_{\pi n}(z, p_T^2) - m_n^2)\right] \; , \tag{1.41}$$

where $R_{\pi n} = 0.93\,\mathrm{GeV}^{-1}$ [Hol96]. The flux factor can be equivalently expressed with respect to z and t, the squared four–momentum transfer between the initial state proton and the final state neutron [Prz97]:

$$f_{\pi^+/p}(z,t) = \frac{2}{3}\frac{3}{4\pi}\frac{g^2_{p\pi N}}{4\pi}(1-z)\frac{-t}{(m_\pi^2 - t)^2}\exp\left[-R^2_{\pi n}\frac{m_\pi^2 - t}{1-z}\right] \; . \tag{1.42}$$

Another evaluation of the flux factor using a reggeized form yields [Kop96]

$$f_{\pi^+/p}(z,t) = \frac{2}{3}\frac{3g^2_{p\pi N}}{16\pi^2}\,(1-z)^{1-2\alpha'_\pi t}\,\frac{-t}{(m_\pi^2 - t)^2}\exp\left[-2R_\pi^2(m_\pi^2 - t)\right] \; , \tag{1.43}$$

where the slope of the pion trajectory $\alpha'_\pi = 1\ \mathrm{GeV}^{-2}$ and the non–perturbative radius is $R_\pi^2 = 0.3\ \mathrm{GeV}^{-2}$. Figure 1.8 demonstrates that the shape and the magnitude of both parameterizations of the pion flux factor are very similar.

Also neutral pions can be exchanged, leading to the production of forward protons. The flux factor $f_{\pi^0/p}$ is exactly half of the charged pion flux factor $f_{\pi^+/p}$:

$$f_{\pi^0/p}(z,t) = \frac{1}{2} f_{\pi^+/p}(z,t) \ , \tag{1.44}$$

because of the different Clebsch–Gordon coefficient (1/3 instead of 2/3). The leading proton, however, cannot provide a conclusive signature for the pion content, since other exchanges ($\mathbb{P}$, f_2, ω) dominate the cross section (see Section 5.7).

The possibility to study the pion structure at low x was the key idea, which inspired the ZEUS and H1 Collaboration to install a forward neutron calorimeter [Bha97, Bec95]. The parton distributions of the pion have previously been constrained only in the $x \gtrsim 0.2$ region by Drell–Yan and prompt photon production measurements of πN scattering (see Section 5.9.1). The determination of $F_2^{LN(4)}$ at HERA would allow to constrain the pion structure function at values of x which are more than an order of magnitude smaller.

In this work, the measurement of $F_2^{LN(4)}$ integrated over $p_T \leq 200\,\mathrm{MeV}$ is carried out. This data is used to constrain F_2^{π} for the first time at HERA (see Section 5.9.2).

1.5.3 Monte Carlo Implementation of the π Exchange Model

The pion exchange formalism is implemented in the RAPGAP and POMPYT Monte Carlo programs [Jun95, Bru96]. Both Monte Carlo generators have been originally developed to simulate diffractive scattering via the exchange of a pomeron.

RAPGAP is a full event generator for deep–inelastic scattering with the capability of simulating diffraction and pion exchange. For the Monte Carlo studies shown in this work, the parameterization of the pion flux factor, which is implemented in the original program (see Figure 1.8), was replaced by the parameterization given in Equation 1.42. The fragmentation in RAPGAP is performed with the Lund string model [And83] as implemented in the JETSET [Sjö94] Monte Carlo program (see Section 1.6.1).

POMPYT also simulates the complete hadronic final state. The same parameterization of the pion flux factor as in the modified RAPGAP version is used. The hard scattering is treated based on the PYTHIA program [Sjö94] and the subsequent hadronization is performed with JETSET.

1.6 An Alternative Approach of Leading Baryon Production

If a DIS process is mediated by a colour–singlet exchange, the proton remnant and the central hadronic system X are colourless, leading to a separation in rapidity[13]. This is not the case in standard DIS. Figure 1.9a shows a typical DIS event initiated by boson–gluon–fusion, which dominates the ep cross section at $x \lesssim 10^{-3}$. The struck gluon takes away colour, which produces a coloured proton remnant as well as a coloured hadronic

---

[13] The rapidity of a produced particle can be approximated by its pseudo–rapidity $\eta = -\ln\tan(\theta/2)$, where θ is the polar angle of the particle.

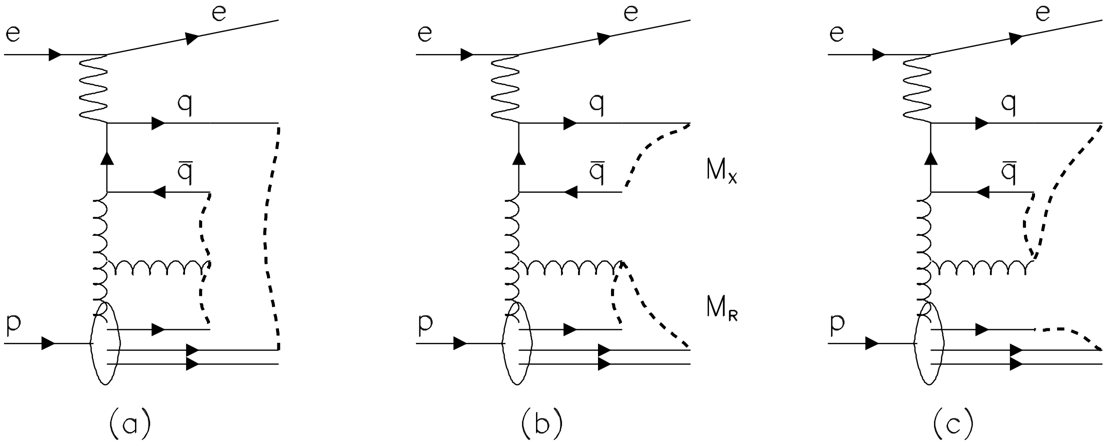

Figure 1.9: Rearrangement of the colour topology in the final state. Shown is the string configuration in a DIS boson–gluon–fusion event: (a) conventional Lund string connection of partons, and (b,c) after reconnection due to soft colour interaction. (b) leads to the dissociation of the remnant into the invariant mass M_R, and (c) results in a leading proton (from [Edi96]).

system, originating from the hard photon–gluon interaction. Thus, both systems are connected via colour strings, which results in the subsequential production of hadrons during the fragmentation process in the entire rapidity region between both systems. Therefore the probability of producing a high–energy baryon or a large rapidity gap is strongly suppressed.

1.6.1 The Fragmentation Process

The *Lund string model* [And83] is nowadays the most successful model to describe hadronization processes in the photon fragmentation region. The JETSET program, which is the Monte Carlo realization of this model [Sjö94], is used by most Monte Carlo event generators to simulate hadronization.

The Lund string model is built on the physical picture of a colour flux tube, which is being stretched between the partons moving apart from the common interaction vertex. Due to confinement, the potential energy of the string rises linearly with its dimension, leading to a break–up of the flux tube and the creation of a quark–antiquark pair. This consequentially results in the formation of new strings. Mesons can be produced by a combination of a quark and an antiquark of two adjacent string breakings. In some cases a colour string also breaks up into an antidiquark–diquark pair, leading to the potential production of baryons.

The production cross section for leading baryons predicted by the Lund string model is, however, much lower than in reality, in particular no baryons with very high z, which cause large rapidity gaps, are produced.

In order to explain those events, without using the pomeron exchange concept, alternative models were introduced, which are based on soft non–perturbative interactions occurring before the hadronization process [Buc95, Edi96].

1.6.2 Soft Gluon Interactions

The model of Buchmüller and Hebecker [Buc95] is based on boson–gluon–fusion as underlying partonic process (compare Figure 1.9a). The quark–antiquark pair, which is originally produced in a colour octet state, changes its colour randomly because of additional soft interactions with the colour field of the proton remnant. With a certain probability the original colour octet state might be transformed into a colour singlet state, so that no colour field is located between the quark–antiquark pair and the proton remnant, yielding a gap in rapidity. For a sufficiently fast rotation of the colour spin, the probability for the different colour states should be statistically distributed. The quark–antiquark pair would be in the colour octet state with a probability of 8/9 and in the colour singlet state with a probability of 1/9. This prediction is in agreement with the observation, that a large rapidity gap event is produced in $\sim 10\%$ of all DIS events [ZEU93, H1C94].

Soft Colour Interactions in the LEPTO Monte Carlo Model

A similar approach is the *soft colour interaction* (SCI) model [Edi96, Edi97]. Before the hadronization process, any pair of partons, which take part in the hard interaction, plus the remaining quarks in the proton remnant, can undergo a soft interaction, exchanging only the colour but no momentum. The probability for an interaction, which can be viewed as the exchange of a soft non–perturbative gluon, is described by a single phenomenological parameter R. The soft colour interaction can change the colour topology of the ep scattering event, such that colour singlet subsystems arise separated in rapidity (compare Figure 1.9b,c), which may lead to the formation of a baryon out of the proton remnant. In the case of boson–gluon–fusion this baryon is most likely a leading proton.

A leading neutron can be produced, if a sea antiquark enters the hard interaction. A partner sea quark in the proton remnant is assigned, which is given a momentum based on the assumption, that both quarks originate from the same gluon splitting.

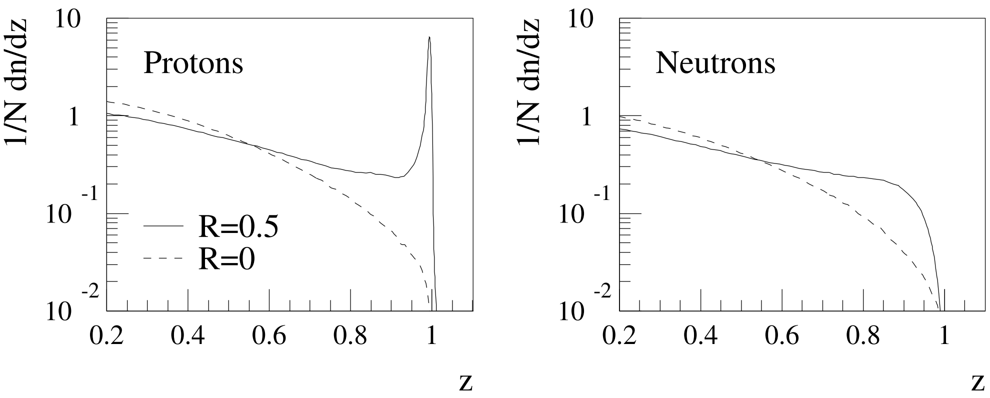

Figure 1.10: z distributions for leading protons and neutrons produced by Lepto. *Shown are the nucleon spectra obtained without ($R = 0$) and with soft colour interaction ($R = 0.5$).*

The proton remnant contains also three valence quarks, which are split into a quark and a diquark. Thus, the remnant partons, together with the interacting sea antiquark, form two colour singlet systems. The situation in which the remnant sea quark is paired with the valence diquark might lead to the production of a neutron.

The SCI model is implemented in the LEPTO Monte Carlo program [Ing97]. LEPTO is a general event generator for deep–inelastic lepton–nucleon scattering, based on leading order electroweak cross sections. QCD matrix elements for gluon radiation and boson–gluon fusion are implemented to first order, and higher order QCD radiation is simulated by parton showers. The fragmentation, which takes place after the soft colour interaction is performed using the JETSET program.

Figure 1.10 demonstrates the effect of the soft colour interaction mechanism. Shown are the z spectra for leading protons and neutrons generated by LEPTO, obtained with and without SCI. The SCI mechanism increases the rate of produced nucleons in the region $z \gtrsim 0.6$. SCI also generates the diffractive peak in the proton spectrum at $z \approx 1$.

Chapter 2

The H1 Experiment at HERA

The physics program outlined in the previous chapter defines the experimental requirements which have to be fulfilled in order to study the production of forward neutrons in deep–inelastic scattering.

First of all, a particle accelerator has to provide the high–energy beams of both electrons (or positrons)[1] and protons. Very high centre–of–mass energies are necessary to study the kinematic region of large values of Q^2 and low values of x. The electron–proton collider HERA (*Hadron–Elektron–Ringanlage*) at DESY (*Deutsches Elektronen Synchrotron*) in Hamburg is dedicated for this purpose.

The scattered electron and most of the hadronic final state in a DIS event have to be measured by a system of nearly hermetic detectors which cover the interaction region. This is the task of the multi–purpose H1 detector. For the detection of leading neutrons and protons, which escape the main detector unseen through the beam pipe, a dedicated *Forward Neutron Calorimeter* (FNC) and a *Forward Proton Spectrometer* (FPS) is used.

In this chapter, the HERA collider and the H1 experiment will be shortly described. A detailed discussion of the FNC will be given in the following chapter.

2.1 The HERA collider at DESY

HERA, which was commissioned in 1992, is composed of two separate storage rings with a circumference of 6.3 km [Wii92]. Electrons and protons are separately accelerated up to energies of 27.5 GeV, respectively 820 GeV [2]. The two beam pipes are brought together at the position of the H1 and ZEUS experiments, allowing the two beams to cross at an angle of 0°.

Besides these collider experiments, which have been taking *ep* scattering data since 1992, HERA accommodates two additional *fixed target* experiments. HERMES, which started operation in 1995, makes use of the polarized electron beam to study the spin structure of nucleons. HERA–B is a high rate experiment using the halo of the proton beam for collisions with a target made of tungsten wires. It is currently being set up and will begin to study the expected CP violation in the B^0–$\bar{B}^0$ system in 1999.

---

[1] Throughout this work the incident and scattered electron or positron are referred to as electron.

[2] In 1998 the proton beam energy was increased to 920 GeV.

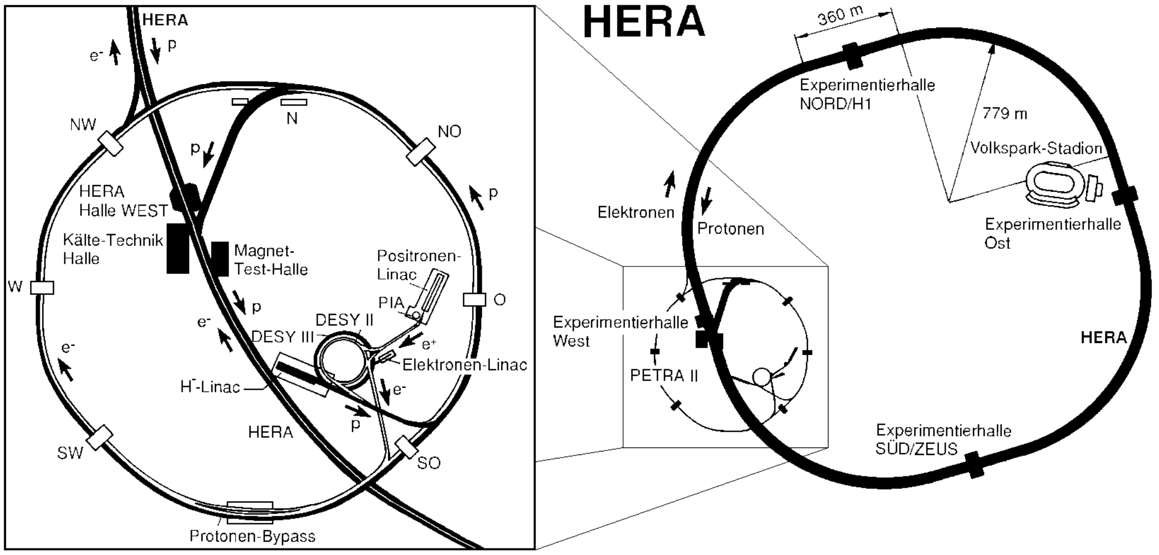

Figure 2.1: The HERA storage ring and its injection and preacceleration system at DESY. The locations of the H1 and ZEUS detector are indicated.

The HERA beams are both structured into 220 bunches separated by 96 ns, of which on average 190 are filled with particles. This leads to a bunch crossing rate of 10.4 MHz. "Crossings" of empty or unpaired bunches can be used for background studies.

2.2 The H1 Experiment

The design of the H1 detector (see Figure 2.2) is comparable to similar detectors being operated at other collider facilities. Tracking detectors, (2) and (3)[3], are positioned close to the nominal interaction point, followed by an electromagnetic and hadronic calorimeter, (4) and (5), a superconducting coil, (6), and the iron yoke which is instrumented with muon chambers, (10). In contrast to the detectors at e^+e^- (LEP) and $p\bar{p}$ (Tevatron) colliders, which are build nearly symmetrical with respect to the interaction point, the H1 detector has a large forward backward asymmetry due to the different types of particle beams and due to the difference in the beam energies. The instrumentation of the H1 detector in the forward region, which is defined by the direction of the proton beam, is more complex, allowing to detect most of the hadronic final state of the deep–inelastic reaction, which is boosted along the direction of the proton beam. The backward region is designed to measure the energy and the angle of the scattered electron covering a kinematic area of four–momentum transfers of $1\,\mathrm{GeV}^2 \lesssim Q^2 \lesssim 100\,\mathrm{GeV}^2$. The detector is nearly hermetic, allowing particles only to escape through the forward and backward beam pipe. However a substantial part of the fragments of the target, and therefore also a large part of the energy flow, escapes

---

[3] Numbers in brackets refer to Figure 2.2.

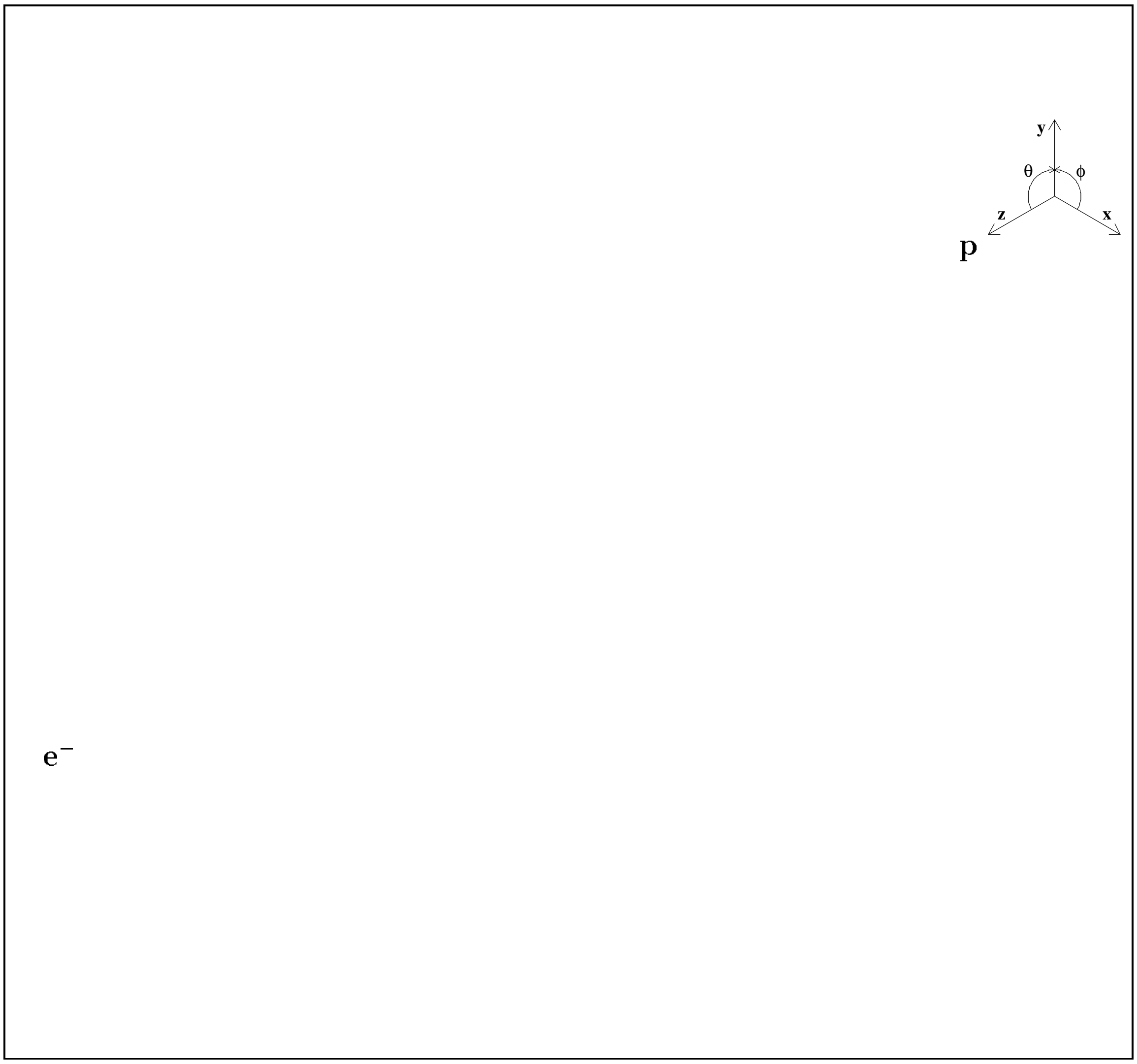

1	Beam pipe and beam magnets	9	Muon chambers
2	Central tracking device	10	Instrumented iron yoke
3	Forward tracking device	11	Forward muon toroid
4	Electromagnetic LAr calorimeter	12	Backward calorimeter (SPACAL)
5	Hadronic LAr calorimeter	13	PLUG calorimeter
6	Superconducting coil (1.15 T)	14	Concrete shielding
7	Compensating magnet	15	Liquid argon cryostat
8	Helium supply for 7		

Figure 2.2: Layout of the H1 detector. It has a size of $\sim 12 \times 10 \times 15$ *m*^{3} *and a weight of* $\sim$ *2800 t. The subdetectors placed in the HERA tunnel are not shown.*

through the forward beam pipe, unseen in the main detector. In order to detect leading protons and neutrons, which are scattered at very low angles close to the proton direction, H1 installed a *Forward Proton Spectrometer* (FPS) and a *Forward Neutron Calorimeter* (FNC), which are located in the HERA tunnel, more than 50 m away from the main detector (not shown in Figure 2.2). The detector components which are relevant for this analysis will be presented shortly in the following. A detailed description of the H1 detector can be found elsewhere [H1C97].

The coordinate system used by the H1 collaboration, and so in this analysis, is indicated in Figure 2.2, with its origin at the position of the nominal interaction point. The polar angle θ is defined with respect to the direction of the z–axis and the azimuthal angle ϕ is in the xy–plane.

- **The Central Tracking Device**, (2) , covers the region of $-1.5\,\mathrm{m} < z < 2.5\,\mathrm{m}$ allowing charged track reconstruction in the central region. It comprises six tracking chambers: two multiwired proportional chambers (MWPC), which supply fast trigger signals, and four drift chambers, providing track reconstruction and particle identification by measuring the differential energy loss of charged particles. These chambers are arranged concentrically around the beam pipe and the *Central Silicon Tracker*.

  Starting from small radii r, the beam pipe is surrounded by the *Central Inner Proportional Chamber* (CIP), the *Central Inner Z–Chamber* (CIZ), the inner *Central Jet Chamber* (CJC1), the *Central Outer Z–Chamber* (COZ) and the outer *Central Jet Chamber* (CJC2). The CJC1, which covers an angular range of $15^\circ < \theta < 165^\circ$, and the CJC2 are optimized to measure particle tracks in the $r\phi$–plane with a space point resolution of $170\,\mu$m. The resolution of those chambers for the measurement of the z–coordinate, which is based on the charge devision technique, is rather poor. A precise measurement of this coordinate with a resolution of $300\,\mu$m is provided by the two z–chambers CIZ and COZ.

- **The Forward Tracking Device**, (3) , detects charged particles which are produced with a polar angle between $7^\circ < \theta < 25^\circ$. It consists of three modules, which include a MWPC for fast triggering, a planar and a radial drift chamber providing track measurements in the θ and ϕ–coordinates respectively, and a transition radiation detector for particle identification.

- **The Backward Drift Chamber** (BDC), close to (12) , is optimized to measure the angle of the scattered electron in a range of $153^\circ < \theta < 177.5^\circ$ and is situated in front of the backward calorimeter [Sch97, Kat97]. The BDC is subdived into eight octants each consisting of 32 drift cells which are arranged in four double layers. The BDC measures the polar angle of isolated tracks with a resolution of $\sim 0.3\,\mathrm{mrad}$ [Kat97].

- **The Liquid Argon Calorimeter** covers the central and forward region (polar angles with $4^\circ < \theta < 153^\circ$) and is divided into an electromagnetic and a hadronic part, providing the precise energy measurement of high Q^2 scattered electrons ($Q^2 \gtrsim 100\,\mathrm{GeV}^2$) and the hadronic final state.

The electromagnetic part, (4) , is a lead–liquid argon (LAr) sampling calorimeter, of which the depth varies between 20 and 30 radiation length. The hadronic part, (5) , which has a depth of 4–8 hadronic interaction length is made of a stainless steel–LAr structure. In both calorimeter sections particle energies are measured by ionization and subsequent charge collection.

The liquid argon calorimeter has a hadronic energy resolution of $\sigma(E)/E = 50\%/\sqrt{E[\mathrm{GeV}]} \oplus 2\%$ as measured in a pion beam [H1C93] and its scale is known with a precision of 4%.

- **The backward calorimeter SPACAL**, (12) , encloses polar angles between 153° and 177.5°. It is a so called *Spaghetti Calorimeter* which is made of a lead–scintillating fibre matrix [H1S96]. It was installed in the H1 detector together with the BDC in the beginning of 1995 replacing the old backward proportional chamber and the old electromagnetic sandwich calorimeter BEMC.

  The SPACAL is divided into two sections: an electromagnetic part with a depth of 27 radiation length and a hadronic part with a thickness of only one hadronic interaction length. The calorimeter has an excellent electromagnetic energy resolution of $\sigma(E)/E = 7.1\%/\sqrt{E[\mathrm{GeV}]} \oplus 1\%$ [H1S97], and the electromagnetic energy scale is known with a precision of 1% to 3% depending on the energy of the incident electron. Since the hadronic final state normally does not extend into the SPACAL, its hadronic section is not optimized for a precise energy determination. Instead this part is mainly used for e/π separation and as a time of flight counter to reject out–of–time background mostly emerging from interactions of the beam with the residual gas in the beam pipe.

  The SPACAL is of particular relevance for this analysis and in general for analysises of deep–inelastic scattering at low and intermediate Q^2. Scattered electrons with $1\,\mathrm{GeV}^2 \lesssim Q^2 \lesssim 100\,\mathrm{GeV}^2$ are within the acceptance region of the SPACAL.

- **The Time of Flight (TOF) System** with a time resolution of 2–4 ns is used to reject the beam induced background. It consists of several scintillation counters which are placed along the beam pipe in the forward and backward region and uses the time separation between ep interactions at the nominal interaction vertex and proton beam induced background.

- **The Forward Neutron Calorimeter** (FNC) located at $z = 107\,\mathrm{m}$ downstream in the HERA tunnel detects high–energy neutrons which are produced at very low scattering angles of $\theta \lesssim 0.6\,\mathrm{mrad}$. A sketch of its position with respect to the HERA beam line is shown in Figure 2.3. The proton beam line is bent up, allowing the detection of forward neutral particles at 0°–scattering angles. A neutron produced at very low angles moves along the beam pipe, undisturbed by the magnetic field of the beam optics and passes the beam pipe at 93 m. At the position of the neutron exit window, the diameter of the beam pipe is conically decreasing in order to reduce the material which the neutron has to pass. No dead material is placed between the exit window and the lead shielding covering the FNC.

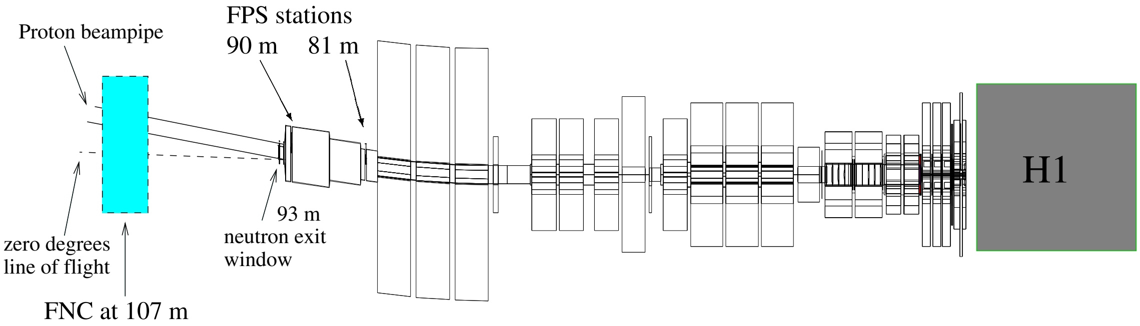

Figure 2.3: Sketch of the HERA forward beam line including FNC and FPS (not to scale). Shown are the positions of the calorimeter at 107 m and of the two vertical roman pot stations at 81 m and 90 m. The magnets of the proton beam optics are also indicated.

This detector is of crucial relevance for the analysis presented in this work and will therefore be described in detail in the following chapter.

- **The Forward Proton Spectrometer** (FPS) is designed to measure the momenta of high–energy protons with scattering angles of $\theta \lesssim 0.5\,\mathrm{mrad}$ with respect to the proton beam [Lis97, H1C96]. The HERA dipole magnets adjacent to the interaction region are employed as spectrometer elements (see Figure 2.3). Protons which have lost more than $\sim$ 10% of their energy in *ep* interactions appear after about 80 m at a distance of several millimeters from the nominal beam orbit so that they can be registered in detectors close to the circulating beam. The detector elements are mounted inside plunger vessels, so called Roman Pots. They are retracted during injection and are brought close to the beam after stable luminosity conditions are reached. Since 1995 H1 has been operating two FPS stations which approach the beam from above and which can detect leading protons with $550\,\mathrm{GeV} < E < 750\,\mathrm{GeV}$. In 1996 two additional horizontal stations were installed which enlarge the kinematic range up to the proton beam energy and enables the measurement of the transverse momentum of the scattered proton.

- **The Luminosity System** (see Figure 2.4) comprises two small crystal calorimeters, which are situated in the backward region upstream in the HERA tunnel. Electrons and photons from the *Bethe–Heitler* (BH) process $ep \to ep\gamma$ [Bet34] are detected in the electron tagger (ET) and the photon detector (PD), situated at z–positions of $-33.4\,\mathrm{m}$ and $-102.9\,\mathrm{m}$ respectively. The photon tagger is protected from the high synchrotron radiation flux by a lead absorber and a water Čerenkov counter which distinguishes between low energetic photons of the synchrotron radiation and high–energy photons from the BH process. The instantaneous luminosity can be measured on–line by counting the rate of coincidences of tagged electrons and photons taking into account the detector acceptance, since the cross section of the BH bremsstrahlung process is very high and theoretically well known. Since 1995, H1 uses the more precise single photon method for the

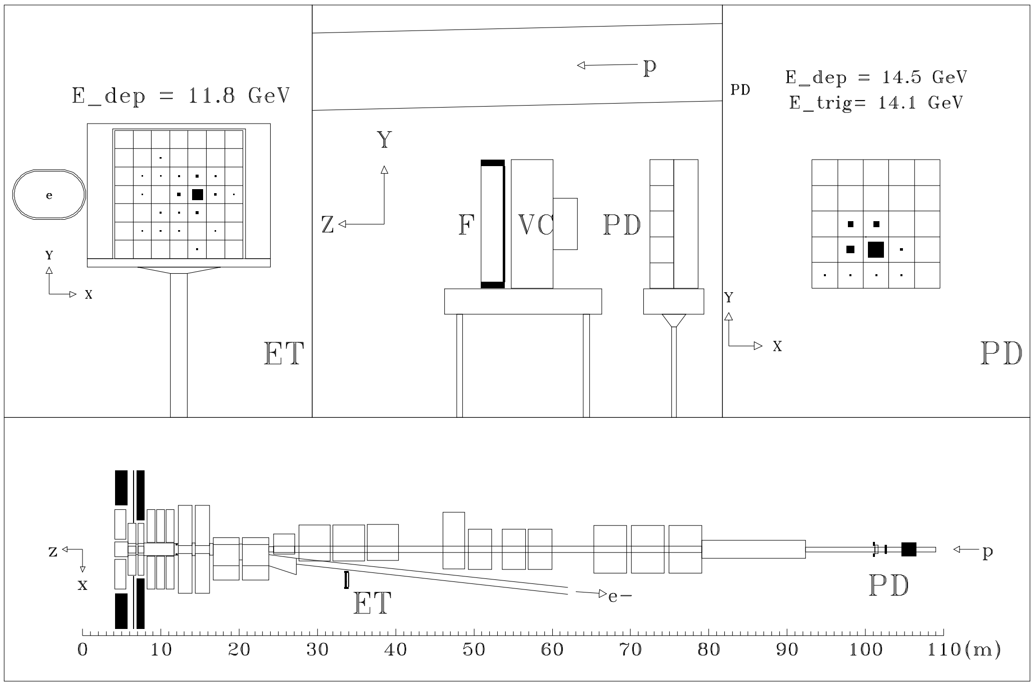

Figure 2.4: Bremsstrahlung event measured by the luminosity system. In the lower picture the luminosity system located in the HERA tunnel is sketched. The upper middle picture shows the photon detector (PD) which is located close to the beam pipe (p) and shielded by a lead filter (F) and a Čerenkov veto counter (VC). The upper left and right panel show the deposited energy of the electron and the photon respectively.

off–line calculation of the integrated luminosity, which is soley based on counting the photon rate above a certain energy threshold [H1C96a]. In 1996, the average luminosity was $2.6 \cdot 10^{30}\text{cm}^{-2}\text{s}^{-1}$ at typical beam currents of $I_p = 60\,\text{mA}$ and $I_e = 21\,\text{mA}$ for protons and electrons respectively. The integrated luminosity of the data stored on tape amounted to approximately $9\,\text{pb}^{-1}$ in 1996.

- **The Trigger and Data Acquisition System**. The task of a trigger system is to select interesting events out of the flow of signals registered in the different detector components. The rate of background events which stem from synchrotron radiation, proton–beam–gas and proton–beam–wall interaction exceeds by far the rate of physically interesting events. The background and *ep* interaction processes with very high cross sections (BH bremsstrahlung, photoproduction) have to be suppressed or heavily prescaled in order to meet the capacity of the readout system.

  H1's trigger and data acquisition system is made of four different steps, so called *levels* (L1, L2, L4, L5).

  The first trigger level L1 is based on simple logical combinations of the information, provided by the different sub-detectors latest $2.3\,\mu$s after the bunch crossing, during which a potential interaction occured. Within this time, which corresponds to the time of 24 bunch crossings, the full event information is stored in pipe lines. This leads to the capability of accepting a new event, which happens already in the first bunch crossing after the previous trigger. Therefore the first trigger level is a dead time free system. The information of the different subdetectors are converted into trigger elements which are subsequently combined into 128 possible subtriggers by the central trigger logic. An event is accepted if at least one subtrigger condition is fulfilled. Subtriggers with very high rate can be prescaled (i. e. only every n–th positive trigger decision is accepted) in order to meet the capacity of the readout bandwidth.

The second level trigger L2 validates the L1 decision within 20 μs. L2 is based on the same trigger elements like L1 but uses more complex algorithms of combining this information. After a positive L2 decision, the event information from the different sub-detectors is fully digitized and transferred to the L4 processor farm. L4 is a software filter running part of the reconstruction code on 32 parallel processors. About 20% of the events pass the L4 selection cut and are written to magnetic tape with a rate of $\sim$ 10 Hz. A small fraction of about 1% of the rejected events is kept for monitoring purposes.

Finally at L5 the accepted events on tape are fully reconstructed and classified according to the underlying physics process, e. g. photoproduction or deep–inelastic scattering. If an event cannot be classified, it is rejected except for 1% of the events which are again kept for monitoring purposes. The main information of the classified events is stored on hard disks in the format of *data summary tapes* (DST). This is usually the starting point for any physics analysis.

Chapter 3

The Forward Neutron Calorimeter

To detect highly energetic neutrons, which are produced at very small scattering angles in *ep* interaction, H1 installed a *Forward Neutron Calorimeter* (FNC) in the beginning of 1996. The FNC consists of a lead–scintillating fibre calorimeter with a depth of 9.5 hadronic interaction lengths, two segmented hodoscopes which are placed in front of the calorimeter to veto charged particles and a tail catcher situated behind the main calorimeter for the measurement of the energy leakage.

This chapter describes the construction, installation, calibration and the performance of the FNC. A brief introductory overview of the principles of calorimetry will be given at the beginning.

3.1 Basics of Calorimetry

A high–energy particle travelling through matter produces a shower of secondary particles. Hadronic interacting particles (baryons and mesons) generate a wide extended hadronic shower with an irregular shape, whereas electrons, positrons and photons produce a narrow electromagnetic shower. The only particles, which normally do not generate a shower (and which do not decay immediately), are neutrinos due to their weak interaction and muons which deposit their energy mostly through ionization.

Therefore a calorimeter in general is made of a dense absorber material, where the shower develops and an active material, where the secondary shower particles are detected by e. g. ionization and subsequent charge collection or scintillation and light collection. In a homogeneous calorimeter, a single material is used which fulfils both tasks at once.

3.1.1 Electromagnetic Showers

Above the critical energy E_c which is of the order of several MeV depending on the specific material, an electron (or positron) loses its energy mainly by the process of *bremsstrahlung*. After having passed a distance of one radiation length X_0 in the material, the energy of the electron has been decreased to e^{-1} times its original value. After the same distance, a photon has been converted to an electron–positron pair with a probability of $(1 - e^{-7/9})$.

The produced particles are subject to the same processes. Therefore an avalanche of particles is generated, until the energy of an individual particle has dropped below the critical energy E_c. At this moment the shower has its maximal size, and subsequent energy loss is dominated by ionization and excitation (for electrons and positrons) or the *Compton* effect and the photoelectric effect (for photons). In addition to the longitudinal expansion, a shower also develops in the transversal direction, which is characterized by the *Molière* radius R_M. Approximately 99% of the incident particle's energy are deposited inside a cone with a radius of $3.5R_M$ [PDG96].

For the Forward Neutron Calorimeter the values of the characteristic quantities are as follows [Aco91]:

$$\begin{aligned} E_c &= 7.6\,\mathrm{MeV}\ , \\ X_0 &= 7.2\,\mathrm{mm}\ , \\ R_M &= 21\,\mathrm{MeV}\cdot\frac{X_0}{E_c} = 20\,\mathrm{mm}\ . \end{aligned} \tag{3.1}$$

3.1.2 Hadronic Showers

Hadrons lose their energy by inelastic scattering with the nuclei of the absorber material. The characteristic length for this process is the nuclear interaction length:

$$\lambda_l = \frac{A}{\sigma_i \rho}\ , \tag{3.2}$$

where A denotes the atomic mass and ρ the density of the absorber substance. σ_i is the total inelastic hadronic cross section. After having passed a distance of λ_l in the material, a hadronic particle has scattered inelastically with a probability of $(1 - e^{-1})$. The nuclear interaction length for lead is $\lambda_{l,Pb} = 17.1\,\mathrm{cm}$ [PDG96] which is approximately 30 times larger than its radiation length X_0, whereas for the lead–scintillating fibre matrix of the FNC the effective length amounts to $\lambda_l = 21\,\mathrm{cm}$ [Aco91].

The development of a hadronic shower is more complex and less regular as compared to the electromagnetic case since a large amount of different secondary particles are produced, e. g. particles which decay immediately or which interact electromagnetically. The latter ones mostly originate from the decay of neutral pions ($\pi^0 \rightarrow \gamma\gamma$) and cause the formation of electromagnetic "sub showers".

3.1.3 Compensation

In contrast to the electromagnetic interaction with matter, in hadronic showers energy is used to break up nuclear bindings and for the creation of neutrinos, muons and slow neutrons. Knowing the fraction of not detectable energy, one could in principle correct the measured energy of an incident hadronic particle for these effects. But this amount fluctuates, since the electromagnetic fraction of a hadronic cascade depends on the particle's energy and also varies at fixed energy, leading to non–linearities in the calorimeter response and a worsening of the energy resolution.

Choosing the right geometry and material, it is possible to build a calorimeter for which the ratio of its response to the electromagnetic part of the shower over

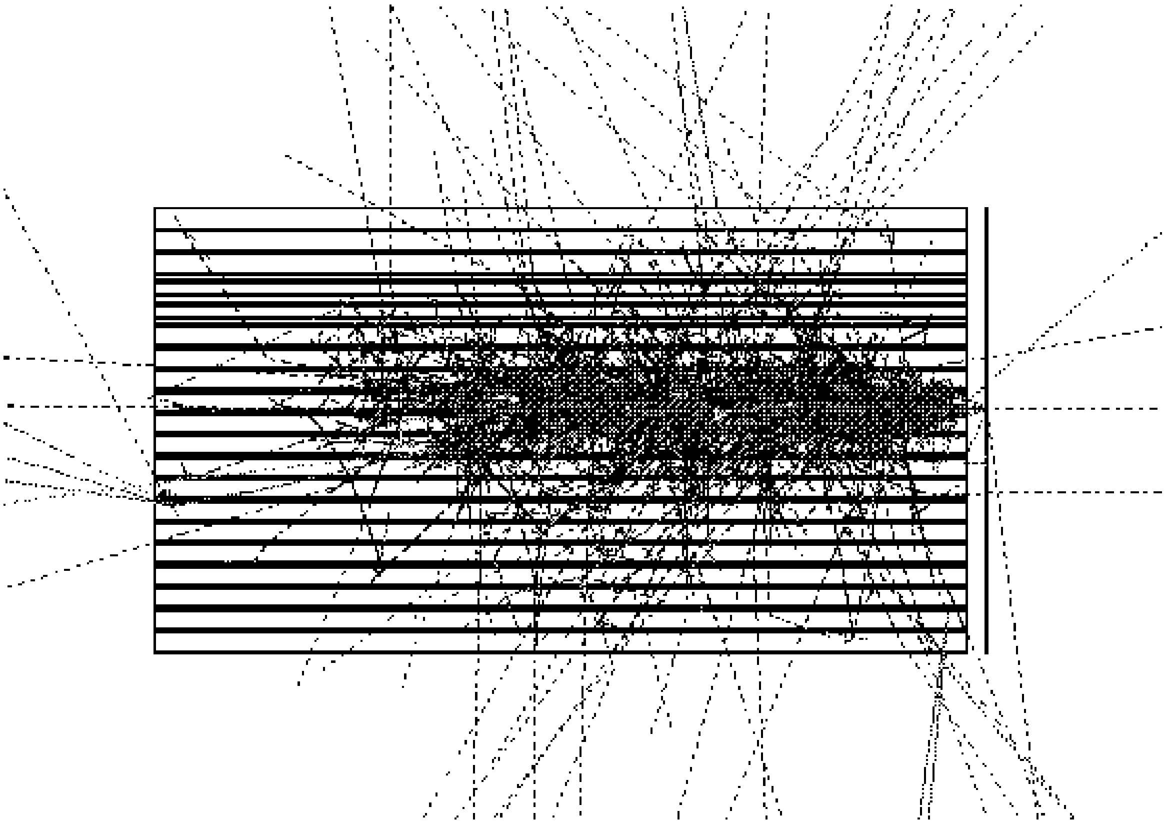

*Figure 3.1: Hadronic shower originating from a 700 GeV neutron in the FNC (*Geant *Monte Carlo simulation [ASG94], neutron is impinging from the right).*

the response to the non–electromagnetic part (e/h) is close to one. This condition is called compensation. Compensation can be accomplished by amplifying the hadronic response and/or suppressing the electromagnetic signal. The non–electromagnetic response can be increased by using a fissionable material as absorber, such as depleted uranium, and detecting the additional energy released in the nuclear fission reaction. One can also make use of the high cross section of the elastic scattering of the produced slow neutrons on protons and the subsequent ionization due to the recoil energy of the charged particle by using a hydrogenous material like plastic scintillator. Since the nuclei of the absorber substance are much heavier, slow neutrons pass the passive medium practically undisturbed and deposit their energy nearly exclusively in the active hydrogenous material. The electromagnetic response can be decreased by combining a low–Z active material[1] with a high–Z absorber material in order to suppress the probability for a photon to deposit its energy in the active medium, since the photoelectric effect is proportional to Z^5.

Calorimeters constructed of lead and scintillator have the advantage of providing a fast signal ($\sim 10\,\text{ns}$), whereas uranium calorimeters require an extended integration time for the signal, since the fission occurs on a time scale of typically $1\,\mu\text{s}$.

---

[1] Z is the atomic number of the material.

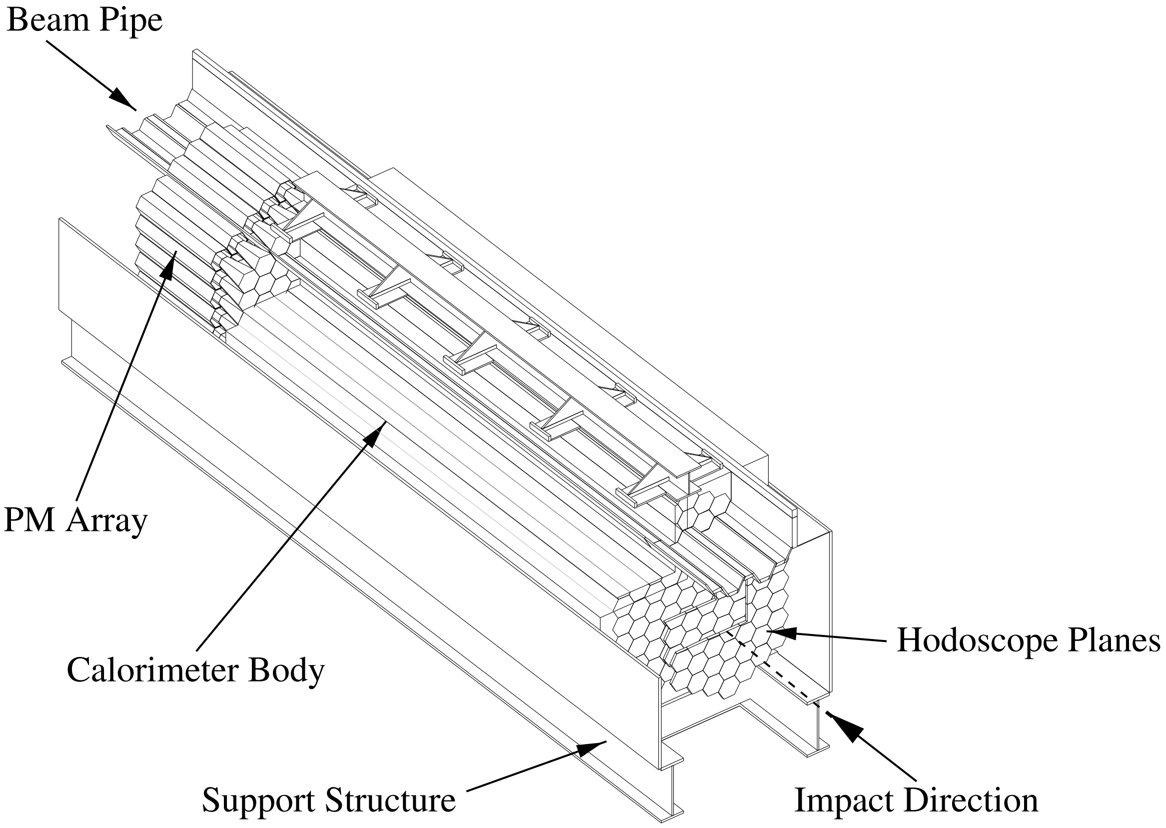

Figure 3.2: Configuration of the H1 Forward Neutron Calorimeter. The calorimeter is composed of interleaved layers of lead and scintillating fibres.

The forward neutron calorimeter FNC consists of a lead–scintillating fibre matrix, resulting in approximate compensation at a ratio $e/h = 1.15 \pm 0.02$ [Aco91a].

3.2 Construction of the FNC

Since 1996, the H1 experiment uses a forward neutron calorimeter made of lead and scintillating fibres. The calorimeter was originally built by the CERN/LAA collaboration [Aco90] and used by the WA89 experiment [WA89-87, Bec96] at CERN. It was modified for the installation in the H1 experiment 107 m downstream of the nominal interaction point and weighs approximately 10 tons. A schematic diagram of the FNC is shown in Figure 3.2 and a compilation of the basic properties of the calorimeter is given in table 3.1. A more detailed description of the construction and the installation of the calorimeter can be found in [Nun96] and [Met98].

Calorimeter modules	75 (67 bottom, 8 top)
Hodoscope modules	43 (plane 1) and 25 (plane 2)
Calorimeter photomultipliers	Philips XP2282B/01
Hodoscope photomultipliers	Hamamatsu R647
Weight	~7.5 t (bottom), ~1.3 t (top)
Dimension	$205 \cdot 65 \cdot 64\,\mathrm{cm}^3$ (bottom), $205 \cdot 39 \cdot 19\,\mathrm{cm}^3$ (top)
Lead sheets	$49.5 \cdot 1.92 \cdot 2000\,\mathrm{mm}^3$
Scintillating fibre type	SCSF38, 1 mm diameter, 2.2 m long
Lead–fibre volume ratio	4:1
Sampling fraction	2.3%
Radiation length	$X_0 = 7.2\,\mathrm{mm}$
Molière radius	$R_M = 20\,\mathrm{mm}$
Nuclear interaction length	$\lambda_I = 21\,\mathrm{cm}$
e/h ratio	1.15 ± 0.02

Table 3.1: Summary of the FNC configuration and its basic properties.

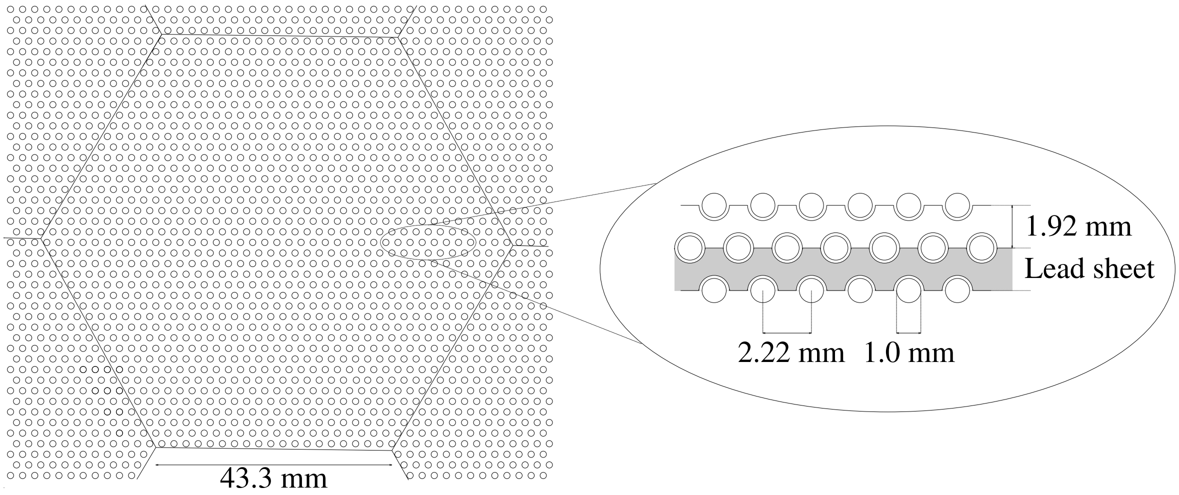

Figure 3.3: Lead fibre matrix. A hexagonal module is defined by coupling 1141 scintillating fibres to a common photomultiplier located at the rear of the detector.

3.2.1 The Calorimeter

The FNC consists of interleaved layers of 2 m long lead strips and longitudinally aligned scintillating fibres. This form of construction is called a *spaghetti–type* calorimeter. The calorimeter is laterally segmented into hexagonal modules, each of which is defined by coupling 1141 scintillating fibres to a common photomultiplier located at the rear of the detector (see Figure 3.3). The height of a hexagonal module is 8.6 cm. The calorimeter is divided into a top and bottom part (see Figure 3.4). A gap between these two parts is necessary in order to have space for the proton beam pipe which passes through the calorimeter. There are 67 modules in the bottom part of the calorimeter and 8 modules in the top part.

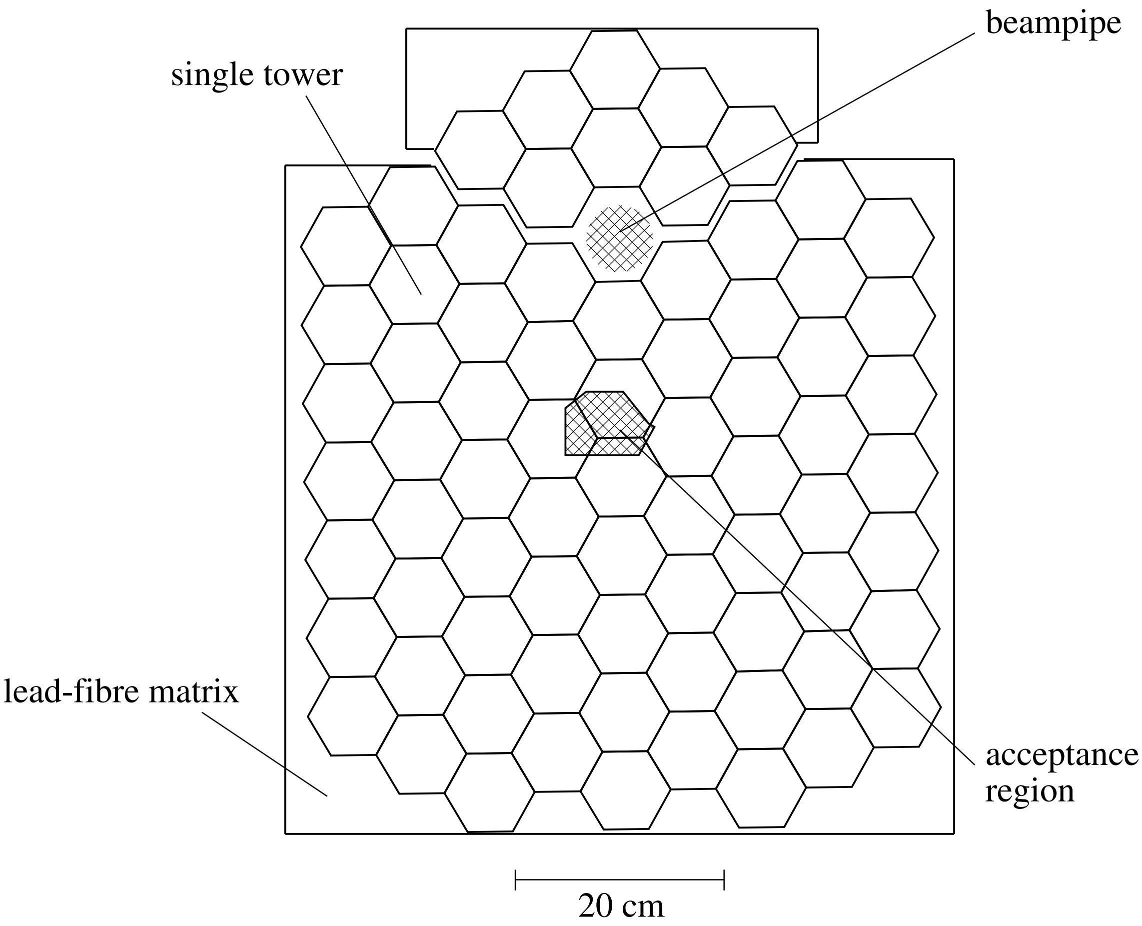

Figure 3.4: Back–view of the FNC. The calorimeter is subdivided into 75 modules. Shown is the position of the proton beam pipe and the acceptance region.

The calorimeter has a lead to fibre volume ratio of 4:1 providing approximate compensation (see section 3.1.3). Due to the small fraction of active material the sampling fraction (the part of the shower energy deposited in the active material) is only 2.3%. This drawback is counterbalanced by the fine granularity of the calorimeter providing a high sampling frequency.

Light Transportation in the Fibres

The scintillating fibres are not only employed as active material, but they also serve for the transportation of the produced light. They have a diameter of 1 mm and consist of a core of doped scintillator material (polystyrene, PS) surrounded by a 29 μm thick acrylic cladding (poly–methyl–metha–acrylate, PMMA). Due to the difference in the refractive index ($n_{PS} = 1.59$, $n_{PMMA} = 1.48$) the emitted light is totally reflected at the boundary between the core and the cladding and therefore guided along the fibres. On the one end the fibres are aluminized in order to reflect and redirect the light to the photomultiplier on the other end.

Since a hadronic shower has a large extension and since its longitudinal showerprofile fluctuates strongly, the attenuation length of the fibres should be much longer than their physical length. Fulfilling this condition, the ratio of the detected light in the photomultiplier over the deposited energy does not depend strongly on the longitudinal location of the energy deposit. If the attenuation length is rather short, light produced at the back end of the calorimeter close to the photomultiplier is attenuated much less than the light emmited at the front of the calorimeter. Therefore the energy of a shower, which develops very late in the calorimeter, is overestimated leading to a worsening of the energy resolution due to a high energy tail.

The attenuation length of the core of a single, separated fibre was measured to be $\lambda_{att} = 3.3\,\mathrm{m}$ [Sch94]. The attenuation curve for a prototype calorimeter build by the CERN/LAA collaboration was measured by scanning the detector along its length with 40 GeV electrons, which were directed perpendicular to the fibre axis [Aco91a]. The average calorimeter signal as a function of the distance z between the impact point and the photomultiplier was fitted by the expression

$$I(z) = I_0(e^{-z/\lambda_{att}} + Re^{-(2L-z)/\lambda_{att}}) + I_1 e^{-z/\lambda_{clad}} \,, \tag{3.3}$$

where $L = 2.2\,\mathrm{m}$ is the length of the fibres. The attenuation length $\lambda_{att} = 3.3\,\mathrm{m}$ and the reflection index $R = 0.85$ were fixed by independent measurements. The three remaining parameters (the attenuation length of the cladding λ_{clad} and the two normalization factors) were determined to be

$$\begin{aligned} \lambda_{clad} &= 0.60\,\mathrm{m}\,, \\ I_0 &= 168\,[\text{arbitrary units}]\,, \\ I_1 &= 79\,[\text{arbitrary units}]\,. \end{aligned} \tag{3.4}$$

The attenuation length of the fibres was remeasured in the HERA setup using cosmic ray muons [Lyt97]. Trigger hodoscopes were placed at several longitudinal positions along the calorimeter in order to define the location of the energy deposit of the muon ionizing the traversed material. Figure 3.5 shows the average signal in the central calorimeter towers as a function of the distance between the energy impact and the photomultipliers. Using the same formula for the attenuation expression as in Equation 3.3 and keeping the values for R and I_0/I_1 the two attenuation lengths were determined to be (Fit A, see Figure 3.5)

$$\begin{aligned} \lambda_{att} &= (0.96 \pm 0.04)\,\mathrm{m}\,, \\ \lambda_{clad} &= (0.26 \pm 0.03)\,\mathrm{m}\,. \end{aligned} \tag{3.5}$$

The quoted errors include fluctuations between fibres belonging to different modules.

Since the value of R used in the fits could have been decreased after the modification of the calorimeter and since the fit parameters given in Equations 3.4 are highly correlated, leading to an unstable ratio of I_0 and I_1, the muon data were refitted to a different, but similar function. The reflection index R was set to a value of $R = 0$, which cancels one addend in expression 3.3, and the two normalizations, I_0 and I_1, were released in the fit. The two attenuation lengths and the ratio of the normalizations

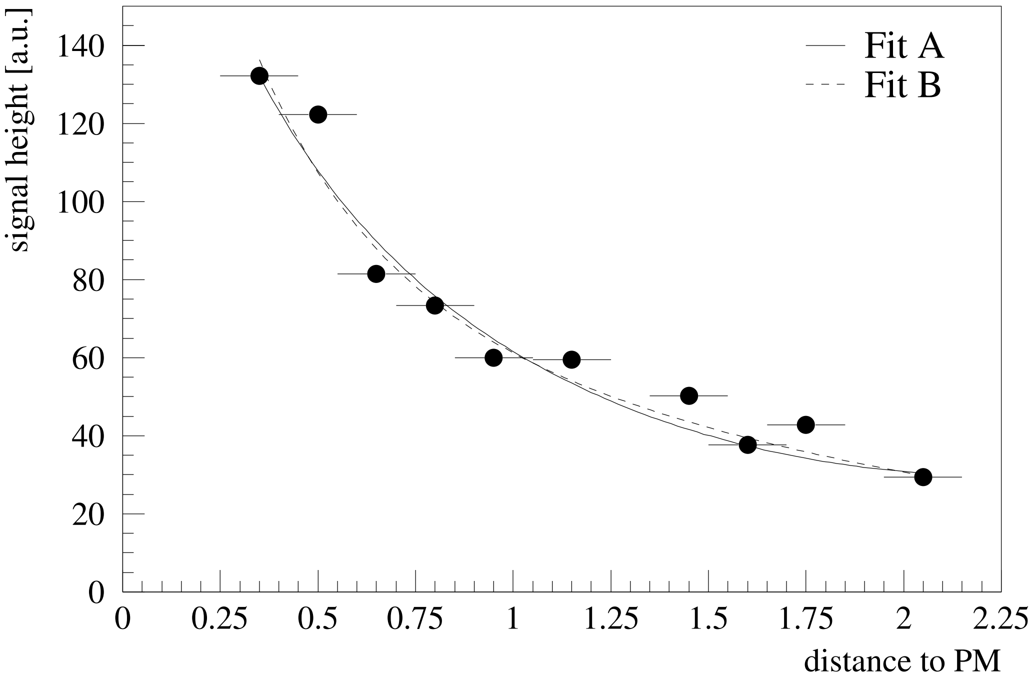

Figure 3.5: Attenuation curve of the scintillating fibres. Shown is the average signal in the central calorimeter towers produced by a cosmic muon traversing the calorimeter as a function of the distance between its trajectory and the photomultipliers. The curves denote two different fits to the attenuation expression given in Equation 3.3 (see text).

were determined to be (Fit B, see Figure 3.5)

$$\begin{aligned} \lambda_{att} &= (1.7 \pm 0.3)\,\mathrm{m}\ , \\ \lambda_{clad} &= (0.31 \pm 0.08)\,\mathrm{m}\ , \\ \frac{I_0}{I_1} &= 0.5 \pm 0.2\ , \end{aligned} \tag{3.6}$$

where the quoted errors again include differences between the fibres, belonging to different calorimeter modules.

Comparing the old result with the new measurements one recognizes that the attenuation length of the core of the scintillating fibres has decreased dramatically. This led to a significant deterioration of the energy resolution of the calorimeter. The measured response of the detector is asymmetrically smeared to higher energy values (see above) causing the high energy tail observed in the data (see section 3.4.1).

3.2.2 The Hodoscope

Situated in front of the calorimeter are two hodoscope planes of scintillator tiles which are used to veto incident charged particles.

Like the calorimeter the two hodoscope planes are segmented into hexagonal modules. The first plane comprises 43 tiles, which are aligned with respect to the corresponding calorimeter modules. The second plane, made of 25 modules, is shifted by half a length of a hexagon with respect to the first plane, so that the gaps between the modules in one plane are covered by the tiles of the other plane. The charge of an incoming particle is defined by the signal of the scintillator tile or tiles in front of its impact position. An event is tagged as charged if the response of one module, of which the centre is at a distance of less than 4.5 cm to the reconstructed impact point, is above a certain threshold. For $\sim 80\%$ of all events only one scintillator module per plane fulfils this geometric condition and has to be checked.

The efficiency of the hodoscope has been measured in the HERA setup using special calibration data (see section 3.5.1). The response of a hodoscope plane was determined using the other plane to trigger on charged particles. The combined efficiency of the two hodoscope planes amounts to $> 99.5\%$ [Met98].

Determination of the Neutron Detection Efficiency

Employing the hodoscope as a veto counter, neutral particles, e. g. neutrons, can be tagged. Back–scattering of charged particles produced in a hadronic shower (also called *albedo*) might fake an incident charged particle, reducing the efficiency of tagging a neutron. In principal, incident charged particles and albedo could be distinguished using the time information of the photomultiplier signal of the hodoscope, since the particles produced in the hadronic shower inside the calorimeter have to travel back to the scintillator tiles. In the setup at HERA the hodoscope is placed too close to the calorimeter body (distance $\sim 10\,\mathrm{cm}$), which does not allow to exploit this effect due to the limited time resolution of the photomultipliers and the readout electronics.

The neutron detection efficiency was determined by measuring the average rate of signals in a hodoscope tile as a function of the radial distance between the centre of the tile and the impact position reconstructed in the calorimeter. For this analysis the complete dataset including the tagged charged events were used. By extrapolating the rate of signals in the hodoscope tiles to the region close to the impact position, the probability due to back–scattering was estimated (see Figure 3.6). Since the data suggest an exponential distribution of the back–scattered particles, the hit probability $P(x)$ for the non–central tiles as a function of the distance to the reconstructed impact position x was fitted to an exponential function, in order to separate the contribution of albedo and incident charged particles to the hit rate in the central hodoscope modules. The fit yields

$$P(x) = 0.082e^{-x/12.2\,\mathrm{cm}} \ , \tag{3.7}$$

which amounts to an average hit probability in the central modules (those which are used for the charge definition) equal to 7%. The part of the measured hit rate in the first bin which is exceeding the extrapolated value is assumed to originate from incident charged particles. The error on the albedo contribution was determined on the basis of two extreme assumptions: a) there are no charged incident particles and therefore any hit in the central modules originate from albedo or b) the hit probability in the central tiles due to albedo is as large as the one in the surrounding tiles. The neutron

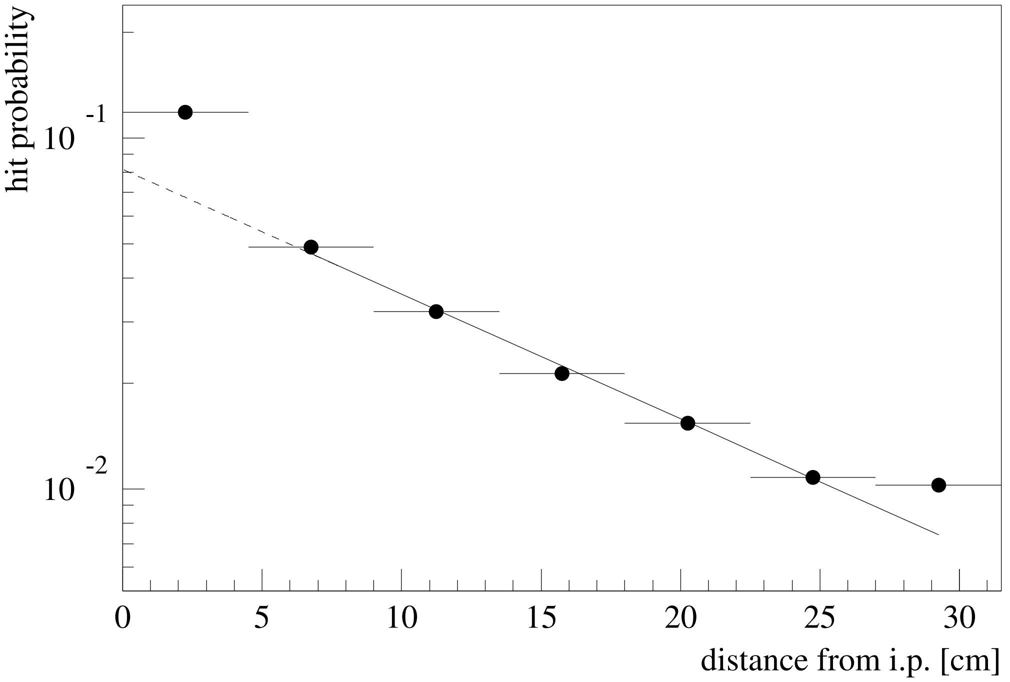

Figure 3.6: Determination of the neutron detection efficiency. Shown is the hit probability of a hodoscope module as a function of its distance to the reconstructed impact point. Hits in the first bin are originating from albedo and incident charged particles. The contribution of albedo is estimated by the exponential extrapolation shown in the plot.

detection efficiency finally amounts to

$$\varepsilon_{nd} = (93 \pm 5)\% \; , \tag{3.8}$$

where the error denotes the systematic uncertainty.

3.2.3 Readout and Trigger

Due to the position of the FNC in the HERA tunnel, approximately 100 m away from the central part of the H1 detector (see section 2.2), the high–voltage supply and the readout electronics cannot be installed close to the calorimeter. Instead the photomultipliers of the calorimeter and the hodoscope receive the high–voltage through $\sim$ 150 m long cables and their signals have to be transported over $\sim$ 140 m long coaxial cables to the readout system located outside the HERA tunnel.

The signals are digitized by FADCs (*Flash Analog to Digital Converter*)[2] which measure the signal voltage with a repetition rate of 104 MHz corresponding to a time distance of 9.6 ns which is a tenth of the time between two subsequent bunch crossings. The central calorimeter modules are in addition connected to 416 MHz FADCs providing four times smaller time intervals which results in a more precise measurement of

---

[2] Struck, F1002.

the signal time. The FADCs have an intrinsic resolution of 8 bits, but since the number of ADC counts does not depend linearly on the signal voltage, the effective resolution for low signals is similar to the one of 12 bit ADCs with the same dynamic range.

The FADCs are read out by a *Digital Signal Processor* (DSP) and fed to H1's central data acquisition via VME[3].

The analog signals of the photomultipliers are employed for triggering purposes as well. The signals of the central modules are added and fed into discriminators defining eight different threshold levels for the energy deposited in the calorimeter. In addition, special triggers are used to tag LED–monitoring events (see section 3.5.2), energy leakage out of the main calorimeter or incident charged particles, respectively. The FNC trigger elements are used to define three subtriggers (see section 2.2): two physics triggers and one monitoring trigger. The photoproduction subtrigger is defined by a triple coincidence between a track in the central drift chamber and an energy deposit in the electron tagger and the neutron calorimeter respectively. The deep–inelastic scattering subtrigger is based on the combination of an energy deposit in the backward electromagnetic calorimeter and in the FNC.

A detailed description of the readout and trigger system of the forward neutron calorimeter is given in [Met98].

3.3 Acceptance of the Calorimeter

Leading neutrons which are produced at the nominal interaction point inside the central H1 detector have to move along the beam pipe to reach the FNC. Therefore the acceptance of the FNC for detecting neutrons is mainly governed by the apertures of the proton beam line elements (bending and focusing magnets) located between the interaction point and the neutron calorimeter.

The acceptance is rapidly cut off if the neutron's trajectory crosses the edge of a magnet. This is demonstrated in Figure 3.7, which shows the acceptance as a function of the position of the impact point of the incident neutron on the calorimeter face. The acceptance has been evaluated in Monte Carlo (MC) studies using LEPTO [Ing97] as event generator and a GEANT [ASG94] simulation of the proton beam line [Lis97]. The superimposed curve in this figure indicates the edge of the acceptance region obtained from the impact point distribution of simulated and accepted neutrons. For those bins which are well contained inside this region, the acceptance is nearly uniform and amounts to $\sim 90\%$.

Figure 3.8 shows the impact point distribution obtained by the GEANT simulation of the proton beam line and the one observed in the data. The distributions are very similar in shape. The rate observed in the data decreases rapidly at the edge of the aperture, which indicates the quality of the impact point reconstruction. The location of the maximum of the impact point distribution, with respect to the shape of the acceptance region, is different in the Monte Carlo simulation compared to the real data. This indicates that the beam slope which is assumed in the Monte Carlo is different than in reality or that there is a certain mismatch of the coordinate systems of the beam line and the central H1 detector.

---

[3] *Versa Module Europa*, a flexible and open data bus system.

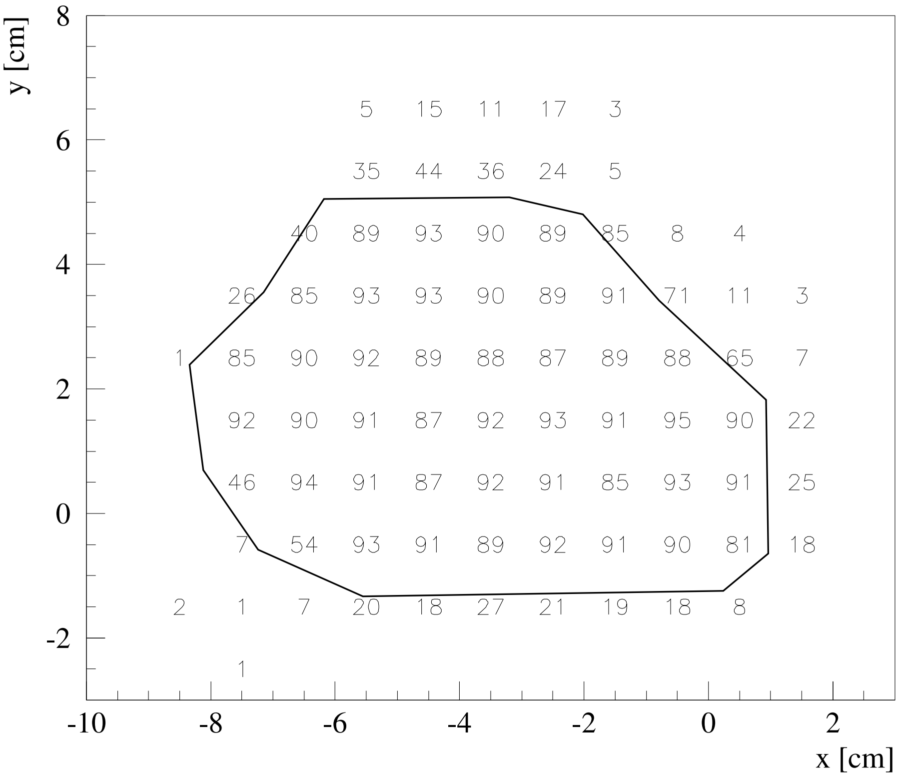

Figure 3.7: Acceptance of the FNC as a function of the impact point position. The numbers in the figure denote the acceptance in a x–y–bin in percent. The superimposed curve indicates the edge of the acceptance region.

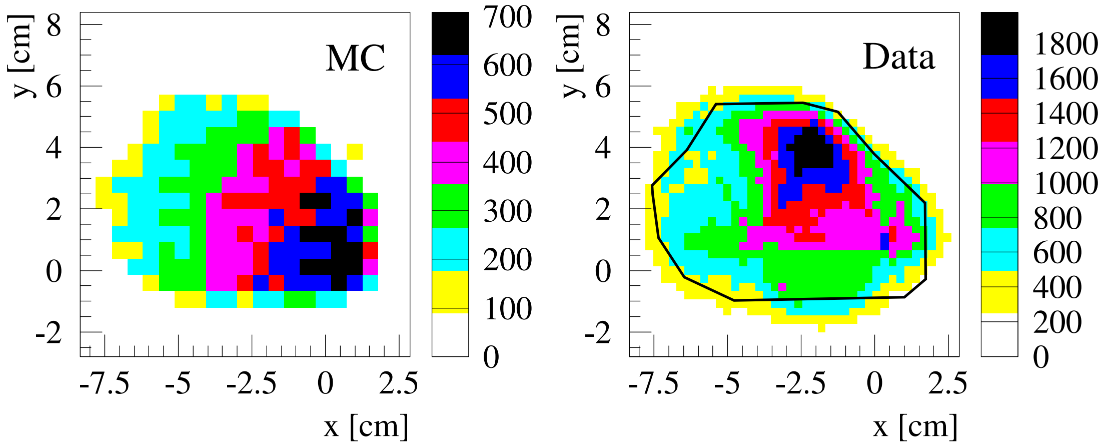

Figure 3.8: The FNC acceptance region observed in Monte Carlo (left plot) and data (right plot). Shown is the spatial distribution of impact points (see scale on the right side of the plots). The impact point distribution in the data is compared to the shape of the acceptance region derived from the Monte Carlo simulation.

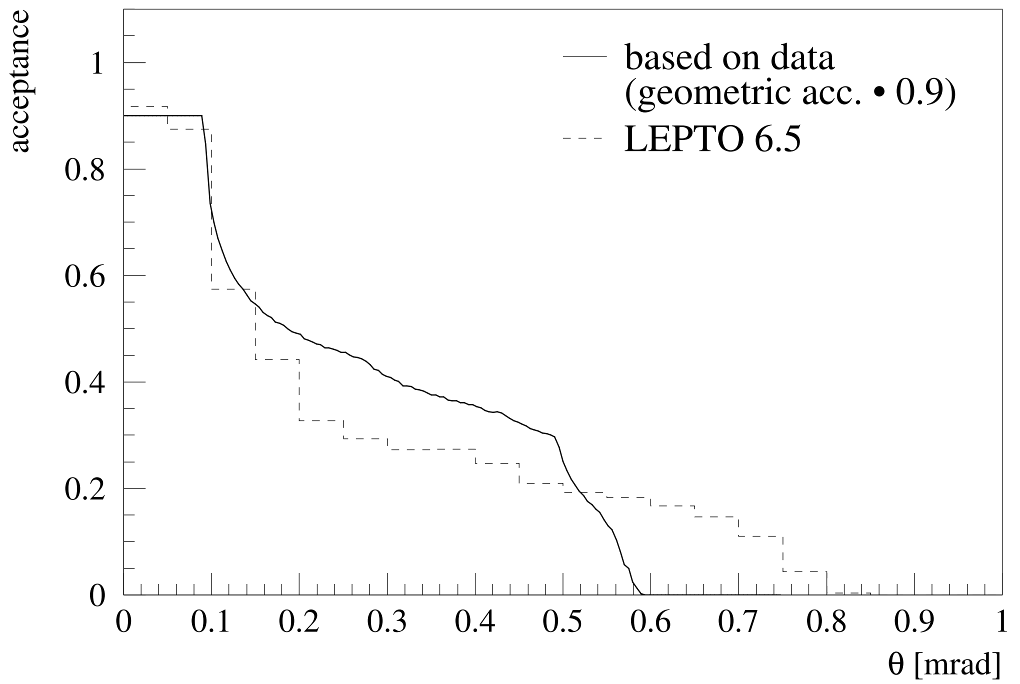

Figure 3.9: Acceptance of the FNC as a function of the scattering angle. It has been calculated using the 0°–direction observed in the data and the shape of the acceptance region. As a comparison the result of the Monte Carlo simulation is shown.

The spatial point with the maximal observed rate can be used to redefine the direction of $\theta = 0°$ in the data, since the production cross section for leading neutrons decreases with increasing scattering angles. By integrating over the polar angle, the observed 0°–direction and the shape of the acceptance region, taken from the Monte Carlo simulation, has been used to determine the geometric acceptance as a function of the scattering angle. The geometric acceptance has been corrected by 10% in order to take into account the limited, but uniform acceptance of $\sim$ 90% inside the aperture. The final result is presented in Figure 3.9 as a function of the scattering angle θ. The acceptance is $\sim$ 90% for scattering angles of $\theta \lesssim 0.1$ mrad and decreases smoothly up to the highest detectable scattering angles of $\sim$ 0.6 mrad. The acceptance derived from the data is compared to the result, which has been obtained with the Lepto Monte Carlo program and a simulation of the beam line. Both distributions are fairly similar in shape, but the Monte Carlo result extends to higher scattering angles and is lower for 0.2 mrad $\lesssim \theta \lesssim$ 0.5 mrad. This difference reveals the systematic uncertainty in the angular acceptance, and results in a large contribution to the systematic error of the measurement of the production cross section for leading neutrons (see Section 4.9.3).

The limited acceptance in the scattering angle has a strong influence on the energy spectrum of the neutrons, which can be detected. Figure 3.10 shows the energy spectra for generated and accepted neutrons obtained with the Lepto MC [Ing97] (including soft colour interaction) and the Pompyt MC [Bru96] (simulating π^+ exchange) respec-

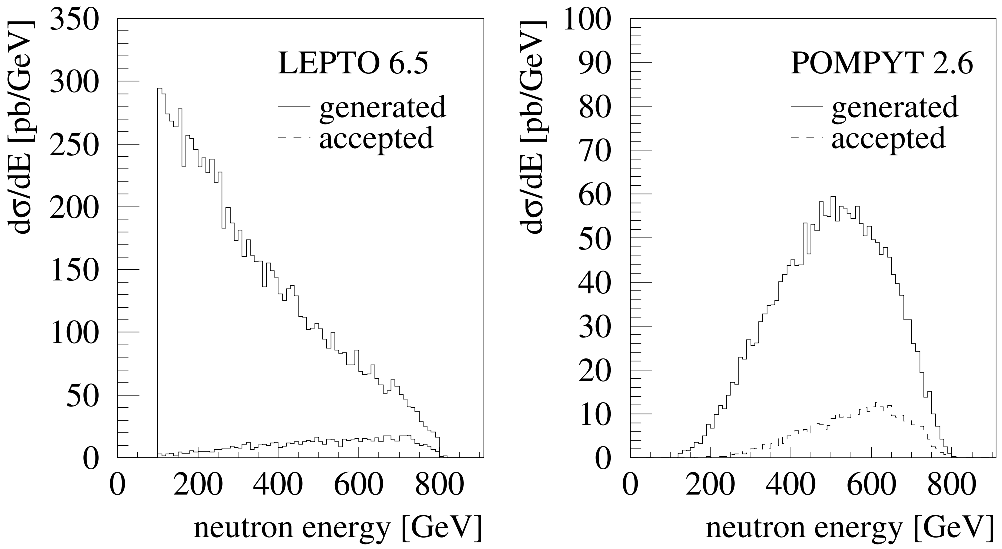

Figure 3.10: Neutron energy spectrum produced by the Lepto *and* Pompyt *Monte Carlo programs (generated and accepted). Shown is the cross section for neutron production as a function of energy, the generated one (solid lines) and the one for neutrons inside the acceptance region of the FNC (dashed line). The spectra are cut at* $E_n = 100$ *GeV.*

tively. Considering the whole phase space, both Monte Carlo models produce neutrons with a very different shape of the energy spectrum. For the pion exchange simulation the generated rate of neutrons has a maximum for energies slightly above half of the proton beam energy, whereas for the Lepto MC this rate is increasing continuously with decreasing neutron energy. Therefore Lepto predicts a larger integrated cross section than Pompyt. When selecting only those neutrons which are produced inside the FNC acceptance, both Monte Carlo models result in energy spectra which are similar in shape and normalization. The bulk of the neutrons produced in the lower energy region by the Lepto MC have a larger scattering angle which is outside the acceptance of the FNC, leading to the large reduction of the observable rate.

3.4 The Performance of the FNC

In this section the different experimental quantities which can be measured with the forward neutron calorimeter are summarized and the resolution of the energy and position measurement is discussed.

With the FNC subsystem, which also includes a segmented hodoscope and a tail catcher besides the calorimeter, the following quantities are measured:

- The energy deposits in the calorimeter modules are clustered with an algorithm based on the concept of *local equivalence relations* [You87]. This procedure defines the **number of clusters** and the **cluster energy**, which is the sum of the energies deposited in the modules comprising the cluster. A correction to the measured energy is applied, which makes use of the energy deposit in the tail catcher [Met98].

- The **x and y coordinate of the impact point** on the calorimeter front face are reconstructed using a correction to the measured centre of gravity of the energy deposit. An empirically determined correction function is applied to cure systematic effects resulting from the geometric structure of the calorimeter [Nun96, Sch94]. The reconstructed impact point provides a measurement of the scattering angle of the forward neutron, and in combination with the measured energy, a determination of its transverse momentum.
- The **timing of a cluster** is defined by the time of the signal in the module of the cluster with the highest energy deposit, which is calculated using the centre of gravity of the photomultiplier signal.
- The **charge of the incident particle** producing the cluster is determined by the response of the hodoscope modules in front of the calorimeter (see Section 3.2.2).

3.4.1 Energy Resolution

The energy resolution of the calorimeter has been determined for electrons and pions of energies $\leq 15\,\text{GeV}$ in a testbeam and for high–energy neutrons by a GEANT simulation of the detector.

The energy resolution of the calorimeter was measured to be [Nun96]

$$\frac{\sigma_E}{E} = 11.4\% \tag{3.9}$$

for 10 GeV electrons and

$$\frac{\sigma_E}{E} = 19.1\% \tag{3.10}$$

for 15 GeV pions.

Extrapolating these results to high energies one would expect the hadronic energy resolution of the calorimeter to be $\sim 5\%$ for neutrons above 400 GeV, if one assumes the same constant term b in the expression for the energy dependence of the energy resolution, $\sigma_E/E = a/\sqrt{E} \oplus b$, as found for the original setup of the calorimeter [Aco91a, Nun96]. However the observed neutron spectrum compared to the predictions of a Monte Carlo model of leading neutron production suggests that the energy resolution at very high energies ($E > 400\,\text{GeV}$) is much worse (see Section 3.5.1).

The deterioration of the energy resolution can be mostly attributed to the short attenuation length of the scintillating fibres (see Section 3.2.1). A GEANT simulation of the longitudinal energy profile of a highly energetic hadronic shower, folded with the attenuation length of the fibres, has shown that a significant part of the events deposit a large amount of energy at the back end of the calorimeter leading to an overestimation of the incident particle's energy, since the produced light is attenuated less than normal. This results in a high energy tail which is observed in the neutron energy spectrum (see Section 3.5.1), which means that the measured energy distribution extends far above the kinematic limit. The Monte Carlo simulation has been used to calculate the correlation between the measured energy and the true energy of the incident particle. An additional Gaussian smearing of 15% was applied to account for other contributions which disturb the energy resolution (*pick–up* noise, electronics etc.). The resulting effective resolution of the calorimeter is approximately constant for neutron energies between 300 GeV and 820 GeV and amounts to [Met98]

$$\frac{\sigma_E}{E} \approx 20\% \ . \tag{3.11}$$

The predicted energy spectrum for leading neutrons, smeared with the evaluated resolution function, agrees well with the observed neutron spectrum in the kinematic region were this prediction is assumed to be valid (see Section 3.5.1).

3.4.2 Position Resolution

For the measurement of the transverse momentum and the scattering angle of a forward neutron, a precise determination of its impact point on the calorimeter face is of high importance. One of the advantages of spaghetti–type calorimeters is their accurate spatial resolution. The longitudinally aligned scintillating fibres are bundled together at the back end of the calorimeter and coupled onto several photomultipliers defining separated calorimeter modules and therefore a lateral segmentation. The impact point of an incident particle is determined using the corrected centre of gravity of the energy deposit in the calorimeter modules.

Throughout this section the spatial or position resolution is meant to be defined with respect to only one coordinate direction, σ_x and σ_y respectively. Therefore the variance of the radial distance between the reconstructed and true impact point is $\sigma_r = \sigma_x \oplus \sigma_y$. Since the construction of the FNC is symmetric and since the impinging particles hit the calorimeter approximately perpendicular to the surface, $\sigma_y \approx \sigma_x$, and both will be denoted as σ_{xy}.

The position resolution of the FNC was measured in a testbeam with the use of a silicon microstrip detector system providing a precise track measurement. For pions with energies of 15 GeV the spatial resolution was measured to be [Nun96] [4]

$$\sigma_{xy} = (1.35 \pm 0.2)\,\mathrm{cm} \ . \tag{3.12}$$

At HERA the spatial resolution of the FNC was determined using charged particles with energies between 70 GeV and 330 GeV and three small scintillator counters (*finger counters*) situated in front of the calorimeter. The scintillators have a size of $3 \times 3 \times 10\ \mathrm{mm}^3$ and they are used in coincidence with a hodoscope tile to define a trigger.

The impact point distribution for events, which were tracked by the finger counters, were fitted in different bins of the particle energy [Tod97]. The resulting spatial resolution, together with the testbeam measurement is shown in Figure 3.11. The energy

---

[4] The given resolution is averaged over the x and y coordinate, which were different in the testbeam due to an inclination of the calorimeter of 3°.

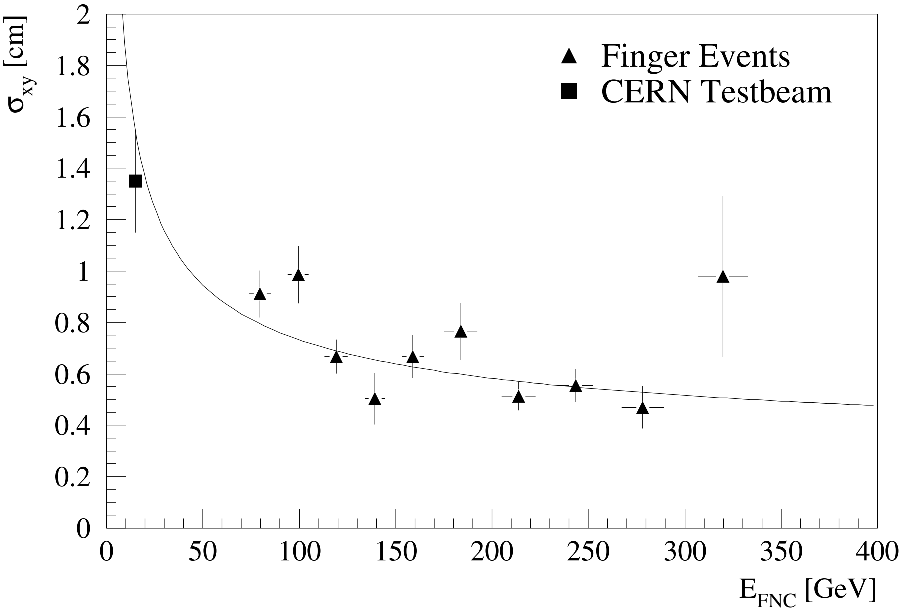

Figure 3.11: The position resolution of the FNC as a function of the incident particle's energy. The result of the testbeam and the measurement at HERA based on charged particles tracked by special finger counters is shown together with a combined fit (see Equation 3.13).

dependence of the spatial resolution of the FNC was determined to be:

$$\sigma_{xy}(E) = \left(\frac{5.13 \pm 0.81}{\sqrt{E\,[\mathrm{GeV}]}} + (0.22 \pm 0.07) \right) \mathrm{cm}\ . \tag{3.13}$$

Extrapolating this fit to higher energies, the spatial resolution for hadronic particles with 400 GeV $< E <$ 820 GeV can be estimated to be $\sigma_{xy} \approx 0.5$ cm.

3.5 Energy Calibration of the FNC

The 75 modules of the FNC were initially calibrated at CERN using a 10 GeV incident electron beam and a 15 GeV pion beam. The FNC was positioned on a movable platform which allowed to focus the beam in the centre of the different calorimeter modules in order to measure the response of each module separately. The electron beam data were used to determine preliminary calibration constants by a matrix inversion procedure [Nun96, Sch94], which makes use of the response not only of the central module but also of the surrounding neighbours. The calibration was cross–checked with the *containment method*, which relies only on the information of the central module, and with the pion–data taken at a beam energy of 15 GeV.

The calibration constants taken at such low energies, and in particular the absolute scale of the calibration, cannot be extrapolated reliably to the energy range which is of interest in the H1 experiment with energies up to 820 GeV. Therefore it is necessary to calibrate the detector *in situ* within the setup of the H1 experiment using high–energy particles, of which the energy distribution has to be known.

3.5.1 Calibration in the H1 Setup

High–energy neutrons can be produced in interactions between the proton beam and the residual gas in the beam pipe[5], which mostly consists of hydrogen, through the reaction $pp \to nX$ at a centre–of–mass energy of $\sqrt{s} \approx 38\,\mathrm{GeV}$. This reaction has been studied extensively at the *Intersection Storage Ring* ISR at CERN [Fla76] and at the *2 m–liquid hydrogen bubble chamber* at the CERN proton synchrotron [Blo78]. The inclusive neutron spectrum for production angles of 0° as a function of $z = E_n/E_{beam}$ has been measured at the ISR at centre–of–mass energies between 22.5 GeV and 62.7 GeV, which is comparable to $\sqrt{s}$ of beam–gas interactions at HERA. In the bubble chamber experiment the energy spectrum was measured for transverse momenta p_T of the produced neutrons between 0 GeV and 1 GeV. The data were taken at incident proton beam momenta of $p_L = 12\,\mathrm{GeV}$ and $p_L = 24\,\mathrm{GeV}$ respectively. In the high z and low p_T range this data are well described by pion exchange and have been used to constrain the pion flux factor [Hol94, Hol96], which is shown in Figure 3.12, where the neutron z spectrum, taken at different values of p_T, is compared to the π exchange model. There are additional small contributions due to ρ exchange.

This result is implemented in the POMPYT Monte Carlo program [Bru96], which has been used to simulate the reaction $pp \to nX$ based upon π exchange. The acceptance and the energy response of the FNC are simulated by tracking the generated neutrons through the GEANT simulation of the H1 beam line and by smearing the energy according to the resolution of the calorimeter (see Section 3.4.1). The resulting energy spectrum serves as a reference distribution, to which the beam–gas data are adjusted.

At H1 special calibration data were taken every few weeks in between the normal luminosity runs during periods with stable proton beam conditions. For these data only the FNC trigger was employed, and only the FNC electronics were read out allowing to take high statistics in a relatively short amount of time (∼100k events written to tape in about 20 to 30 minutes). Run–dependent calibration constants were determined by adjusting the high energy spectrum of the observed neutrons with the reference distribution obtained with the $pp \to nX$ Monte Carlo. Since the pion flux factor implemented in this Monte Carlo is constrained by measured hadronic data, the FNC is effectively calibrated with respect to previous experimental results.

Figure 3.13 shows the calibrated neutron energy spectrum, which has been observed in proton beam–gas interactions and which has not been corrected for acceptance or trigger efficiency, compared to the results of the Monte Carlo simulation. The two distributions are normalized to the same number of entries above 500 GeV. The peak position and the high energy tail observed in the data are in good agreement with the simulation. Since the rate of neutron production with $z < 0.5$ is known to be underestimated by pion exchange [Hol96], the proton beam–gas data in this energy range is not exploited for calibration purposes. In addition the efficiency of the trigger used for taking the beam–gas data is less than 100% for energies below 300 GeV.

This comparison, between proton beam–gas interactions and the pion exchange Monte Carlo simulation, is the method which is employed to determine the absolute energy scale of the FNC. A 5% energy scale uncertainty for the FNC is estimated

---

[5] In the following called beam–gas interactions.

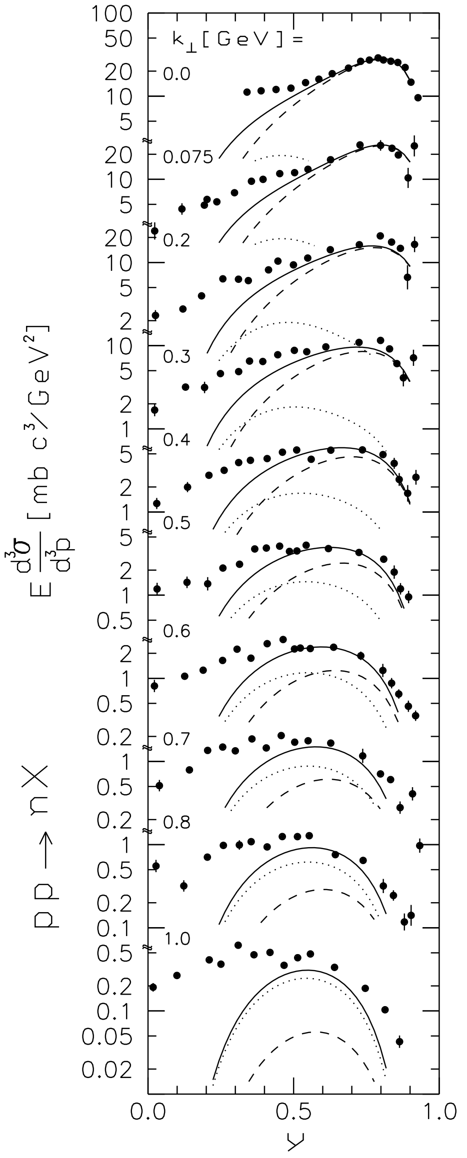

Figure 3.12: Inclusive neutron z spectrum in the reaction $pp \to nX$ for different fixed values of the neutron's transverse momentum p_T. The variable y in the figure denotes what in this analysis is referred to as z, $k_\perp$ is the same as p_T. The data are compared to the contributions of π exchange (dashed line) and of ρ exchange (dotted line), and to the sum of both contributions (solid line). The figure is taken from [Hol96] and includes data from [Fla76] and [Blo78].

which is demonstrated in Figure 3.15, where the energy spectrum of neutrons obtained in beam–gas interactions has been shifted by ±5%. The shifted distributions differ significantly from the Monte Carlo prediction.

In addition to the determination of the absolute energy scale of the FNC, the relative intermodule calibration obtained in the testbeam was corrected with the use of the lateral shower profile of high–energy neutrons. This profile distribution has been obtained by measuring the average energy deposit in a calorimeter module as

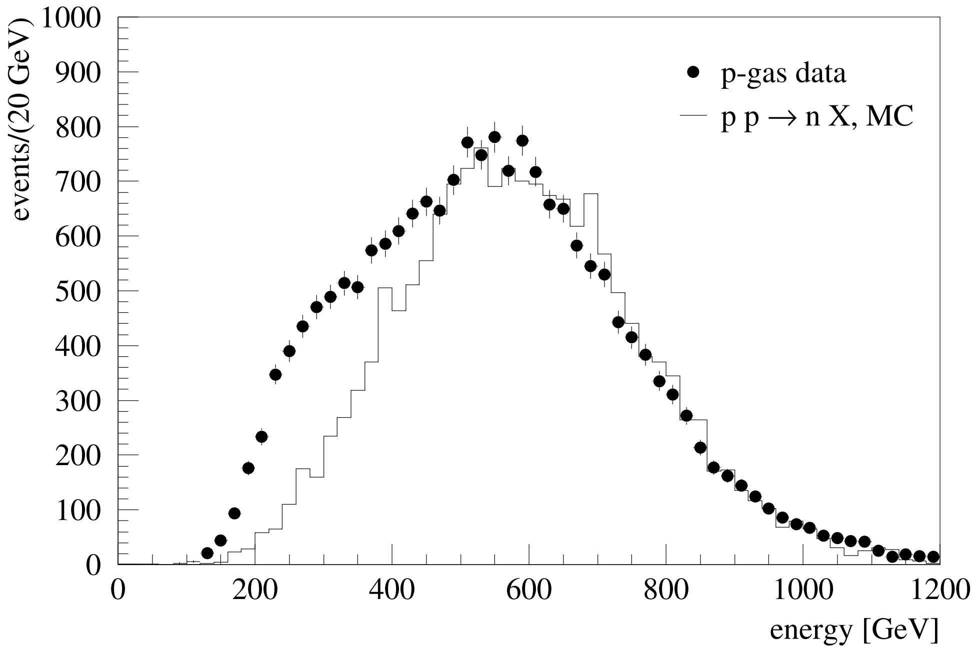

Figure 3.13: The observed neutron energy spectrum in proton beam–gas interactions compared to the results of a $pp \rightarrow nX$ Monte Carlo simulation based upon pion exchange. The simulation of the acceptance and resolution of the FNC is included in the Monte Carlo.

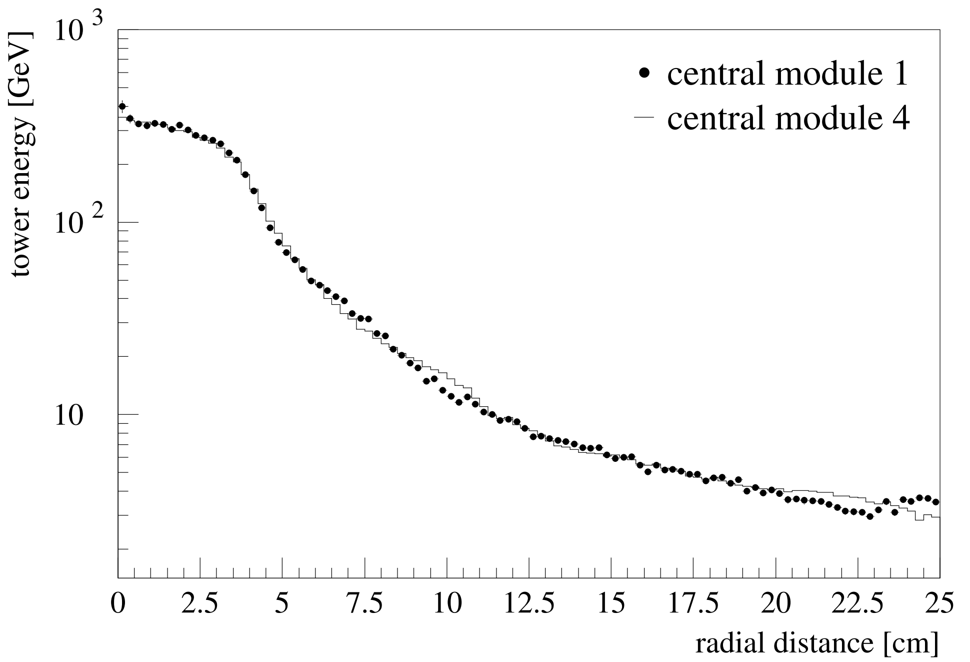

Figure 3.14: Lateral shower profile for neutrons with energies between 500 GeV and 600 GeV. Shown is the average energy deposit in a module as a function of its distance to the impact point. The profile is shown for two different central modules indicating the quality of the relative intermodule calibration.

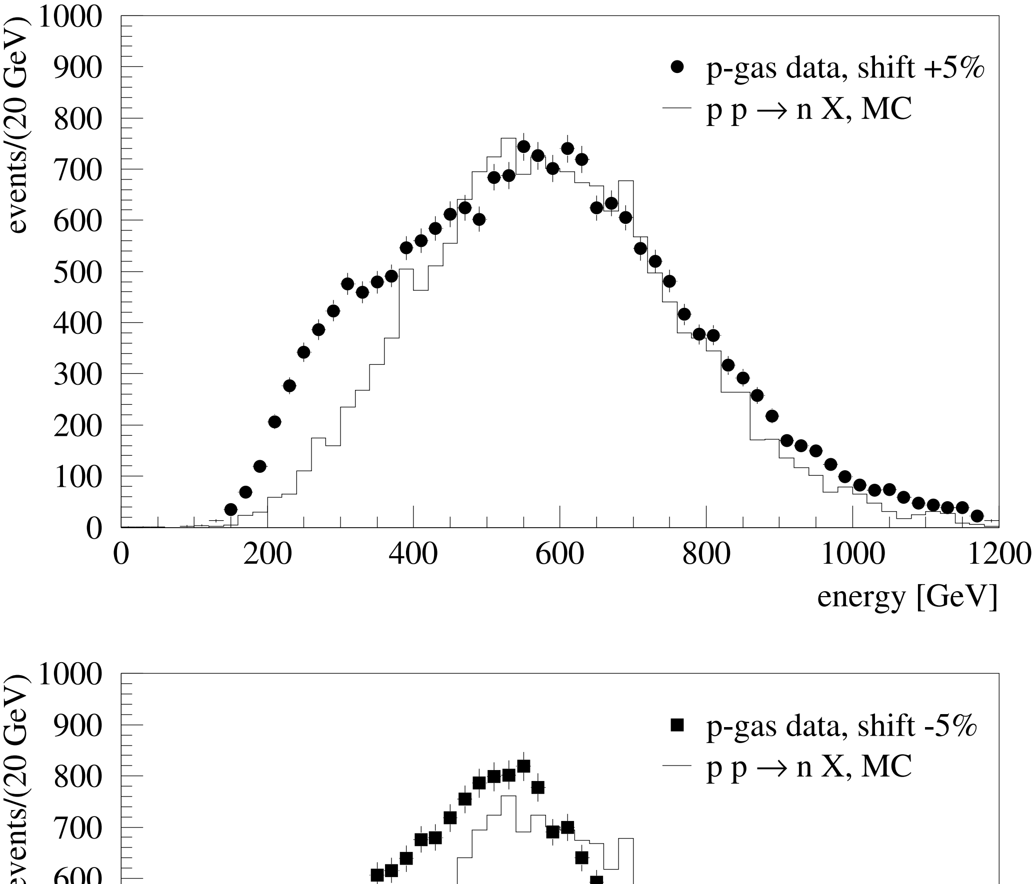

Figure 3.15: Estimation of the energy scale uncertainty of the FNC. The energy spectrum of neutrons obtained in beam–gas interactions has been shifted by ±5% and is compared to the predictions of the Monte Carlo simulation.

a function of the distance between the centre of the module and the impact point of the incident particle. Having a correct relative intermodule calibration, the shape of the lateral shower profile does not depend on the impact point or in particular on the central module. The relative calibration constants have been iteratively adjusted in order to fulfil this condition, which is demonstrated in Figure 3.14, where the shower profiles of events with different central modules are compared. Both distributions agree in magnitude and shape which indicates the quality of the relative intermodule calibration of the FNC.

3.5.2 Monitoring of the Short–Term Variations

The short–term gain variation of the FNC photomultipliers is measured by a LED monitoring system [Nun96, Met98]. The light from seven light–emitting–diodes (LEDs), which are flashed regularly with a rate of $\sim 1\,\mathrm{Hz}$ during data taking, is coupled by optical fibres to the entrance windows of all the photomultipliers. The average response of the photomultipliers to the LED light is used on a run–by–run basis to correct for small changes in the gain of the photomultipliers. When there are stable beam conditions, the gain variation of the photomultipliers is $\sim 0.01\%$ during a run, which has an average duration of 5–20 minutes [Met98].

3.5.3 Linearity of the Energy response

The linearity of the energy response of the FNC has been measured during dedicated energy rampings of the proton beam. For this purpose the proton beam which is injected at $E_p = 40\,\mathrm{GeV}$ was not directly accelerated to its maximal energy of $820\,\mathrm{GeV}$ as normally, but instead it is kept at intermediate constant values allowing to measure the neutron energy spectrum obtained in beam–gas interactions at different nominal beam energies.

It has been shown that the shape of the neutron spectrum as a function of $z = E'_n/E_p$ does not depend on the momentum of the proton beam [Fla76]. Therefore the peak position of the observed energy spectrum is expected to scale with the proton beam energy. Figure 3.16 shows the neutron spectra taken at different intermediate beam energies during the proton beam ramping. The peak positions of these distributions have been fitted and the result of these fits is plotted in Figure 3.17 as a function of the beam energy. The comparison to a linear interpolation shows that the calorimeter response is linear to a level of better than 10%. This estimate can be considered as an upper limit since the proton beam was not tuned for the intermediate energy levels which introduces systematic deviations due to the different beam conditions.

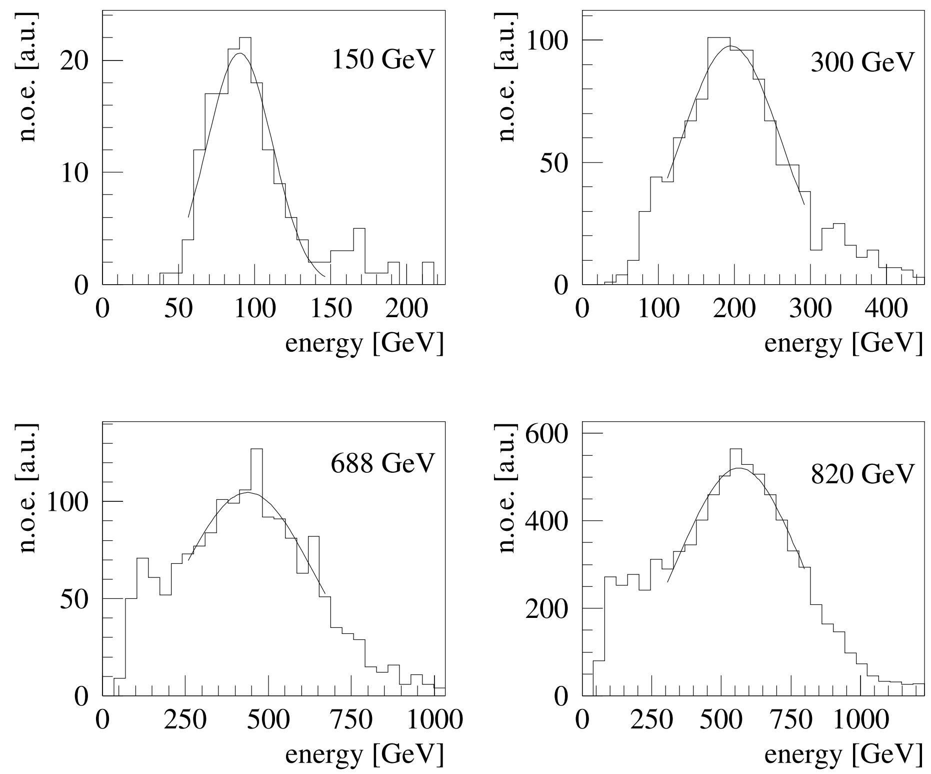

Figure 3.16: The neutron energy spectrum obtained in beam–gas interactions with four different nominal proton beam momenta. The peak position of each distribution has been fitted with a Gaussian.

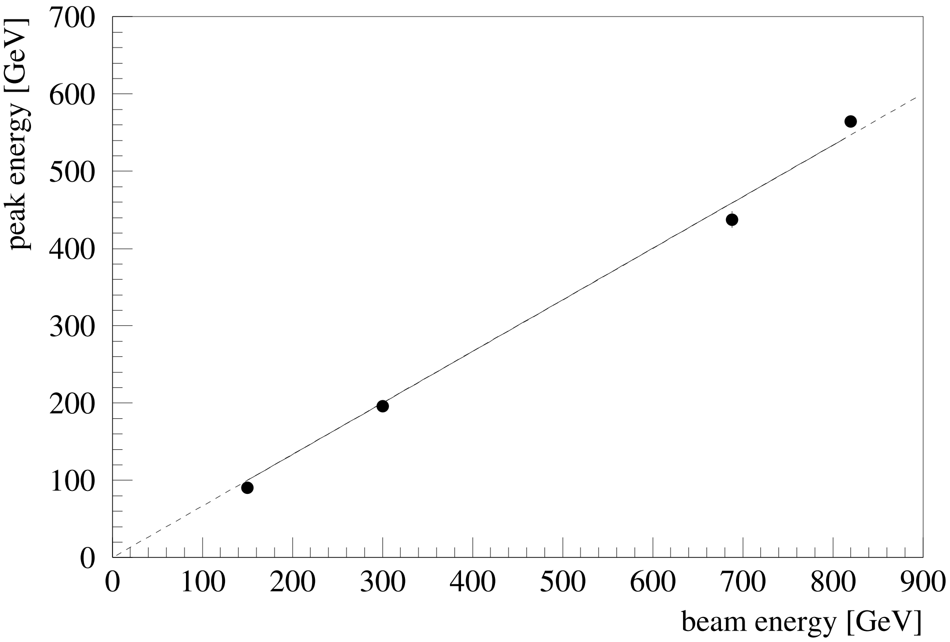

Figure 3.17: The linearity of the energy response of the FNC. Shown are the peak positions of the neutron energy distributions (see Figure 3.16) as a function of the proton beam energy and a comparison to a linear interpolation.

Chapter 4

Measurement of the Cross Section of Leading Neutron Production in Deep–Inelastic Scattering

In this chapter the measurement of leading neutron production in deep–inelastic ep scattering is described. The triple–differential cross section $\mathrm{d}^3\sigma/(\mathrm{d}x\,\mathrm{d}Q^2\,\mathrm{d}z)$ for the process $ep \to enX$ with a leading neutron of transverse momentum $p_T \leq 200\,\mathrm{MeV}$ has been measured in analogy to an earlier measurement of leading proton production in the same p_T range [Lis97].

This measurement is used to determine the semi–inclusive leading neutron structure function $F_2^{LN(3)}(x, Q^2, z)$, which is defined in a similar way like the inclusive proton structure function.

The chapter is organized as follows: At the beginning the method used for the extraction of the leading neutron structure function $F_2^{LN(3)}$ is explained. A brief outline of the data selection and the event reconstruction is given in the following section. The determination of the migration and acceptance corrections is separated into two parts: First the efficiencies and the correction factors, which only depend on the inclusive variables x and Q^2 are described. The following sections are devoted to the part of the analysis which involves the measurement of the kinematics of the produced neutron. The corrected z spectrum of the leading neutrons is determined using an unfolding method. At the end of this chapter a compilation of the systematic errors of this analysis is given and finally the result of the measurement of the semi–inclusive structure function $F_2^{LN(3)}(x, Q^2, z)$ is presented.

4.1 The Semi–Inclusive Structure Function $F_2^{LN(3)}$

Analogous to the inclusive structure function F_2 of the proton, the leading neutron structure function $F_2^{LN(3)}(x, Q^2, z)$ is defined with respect to the triple–differential *Born* cross section $\mathrm{d}^3\sigma_{Born}/(\mathrm{d}x\,\mathrm{d}Q^2\,\mathrm{d}z)$, which describes ep scattering in the single photon exchange approximation to the lowest order in the electromagnetic coupling constant α. It is not possible to measure the Born cross section directly since the physical cross section always comprises contributions to all orders in α. Corrections arise from the radiation of real photons from the incident or scattered electron (see Section 4.7). Denoting these corrections with $\delta_{rc}(x, Q^2)$, the semi–inclusive structure function $F_2^{LN(3)}(x, Q^2, z)$ is defined with respect to the measured cross section $\mathrm{d}^3\sigma/(\mathrm{d}x\,\mathrm{d}Q^2\,\mathrm{d}z)$ for the production of leading neutrons with transverse momentum $p_T \leq 200\,\mathrm{MeV}$ according to the following equation:

$$\frac{\mathrm{d}^3\sigma(ep \to enX)}{\mathrm{d}x\,\mathrm{d}Q^2\,\mathrm{d}z}(x, Q^2, z) = \kappa(x, Q^2, z) \cdot (1 + \delta_{rc}(x, Q^2)) \cdot F_2^{LN(3)}(x, Q^2, z) \ , \tag{4.1}$$

which includes the kinematic term

$$\kappa(x, Q^2, z) = \frac{4\pi\alpha^2}{x\,Q^4}\left(1 - y + \frac{y^2}{2\,(1 + R\,(x, Q^2, z))}\right) \ . \tag{4.2}$$

$R = \sigma_L/\sigma_T$ is the ratio between the absorption cross sections for longitudinally and transversely polarized virtual photons. In the kinematic range covered by this analysis, the structure function $F_2^{LN(3)}$ is rather insensitive to the value of R, so that $R = 0$ is assumed. The variation from $R = 0$ to $R = \infty$ leads to a 9% change at most in the resulting value of $F_2^{LN(3)}$ for the range of y covered in this measurement.

Using measured or calculable quantities the structure function $F_2^{LN(3)}$ can be expressed by the following relation:

$$F_2^{LN(3)}(x, Q^2, z) = \frac{N_{data,ijk} - N_{bg,ijk}}{\mathcal{L}}\, A_{ijk}^{-1}\,(1 + \delta_{rc,ij})^{-1}\,(\mathcal{I}_{ij}\,\Delta z_k)^{-1}\,C_{binc,ijk} \ , \tag{4.3}$$

where

- $N_{data,ijk}$ is the number of events observed in a specific (x_i, Q_j^2, z_k)–bin.
- The number of events originating from potential background processes $N_{bg,ijk}$ is subtracted.
- $\mathcal{L}$ is the integrated luminosity of the data sample which is used in the analysis.
- Trigger efficiencies, acceptance and resolution effects are taken into account by the migration and acceptance correction factor A_{ijk}. These corrections can be separated into an (x, Q^2) and a z–dependent part, which is demonstrated in Section 4.4.
- $\delta_{rc,ij}$ denotes the radiative corrections, which only depend on the inclusive variables x and Q^2.
- The measured cross section has to be divided by the integral of the kinematic factor κ:

  $$\int_{x_i} \mathrm{d}x \int_{Q_j^2} \mathrm{d}Q^2 \int_{z_k} \mathrm{d}z\,\kappa(x, Q^2, z) = \mathcal{I}_{ij}\,\Delta z_k \ , \tag{4.4}$$

  where

  $$\begin{aligned} \mathcal{I}_{ij} &= \frac{4\pi\alpha^2}{x\,Q^4}\int_{x_i} \mathrm{d}x \int_{Q_j^2} \mathrm{d}Q^2\,(1 - y + \frac{y^2}{2}) \ , \qquad (4.5) \\ \Delta z_k &= \int_{z_k} \mathrm{d}z \ , \end{aligned}$$

and the integration is performed over the full size of the (x_i, Q^2_j, z_k)–bin, i. e. $x_{i,min} \leq x \leq x_{i,max}$, $Q^2_{j,min} \leq Q^2 \leq Q^2_{j,max}$ and $z_{k,min} \leq z \leq z_{k,max}$.

- The factor which transforms the original measurement, which is averaged over the size of the (x_i, Q^2_j, z_k)–bin, into a measurement at a specific point in the centre of that bin, $(x_{i,cen}, Q^2_{j,cen}, z_{k,cen})$, is expressed by the bin centre correction $C_{binc,ijk}$.

In the following sections, the determination of these experimental quantities and correction factors is described in detail.

4.2 Event Reconstruction and Selection

This section deals with the reconstruction of the event kinematics and with the selection of a data sample of good quality which consists of deep–inelastic events with a forward neutron. The measurement is performed in the region of $2\,\mathrm{GeV}^2 \leq Q^2 \leq 50\,\mathrm{GeV}^2$, for which the scattered electron is always contained in the backward calorimeter SPACAL.

4.2.1 Reconstruction of the Event Kinematics

In inclusive DIS only two independent kinematic variables are needed besides the centre–of–mass energy $\sqrt{s}$, which is fixed by the beam energies, to define the kinematics of the lowest order process completely and unambiguously. Usually one describes the kinematics of inclusive DIS by the *Lorentz* invariant variables x, Q^2 and y. Only two out of these variables are independent, since $Q^2 = x\,y\,s$, if masses are neglected.

At HERA one can separately measure four kinematic quantities, which can be used to calculate the inclusive Lorentz invariant variables: the energy and the scattering angle of the outgoing electron and the hadronic final system respectively. Therefore the event kinematics is over–constrained and one has several possibilities to combine the measured quantities. The choice can be optimized in order to minimize the detector resolution effects and the influence from higher order effects (radiative corrections). A detailed discussion of the different methods to reconstruct the event kinematics is given in [Ben92]. For this analysis the so–called Σ–method was used [Bas95], which has only a small dependence on radiative effects and provides a uniformly good resolution of the kinematic variables x and Q^2 over a wide kinematic range.

The Σ–method combines the scattered positron energy and angle measurements with the quantity Σ, which is the sum over all hadronic final state particles (h) of the differences between energy and longitudinal momentum:

$$\Sigma = \sum_h (E_h - p_{z,h}) \ . \tag{4.6}$$

The variable Σ can be measured with good precision, since for the part of the hadronic final state, which escapes detection through the forward acceptance hole of the detector, $E_h \simeq p_{z,h}$. Thus, the contribution of these particles to the sum over the entire hadronic final state is negligible. There are practically no losses in the backward region since the hadronic final state is boosted in the proton direction. In this analysis the quantity Σ is calculated using the energy deposits in the calorimeter cells.

The reconstructed inclusive kinematic variables are defined in the following way:

$$\begin{aligned} y_\Sigma &= \frac{\Sigma}{\Sigma + E'_e(1-\cos\theta_e)}\,, \qquad (4.7)\\ Q^2_\Sigma &= \frac{E'^2_e \sin^2\theta_e}{1-y_\Sigma}\,,\\ x_\Sigma &= \frac{Q^2_\Sigma}{y_\Sigma s}\,, \end{aligned} \qquad (4.8)$$

where E'_e and θ_e are the energy and the angle of the scattered electron and $s = 4E_eE_p = 90200\,\mathrm{GeV}^2$ is the square of the ep centre–of–mass energy. The four–vector of the scattered electron is determined using the energy measurement of the backward calorimeter SPACAL and the determination of the scattering angle provided by the backward drift chamber BDC [Mar96].

The fractional energy $z = E'_n/E_p$ and the transverse momentum p_T of the forward neutron are measured using the FNC, which is described in detail in Section 3.4.

4.2.2 Run Selection

The data used for this analysis were taken during 1996, in which HERA was running with a positron beam of $E_e = 27.5\,\mathrm{GeV}$ and a proton beam of $E_p = 820\,\mathrm{GeV}$. A trigger which required an energy deposit in the SPACAL and the absence of out–of–time background signals was used to obtain the DIS data containing a high–energy neutron. During 1996 H1 recorded an integrated luminosity of $8.9\,\mathrm{pb}^{-1}$ on tape. Part of this data sample had to be rejected for this analysis. Only runs were selected, during which all important detector components were working reliably. The selection criteria are as follows[1]:

- The quality of the selected runs has to be categorized as good or medium and the trigger setup has to correspond to luminosity condition (trigger phase 2 to 4).
- The integrated luminosity of a single run has to be at least $0.1\,\mathrm{nb}^{-1}$ in order to guarantee statistical significance. Suspicious runs for which the expected number of events differs considerably from the observed number of events were rejected, e. g. if the statistical probability for this deviation is below 10^{-4}. This selection criterion mainly ensures that run periods with obvious defects of the trigger or other parts of the detector are discarded.
- Runs are rejected if for more than 20% of the integrated luminosity of this run, the high–voltage alarm of one relevant detector component is on in order to ensure that the detector is operational. For accepted runs, events which take place during a malfunction of the detector are discarded and the luminosity is corrected appropriately.

---

[1] The run selection and the calculation of the integrated luminosity was performed using [Egl96].

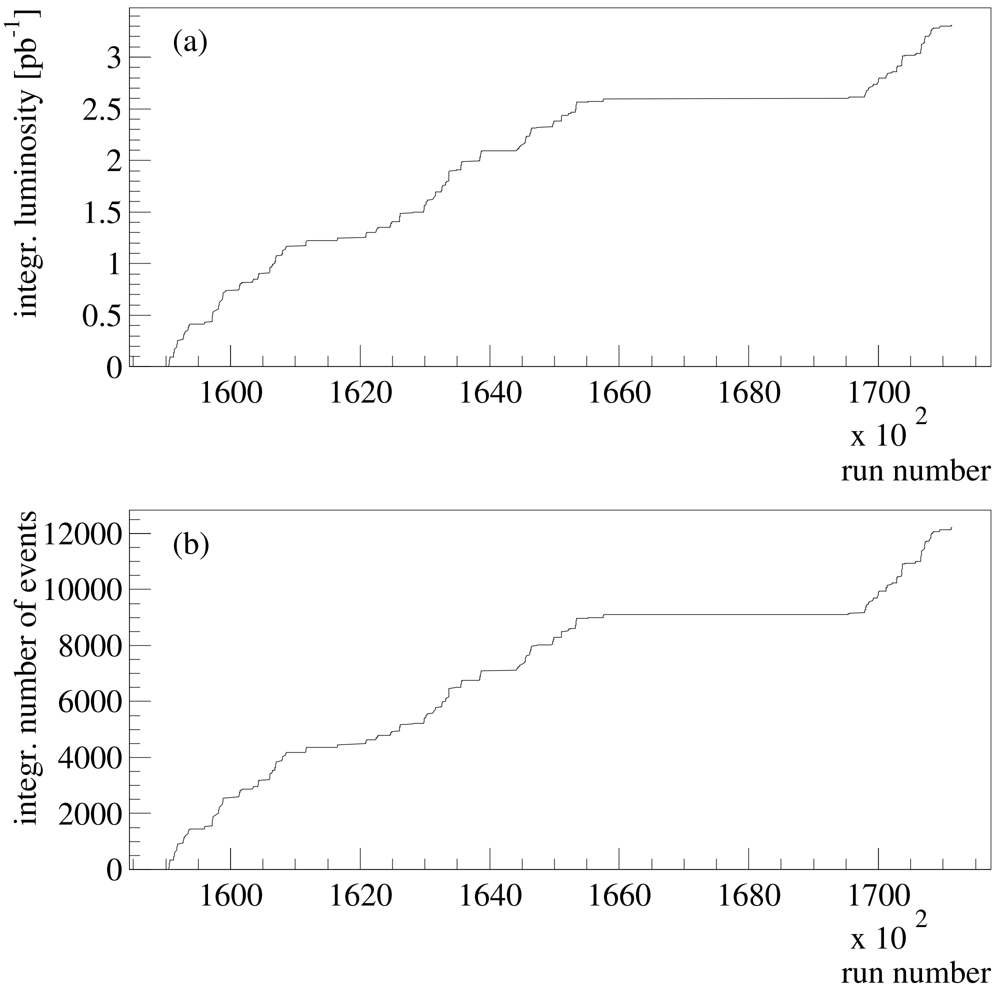

Figure 4.1: The integrated luminosity of the selected data sample (a) and the integrated number of selected events (b) versus the run number. None of the data with run numbers between 166072 and 169525 could be used in this analysis due to a malfunction of the selected trigger.

- The correction of the luminosity due to satellite bunches has to be smaller than 20% in order to ensure an accurate determination of the luminosity. The corrections have been calculated according to the cuts on the z–coordinate of the vertex position, which have been applied for the final event selection.
- Additional runs are discarded, for which the efficiency of the selected trigger is significantly lower than on average (see Section 4.5).

The integrated luminosity of the selected data sample was determined to be $\mathcal{L} = (3.38 \pm 0.07)\,\mathrm{pb}^{-1}$, where the systematic error includes the uncertainty of the satellite bunch corrections. Figure 4.1 shows the integrated luminosity and the integrated number of events as a function of the run number. The data with run numbers between 166072 and 169525 were discarded due to a malfunction of the selected trigger (see Section 4.5).

DIS Selection Criteria	
Electron energy	$E'_e \geq 12\,\mathrm{GeV}$
Electron scattering angle	$156^\circ \leq \theta_e \leq 177^\circ$
Lateral shower profile	$ECRA < 3.5\,\mathrm{cm}$
Kinematic region	$2\,\mathrm{GeV}^2 \leq Q^2 \leq 50\,\mathrm{GeV}^2$ $6 \cdot 10^{-5} \leq x \leq 6 \cdot 10^{-3}$ $0.02 \leq y \leq 0.6$
Momentum conservation	$\sum_i (E_i - p_{z,i}) \geq 40\,\mathrm{GeV}$
Vertex position	$-25\,\mathrm{cm} \leq z_{vtx} \leq 35\,\mathrm{cm}$
Trigger selection	actual subtrigger $s4$
Bunch crossing	ep colliding
Luminosity condition	high–voltage on, run quality

Final State Neutron Selection Criteria	
Number of clusters in FNC	$n_{cl} = 1$
Charge of cluster	neutral, $q = 0$
Reconstructed energy	$E'_n \geq 100\,\mathrm{GeV}$
Transverse momentum	$p_T \leq 200\,\mathrm{MeV}$
Impact point	inside acceptance region
Timing of the cluster	$t_{cl} \leq 0\,\mathrm{ns}$

Table 4.1: Summary of the selection criteria.

4.2.3 Selection of DIS Events with a Forward Neutron

Criteria were applied to the data sample in order to select deep–inelastic scattering events and suppress beam related backgrounds, events due to photoproduction and events from reactions in which the incoming positron lost a significant amount of energy by radiation (*initial state radiation*). Additional cuts ensure that the selected events contain a neutron with a transverse momentum $p_T \leq 200\,\mathrm{MeV}$. The DIS selection criteria used in the analysis are:

- A positron with energy $E'_e \geq 12\,\mathrm{GeV}$ in the angular range $156^\circ \leq \theta_e \leq 177^\circ$ is required which ensures that the scattered positron is within the acceptance region of the SPACAL electromagnetic calorimeter.

- The DIS kinematic variables are required to be in the range $2\,\mathrm{GeV}^2 \leq Q^2 \leq 50\,\mathrm{GeV}^2$, $6 \cdot 10^{-5} \leq x \leq 6 \cdot 10^{-3}$ and $0.02 \leq y \leq 0.6$.

- The quantity $\sum_i (E_i - p_{z,i})$, which is calculated using the energy E_i and the longitudinal momentum $p_{z,i}$ of all final state particles including the scattered electron, is expected to be twice the electron beam energy. This quantity is required to be ≥ 40 GeV in order to suppress radiative events and photoproduction background.

- Photoproduction background is also suppressed by a cut on the lateral shower profile of the reconstructed electron: The so–called *Energy weighted Cluster RAdius ECRA* has to be less than 3.5 cm.

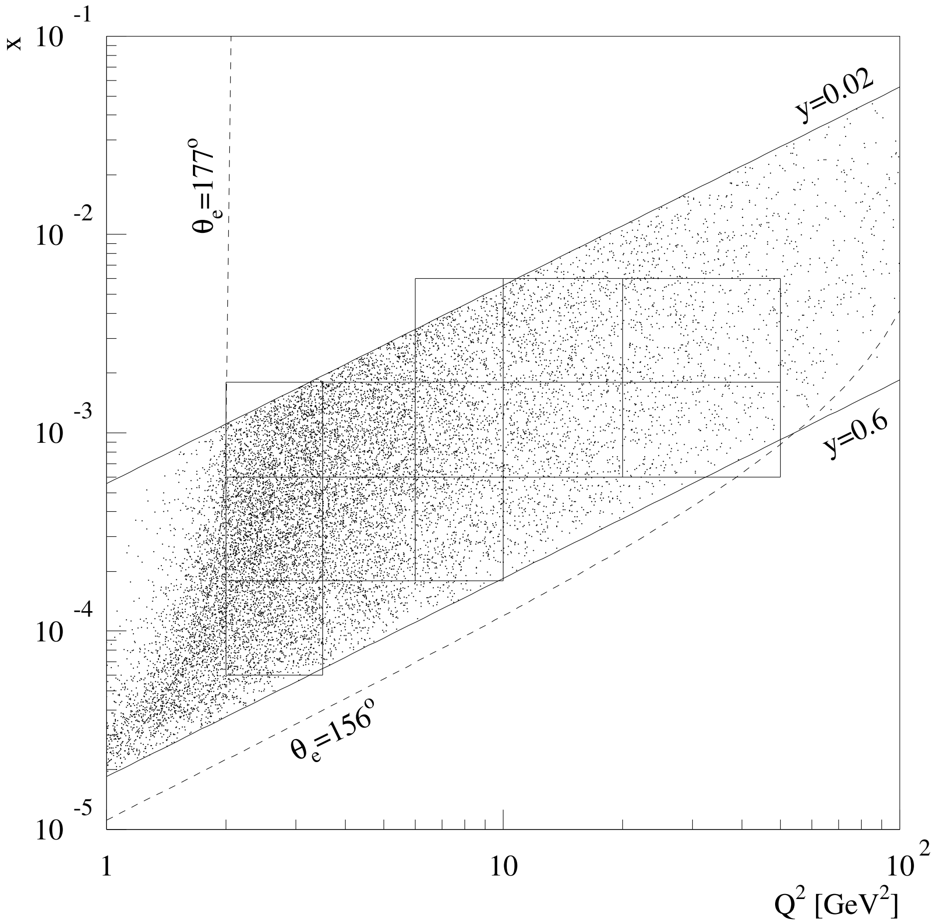

Figure 4.2: Distribution of the selected events in the (x, Q^2)–plane. Shown are all events which pass the selection criteria except of the cuts in x and Q^2. The 12 (x, Q^2)–bins, the cut on y and on the electron scattering angle θ_e are indicated.

- Only events with a reconstructed vertex are selected. The vertex position is required to be within ±30 cm of the nominal vertex position in z, which is at $z_{vtx} = 5\,\text{cm}$ for the 1996 data taking period.
- In addition it has been checked for the selected events, that they originate from real bunch crossings (empty bunches or pilot bunches are rejected) and that they occur during runs or part of runs which enter into the determination of the integrated luminosity of the data sample used in this analysis. The actual trigger bit of the selected subtrigger (subtrigger $s4$) has to be set.

Cuts related to the final state neutron are:

- One neutral cluster with $E'_n \geq 100\,\text{GeV}$ and $p_T \leq 200\,\text{MeV}$ is required to be reconstructed in the FNC.
- The reconstructed impact point of the cluster is demanded to be inside the acceptance region defined by the Monte Carlo simulation of the forward beam line (see

Section 3.3). This cut rejects in particular protons which are deflected upwards by the dipole magnets of the proton beam line and which hit the top part of the calorimeter.

- The timing of the cluster signal has to be compatible with the time of the bunch crossing, in which the deep–inelastic event happened. This cut ensures that the cluster does not originate from a different bunch crossing.

A summary of the selection criteria can be found in Table 4.1.

4.3 Division of the Kinematic Plane

In order to allow a direct comparison of the leading neutron and proton data, the neutron data sample was grouped into the same 12 (x, Q^2)–bins like in the previously performed leading proton analysis [Lis97]. The kinematic region was divided into 4 x–intervals, which in each case cover a range in x of about a factor of three. The Q^2–range was partitioned into 5 intervals, which are growing in dimension for increasing values of Q^2.

(x, Q^2) bin l	Q^2 bin j	x bin i	range in Q^2	range in x
1	1	1	$2\,\mathrm{GeV}^2 \leq Q^2 < 3.5\,\mathrm{GeV}^2$	$6.0 \cdot 10^{-5} \leq x < 1.8 \cdot 10^{-4}$
2	1	2	$2\,\mathrm{GeV}^2 \leq Q^2 < 3.5\,\mathrm{GeV}^2$	$1.8 \cdot 10^{-4} \leq x < 6.0 \cdot 10^{-4}$
3	1	3	$2\,\mathrm{GeV}^2 \leq Q^2 < 3.5\,\mathrm{GeV}^2$	$6.0 \cdot 10^{-4} \leq x < 1.8 \cdot 10^{-3}$
4	2	2	$3.5\,\mathrm{GeV}^2 \leq Q^2 < 6\,\mathrm{GeV}^2$	$1.8 \cdot 10^{-4} \leq x < 6.0 \cdot 10^{-4}$
5	2	3	$3.5\,\mathrm{GeV}^2 \leq Q^2 < 6\,\mathrm{GeV}^2$	$6.0 \cdot 10^{-4} \leq x < 1.8 \cdot 10^{-3}$
6	3	2	$6\,\mathrm{GeV}^2 \leq Q^2 < 10\,\mathrm{GeV}^2$	$1.8 \cdot 10^{-4} \leq x < 6.0 \cdot 10^{-4}$
7	3	3	$6\,\mathrm{GeV}^2 \leq Q^2 < 10\,\mathrm{GeV}^2$	$6.0 \cdot 10^{-4} \leq x < 1.8 \cdot 10^{-3}$
8	3	4	$6\,\mathrm{GeV}^2 \leq Q^2 < 10\,\mathrm{GeV}^2$	$1.8 \cdot 10^{-3} \leq x \leq 6.0 \cdot 10^{-3}$
9	4	3	$10\,\mathrm{GeV}^2 \leq Q^2 < 20\,\mathrm{GeV}^2$	$6.0 \cdot 10^{-4} \leq x < 1.8 \cdot 10^{-3}$
10	4	4	$10\,\mathrm{GeV}^2 \leq Q^2 < 20\,\mathrm{GeV}^2$	$1.8 \cdot 10^{-3} \leq x \leq 6.0 \cdot 10^{-3}$
11	5	3	$20\,\mathrm{GeV}^2 \leq Q^2 \leq 50\,\mathrm{GeV}^2$	$6.0 \cdot 10^{-4} \leq x < 1.8 \cdot 10^{-3}$
12	5	4	$20\,\mathrm{GeV}^2 \leq Q^2 \leq 50\,\mathrm{GeV}^2$	$1.8 \cdot 10^{-3} \leq x \leq 6.0 \cdot 10^{-3}$

Table 4.2: Definition of the 12 bins in x and Q^2.

z–bin k	range in z
1	$0.2 \leq z < 0.4$
2	$0.4 \leq z < 0.6$
3	$0.6 \leq z < 0.8$
4	$0.8 \leq z \leq 1.0$

Table 4.3: Definition of the 4 bins in z.

The limits of the 12 (x, Q^2)–bins are given in Table 4.2. They are also indicated in Figure 4.2, where all the events which pass the selection criteria – except of the cuts in x and Q^2 – are shown. There are in total 12213 events passing all the selection cuts, of which 10366 events belong to one of the 12 bins.

The z–range between 0.2 and 1 was divided into 4 intervals with a common width of $\Delta z = 0.2$ (see Table 4.3).

4.4 Separation of the Migration and Acceptance Corrections

In this analysis the acceptance and migration corrections are divided into two parts, i. e. migration and acceptance effects in (x, Q^2) and z are separately corrected for. This separation can be justified, since there is no evidence for a dependence of the final state neutron on the scattered positron in the kinematic range covered by this measurement. This independence assumption was also done in H1's measurement of leading proton production [Lis97] and in an analysis on the event properties of leading protons performed by ZEUS [ZEU97].

The shape of the uncorrected z distribution is similar in all (x, Q^2)–bins, which is demonstrated in Figure 4.3, as well as the uncorrected x and Q^2 distributions, of which the shapes are not significantly different for the 4 individual intervals in z (see Figures 4.4 and 4.5).

In the following the true z and (x, Q^2)–bin are signified by k and l and the smeared (reconstructed) bins by m and n respectively. Furthermore the number of generated events in the k–th z and l–th (x, Q^2)–bin is denoted by $\mathcal{C}_{kl}$ and the number of reconstructed, smeared events in the m–th z and n–th (x, Q^2)–bin by $\mathcal{D}_{mn}$. The projection from the true to the smeared bins can be expressed by a transformation matrix $\mathcal{M}_{klmn}$:

$$\mathcal{D}_{mn} = \mathcal{M}_{klmn} \cdot \mathcal{C}_{kl} \ . \tag{4.9}$$

The definition of the transformation matrix $\mathcal{M}_{klmn}$ is visualized in Figure 4.6, where the arrows symbolize different components of the matrix. The non–diagonal components of $\mathcal{M}_{klmn}$ have the following relations:

- Migration in z: since the z distribution is similar in all (x, Q^2)–bins, the following equation holds (compare the dashed arrows in the figure):

$$\mathcal{M}_{\alpha p \beta p} = \mathcal{M}_{\alpha q \beta q} \quad \forall\, p, q \text{ and fixed } \alpha, \beta. \tag{4.10}$$

- Migration in x and Q^2: since the x and Q^2 distribution are similar in all z–bins, also the following expression is valid (compare the solid arrows in the figure):

$$\mathcal{M}_{r \gamma r \delta} = \mathcal{M}_{s \gamma s \delta} \quad \forall\, r, s \text{ and fixed } \gamma, \delta. \tag{4.11}$$

Therefore (compare the dotted arrow in the figure):

$$\mathcal{M}_{\beta\gamma\beta\delta} \cdot \mathcal{M}_{\alpha\gamma\beta\gamma} = \mathcal{M}_{\alpha\delta\beta\delta} \cdot \mathcal{M}_{\alpha\gamma\alpha\delta} \overset{!}{=} \mathcal{M}_{\alpha\gamma\beta\delta} \ , \tag{4.12}$$

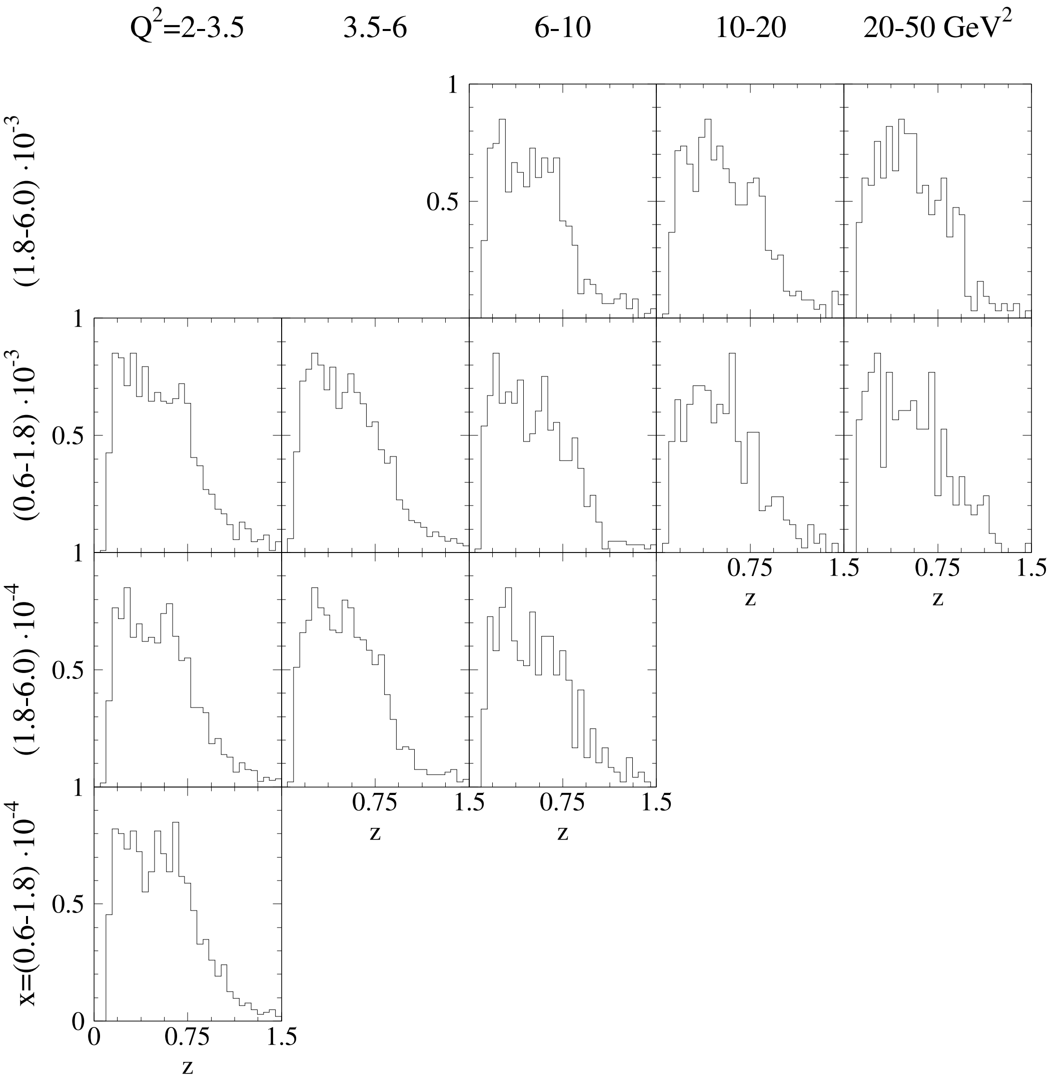

Figure 4.3: Uncorrected z spectrum in the 12 (x, Q^2)–bins (arbitrary scale).

where the last equation holds, since there is no evidence for a correlation between the x and Q^2 values and the z values observed in the data.

Consequently the acceptance and migration correction can be separated into an (x, Q^2) and a z dependent part, i. e. the correction factor A_{ijk}, which was defined in Equation 4.3, factorizes:

$$A_{ijk} = \tilde{A}_l \cdot \hat{A}_k \ , \tag{4.13}$$

where $\tilde{A}_l$ denotes the correction[2], which depend on x and Q^2 and $\hat{A}_k$ the one which depends on z. $\tilde{A}_l$ is the product of the trigger efficiency T_l and of the reconstruction efficiency $R_{incl,l}$ for the inclusive quantities:

$$\tilde{A}_l = T_l R_{incl,l} \ . \tag{4.14}$$

---

[2] The indices i and j are combined into a single index l.

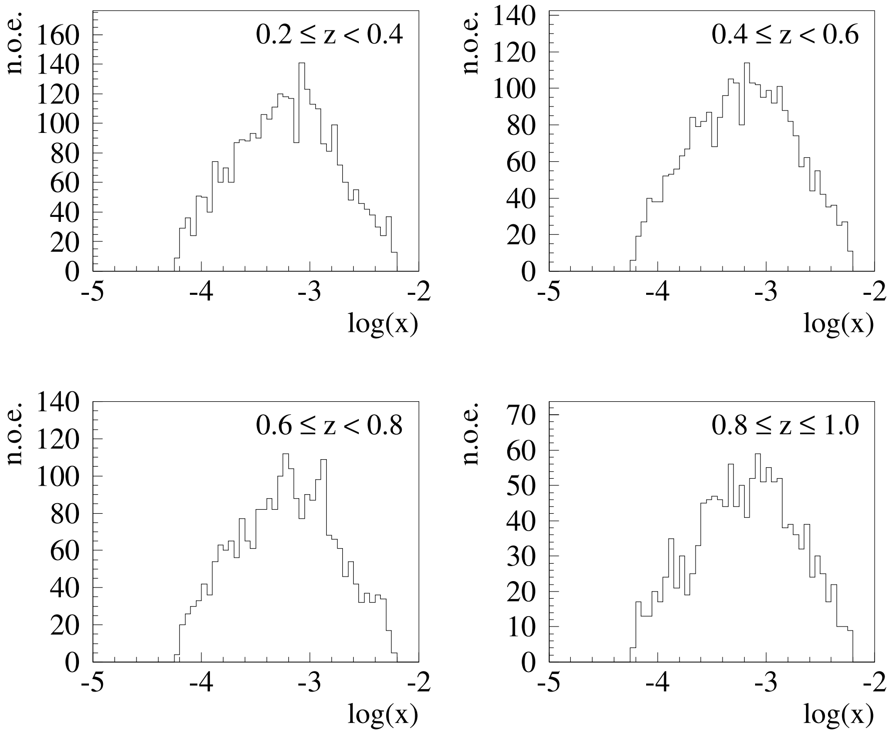

Figure 4.4: Uncorrected $\log x$ *spectrum in the 4* z*–bins.*

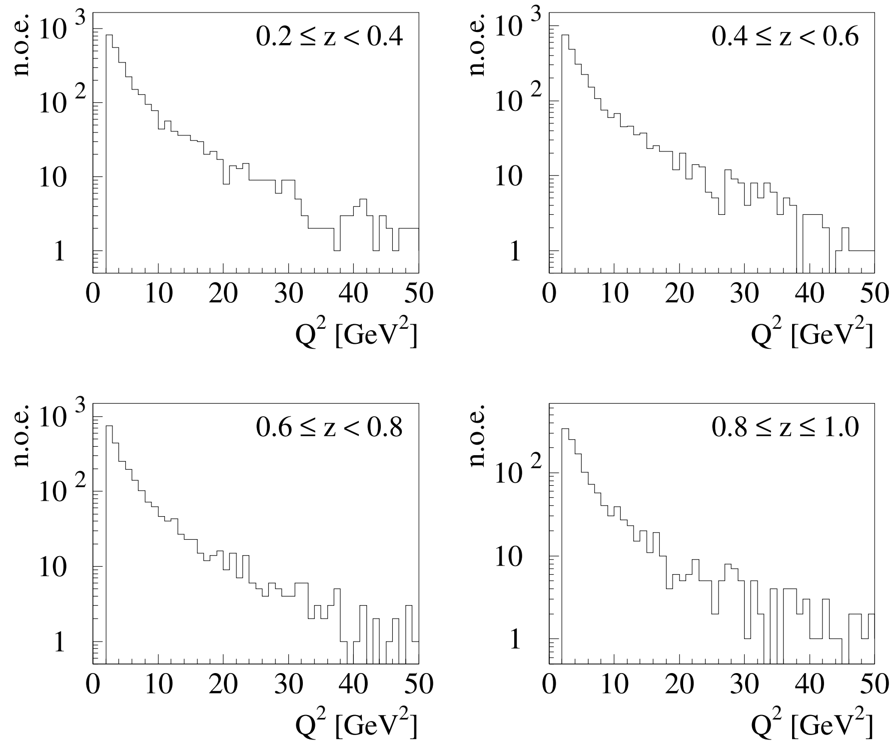

Figure 4.5: Uncorrected Q^2 *spectrum in the 4* z*–bins.*

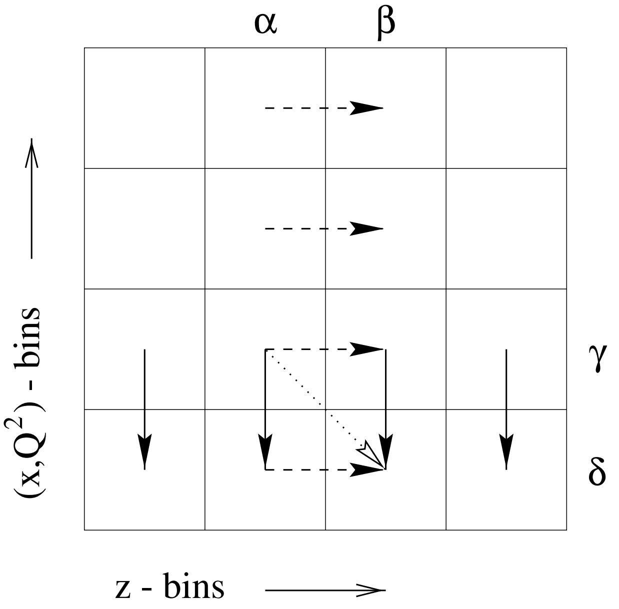

Figure 4.6: Factorization of the migration and acceptance corrections. The (x, Q^2)–bins are arranged in the vertical direction, whereas the z–bins are grouped in the horizontal direction. The arrows symbolize different components of the transformation matrix which projects the true bins to the smeared (reconstructed) bins.

The correction factor $\hat{A}_k$ is given by

$$\hat{A}_k = \varepsilon_{nd} R_{FNC,k} \ , \tag{4.15}$$

where ε_{nd} is the neutron detection efficiency (see Equation 3.8) and $R_{FNC,k}$ denotes the corrections due to the limited acceptance and the energy resolution of the forward neutron calorimeter.

4.5 Trigger Selection

Every high–rate experiment demands a complex trigger system which selects events of particular physics classes with high efficiency. An overview of H1's trigger system is given in Section 2.2.

The events which fulfil the selection criteria of this analysis are characterized by an scattered electron which is detected by the backward calorimeter SPACAL. Therefore a trigger was chosen which is mainly based on an energy deposit in the SPACAL: the subtrigger $s4$. This subtrigger requires:

- a local energy deposit of $\gtrsim 6$ GeV in the electromagnetic part (Trigger elements: `SPCLe_IET>2` or `SPCLe_IET_Cen3`) [Bou95],
- a total energy deposit of $\gtrsim 15$ GeV in the electromagnetic part, which is inside a time interval of ~ 20 ns around the bunch–crossing (`SPCLe_TOF_E_2`),

- the absence of out–of–time background indicated by the veto signal of the *Time–of–Flight* counters (see Section 2.2),

- and a combination of general vertex trigger conditions.

The subtrigger $s4$ has the advantage over the other DIS trigger used in the 1996 running period that it was highly efficient in the low Q^2–region ($Q^2 \approx 2\,\mathrm{GeV}^2$) and that it was usually not prescaled during the 1996 data taking. In the data sample used for the present measurement, no prescale factor was applied at any time to the subtrigger $s4$.

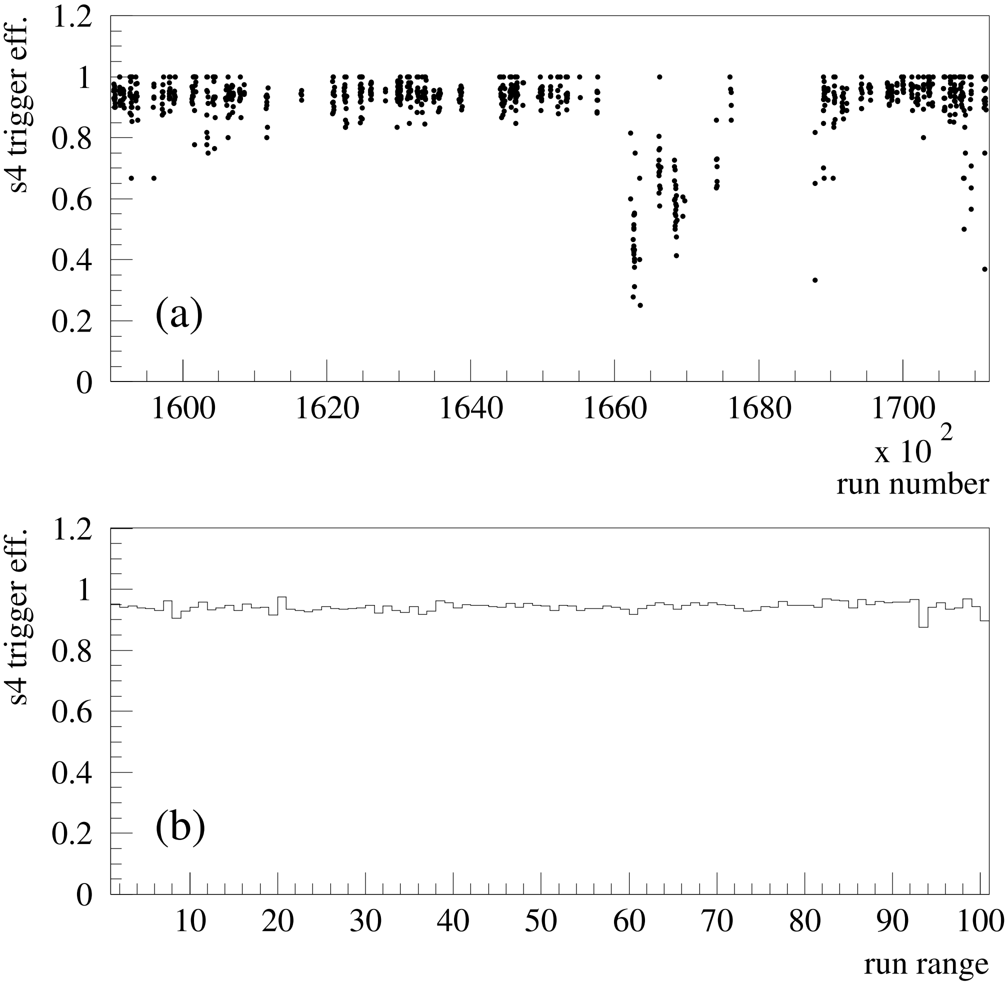

Figure 4.7: Trigger efficiency as a function of:
(a) run number, shown is the efficiency of subtrigger s4 averaged over the entire kinematic range;
(b) run range, the runs with malfunction of the trigger have been discarded; neighbouring runs have been combined.

4.5.1 Trigger Efficiencies

The efficiency of subtrigger $s4$ is calculated from the data using a sample of events triggered independently of the SPACAL, i. e. no trigger element, which is provided by the SPACAL, is used in the definitions of the SPACAL–independent triggers. Events are accepted for the trigger sample if they fulfil the DIS–selection criteria. The cuts related to the final state neutron are not applied in order to increase the statistical significance. The trigger efficiency is subsequentially given as the ratio of events in the trigger sample, for which the actual subtrigger $s4$ has been set, over the total number of events contained in this sample.

Figure 4.7a shows the calculated trigger efficiency as a function of the run number. The efficiency averaged over the whole kinematic range of the measurement is $\sim 95\%$ for most of the runs, except for the period between the run numbers 166022 and 169525, in which the efficiency dropped dramatically. This malfunction of the trigger was due to a shift of the timing of the HERA beams leading to the condition, that the signal caused by the energy deposit in the SPACAL was not fully contained in the time interval around the nominal bunch crossing which is assigned to in–time signals. Thus, the trigger element `SPCLe_TOF_E_2` did not fire regularly. Since the affected runs do not allow an accurate determination of the trigger efficiencies, they were discarded from the analysis. For the final data sample the trigger efficiency is nearly constant, which is demonstrated in Figure 4.7b, where neighbouring runs have been combined in order to increase the statistics.

The trigger efficiency T_l has been calculated separately in the (x, Q^2)–bins. The result is given in Table 4.4. A common systematic error of 1% was added to the statistical error of the trigger efficiency which reflects possible event losses due to the background veto of the ToF counters [Mey97].

(x, Q^2)–bin l	trigger efficiency T_l	stat. error in %
1	0.905	0.32
2	0.977	0.16
3	0.987	0.20
4	0.914	0.31
5	0.973	0.24
6	0.921	0.37
7	0.953	0.33
8	0.963	0.48
9	0.966	0.26
10	0.974	0.28
11	0.949	0.34
12	0.982	0.20

Table 4.4: Trigger efficiency in the 12 (x, Q^2)–bins. Shown is the efficiency T_l of subtrigger s4 and the corresponding statistical error. There is an additional common systematic error of 1%. For the definition of the bins see Table 4.2.

4.6 Reconstruction Efficiency in the (x, Q^2)–Plane

The reconstruction of a deep–inelastic event and of its inclusive kinematic quantities x and Q^2 is influenced by the following two effects:

- **Smearing and bin migration**: Due to the limited resolution of the detector the values of the variables x and Q^2 can be significantly smeared, leading to the possibility that an event, which is produced in a certain (x, Q^2)–bin, is finally reconstructed in a different bin.

- **Acceptance**: The track and the cluster of the scattered electron and the vertex are only reconstructed with a probability smaller than 100%, which leads to event losses.

For the evaluation of these effects and the determination of the correction factors the DJANGO Monte Carlo program [Sch92, Spi96] was used, which simulates deep–inelastic *ep* scattering including QED and QCD radiative effects[3]. Events are generated according to the GRV–LO [Glü95] parton distributions. The identities and the four–momenta of all final state particles are fed into a simulation of the H1 detector (H1SIM [H1C97]) which is based on GEANT [ASG94]. The detector response is simulated taking the detector geometry and the resolution of the detector components into account. The Monte Carlo events are subsequentially reconstructed and analyzed as if they were real data. In particular the DIS–selection criteria (see Table 4.1) are also imposed to the Monte Carlo sample.

Figure 4.8 shows a comparison between the data and the reconstructed DJANGO Monte Carlo for one of the (x, Q^2)–bins. There is a good agreement between the observed distributions of the inclusive quantities. Also the comparisons in the other (x, Q^2)–bins yield similar results, which shows that the DJANGO Monte Carlo and the detector simulation give a correct description of the underlying physics processes and the detector response respectively. Thus, it is justified to use this Monte Carlo simulation for the determination of the reconstruction efficiency.

Denoting the number of generated events in the l–th bin by $N_{gen,l}$ and the number of reconstructed events in this bin by $N_{rec,l}$ (where the events do not necessarily originate from the same bin), the reconstruction efficiency $R_{incl,l}$ for the l–th bin can be expressed by

$$R_{incl,ij} = \frac{N_{rec,l}}{N_{gen,l}} \; . \tag{4.16}$$

$N_{rec,l}$ has been computed using the same DIS selection as for the data (see Table 4.1). No selection criteria, in particular no cuts on y, have been applied for the evaluation of $N_{gen,l}$. The generated events have been assigned to the different (x, Q^2)–bins according to the value of x and Q^2 at the photon–proton vertex, i. e. those values which the parton distribution functions are defined with respect to. The result for the 12 (x, Q^2)–bins is given in Table 4.5 and it is in addition displayed in Figure 4.9a. The bin stability, which denotes the fraction of events which are reconstructed in the same bin as they were generated in, is shown in Figure 4.9b. It is about 60–70%.

---

[3] DJANGO is an interface of the Monte Carlo programs HERACLES [Kwi93] and LEPTO [Ing97].

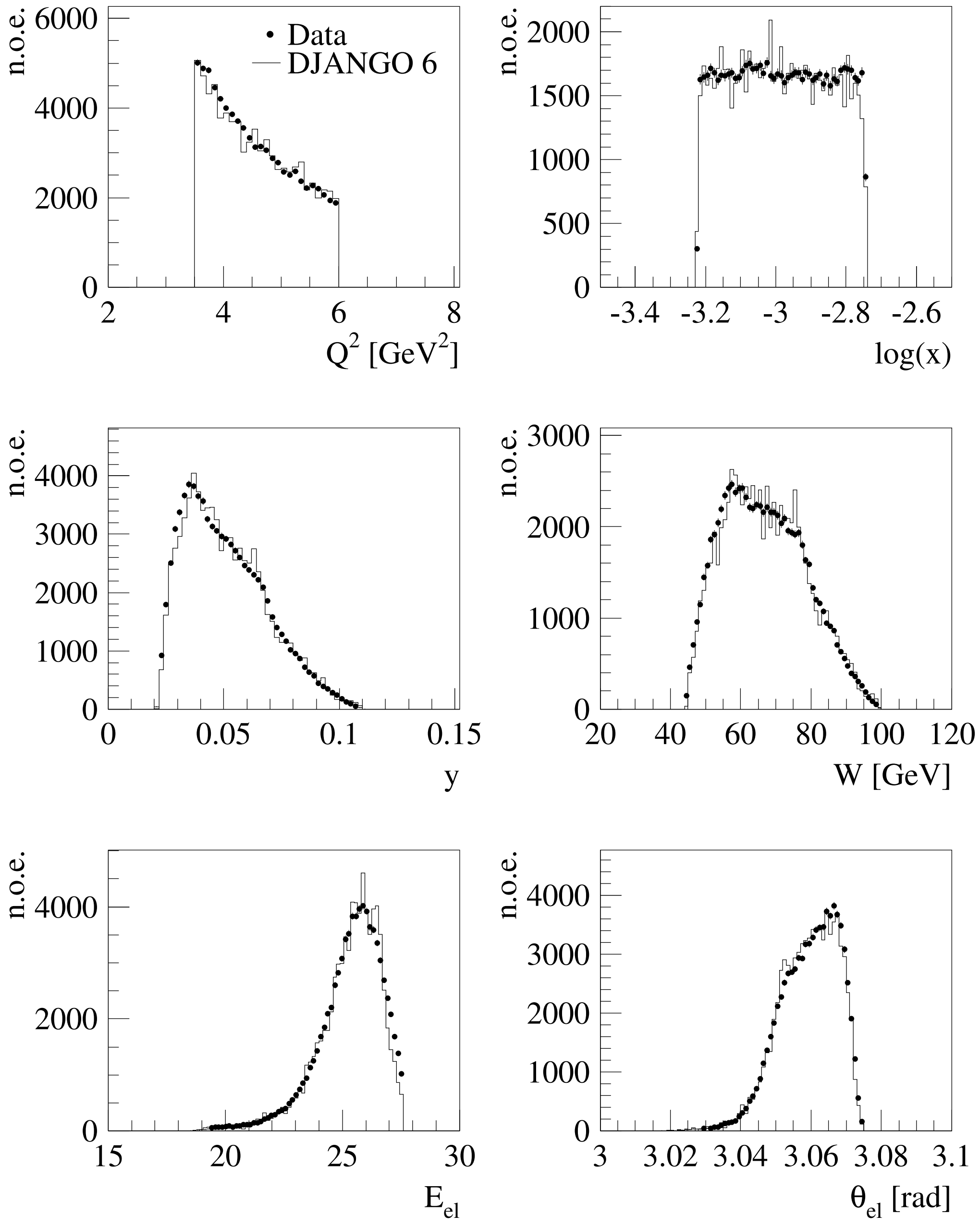

Figure 4.8: Comparison between data and reconstructed DJANGO *Monte Carlo for one of the (x, Q^2)–bins (bin number 5). The Monte Carlo is normalized according to the integrated luminosity and weighted by the trigger efficiency.*

(x, Q^2)–bin l	Reconstruction efficiency R_l	stat. error in %
1	0.928	1.5
2	1.348	1.3
3	1.080	1.5
4	0.878	1.6
5	1.144	1.7
6	0.736	2.1
7	1.018	2.1
8	0.810	2.4
9	0.850	2.3
10	1.070	2.4
11	0.688	3.1
12	0.972	3.0

Table 4.5: Reconstruction efficiency R_l in the 12 (x, Q^2)–bins as determined with the DJANGO *Monte Carlo and corresponding statistical error. The vertex reconstruction probability is included in R_l. For the definition of the bins see Table 4.2.*

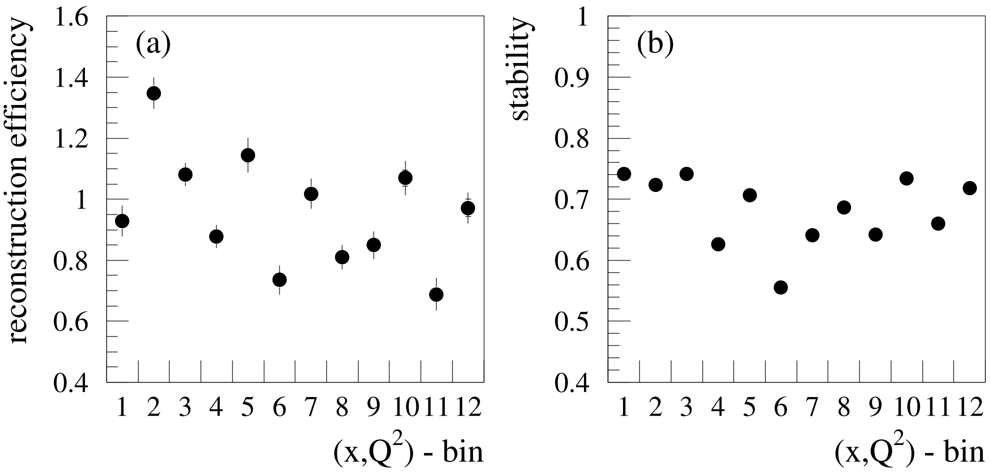

Figure 4.9: (a) Reconstruction efficiency R_l in the 12 (x, Q^2)–bins. The vertex reconstruction probability is included in R_l. The inner error bars show the statistical error and the outer error bar the statistical and systematic error added in quadrature. The systematic error is determined in Section 4.6.1.
(b) The stability in the 12 (x, Q^2)–bins. It is defined as the fraction of events which are reconstructed in the same bin as they are generated in.

4.6.1 Systematic Error of the Reconstruction Efficiency

The accuracy of the determination of the reconstruction efficiency R_l depends on the precision of the energy and track measurement of the final state particles and in particular of the scattered electron. Besides the resolution of the detector components, which is already taken into account in the detector simulation, there are additional uncertainties in the absolute energy scale of the calorimeter and in the alignment of the tracker. The most prominent sources for systematic errors are:

- **The absolute electromagnetic energy scale of the SPACAL** for the measurement of the scattered electron's energy. The kinematic variables were recalculated, while increasing (and decreasing) the reconstructed energy of the scattered electron according to the absolute energy scale uncertainty, which was determined to be 1% at 27.5 GeV increasing linearly to 3% at 7 GeV [H1C97a]. The larger deviation was taken to estimate the systematic error on the reconstruction efficiency, which is 0.03% to 4.1% depending on the particular (x, Q^2)–bin.

- **Potential misalignment of the BDC** for the determination of the scattering angle of the final state electron. The scattering angle was varied by ±0.5 mrad, according to the accuracy of the BDC alignment [Kat97], which results in a systematic error of 1.1% to 5.3%.

- **The hadronic energy scale of the Liquid–Argon–calorimeter** for the measurement of the kinematic quantity Σ of the hadronic final state. The hadronic energy scale of the LAr–calorimeter is known to 4% [H1C96b]. This leads to a systematic uncertainty on the reconstruction efficiency of 0.6% to 2.5%.

Adding this uncertainties in quadrature the systematic error on the reconstruction efficiency R_l can be estimated to be 2.2% to 6.9% depending on the specific (x, Q^2)–bin.

4.7 Radiative Corrections

As described in Section 4.1, the leading neutron structure function $F_2^{LN(3)}$ is defined with respect to the Born level, which describes *ep* scattering to lowest order perturbation theory. Therefore the measured cross section, which comprises all higher order electroweak diagrams, has to be corrected for these additional processes.

4.7.1 Outline of QED Radiation

The corrections of $\mathcal{O}(\alpha)$ are dominated by processes, where a photon is radiated from the electron or the struck quark, either in the initial or final state [Spi92]. Compared to the *leptonic* radiation, the *quarkonic* corrections are supressed due to the smaller charge and higher mass of the quarks. Interference terms between the lepton and quark line contribute less than 1% to the radiative effects. Corrections, involving the heavy vector bosons of the weak interaction (Z^0, $W^\pm$), are tiny for low and intermediate values of Q^2 ($Q^2 < 100\,\mathrm{GeV}^2$).

(x, Q^2) bin $\#l$	Error on E'_e [%]	Error on θ_e [%]	Error on Σ [%]	Combined error $\sigma_{rec,l}$ [%]
1	3.45	2.50	1.99	4.70
2	1.11	1.94	1.73	2.83
3	1.73	1.11	0.77	2.20
4	2.14	2.20	1.49	3.42
5	0.45	3.19	2.45	4.05
6	3.51	4.09	1.60	5.62
7	0.85	3.33	1.41	3.72
8	0.91	2.99	1.79	3.60
9	1.58	3.60	1.64	4.25
10	0.03	3.77	1.42	4.02
11	4.08	5.33	1.54	6.89
12	1.03	3.42	0.63	3.63

Table 4.6: Systematic error on the reconstruction efficiency R_l. It has been evaluated by varying the electron energy E'_e and scattering angle θ_e and the kinematic quantity Σ of the hadronic final state. For the definition of the bins see Table 4.2.

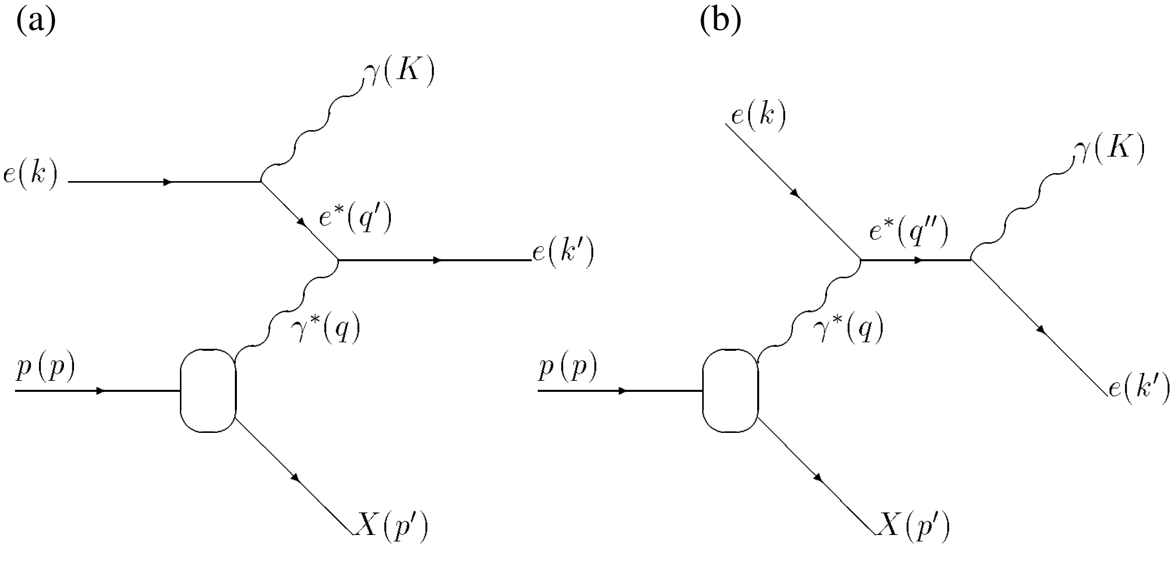

Figure 4.10: The dominant contribution to the process $ep \to ep\gamma$: (a) initial state radiation (ISR), (b) final state radiation (FSR). $p(p)$, $e(k)$, $X(p')$ and $e(k')$ denote the four–vectors of the incident proton and electron, of the hadronic final state and the scattered electron respectively. $\gamma(K)$ corresponds to the radiated photon. The four–momentum squared of the virtual photon and electron is given by q^2 and q'^2 (q''^2).

Thus, the radiative corrections are dominated by initial state radiation from the incoming electron or by final state radiation from the outgoing, scattered electron. The Feynman diagrams of these processes are sketched in Figure 4.10, where also the relevant four–vectors are defined. Based on the kinematic domain and the corresponding event topology one can define the following three classes of radiative events [Cou92, H1C95]:

- The **bremsstrahlung process** corresponds to the singularities in both the virtual electron and photon propagators, where the electron and the photon are scattered at very low angles. The case of elastic scattering, also known as Bethe–Heitler process, which has a verly large cross section is employed for the measurement of the luminosity (see Section 2.2). The radiated photon, as well as the electron and proton, disappear through the beam pipe and are not detected by the central detector.

- In the **QED Compton process** the negative four–momentum squared $-q^2$ of the virtual photon is much smaller than $-q'^2$ or q''^2 of the virtual electron, which is linked to the real photon. The dominant contribution to Compton scattering is the elastic channel ($ep \rightarrow ep\gamma$), of which the signature is given by two electromagnetic clusters in the backward calorimeter. Also for the inelastic channel, no additional particles are within the acceptance for most of the events, so that no vertex can be reconstructed. Therefore, in the present analysis the background contribution due to QED Compton scattering is negligible.

- In the case of **radiative DIS processes** the virtuality $-q^2$ of the photon is large ($-q^2 \gtrsim 1\,\mathrm{GeV}^2$), while $-q'^2$ (q''^2) is small, leading to the (nearly) collinear radiation of a real photon either in the initial or final state. Thus, radiative DIS events are contained in the selected data sample.

For the Born diagram, the inclusive kinematic variables x and Q^2 can be defined unambiguously. This is not the case for radiative events, where the corresponding values are dissimilar at the electron–photon and the photon–proton vertex respectively, so that the kinematics are reconstructed differently depending on the chosen reconstruction method. Since the structure function parameterizes the photon–proton vertex and since the leptonic radiation is dominant, the electron method has the largest corrections to the measured cross section. Therefore, the Σ method which is less influenced by radiative corrections is used in this analysis.

4.7.2 Determination of the Radiative Corrections

The reconstruction efficiency in the (x, Q^2)–plane (see Section 4.6) was determined using the DJANGO Monte Carlo [Sch92, Spi96], which calculates QED radiative corrections using the HERACLES program [Kwi92, Kwi93]. The measured cross section was corrected with respect to the kinematic variables x and Q^2 as defined at the photon–proton vertex. Therefore the calculated efficiencies already include the influence of the radiative effects on the reconstructed variables, leaving only the correction of the measured cross section to the Born level still to be evaluated.

(x, Q^2)–bin # l	radiative correction $(1+\delta_l)$	statistical error in [%]
1	1.006	1.4
2	0.967	1.3
3	0.992	1.5
4	1.005	1.5
5	1.003	1.7
6	1.007	1.8
7	0.999	2.0
8	1.040	2.2
9	1.039	2.1
10	1.054	2.3
11	1.025	2.7
12	1.046	2.8

Table 4.7: Radiative Corrections in the 12 (x, Q^2)–bins. The correction factors $(1+\delta_l)$ were evaluated using the DJANGO *Monte Carlo. For the definition of the bins see Table 4.2.*

These radiative corrections, denoted as $\delta_{rc,l}$, are calculated for each (x, Q^2)–bin using the DJANGO Monte Carlo on the generator level (without detector simulation). The correction factors are equal to:

$$(1+\delta_{rc,l}) = \frac{N_{\text{rad on},l}}{N_{\text{rad off},l}} , \tag{4.17}$$

where $N_{\text{rad on},l}$ denotes the number of events generated in the l–th (x, Q^2)–bin, when the radiative corrections are simulated, and $N_{\text{rad off},l}$ is the corresponding number of events at the Born level.

The result for $(1+\delta_{rc,l})$ and the corresponding statistical errors are given in Table 4.7. An additional systematic error of 2% is assumed due to higher order processes which are not simulated by the DJANGO Monte Carlo program.

4.8 Detection of Leading Neutrons

The detection and measurement of neutrons with the Forward Neutron Calorimeter FNC is described in detail in chapter 3. Here only those features, which are crucial for the cross section measurement are briefly summarized.

Neutral particles are identified by two segmented hodoscope planes in front of the detector. Their combined efficiency for tagging a charged particle is 99.5% (see Section 3.2.2). The contribution of charged particles to the total rate of particles impinging on the acceptance region of the calorimeter is $\approx 5\%$ (see Section 3.2.2). Therefore the contamination of the event sample with charged particles is estimated to be less than 0.05%.

In this analysis it is assumed that all neutral clusters are produced by neutrons. Using the LEPTO Monte Carlo program [Ing97] and a GEANT [ASG94] simulation of the H1 beam line, the background contribution has been estimated to be 6% for events with $z = E'_n/E_p \geq 0.2$ and to consist mostly of K_L^0 and photons, where the latter do not convert in the lead shielding in front of the detector, which has a thickness of 0.9 radiation lengths. The background is further suppressed at higher values of z and amounts to 3% for $z \geq 0.4$ and 2% for $z \geq 0.6$.

The efficiency for tagging neutrons has been determined to be $\varepsilon_{nd} = (93 \pm 5)\%$ (see Section 3.2.2). The losses are due to coincidences in the veto hodoscopes which mostly originate from the back–scattering of charged particles produced during the neutron's hadronic shower. This back–scattering is also known as *albedo*.

4.9 The Corrected Neutron z Spectrum

The kinematics of the leading neutron is determined using the cluster energy E_{cl} and the position (x_{cl}, y_{cl}) of the reconstructed impact point as measured by the FNC. With the proton beam energy $E_p = 820\,\mathrm{GeV}$, the fractional energy z of the neutron and its transverse momentum p_T can be expressed by

$$\begin{aligned} z &= \frac{E_{cl}}{E_p} \ , \\ p_T &= \frac{\sqrt{(x_{cl} - x_{vtx})^2 + (y_{cl} - y_{vtx})^2}}{l - z_{vtx}} E_{cl} \ , \end{aligned} \tag{4.18}$$

where x_{vtx}, y_{vtx} and z_{vtx} denote the position of the reconstructed vertex and $l = 107\,\mathrm{m}$ is the distance between the calorimeter and the nominal interaction point.

Due to the modest energy resolution of the FNC (see Section 3.4.1), the corrected leading neutron z spectrum was determined using an unfolding procedure [Blo84], which simultaneously corrects the observed neutron energy spectrum for acceptance and migration effects.

4.9.1 The Unfolding Technique

The correction of the z spectrum was performed using a program [Blo96] based on the concept of *regularized unfolding* [Blo84]. This method uses generated and reconstructed Monte Carlo events as input, which define implicitly the acceptance of the detector and its resolution. This "response" of the detector is also denoted as the *resolution function* $A(x_m, x_t)$, which describes the probability that the true variable x_t is reconstructed as the measured quantity x_m. The relation between the true distribution $f(x_t)$ and the measured distribution $g(x_m)$ is given by the *Fredholm* integral equation:

$$g(x_m) = \int \mathrm{d}x_t \, A(x_m, x_t) f(x_t) + b(x_m) \ , \tag{4.19}$$

where $b(x_m)$ represents potential background contribution to the observed distribution.

The input Monte Carlo provides a set of pairs (x_t, x_m) of the generated and reconstructed quantity[4], which defines the resolution function $A(x_m, x_t)$, the generated

---

[4] x_m can also denote an event loss.

(true) distribution $f_0(x_t)$ and the reconstructed (observed) distribution $g_0(x_m)$. The evaluated resolution function, and consequentially the result of the unfolding, should not depend on the input function $f_0(x_t)$ which may differ considerably from the true function $f(x_t)$. The unfolding program optimizes a weighting–function $w(x_t)$, which is used to calculate for each Monte Carlo event a weight–factor, depending only on the true variable x_t. As a result, the reweighted and reconstructed Monte Carlo distribution fits the measured distribution $g(x_m)$. Consequentially the true distribution $f(x_t)$ is given by

$$f(x_t) = w(x_t) f_0(x_t) \; . \tag{4.20}$$

4.9.2 Unfolding the *z* Spectrum

For each bin in (x, Q^2) the corrected z spectrum is determined separately by performing the unfolding procedure over the sub–sample of the data contained within this bin. The correction factor $R_{FNC,k}$ defined in Equation 4.15 is evaluated individually for the 12 (x, Q^2)–bins.

The Monte Carlo data sample used in the unfolding procedure consists of events generated with the Lepto MC [Ing97], of which only the produced neutrons were passed through the Geant [ASG94] simulation of the forward beam line. The energy deposit of the neutrons impinging on the calorimeter was smeared according to the resolution of the FNC (see Section 3.4.1). Since the Lepto Monte Carlo generator does not sufficiently reproduce the p_T spectrum observed in the data, the generated events were weighted in p_T by assigning to every event a weight–factor $a(p_T)$, which is calculated with a third order polynomial:

$$a(p_T) = 0.430 + 9.3903\,\mathrm{GeV}^{-1} \cdot p_T - 26.500\,\mathrm{GeV}^{-2} \cdot p_T^2 - 13.291\,\mathrm{GeV}^{-3} \cdot p_T^3 \; . \tag{4.21}$$

Events with neutrons of $p_T > 0.2\,\mathrm{GeV}$ were reweighted with $a(0.2\,\mathrm{GeV})$. Those neutrons, of which the generated transverse momentum of $p_T > 0.2\,\mathrm{GeV}$ was reconstructed inside the range of the selection cut $p_T \leq 0.2\,\mathrm{GeV}$, were treated as a background contribution to the measurement, which is subtracted consequentially.

The principle of the unfolding procedure is demonstrated in Figure 4.11: The weighting function $w(z)$, which is applied to the Monte Carlo sample, is optimized until the reconstructed (accepted) and reweighted Monte Carlo distribution agrees well with the observed data. The generated Monte Carlo distribution multiplied by the weighting function $w(z)$ gives the final result for the unfolded data. In addition the program calculates a statistical error based on the number of events in the data and Monte Carlo samples and bin–to–bin correlations.

Figure 4.12 shows the observed neutron z and p_T spectra integrated over the whole kinematic range in x and Q^2. The data are compared to the reweighted Monte Carlo simulation which results from the unfolding procedure. The data and Monte Carlo z distributions, shown in Figure 4.12a, are in agreement by construction. Figure 4.12b is a control plot, which demonstrates that the reweighted Monte Carlo gives a good description of the p_T distribution, which is not used in the fit. The z and p_T spectra in the individual (x, Q^2)–bins are shown in Figures 4.13 to 4.15.

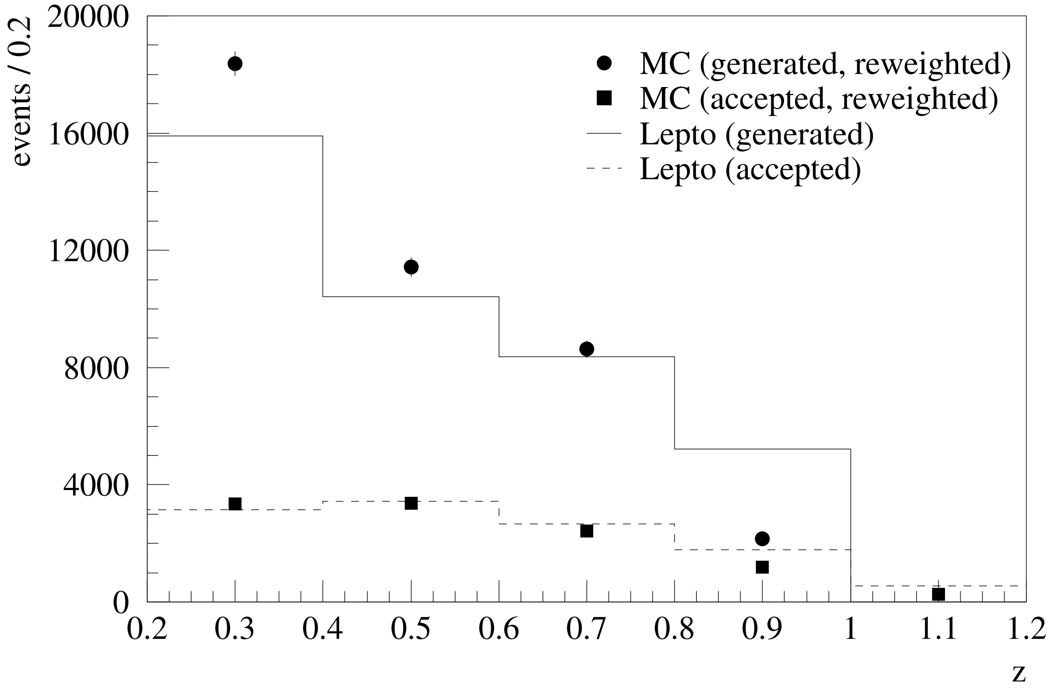

Figure 4.11: Unfolding of the neutron z spectrum. Shown are the generated and accepted distributions produced by the Lepto *Monte Carlo and the distributions resulting from the Monte Carlo, which has been reweighted in z in the unfolding procedure. The generated and reweighted Monte Carlo distribution defines the result for the unfolded data.*

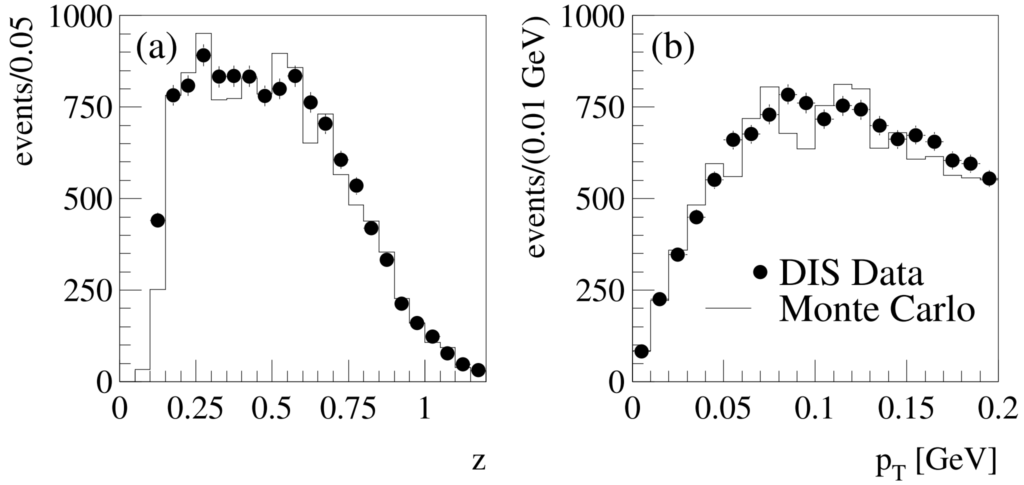

Figure 4.12: The observed neutron z and p_T spectra compared to the reweighted Monte Carlo distribution which result from the unfolding procedure (integrated over all (x, Q^2)–bins). The Monte Carlo distributions are normalized to the total number of events in the data.

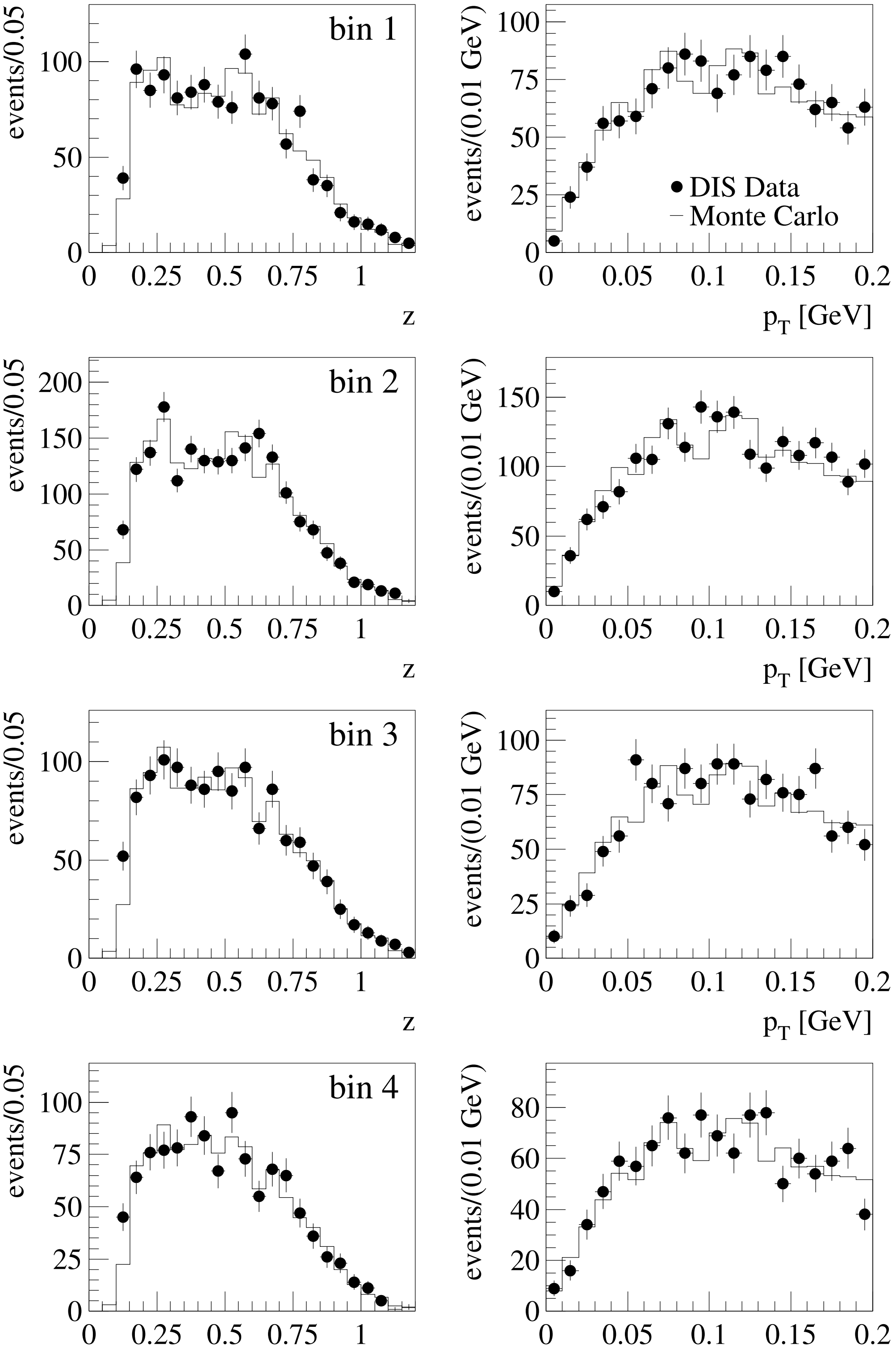

Figure 4.13: The observed neutron z and p_T spectra compared to the reweighted Monte Carlo distribution. Shown are the distributions for the (x, Q^2)–bins 1 to 4.

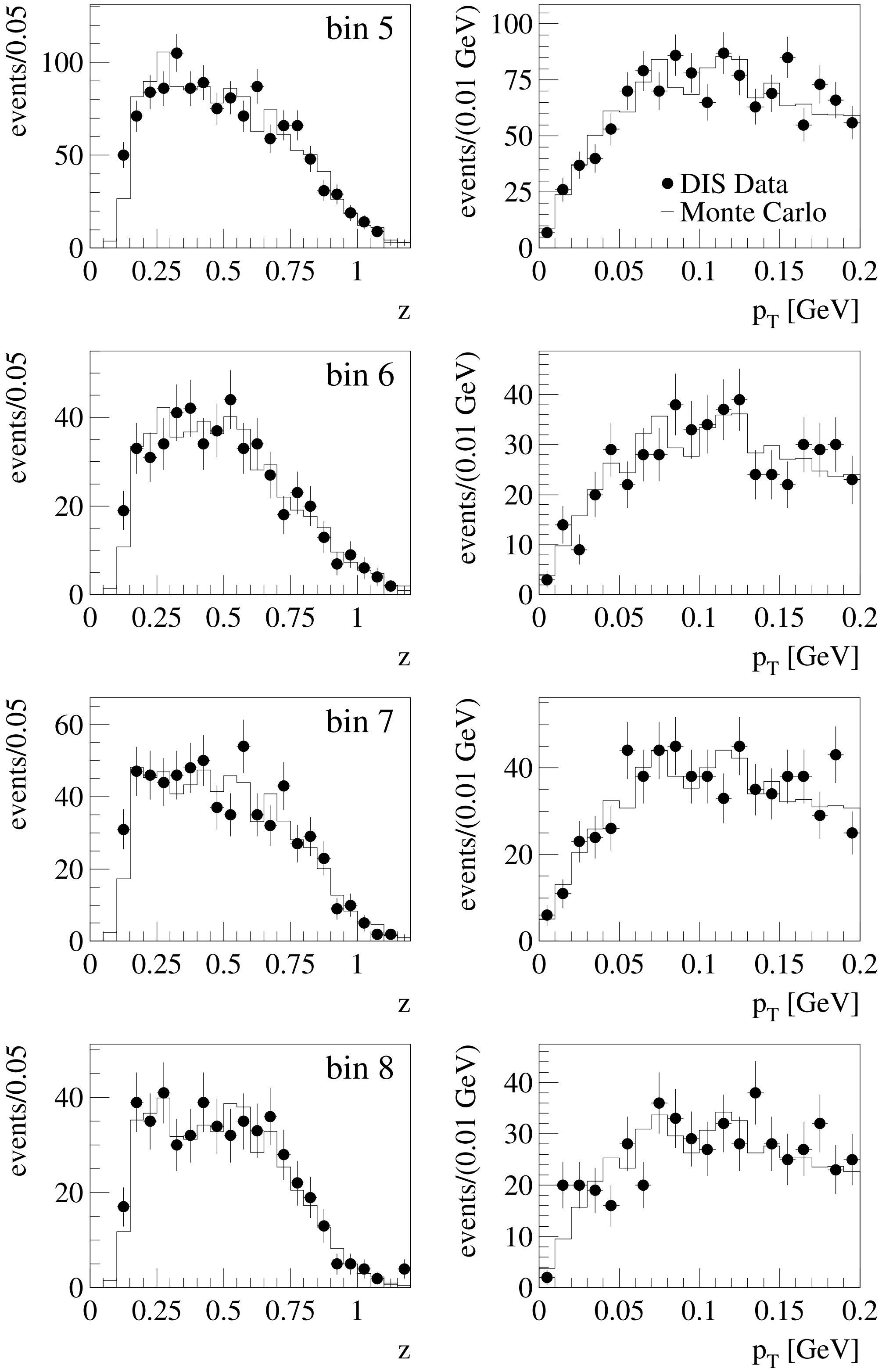

Figure 4.14: The observed neutron z and p_T spectra compared to the reweighted Monte Carlo distribution which results from the unfolding procedure. Shown are the distributions for the (x, Q^2)–bins 5 to 8.

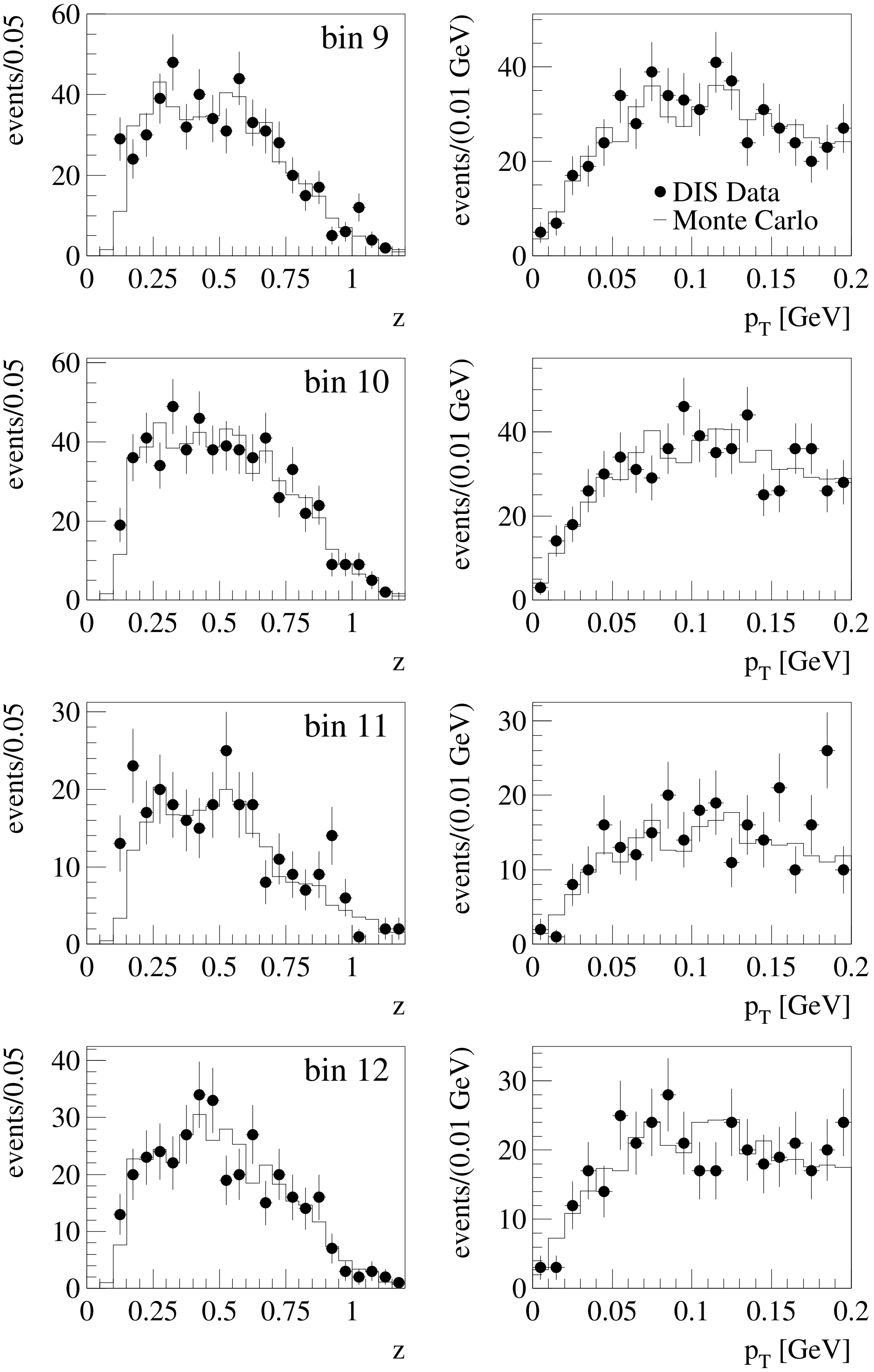

Figure 4.15: The observed neutron z and p_T spectra compared to the reweighted Monte Carlo distribution. Shown are the distributions for the (x, Q^2)–bins 9 to 12.

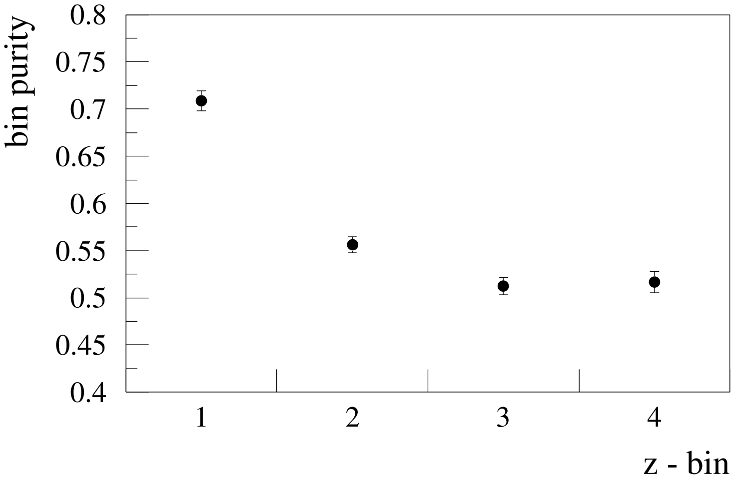

Figure 4.16: Bin purity in the 4 z–bins. Only the statistical error is shown. For the definition of the bins see Table 4.3.

The bin purity, which is defined as the fraction of events in a bin of the reconstructed variable which originate from the same bin, is shown in Figure 4.16. The bin purity is always above 50%.

4.9.3 Systematic Errors on the Unfolded z Spectrum

The systematic error on the unfolded z distribution was determined in the following way:

- The energy scale of the FNC was varied by ±5% (see Section 3.5.1). The resulting difference in the unfolded distribution ranges between 8% and 51% depending on the particular z–bin.
- The Monte Carlo sample, which is used in the unfolding procedure, was reweighted in p_T. Events were either suppressed or enhanced with a linear weighting–function depending on the value of p_T. The effect of this reweighting is demonstrated in Figure 4.17, which shows that the reweighted Monte Carlo distributions differ significantly from the observed p_T spectra. The systematic error due to the uncertainty in the p_T distribution was estimated to be 4% to 9%.
- The acceptance of the FNC was recalculated using the geometric acceptance determined on the basis of the 0°–direction as observed in the data (see Section 3.3). This results in a systematic error of 7% to 30%.
- The result of the unfolding procedure depends on the number of knots used for the spline function, which defines the weighting function $w(z)$ (see above). An additional error of 10% due to this effect was determined.

In each case the error was evaluated by performing the unfolding procedure over the entire data sample in order to increase the statistical significance. The positive and

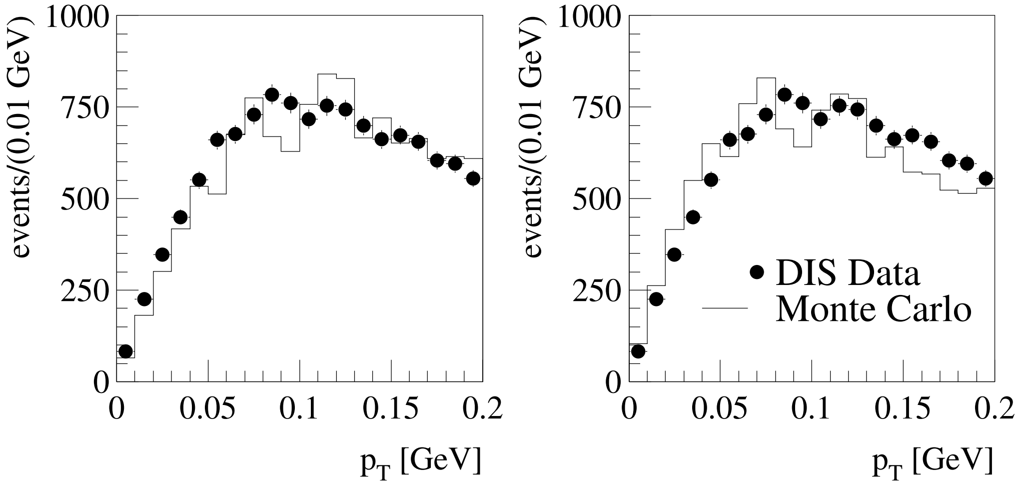

Figure 4.17: Reweighted Monte Carlo p_T distributions compared to the observed data. The Monte Carlo events were reweighted in order to determine the systematic error due to the p_T spectra of the Monte Carlo used in the unfolding procedure.

z–bin Nr. k	Error on energy scale pos. shift [%]	Error on energy scale neg. shift [%]	Error on p_T weighting a) [%]	Error on p_T weighting b) [%]	Error on acceptance [%]	Combined error [%]
1	-0.9	8.2	8.9	-6.9	20.0	25
2	-11.0	3.2	2.2	-4.9	-30.5	34
3	10.6	1.1	4.2	3.0	-6.6	16
4	51.1	-41.7	3.0	-4.9	23.1	57

Table 4.8: Systematic error on the unfolded z spectrum. The influence of the uncertainty in the energy scale, the p_T weighting and the acceptance has been evaluated. The combined errors include an additional error due to the unfolding procedure, which is 10%. For the definition of the bins see Table 4.3.

negative deviations from the original result were added in quadrature and the larger value was taken as the total systematic error. The final result for the four intervals in z is given in Table 4.8. The unfolding was redone using the POMPYT Monte Carlo [Bru96] as the event generator in order to demonstrate that the result of the unfolding does not depend on the Monte Carlo employed in the procedure.

4.10 Measurement of the Semi–Inclusive Structure Function $F_2^{LN(3)}$

The relation between the measured number of events $N_{data,ijk}$ in a (x, Q^2, z)–bin containing a leading neutrons with transverse momentum $p_T \leq 200\,\text{MeV}$ and the leading neutron structure function $F_2^{LN(3)}$, as defined in Section 4.1, is given by Equation 4.3. The different quantities, which enter the relation, have been defined in Equation 4.1 and have been evaluated in the previous sections except of the number of background events $N_{bg,ijk}$, the integral $\mathcal{I}_{ij}$ over x and Q^2 of the kinematic factor and the bin centre correction $C_{binc,ijk}$. These remaining quantities will be determined in the following.

4.10.1 Background

Potential background can originate from the following processes:

- **Photoproduction:** The signature of the scattered electron can be faked by particles from the hadronic final state. A typical contribution are photons from π^0 decays ($\pi^0 \to \gamma\gamma$), which convert into $e^\pm$ in the dead material of the detector. This background is greatly suppressed by the cut on $\sum_i(E_i - p_{z,i})$, the lateral shower profile and the minimal energy of the scattered electron ($E'_e \geq 12\,\mathrm{GeV}$). In particular the cut on E'_e ensures that the photoproduction background can be neglected in this analysis.

- **Non–*ep* background:** 0.02% of the events, which fulfil all selection criteria (see Table 4.1), except of the colliding bunch condition, originate from proton–pilot bunches (unpaired bunch crossing with proton beam only). In 1996 HERA was running on average with 10 proton–pilot and 174 colliding bunches. Therefore the probability, that an event, which is happening during a real bunch crossing, is produced by a non–*ep* interaction is $\sim$ 0.4%. Thus, the non–*ep* background can be estimated to be $\sim$ 0.4%. There are no selected events resulting from electron–pilot or empty bunches.

- **Overlapping events**: There is a certain possibility that in a bunch crossing an *ep* scattering event and a beam–gas event occur simultaneously. For 0.04% of all the events which satisfy the standard selection, except of the cut on the timing of the FNC signal, the signal of the central calorimeter module takes place later than normal. This indicates that the neutron was not produced in the nominal, but in the following bunch–crossing.

- **Misidentified neutrons:** It is assumed that all neutral clusters in the FNC are produced by neutrons. The contribution of other particles has been estimated in Section 4.8 using the LEPTO Monte Carlo.

Since the background contribution is much smaller than the systematic error of this analysis, it is neglected and not subtracted from the measured cross section.

4.10.2 Integration of the Kinematical Factor

The measured cross section is proportional to the integral of the kinematical factor $\kappa(x, Q^2, z) = 4\pi\alpha^2/(x\,Q^4)$ over the (x, Q^2)–bin:

$$\mathcal{I}_{ij} \;=\; \frac{4\pi\alpha^2}{x\,Q^4}\int_{x_i}\mathrm{d}x\int_{Q^2_j}\mathrm{d}Q^2(1 - y + \frac{y^2}{2}) \;, \tag{4.22}$$

(x, Q^2)–bin Nr. l	Integral $\mathcal{I}_l$ [nb^{-1}]
1	46.342
2	61.273
3	59.575
4	31.853
5	32.398
6	16.074
7	17.523
8	20.350
9	12.286
10	14.929
11	6.239
12	8.449

Table 4.9: Integral of the kinematical factor in the 12 (x, Q^2)–bins. For the definition of the bins see Table 4.2.

where the integration is performed over the entire bin size. The value of the integral in the 12 bins in x and Q^2 is given in Table 4.9.

4.10.3 Bin Centre Correction

The measured cross section, averaged over the size of the (x_i, Q^2_j, z_k)–bin, has to be transformed into a measurement at a specific point in the centre of that bin. This is carried out by the bin centre correction $C_{binc,ijk}$.

For the central values of x and Q^2 the effective bin centre was chosen, so that no bin centre correction in x and Q^2 has to be applied. The dependence of the cross section on x and Q^2 can be approximated with

$$\frac{\mathrm{d}^2\sigma}{\mathrm{d}x\,\mathrm{d}Q^2} \propto \frac{1}{xQ^4} \ . \tag{4.23}$$

Transforming the variables into $\xi = \ln x$ and $\omega = -Q^2$, the differential cross section as a function of the new variables is approximately constant:

$$\frac{\mathrm{d}^2\sigma}{\mathrm{d}\xi\,\mathrm{d}\omega} \approx \text{const.} \ , \tag{4.24}$$

which means that the cross section depends linearly on the variables ξ and ω. For the central $x_{cen,i}$ and $Q^2_{cen,j}$ values, those values are chosen, which corresponds to the average of ξ and ω respectively:

$$x_{cen,i} = \exp\left[\frac{1}{2}\left(\ln x_{min,i} + \ln x_{max,j}\right)\right] \ , \tag{4.25}$$

$$Q^2_{cen,j} = \left[\frac{1}{2}\left(\frac{1}{Q^2_{min,j}} + \frac{1}{Q^2_{max,j}}\right)\right]^{-1} \ .$$

For the central z values, the arithmetic mean was chosen:

$$z_{cen,k} = \frac{1}{2}\left(z_{min,k} + z_{max,k}\right) \ . \tag{4.26}$$

The bin centre correction in z was evaluated using the shape of the z distribution as generated with the LEPTO and the POMPYT Monte Carlo generators. Only the bin at $z_{cen} = 0.9$ has a correction factor which differs from unity. It amounts to $C_{ij4} = 1.1 \pm 10\%$. To the other bins in z, a common systematic error of 5% was assigned due to the uncertainty in the z–bin centre correction.

4.10.4 Systematic Errors

There are three types of systematic errors: normalization errors, errors which depend on the final state neutron and errors which are different for each (x, Q^2)–bin:

- **The systematic error on the normalization**, which is the same in all bins of (x, Q^2, z) amounts to 5.7% and comprises the uncertainty of the neutron detection efficiency (5.4%, see Section 4.8) and the error of the luminosity determination (2%, see Section 4.2.2).
- **The final state neutron systematic error** includes the error of the unfolded z spectrum (see Section 4.9.3) and the uncertainty in the bin centre correction (see Section 4.10.3). The combined error ranges between 16% and 58%.
- **The systematic error which depend upon x and Q^2** ranges between 3.1% and 7.2%. The main source of this error is the uncertainty in the acceptance and in the migration as a function of x and Q^2 (see Section 4.6.1). The error includes in addition the uncertainty in the trigger efficiency (see Section 4.5.1) and the error on the radiative corrections (see Section 4.7.2).

4.10.5 Results

A compilation of the result for the semi–inclusive structure function $F_2^{LN(3)}(x, Q^2, z)$, which parameterizes the production cross section for leading neutrons with a transverse momentum of $p_T \leq 200$ MeV, is given in Table 4.10 and displayed in Figure 4.18, where the data are shown in the 12 (x, Q^2)–bins as a function of z. The table gives in addition the corresponding values for $\beta = x/(1-z)$. The shape of the neutron spectrum is similar in the different bins of x and Q^2. The structure function is in general decreasing with increasing values of z, but neutrons with $z \geq 0.6$ nevertheless comprise a substantial part of the cross section. A detailed discussion of the result and its interpretation will be presented in the following chapter.

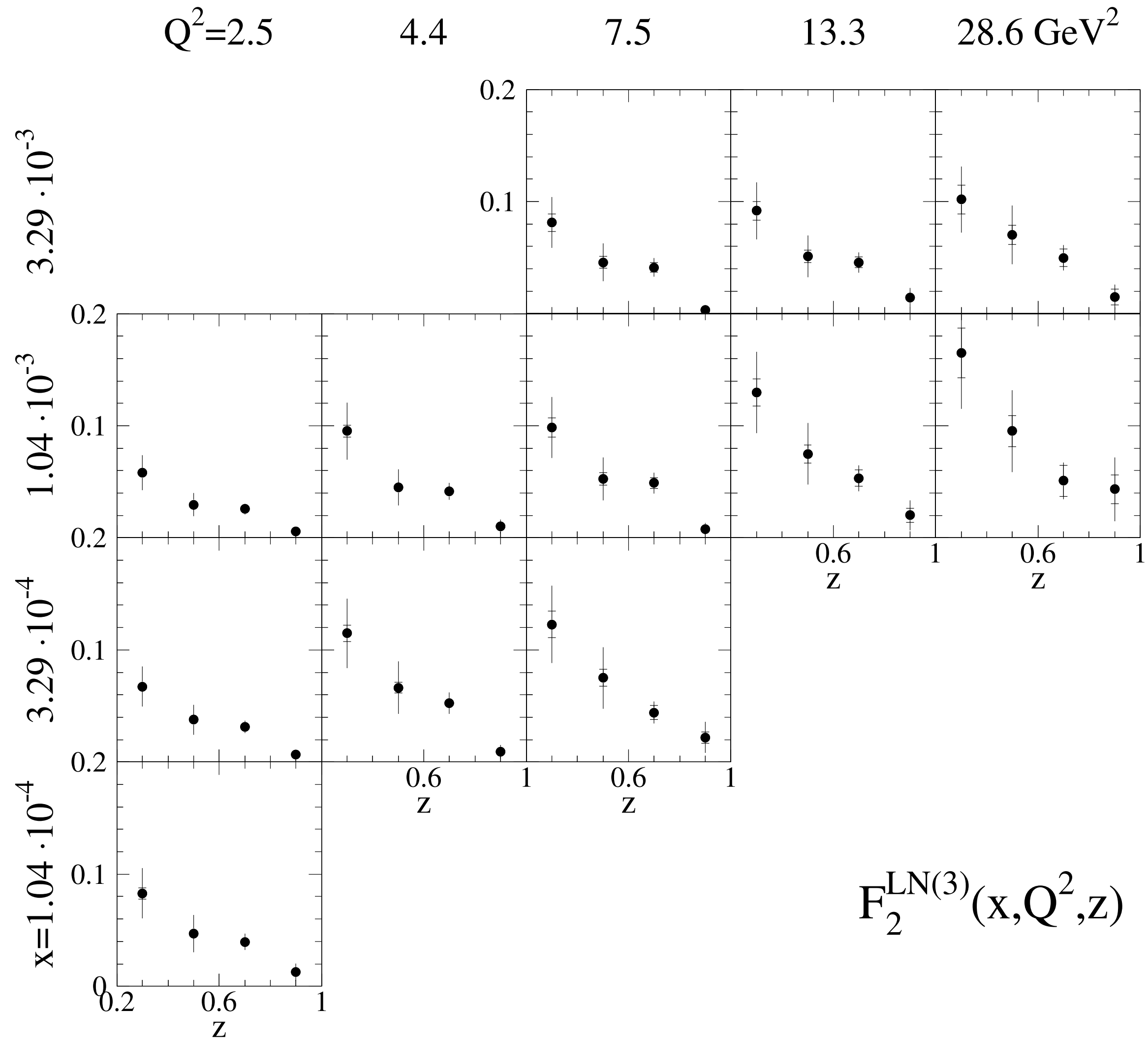

Figure 4.18: The leading neutron structure function $F_2^{LN(3)}$ as a function of z in the 12 (x, Q^2)–bins. The bins are arranged as follows: Q^2 is increasing from left to right, whereas x is increasing from bottom to top. The inner error bars show the statistical errors and the full error bars show the statistical and systematic errors added in quadrature. There is an additional 5.7% overall normalization error for the data points which has not been included in the error bars.

x	Q^2 [GeV^2]	z	β	$F_2^{LN(3)} \pm \mathrm{stat} \pm \mathrm{syst}(z) \pm \mathrm{syst}(x, Q^2) \pm \mathrm{norm}$
0.00010	2.5	0.3	0.00015	0.0829 ± 0.0051 ± 0.0215 ± 0.0043 ± 0.0048
0.00010	2.5	0.5	0.00021	0.0470 ± 0.0033 ± 0.0163 ± 0.0024 ± 0.0027
0.00010	2.5	0.7	0.00035	0.0396 ± 0.0030 ± 0.0065 ± 0.0021 ± 0.0023
0.00010	2.5	0.9	0.00104	0.0125 ± 0.0023 ± 0.0072 ± 0.0006 ± 0.0007
0.00033	2.5	0.3	0.00047	0.0673 ± 0.0032 ± 0.0174 ± 0.0024 ± 0.0039
0.00033	2.5	0.5	0.00066	0.0378 ± 0.0020 ± 0.0131 ± 0.0014 ± 0.0022
0.00033	2.5	0.7	0.00110	0.0315 ± 0.0018 ± 0.0051 ± 0.0011 ± 0.0018
0.00033	2.5	0.9	0.00329	0.0066 ± 0.0013 ± 0.0038 ± 0.0002 ± 0.0004
0.00104	2.5	0.3	0.00148	0.0582 ± 0.0034 ± 0.0151 ± 0.0018 ± 0.0033
0.00104	2.5	0.5	0.00208	0.0296 ± 0.0021 ± 0.0103 ± 0.0009 ± 0.0017
0.00104	2.5	0.7	0.00346	0.0257 ± 0.0019 ± 0.0042 ± 0.0008 ± 0.0015
0.00104	2.5	0.9	0.01039	0.0059 ± 0.0013 ± 0.0034 ± 0.0002 ± 0.0003
0.00033	4.4	0.3	0.00047	0.1150 ± 0.0073 ± 0.0298 ± 0.0047 ± 0.0066
0.00033	4.4	0.5	0.00066	0.0664 ± 0.0047 ± 0.0230 ± 0.0027 ± 0.0038
0.00033	4.4	0.7	0.00110	0.0526 ± 0.0039 ± 0.0086 ± 0.0021 ± 0.0030
0.00033	4.4	0.9	0.00329	0.0091 ± 0.0028 ± 0.0053 ± 0.0004 ± 0.0005
0.00104	4.4	0.3	0.00148	0.0952 ± 0.0055 ± 0.0247 ± 0.0044 ± 0.0055
0.00104	4.4	0.5	0.00208	0.0450 ± 0.0035 ± 0.0156 ± 0.0021 ± 0.0026
0.00104	4.4	0.7	0.00346	0.0414 ± 0.0030 ± 0.0067 ± 0.0019 ± 0.0024
0.00104	4.4	0.9	0.01039	0.0101 ± 0.0019 ± 0.0058 ± 0.0005 ± 0.0006
0.00033	7.5	0.3	0.00047	0.1228 ± 0.0116 ± 0.0318 ± 0.0074 ± 0.0070
0.00033	7.5	0.5	0.00066	0.0752 ± 0.0075 ± 0.0261 ± 0.0046 ± 0.0043
0.00033	7.5	0.7	0.00110	0.0442 ± 0.0064 ± 0.0072 ± 0.0027 ± 0.0025
0.00033	7.5	0.9	0.00329	0.0220 ± 0.0050 ± 0.0127 ± 0.0013 ± 0.0013
0.00104	7.5	0.3	0.00148	0.0984 ± 0.0085 ± 0.0255 ± 0.0043 ± 0.0056
0.00104	7.5	0.5	0.00208	0.0527 ± 0.0054 ± 0.0183 ± 0.0023 ± 0.0030
0.00104	7.5	0.7	0.00346	0.0488 ± 0.0047 ± 0.0080 ± 0.0021 ± 0.0028
0.00104	7.5	0.9	0.01039	0.0080 ± 0.0029 ± 0.0046 ± 0.0003 ± 0.0005
0.00329	7.5	0.3	0.00469	0.0812 ± 0.0079 ± 0.0210 ± 0.0034 ± 0.0047
0.00329	7.5	0.5	0.00657	0.0458 ± 0.0051 ± 0.0159 ± 0.0019 ± 0.0026
0.00329	7.5	0.7	0.01095	0.0412 ± 0.0043 ± 0.0067 ± 0.0017 ± 0.0024
0.00329	7.5	0.9	0.03286	0.0033 ± 0.0028 ± 0.0019 ± 0.0001 ± 0.0002
0.00104	13.3	0.3	0.00148	0.1295 ± 0.0121 ± 0.0336 ± 0.0062 ± 0.0074
0.00104	13.3	0.5	0.00208	0.0749 ± 0.0081 ± 0.0260 ± 0.0036 ± 0.0043
0.00104	13.3	0.7	0.00346	0.0533 ± 0.0073 ± 0.0087 ± 0.0026 ± 0.0031
0.00104	13.3	0.9	0.01039	0.0202 ± 0.0063 ± 0.0117 ± 0.0010 ± 0.0012
0.00329	13.3	0.3	0.00469	0.0918 ± 0.0082 ± 0.0238 ± 0.0042 ± 0.0053
0.00329	13.3	0.5	0.00657	0.0512 ± 0.0054 ± 0.0177 ± 0.0024 ± 0.0029
0.00329	13.3	0.7	0.01095	0.0457 ± 0.0048 ± 0.0074 ± 0.0021 ± 0.0026
0.00329	13.3	0.9	0.03286	0.0141 ± 0.0037 ± 0.0082 ± 0.0006 ± 0.0008
0.00104	28.6	0.3	0.00148	0.1650 ± 0.0224 ± 0.0428 ± 0.0119 ± 0.0095
0.00104	28.6	0.5	0.00208	0.0952 ± 0.0140 ± 0.0330 ± 0.0069 ± 0.0055
0.00104	28.6	0.7	0.00346	0.0509 ± 0.0137 ± 0.0083 ± 0.0037 ± 0.0029
0.00104	28.6	0.9	0.01039	0.0433 ± 0.0127 ± 0.0251 ± 0.0031 ± 0.0025
0.00329	28.6	0.3	0.00469	0.1018 ± 0.0129 ± 0.0264 ± 0.0043 ± 0.0058
0.00329	28.6	0.5	0.00657	0.0702 ± 0.0086 ± 0.0243 ± 0.0030 ± 0.0040
0.00329	28.6	0.7	0.01095	0.0499 ± 0.0077 ± 0.0081 ± 0.0021 ± 0.0029
0.00329	28.6	0.9	0.03286	0.0148 ± 0.0071 ± 0.0086 ± 0.0006 ± 0.0008

Table 4.10: The measured values of $F_2^{LN(3)}$ for neutrons with $p_T \leq 200\,\mathrm{MeV}$.

Chapter 5

$F_2^{LN(3)}$: Results and Interpretations

After having described the different steps of the analysis in the previous chapter, this chapter will be devoted to a discussion of the result of the measurement and its interpretation.

The semi–inclusive cross section $\mathrm{d}^3\sigma/(\mathrm{d}x\,\mathrm{d}Q^2\,\mathrm{d}z)$ for the production of leading neutrons with a transverse momentum $p_T \leq 200\,\mathrm{MeV}$ has been measured in the kinematic region

$$\begin{aligned} 2\,\mathrm{GeV}^2 &\leq Q^2 \leq 50\,\mathrm{GeV}^2\ , \\ 6\cdot 10^{-5} &\leq x \leq 6\cdot 10^{-3}\ , \\ 0.2 &\leq z \leq 1\ . \end{aligned} \tag{5.1}$$

Assuming that the ratio between the absorption cross sections for longitudinally and transversely polarized virtual photons $R = 0$, the triple–differential cross section is parameterized by the leading neutron structure function $F_2^{LN(3)}(x, Q^2, z)$ defined by

$$\frac{\mathrm{d}^3\sigma}{\mathrm{d}x\,\mathrm{d}Q^2\,\mathrm{d}z}(x, Q^2, z) = \frac{4\pi\alpha^2}{x\,Q^4}\left(1 - y + \frac{y^2}{2}\right) F_2^{LN(3)}(x, Q^2, z) \tag{5.2}$$

Since $\beta = x/(1-z)$, this equation can be rewritten with respect to the variable β:

$$\frac{\mathrm{d}^3\sigma}{\mathrm{d}\beta\,\mathrm{d}Q^2\,\mathrm{d}z}(\beta, Q^2, z) = \frac{4\pi\alpha^2}{\beta\,Q^4}\left(1 - y + \frac{y^2}{2}\right) F_2^{LN(3)}(\beta, Q^2, z)\ , \tag{5.3}$$

so that

$$F_2^{LN(3)}(\beta, Q^2, z) = F_2^{LN(3)}(x = \beta/(1-z), Q^2, z)\ . \tag{5.4}$$

There are two different approaches which try to explain the production of leading neutrons in deep–inelastic scattering.

In the pion exchange model (see Section 1.5.2), the production cross section is determined by the product of the pion flux $f_{\pi^+/p}(z, p_T)$ and the pion structure function F_2^π evaluated at (β, Q^2). Therefore $F_2^{LN(3)}(\beta, Q^2, z)$ can be interpreted as follows:

$$F_2^{LN(3)}(\beta, Q^2, z) = \left[\int\limits_{0\,\mathrm{MeV}}^{200\,\mathrm{MeV}} \mathrm{d}p_T\, f_{\pi^+/p}(z, p_T)\right] \cdot F_2^\pi(\beta, Q^2)\ , \tag{5.5}$$

where β may be identified with the fraction of the momentum of the pion carried by the struck quark or gluon interacting with the virtual pion. This model is implemented in the Monte Carlo generators POMPYT [Bru96] and RAPGAP [Jun95].

Alternatively one may assume models, which are based on the concept of soft colour interaction [Buc95, Edi96] (see Section 1.6.2): The colour topology is rearranged, so that the common colour field between the struck quark and the proton remnant breaks up, which can lead to the production of a final–state baryon. In such an approach, which is for example realized in the LEPTO Monte Carlo program [Ing97], the variable β can no longer be interpreted as a momentum fraction.

These two different approaches constitute the guideline for the discussion and interpretation of the leading neutron data in the following sections. The predictions of the LEPTO and RAPGAP Monte Carlo generators are confronted with the measurement, before the data are used to test different factorization hypotheses. The leading neutron data are compared to a similar measurement of leading proton production. In the region $0.7 \leq z \leq 0.9$, both semi–inclusive cross sections can be described by a Regge model of leading baryon production, which consists of pion, pomeron and secondary reggeon exchanges. In the framework of this model, the leading neutron structure function $F_2^{LN(3)}$ is used to estimate for the first time the structure of the pion at small Bjorken–x.

5.1 Comparison with the Predictions of LEPTO

The LEPTO Monte Carlo program[1] [Ing97] simulates soft colour interactions between the partons in the final state. The probability for an interaction, which can be viewed as the exchange of a soft non–perturbative gluon, is described by a single phenomenological parameter R. The default value of this parameter, as implemented in the LEPTO Monte Carlo, is $R = 0.5$, but the program allows one to change this parameter to any value of $0 \leq R \leq 1$ [2]. The soft colour interaction can change the colour topology of the hadronic final state, such that colour singlet subsystems arise separated in rapidity, which may lead to the formation of a proton or neutron.

Figure 5.1 shows the measurement of $F_2^{LN(3)}$ compared to the predictions of the LEPTO Monte Carlo, which have been calculated for the default value of $R = 0.5$ and by using the leading order parton distributions of the proton by Glück, Reya and Vogt (GRV-LO) [Glü95]. Measurements at HERA [H1C96b, H1C97a, ZEU96, ZEU97a] have shown that the GRV parameterization gives a good description of the inclusive structure function F_2^p of the proton for $Q^2 \gtrsim 1\,\mathrm{GeV}^2$. The LEPTO Monte Carlo model describes the general shape and magnitude of the neutron data over the entire z range. However it tends to underestimate the cross section at $z \approx 0.7$.

It is instructive to study the influence of the chosen probability R for soft colour interactions on the rate of leading neutron production. In Figure 5.2 the measurements of $F_2^{LN(3)}$ at $Q^2 = 4.4\,\mathrm{GeV}^2$ and $x = 1.04 \cdot 10^{-3}$ are compared to the LEPTO predictions with R equal to 0, 0.25, 0.5 and 1. In the region of high z ($z > 0.5$), the production cross section does not increase significantly for values of R larger than 0.25. The simulation

---

[1] Version 6.5.1 was used.

[2] The corresponding steering parameter is `PARL(7)`.

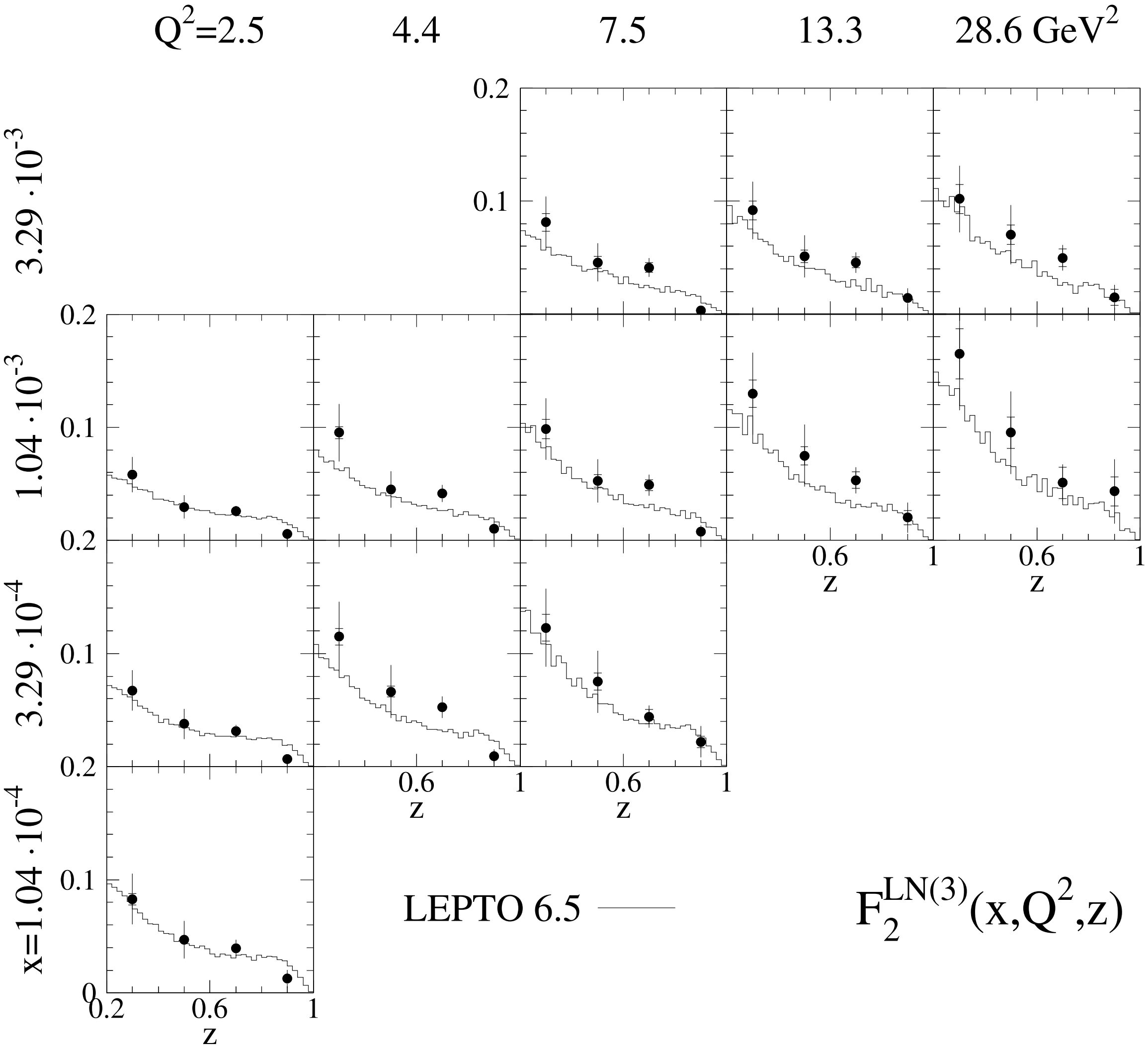

Figure 5.1: The semi–inclusive structure function $F_2^{LN(3)}$*, for neutrons with* $p_T \leq 200\,\mathrm{MeV}$*, compared to the predictions of the* Lepto *Monte Carlo, using* $R = 0.5$*. The inner error bars show the statistical errors and the full error bars show the statistical and systematic errors added in quadrature. There is an additional 5.7% overall normalization uncertainty for the data points which has not been included in the error bars.*

with $R = 0$, which corresponds to the situation without any soft colour interaction, yields a rate of leading neutrons with $z \geq 0.7$ which is approximately a factor of four lower. In this case the neutrons are solely produced by the string fragmentation process.

In this context it should be mentioned, that the Lepto Monte Carlo, which gives a fair description of the neutron data, fails to describe the production of leading protons, since it underestimates the cross section by a factor of ≈ 2 [Lis97, H1C98] (see Section 5.6).

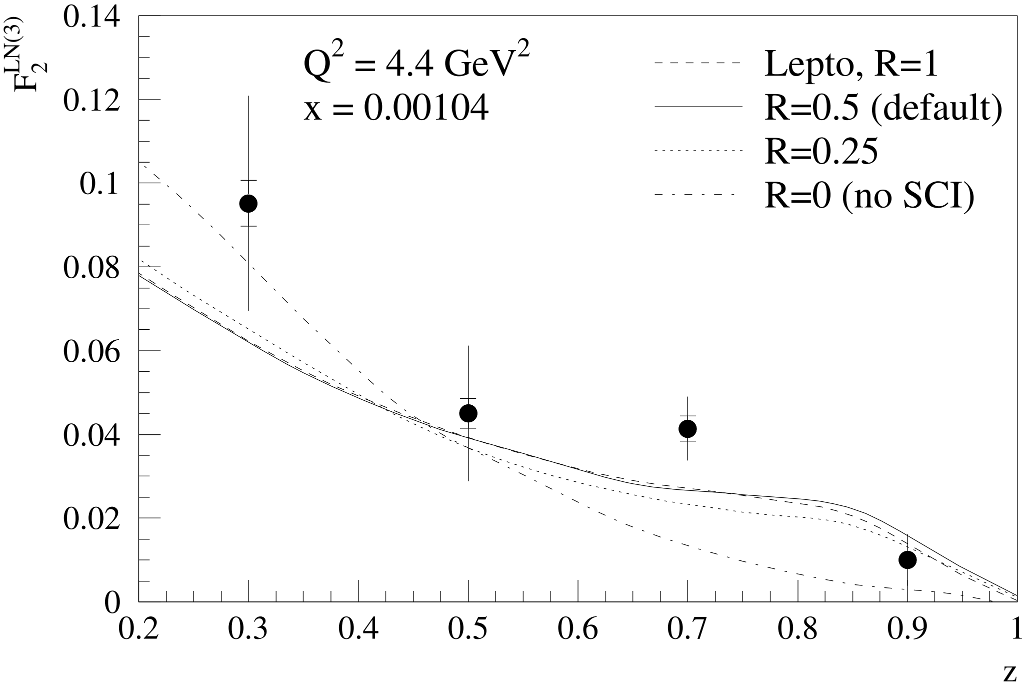

Figure 5.2: Dependence of the predicted neutron rate on the value of the SCI parameter R. The $F_2^{LN(3)}$ data at $Q^2 = 4.4\,\mathrm{GeV}^2$ and $x = 1.04 \cdot 10^{-3}$ are compared to the LEPTO *simulation with R equals to 0, 0.25, 0.5 and 1.*

5.2 Comparison with the Predictions of RAPGAP

The RAPGAP Monte Carlo generator[3] [Jun95] simulates leading neutron production using π^+ exchange. In the Monte Carlo program, the cross section for leading neutron production is proportional to the product of the pion flux factor $f_{\pi^+/p}$ and the pion structure function F_2^π. The pion flux factor determines the energy and p_T spectra of the final state neutron. For the RAPGAP Monte Carlo prediction shown in Figure 5.3 the pion flux factor determined by Holtmann *et al.* [Hol94, Hol96] was used, which has been evaluated on the basis of the measured neutron production cross section in the reaction $pp \to nX$ (see Section 3.5.1). This flux factor is given by [Hol94, Prz97]

$$f_{\pi^+/p}(z,t) = \frac{2}{3}\frac{3}{4\pi}\frac{g^2_{p\pi N}}{4\pi}(1-z)\frac{-t}{(m_\pi^2-t)^2}\exp\left[-R^2_{\pi n}\frac{m_\pi^2-t}{1-z}\right] . \tag{5.6}$$

The pion flux factor, which is implemented in the default version of RAPGAP (see [Fra89]), was not used since it cannot reproduce the neutron production cross section observed in pp scattering [Fla76, Blo78] (compare Section 3.5.1). The rate of leading neutron production depends also upon the values of the pion parton distributions (see Equation 5.5), for which the leading order parameterization by GRV [Glü92] has been taken.

---

[3] Version 2.06 was used.

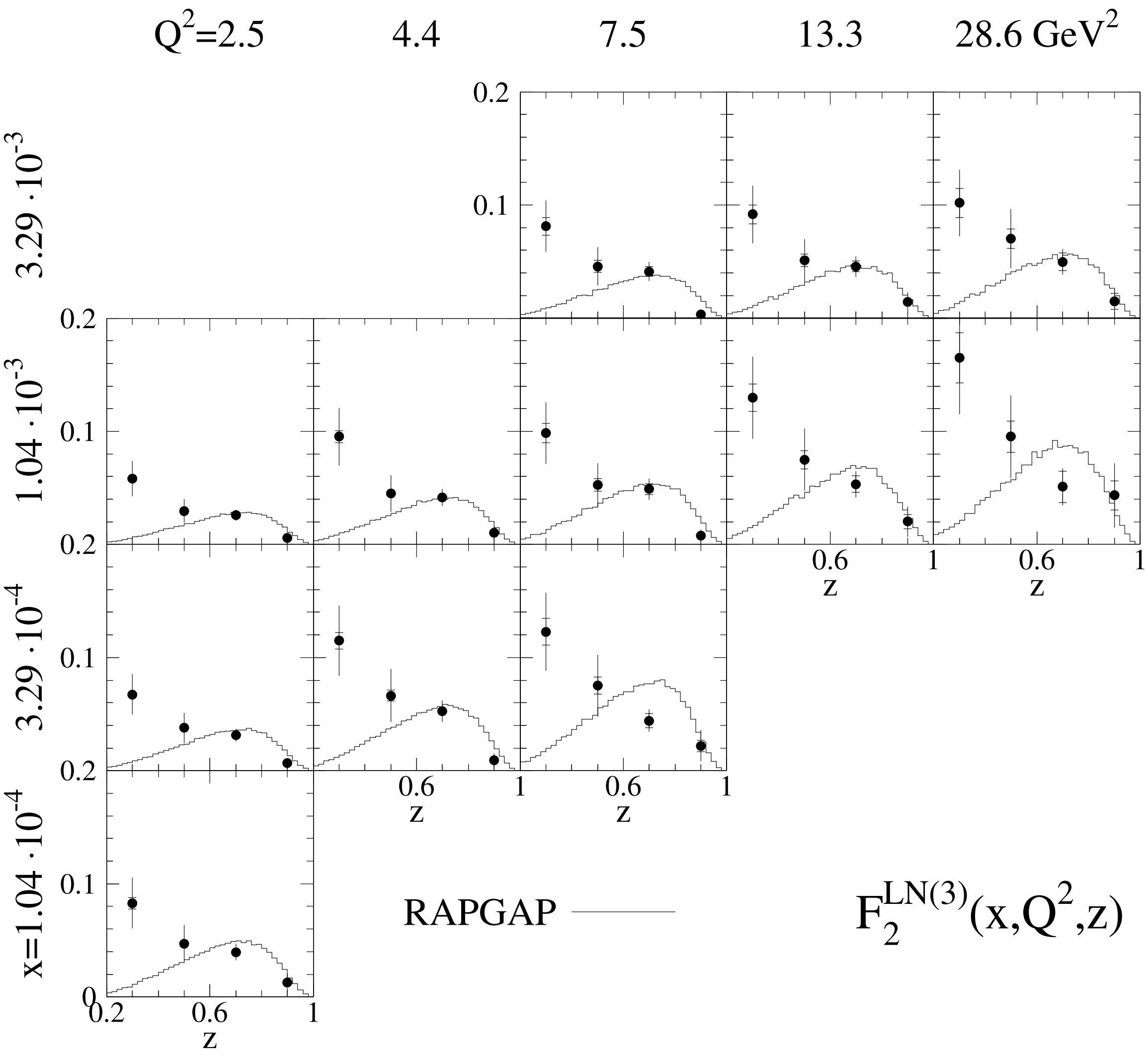

Figure 5.3: The semi–inclusive structure function $F_2^{LN(3)}$, for neutrons with $p_T \leq 200\,\mathrm{MeV}$, compared to the predictions of the RAPGAP *Monte Carlo. The* RAPGAP *calculation was performed using the pion flux factor as determined by Holtmann et al. [Hol94, Hol96, Prz97] and the GRV-LO parameterization of the pion structure function [Glü92].*

The RAPGAP Monte Carlo gives a reasonable description of the high–energy neutron data with $z \geq 0.7$. In the low–energy region where the final state neutron has less than 70% of the incident proton's energy, the RAPGAP Monte Carlo program cannot reproduce the observed cross section since additional physical processes, not simulated by the program, contribute significantly to the production of neutrons. A similar observation has also been made for the $pp \to nX$ data (compare Figure 3.12).

z	β	x	$Q^2[\mathrm{GeV}^2]$	$a \pm \Delta a$	$b \pm \Delta b$
0.3	0.00047	0.00033	2.5 – 7.5	0.009 ± 0.013	0.147 ± 0.026
0.5	0.00066	0.00033	2.5 – 7.5	0.000 ± 0.008	0.094 ± 0.016
0.7	0.00110	0.00033	2.5 – 7.5	0.013 ± 0.007	0.048 ± 0.013
0.9	0.00329	0.00033	2.5 – 7.5	-0.003 ± 0.004	0.023 ± 0.009
0.3	0.00148	0.00104	2.5 – 28.6	0.019 ± 0.008	0.100 ± 0.013
0.5	0.00208	0.00104	2.5 – 28.6	0.006 ± 0.005	0.059 ± 0.008
0.7	0.00346	0.00104	2.5 – 28.6	0.011 ± 0.004	0.041 ± 0.007
0.9	0.01039	0.00104	2.5 – 28.6	0.000 ± 0.003	0.015 ± 0.005
0.3	0.00469	0.00329	7.5 – 28.6	0.050 ± 0.030	0.036 ± 0.027
0.5	0.00657	0.00329	7.5 – 28.6	0.010 ± 0.019	0.039 ± 0.018
0.7	0.01095	0.00329	7.5 – 28.6	0.028 ± 0.017	0.015 ± 0.016
0.9	0.03286	0.00329	7.5 – 28.6	-0.019 ± 0.012	0.026 ± 0.012

Table 5.1: Scaling violations in $F_2^{LN(3)}$ for fixed values of β. The data were fitted separately for each value of β and z to the form $F_2^{LB(3)}(\beta, Q^2, z) = a(\beta) + b(\beta) \cdot \log \frac{Q^2}{1\,\mathrm{GeV}^2}$.

5.3 Observation of Scaling Violations

The measurement as presented in Figure 4.18 suggests that the semi–inclusive structure function $F_2^{LN(3)}$ increases with Q^2 for fixed values of x and z. Scanning the data points in the figure from left to right (which means increasing Q^2), one can recognize the tendency, that $F_2^{LN(3)}$ rises with increasing Q^2.

In order to quantify these scaling violations, $F_2^{LN(3)}(\beta, Q^2, z)$ has been fitted separately for each fixed values of β and z to the form[4]

$$F_2^{LN(3)}(\beta, Q^2, z) = a(\beta) + b(\beta) \cdot \log \frac{Q^2}{1\,\mathrm{GeV}^2} \; . \tag{5.7}$$

The fit was performed on the basis of the statistical and systematic errors, which depend on x and Q^2. The normalization error and the error, which depends on z, are correlated in the different (x, Q^2)–bins, so that they were consequently not considered. The measurement of $F_2^{LN(3)}$ in the lowest x bin has not been used since there is only a single Q^2 value.

The result of the fit is summarized in Table 5.1. For 10 out of the 12 different values of β, the slope parameter $b(\beta)$ is by more than two standard deviations larger than zero. Thus, significant scaling violations have been observed in $F_2^{LN(3)}$. The values of $b(\beta)/F_2^{LN(3)}$, which are a measure of the normalized scaling violations, are plotted in Figure 5.4. Only the results which arise from z equal to 0.3, 0.5 and 0.7 are shown, since for $z = 0.9$ the relative errors of the data points are very large. The data are compared to the normalized scaling violations $\mathrm{d}F_2/\mathrm{d}(\log Q^2)/F_2$ predicted and observed in the inclusive structure functions of the pion and proton respectively. The structure

---

[4] Note that throughout this work "log" refers to the decimal logarithm. Unfortunately this symbol is not unambiguously used in the literature.

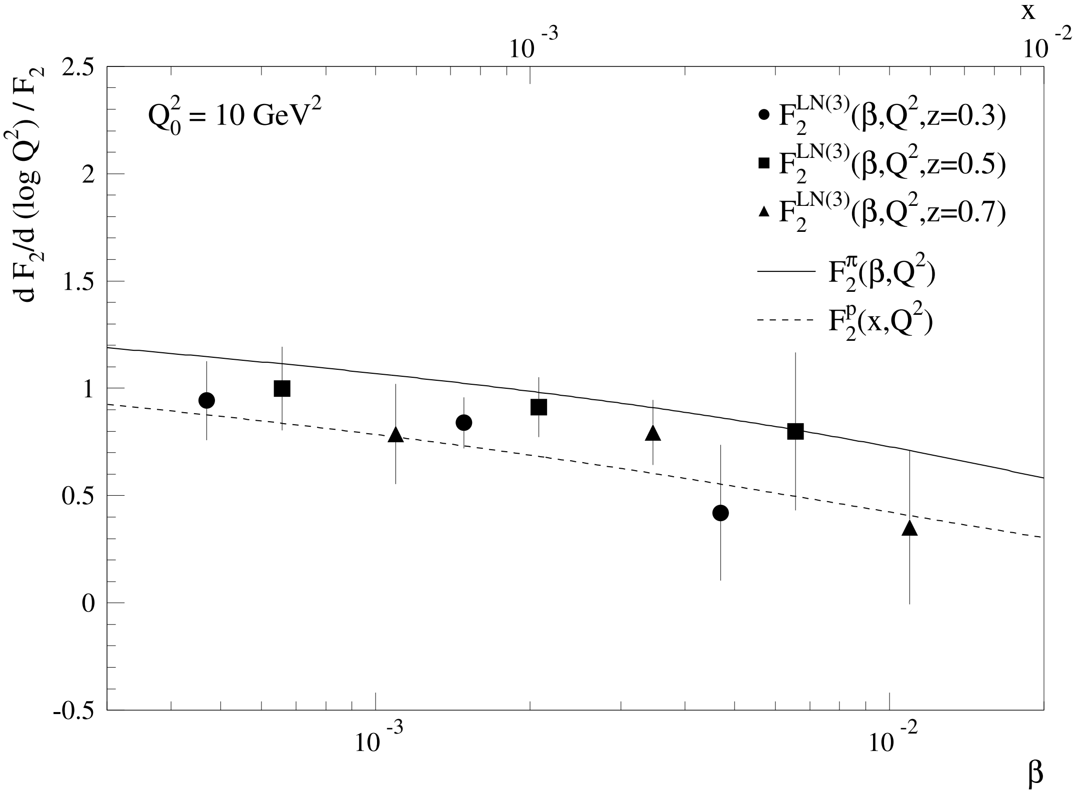

Figure 5.4: Normalized scaling violations $b(\beta)/F_2^{LN(3)}$ observed in the leading neutron structure function $F_2^{LN(3)}$, computed at $Q_0^2 = 10\,\mathrm{GeV}^2$. The data are compared to the expectations derived from the GRV-LO parameterizations of the inclusive structure functions of the pion and the proton. The scaling violations of the pion structure function have been evaluated as a function of β (lower scale), whereas for the proton structure function, they have been evaluated as a function of x (upper scale). The x–scale is adjusted for $z = 0.5$.

functions have been calculated using the GRV leading order parameterizations of the parton densities [Glü92, Glü95]. The scaling violation observed in the semi–inclusive structure function $F_2^{LN(3)}$ is similar in size and shape to those seen in the GRV-LO parameterizations of the pion and proton structure functions.

5.4 Test of Factorization Assumptions

Presuming that leading neutrons emerge from reactions where the virtual photon is absorbed by a colourless object inside the proton, the structure function $F_2^{LN(3)}$ should factorize into a flux factor $f(z)$ which is only a function of z, and a structure function $\widetilde{F}_2^{LB(2)}$ which depends upon Q^2 and β, which can be interpreted as the Bjorken variable of the exchanged object.

An alternative approach is the concept of soft colour interactions [Buc95, Edi96] which is not based on the exchange of colourless objects, so that β can no longer be interpreted as a momentum fraction. In such a scenario, one might expect factorization in the variables x, Q^2 and z, if the deep–inelastic scattering process off the proton is independent of the proton fragmentation. The "hypothesis of limiting fragmentation" [Ben69, Cho94], which states that target fragmentation is independent of the incident projectile's energy, also implies that final state neutrons emerge from a process which is insensitive to x and Q^2.

To test both factorization hypotheses, global fits were made to $F_2^{LN(3)}$ assuming the following general forms for $F_2^{LN(3)}$:

$$F_2^{LN(3)}(\beta, Q^2, z) = f(z) \cdot \widetilde{F}_2^{LN(2)}(\beta, Q^2) \qquad \text{(fit a)}, \tag{5.8}$$

$$F_2^{LN(3)}(x, Q^2, z) = f(z) \cdot \widetilde{F}_2^{LN(2)}(x, Q^2) \qquad \text{(fit b)}. \tag{5.9}$$

$f(z)$ is a discrete step–function, which is expressed by four parameters r_j ($j = 1..4$) referring to the four different values of z (in increasing order). The value of r_2 corresponding to $z = 0.5$ is fixed by $r_2 = 1$ and the remaining three parameters are determined by the fit. $\widetilde{F}_2^{LN(2)}(\beta, Q^2)$ in Equation 5.8 is parameterized as

$$\widetilde{F}_2^{LN(2)}(\beta, Q^2) = a \cdot \beta^b + c \cdot \beta^d \cdot \log \frac{Q^2}{1\,\mathrm{GeV}^2} \;, \tag{5.10}$$

where a, b, c and d are four additional fit parameters. The chosen function is based on the leading terms of a phenomenological parameterization of the inclusive proton structure function [H1C95b, H1C96b], which is of the form

$$F_2^p(x, Q^2)$$
$$= \left[a \cdot x^b + c \cdot x^d \cdot (1 + e\sqrt{x}) \cdot \left(\ln \tfrac{Q^2}{1\,\mathrm{GeV}^2} + f \left(\ln \tfrac{Q^2}{1\,\mathrm{GeV}^2} \right)^2 + \tfrac{h}{Q^2} \right) \right] \cdot (1 - x)^g \;.$$

For $\widetilde{F}_2^{LN(2)}(x, Q^2)$ in Equation 5.9, β was replaced by x in Equation 5.10.

The fits were performed by minimizing the χ^2, which was calculated on the basis of the statistical and the (x, Q^2)–dependent systematic error added in quadrature [Jam94]. As a cross check the fits were redone using only statistical errors, which yield practically the same results. The fitted values of the parameters changed only by a small fraction of their errors. The result of the fits can be found in Table 5.2. The quality of the fit, assuming factorization in β, Q^2 and z, is demonstrated in Figure 5.5, which shows the difference of the measurement of $F_2^{LN(3)}$ and the fitted parameterization. The other fit, assuming factorization in x, Q^2 and z, gives almost the same result.

The data are consistent with both factorization hypotheses and the fit results yield similar χ^2/ndf. A possible explanation for this result is that $\widetilde{F}_2^{LN(2)}$ is proportional to the proton structure function which for $x < 0.1$ is of the form $F_2^p \sim x^{-\lambda(Q^2)}$ [H1C96b]. Since β and x are highly correlated and have similar magnitude due to the restricted range of z, this also implies that $\widetilde{F}_2^{LN(2)} \sim \beta^{-\lambda(Q^2)}$. The data have therefore relatively limited sensitivity to a difference of factorization in these two variables.

It is interesting to note, that also the semi–inclusive structure function $F_2^{LP(3)}$, which parameterizes leading proton production with $p_T \leq 200\,\mathrm{MeV}$, is consistent with both factorization assumptions [Lis97].

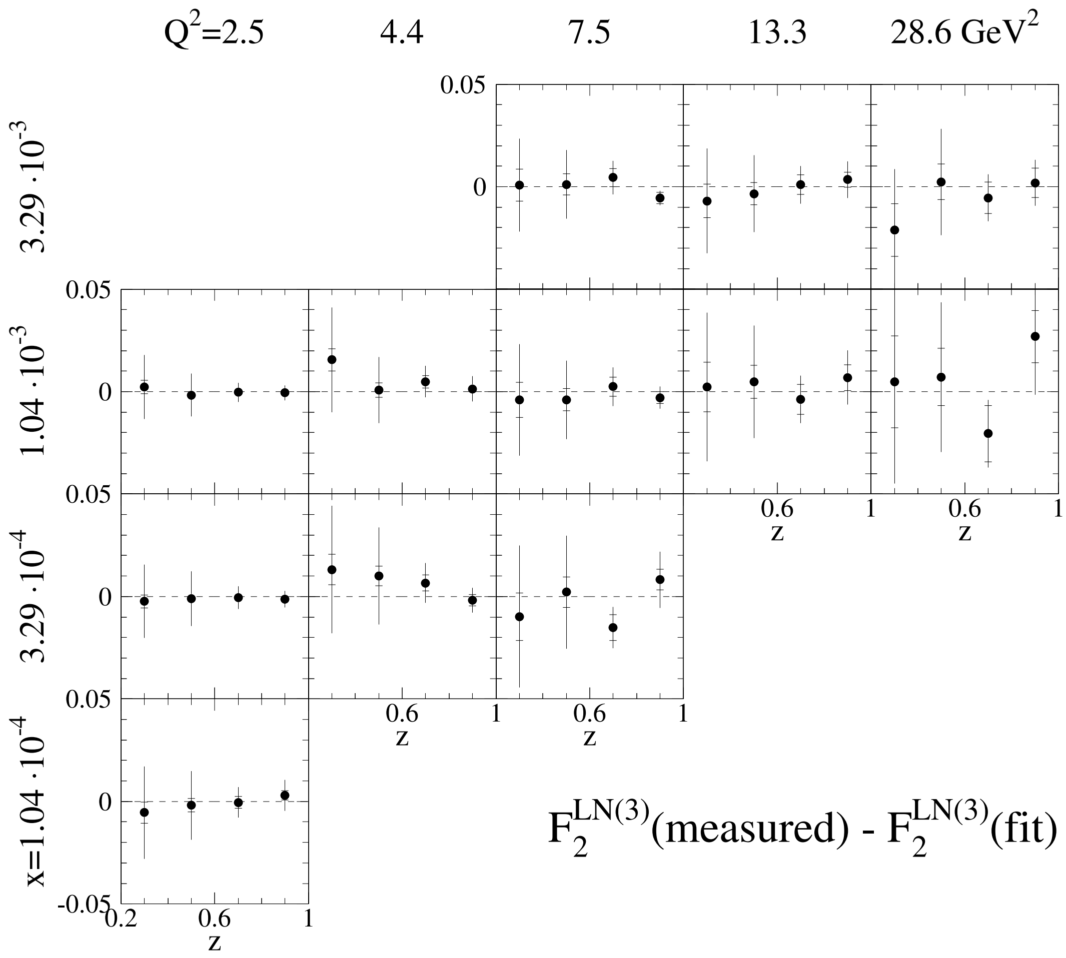

Figure 5.5: Comparison of the measured values of $F_2^{LN(3)}$ with the global fit, assuming factorization in β, Q^2 and z. Plotted is the difference between the measured and calculated values.

Parameter	r_1	r_2	r_3	r_4	a	b	c	d	χ^2/ndf, CL
Fit a	1.68	1.00	0.91	0.27	0.011	0.03	0.011	-0.26	47.9/41
±	0.07	0.00	0.04	0.03	0.005	0.07	0.002	0.02	21.4%
Fit b	1.80	1.00	0.82	0.20	0.025	0.14	0.007	-0.29	46.7/41
±	0.07	0.00	0.03	0.02	0.011	0.05	0.001	0.02	24.8%

Table 5.2: Result of the global fits to $F_2^{LN(3)}$. The leading neutron structure function was fitted to Equation 5.8 (fit a) and 5.9 (fit b) respectively. Shown are the calculated values for the fit–parameters with errors, the normalized χ^2 and the corresponding confidence level (CL) for the two different fits.

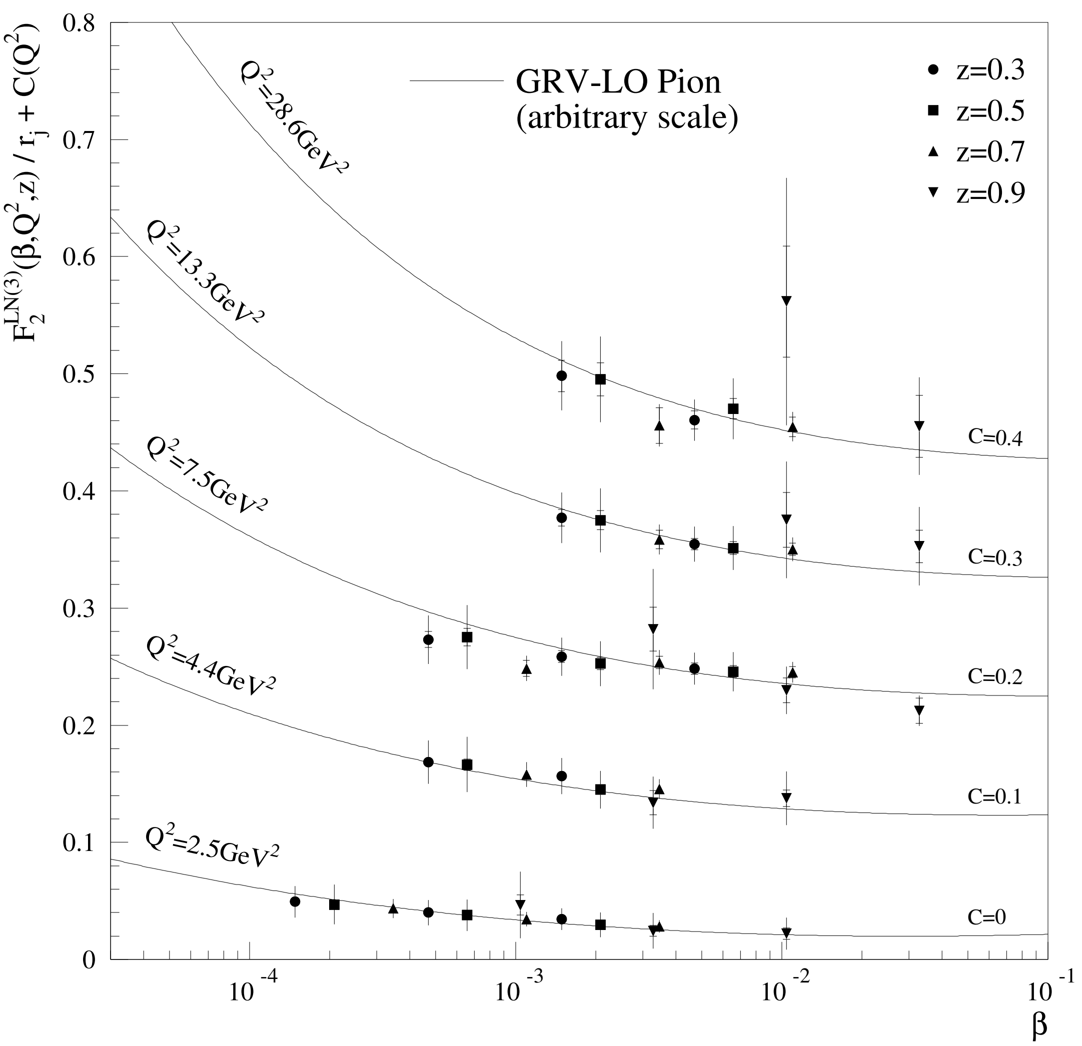

Figure 5.6: $F_2^{LN(3)}$ as a function of β in different bins of Q^2. The curves represent the GRV-LO pion structure function with arbitrary normalization. For the reason of comparability, the data points are scaled by $1/r_j$, determined by fit a (see Table 5.2), and shifted by $C(Q^2)$.

The observation that the leading neutron structure function $F_2^{LN(3)}$ can equivalently be parameterized with respect to x, Q^2 and z and in terms of β, Q^2 and z, is demonstrated in Figures 5.6 to 5.9. In these figures the $F_2^{LN(3)}$ data points were scaled by $1/r_j$ determined by the global fits, in order to allow the comparison of data points originating from non–identical values of z.

Figure 5.6 shows $F_2^{LN(3)}$ as a function of β for fixed values of Q^2, demonstrating the dependence of the structure function on the scaling variable β. The data are compared to the GRV-LO parameterization of the pion structure function (arbitrarily scaled) which is in good accordance with the data. It should be mentioned, however, that this agreement cannot be considered as a strong evidence for pion exchange, since all hadronic structure functions at low x (β) are expected to be similar in shape (see Section 5.9.3). Also the comparison of the data to the predictions of the RAPGAP

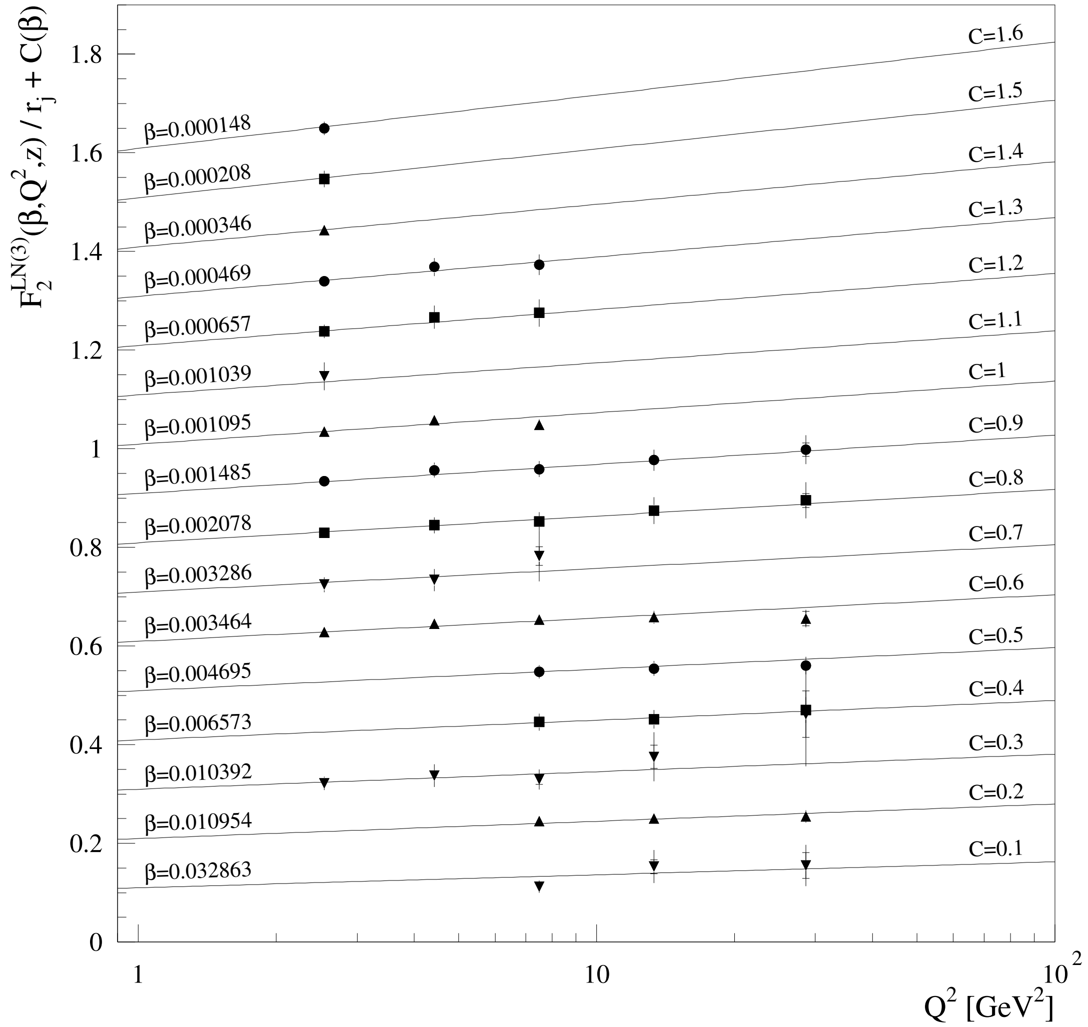

Figure 5.7: $F_2^{LN(3)}$ as a function of Q^2 in different bins of β, compared to the result of the global fit assuming factorization in β, Q^2 and z. For the reason of comparability, the data points are scaled by $1/r_j$, determined by fit a (see Table 5.2), and shifted by $C(Q^2)$.

Monte Carlo revealed that pion exchange is not the main production mechanism for $z \leq 0.3$.

Figure 5.7 shows the evolution of $F_2^{LN(3)}$ with Q^2 for fixed values of β. The structure function rises with increasing values of Q^2 (scaling violations), which is also seen in the superimposed curves representing the result of the global fit to $F_2^{LN(3)}$ (fit a).

The equivalent Figures 5.8 and 5.9 are based on the assumption of factorization in x, Q^2 and z. In Figure 5.8 $F_2^{LN(3)}$ is plotted as a function of x in the five different bins of Q^2 in comparison to the structure function of the proton, which has been normalized arbitrarily. Figure 5.9 shows the increase in $F_2^{LN(3)}$ as a function of Q^2 for fixed values of x. The superimposed lines correspond to the parameterization of the global fit to $F_2^{LN(3)}$ (fit b).

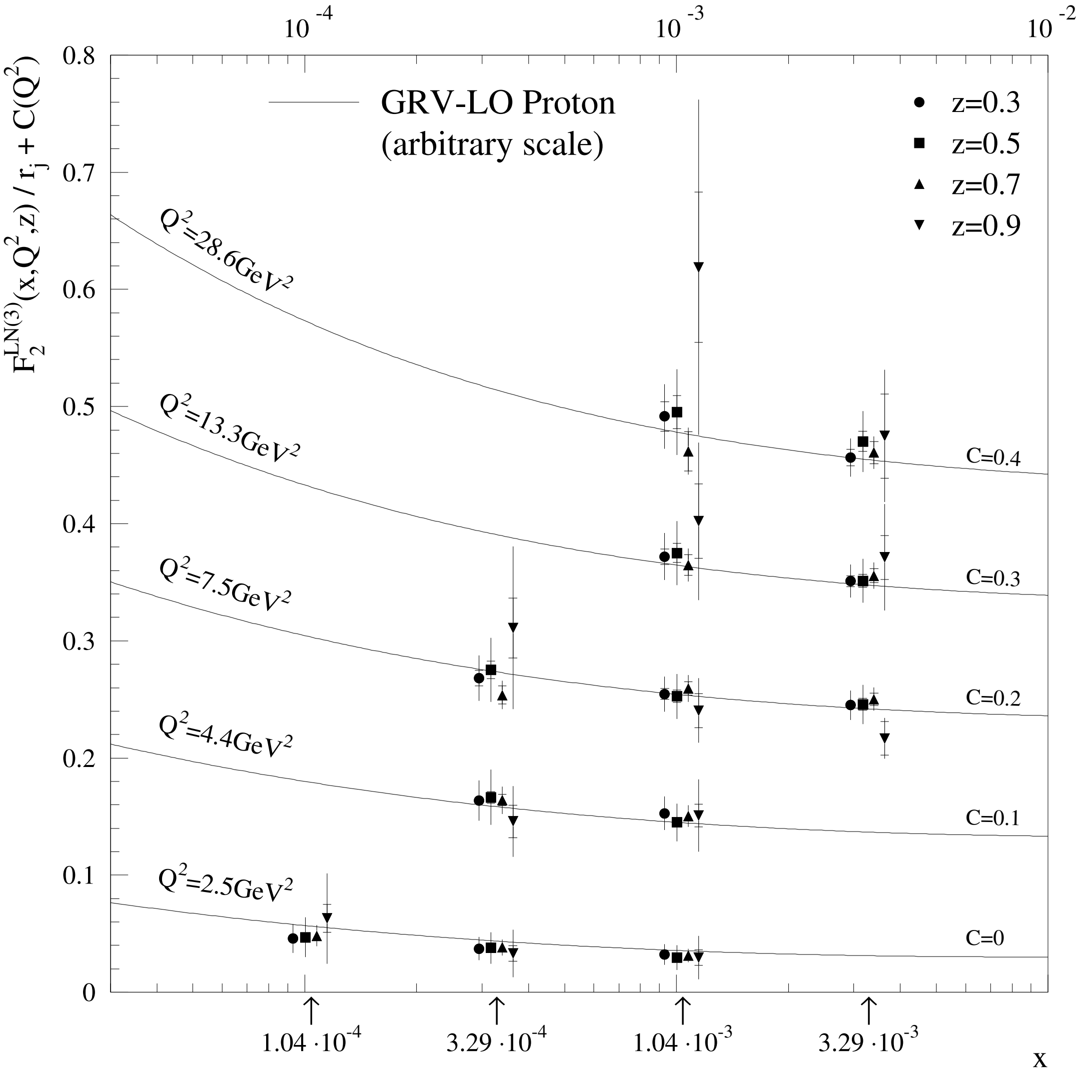

Figure 5.8: $F_2^{LN(3)}$ as a function of x in different bins of Q^2. Superimposed is the GRV-LO parameterization of the proton structure function with arbitrary normalization. For the reason of comparability, the data points are scaled by $1/r_j$, determined by fit b (see Table 5.2), and shifted by $C(Q^2)$.

5.5 The Contribution of $F_2^{LN(3)}$ to the Proton Structure Function

Besides the observation that the measurement of $F_2^{LN(3)}$ is consistent with the assumption of factorization in x, Q^2 and z, Figure 5.8 suggests that $F_2^{LN(3)}$ is proportional to the proton structure function. In order to test this hypothesis, $F_2^{LN(3)}$ was fitted to the form

$$F_2^{LN(3)}(x, Q^2, z) = r_j \cdot F_2^p(x, Q^2) \ , \tag{5.11}$$

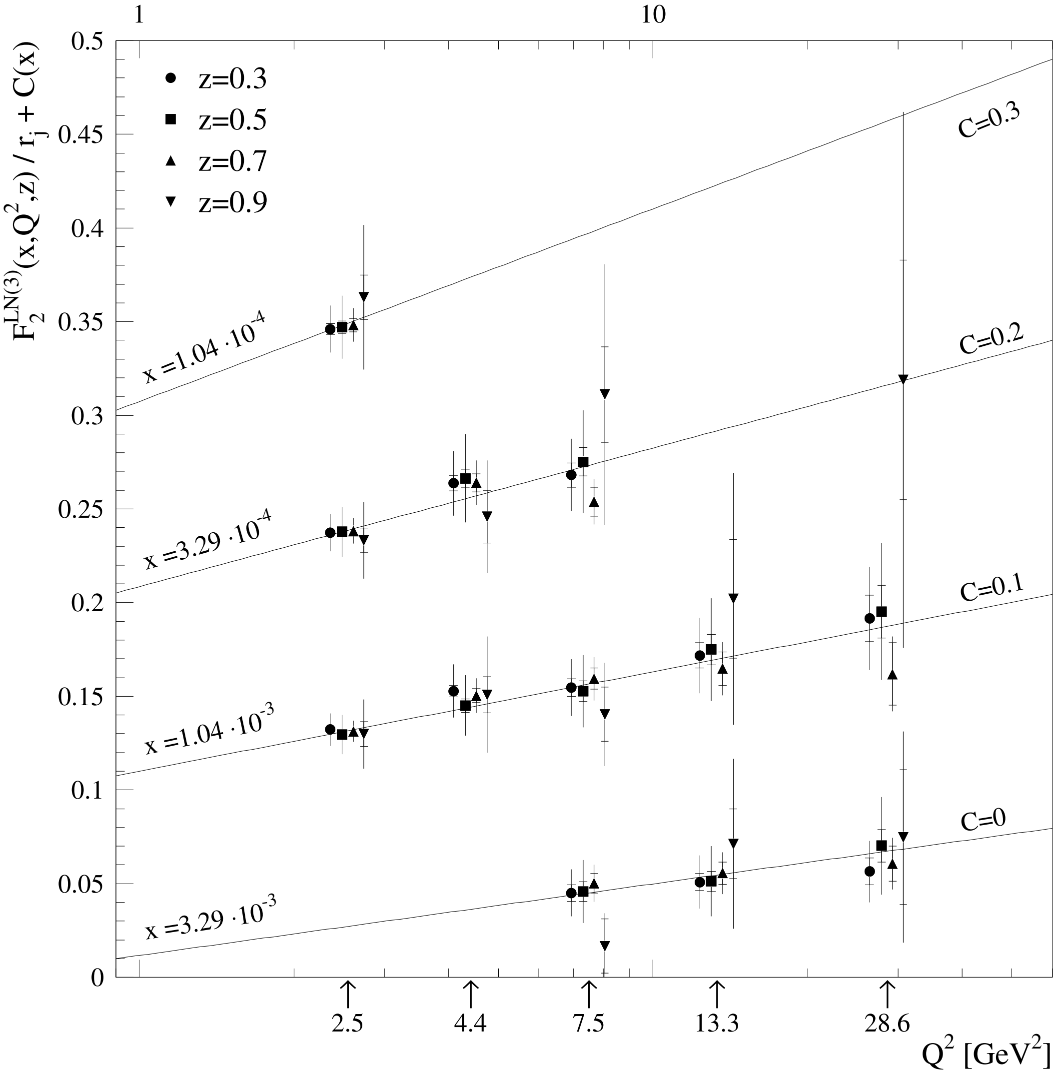

Figure 5.9: $F_2^{LN(3)}$ as a function of Q^2 in different bins of x, compared to the result of the global fit assuming factorization in x, Q^2 and z. For the reason of comparability, the data points are scaled by $1/r_j$, determined by fit b (see Table 5.2), and shifted by $C(Q^2)$.

where the fit–parameters r_j ($j = 1..4$) are constant factors for the four different z–bins. For the proton structure function F_2^p, the GRV-LO parameterization [Glü95] was taken. Performing the fit on the basis of the statistical and (x, Q^2)–dependent errors, the ratios r_j were determined to be:

$$
\begin{aligned}
r_1 &= 0.1346 \pm 0.0034 \ , \qquad r_2 = 0.0747 \pm 0.0021 \ , \\
r_3 &= 0.0611 \pm 0.0018 \ , \qquad r_4 = 0.0148 \pm 0.0012 \ ,
\end{aligned}
\tag{5.12}
$$

and the fit yields $\chi^2/\mathrm{ndf} = 49.8/44 = 1.13$ (CL = 25%). Considering only statistical errors, the χ^2/ndf amounts to $60.1/44 = 1.37$ (CL = 5.4%).

Thus, the ratio of $F_2^{LN(3)}(x, Q^2, z)$ over $F_2^p(x, Q^2)$ is compatible with being constant

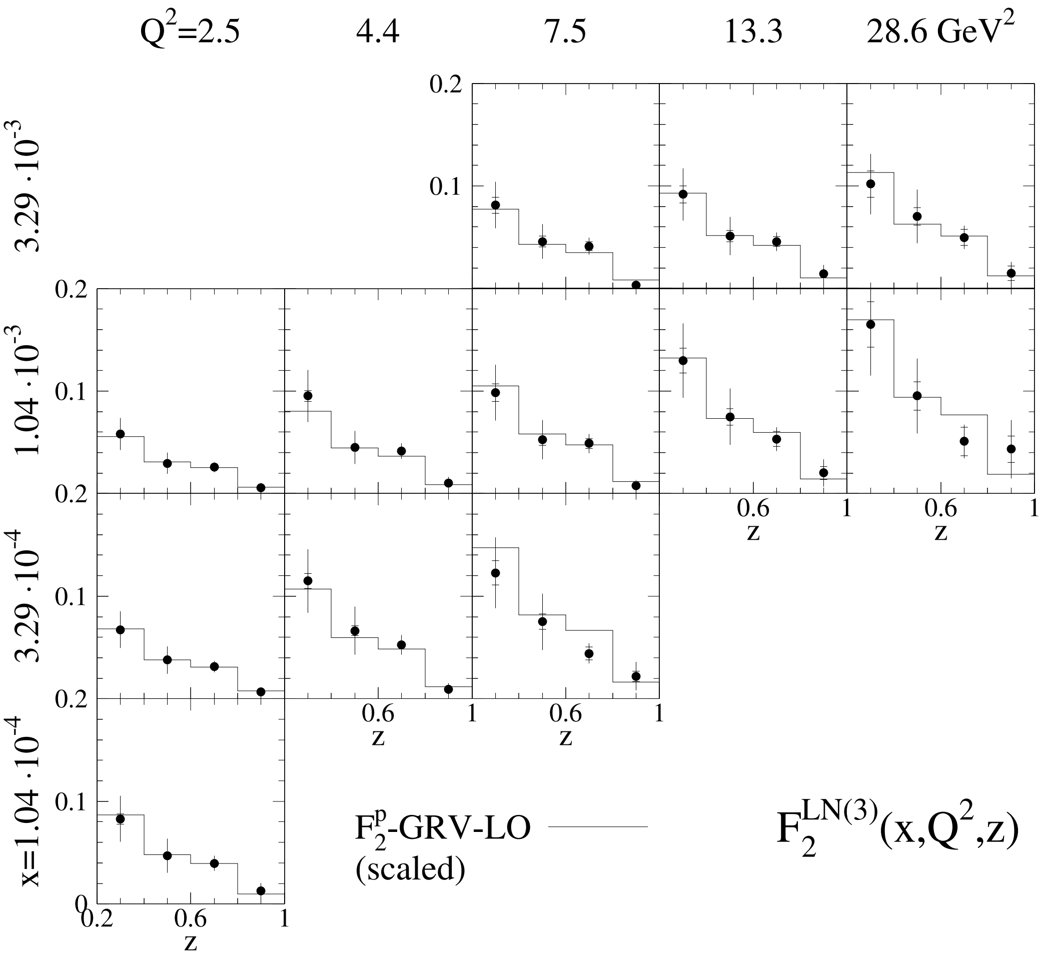

Figure 5.10: $F_2^{LN(3)}$ compared to the proton structure function, which has been scaled by r_j (see Equation 5.12) in the different z–bins.

for fixed values of z in the kinematic region of the measurement. This is also demonstrated in Figure 5.10, where $F_2^{LN(3)}$ is compared to the proton structure function, which has been scaled by the factors r_j in the different bins of z.

Using the total systematic error of the measurement (except of the error on the bin centre correction, see Section 4.10.4), the contribution of events with a leading neutron to the total inclusive deep–inelastic cross section can be determined. In $(5.7 \pm 1.6)\%$ of all deep–inelastic events a leading neutron with transverse momentum $p_T \leq 200\,\mathrm{MeV}$ and $z \geq 0.2$ is produced. For $z \geq 0.6$ this ratio amounts to $(1.5 \pm 0.4)\%$.

5.6 Comparison with the Leading Proton Data

As already mentioned, the measurement of leading neutron production in deep–inelastic scattering was performed in the same kinematic region of x, Q^2 and p_T as H1's measurement of leading proton production [Lis97, H1C98], based on data taken in 1995.

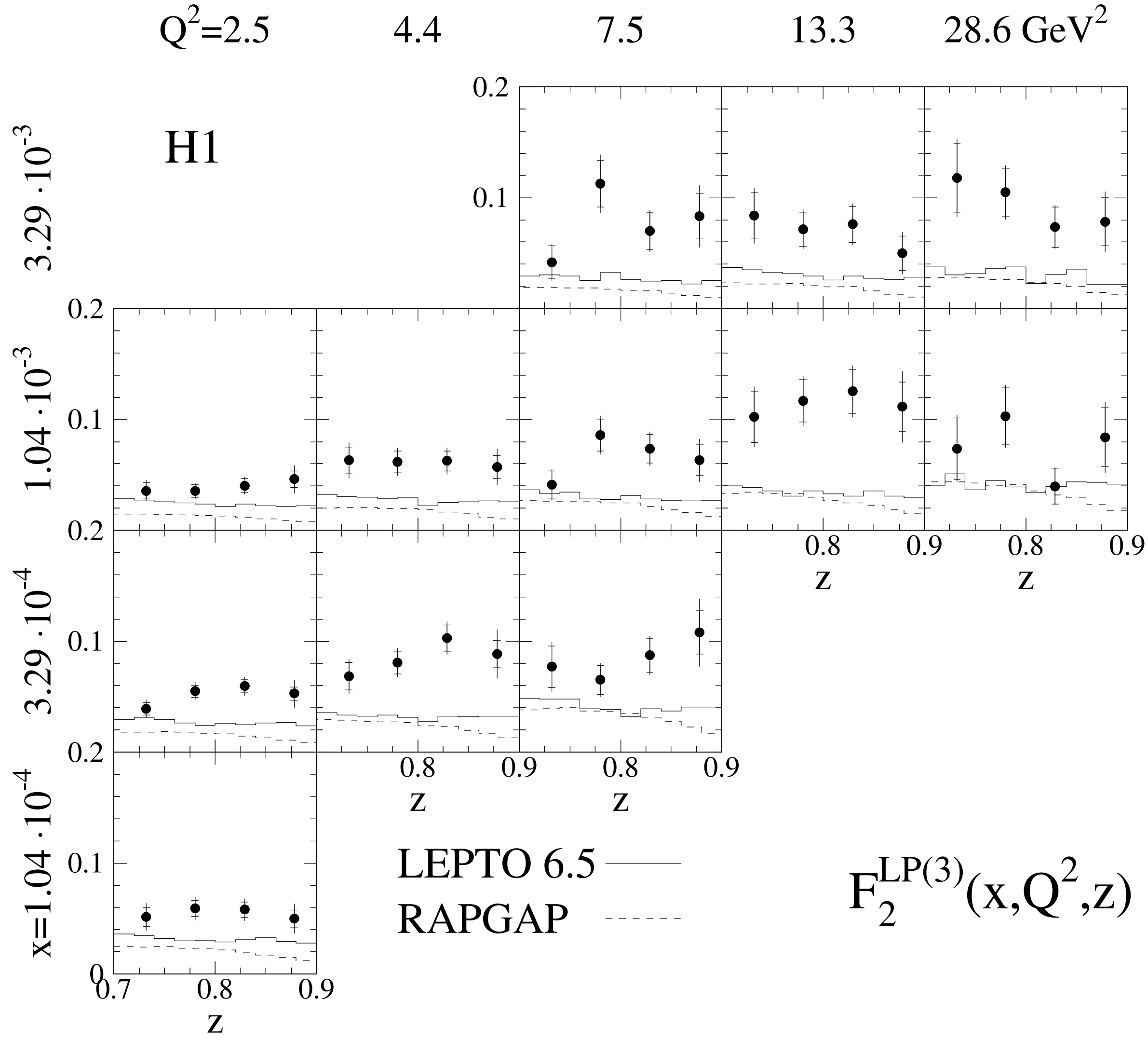

Figure 5.11: Measurement of $F_2^{LP(3)}$, for protons with $p_T \leq 200\,\mathrm{MeV}$, compared to the predictions of the Lepto *and* Rapgap *Monte Carlo models calculated using GRV leading order parton distributions for the proton and the pion respectively. The inner error bars show the statistical errors and the full error bars show the statistical and systematic errors added in quadrature. There is an additional 5.6% overall normalization uncertainty for the data points which has not been included in the full error bars.*

The leading proton structure function $F_2^{LP(3)}$ is defined in the same way as the leading neutron structure function $F_2^{LN(3)}$. In the following, both semi–inclusive structure functions will be denoted by the common symbol $F_2^{LB(3)}$, were LB stands for leading baryon. In order to allow a direct comparison of the two data sets, the same bins in x and Q^2 were chosen for both measurements.

The measurement of $F_2^{LP(3)}$, for leading protons with $p_T \leq 200\,\mathrm{MeV}$ is shown in Figure 5.11. The measurement, which has been carried out for $0.71 \leq z \leq 0.90$, is compared to the predictions of the Lepto and Rapgap Monte Carlo models [Ing97, Jun95], which have been calculated in the same way as for the comparison to the leading neutron structure function (see Sections 5.1 and 5.2). The pion flux factor implemented in the Rapgap Monte Carlo model is exactly a factor of two lower for proton compared to neutron production, due to the difference in the Clebsch–Gordon coefficients for the $\pi^+ n$ and $\pi^0 p$ isospin 1/2 states.

In contrast to its fair agreement with the neutron data, the Lepto Monte Carlo fails to describe the rate of leading proton production and the rise in $F_2^{LP(3)}$ as a function of Q^2.

The Rapgap Monte Carlo fails to reproduce the absolute rate of leading proton production as well. Comparing the magnitudes of $F_2^{LP(3)}$ and $F_2^{LN(3)}$ one notices, that for $z \geq 0.7$, the semi–inclusive cross section for proton production is larger than the cross section for neutron production in any specific (x, Q^2)–bin. This result rules out pion exchange as the main production mechanism for leading protons since pion exchange models predict that the ratio of neutron and proton production should be equal to two.

5.7 A Regge Model of Leading Baryon Production

Assuming a simple Regge expansion and the dominance of a single Regge exchange, the differential cross section for leading baryon production as a function of z at fixed t should be proportional to $(1-z)^n$ for fixed values of β and Q^2. Here $n = 1 - 2\alpha(t)$, where $\alpha(t)$ specifies the Regge trajectory of the dominant exchange (see Section 1.4).

Based on these general ideas, the measurements of $F_2^{LB(3)}(x, Q^2, z)$ in the region of $z \geq 0.7$ were interpolated to fixed bins in β in order to determine the exponential function. For the bin centres, values for β were chosen, which corresponds to $z = 0.8$, which means:

$$\beta_i = \frac{x_i}{1-z} = \frac{x_i}{0.2} \ , \tag{5.13}$$

where x_i $(i = 1..4)$ are the central values of the x–bins. The interpolation was performed, using the result of the global fits to $F_2^{LB(3)}$, which assumed factorization in β, Q^2 and z.

The interpolated measurement is plotted in Figure 5.12 in the 12 (β, Q^2)–bins. The data points are superimposed by separate fits to $F_2^{LP(3)}$ and $F_2^{LN(3)}$ of the form

$$F_2^{LB(3)}(\beta, Q^2, z) \propto (1-z)^{n_b} \ . \tag{5.14}$$

Using the full errors the fit results yield:

- for $F_2^{LP(3)}$: $n_p = -0.30 \pm 0.32$, which corresponds to $\alpha(t) = 0.65 \pm 0.16$;
- for $F_2^{LN(3)}$: $n_n = 1.26 \pm 0.66$, which corresponds to $\alpha(t) = -0.13 \pm 0.33$.

It should be noted, however, that $F_2^{LB(3)}$ is defined for $p_T \leq 200\,\text{MeV}$ and that the corresponding range in t depends strongly on the specific value of z, since t and p_T are

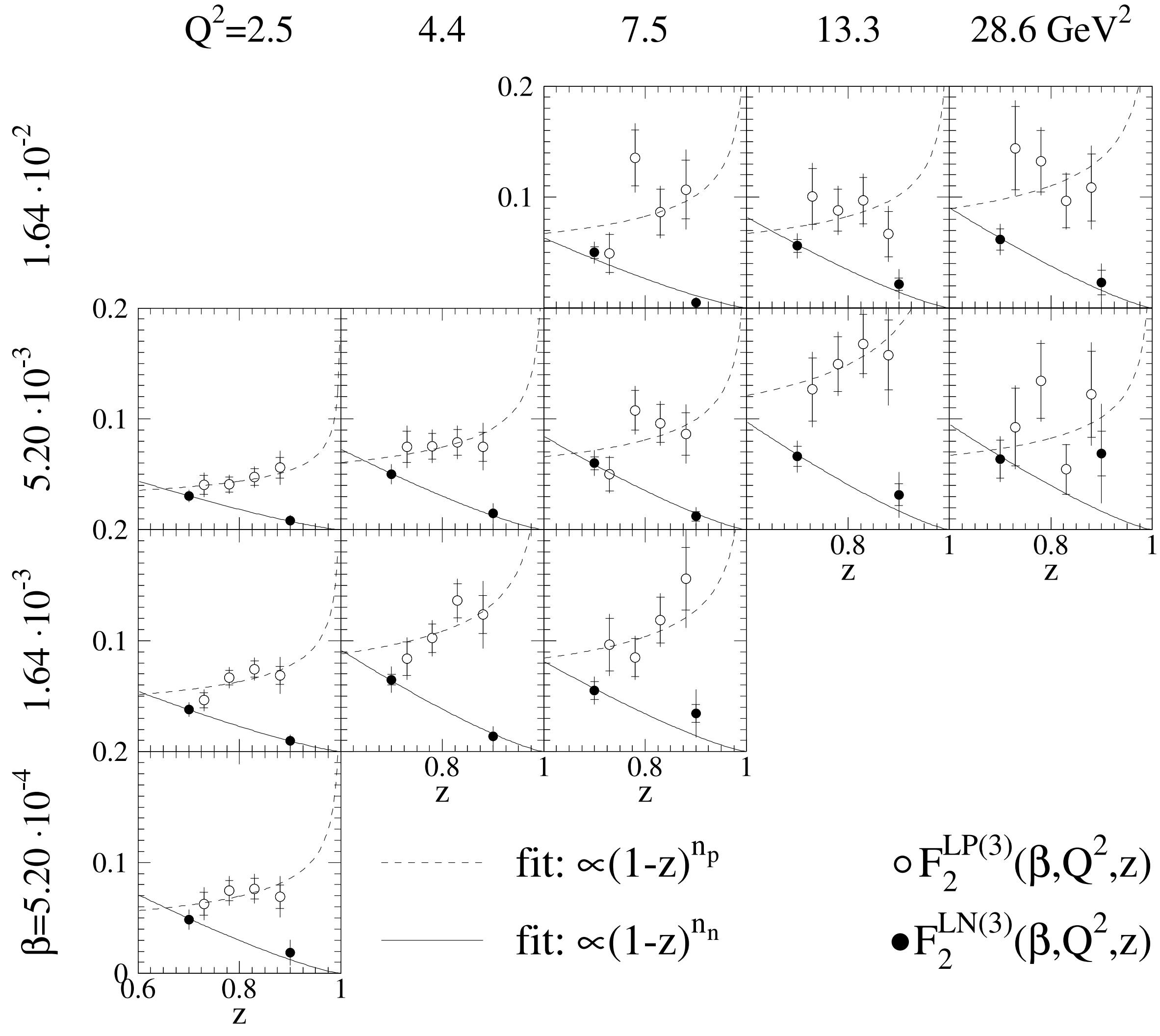

Figure 5.12: The measured values of $F_2^{LN(3)}$ and $F_2^{LP(3)}$ with $z \geq 0.7$ interpolated to fixed values of β. The superimposed curves mark the results of fits to the data points of the form $F_2^{LB(3)}(\beta, Q^2, z) \propto (1-z)^{n_b}$. See text for details.

related by

$$t = -\frac{p_T^2}{z} - (1-z)\left(\frac{m_N^2}{z} - m_p^2\right) , \tag{5.15}$$

where m_p and m_N are the masses of the proton and the produced nucleon respectively. Therefore the values of α, which result from the fit, cannot be directly interpreted as the Regge trajectory of the dominant exchange, since the fitted values of n are averaged over the t-dependence of the baryon production cross sections.

Nevertheless the fits demonstrate, that the neutron data are consistent with an average value of $\alpha(t) \simeq 0$, which is naively the expectation of pion exchange. For the proton data, the average value of $\alpha(t)$ is obviously larger than the value suggested by the neutron data. The proton data are consistent with the dominance of a trajectory with the intercept $\alpha(0) \simeq 0.5$ which was found to be the sub–leading contribution in the diffractive region at larger z [H1C97b].

In the past, data on the reaction $pp \to pX$ were successfully analyzed in the framework of Regge phenomenology [Kaz76]. Many experiments measured this cross section (see references in [Kaz76]) providing an extensive statistical basis. Thus, the analysis by Kazarinov *et al.* was able to determine the different contributions to the cross section, which were parameterized in terms of three-reggeon diagrams. These diagrams can be interpreted as exchanges of pomerons, reggeons and pions including interference terms. The measurements of $F_2^{LN(3)}$ and $F_2^{LP(3)}$ cannot provide a sufficient statistical basis for a similar analysis. In particular, the $F_2^{LP(3)}$ data are restricted to the region of $z \leq 0.9$ and are therefore not very sensitive to the diffractive contribution (pomeron exchange). Instead of fitting the data points, the leading baryon structure functions $F_2^{LN(3)}$ and $F_2^{LP(3)}$ are compared to a Regge model of baryon production, of which the different contributions are mainly fixed by hadron–hadron data.

Figure 5.13 shows a comparison between the leading baryon structure functions with $0.7 \leq z \leq 0.9$ and the Regge model of baryon production. In the model, the contribution of a specific exchange $\mathcal{P}$ is determined by the product of its particle flux $f_{\mathcal{P}/p}(z,t)$ and its structure function $F_2^{\mathcal{P}}$ evaluated at (β, Q^2) (see Section 1.4). The leading baryon structure functions, which are defined for $p_T \leq 200\,\mathrm{MeV}$, can therefore be expressed by

$$F_2^{LB(3)}(\beta, Q^2, z) = \sum_{\mathcal{P}} \left(\int_{t_0}^{t_{\min}} \mathrm{d}t\, f_{\mathcal{P}/p}(z,t) \right) \cdot F_2^{\mathcal{P}}(\beta, Q^2)\ , \tag{5.16}$$

where $\mathcal{P}$ denotes the pion, the pomeron and secondary reggeons (for example ρ, ω, a_2 and f_2). The integration limits t_0 and $t_{\min}$ are given by

$$t_{\min} = -(1-z)\left(\frac{m_N^2}{z} - m_p^2\right)\ , \qquad t_0 = -\frac{(200\,\mathrm{MeV})^2}{z} + t_{\min}\ . \tag{5.17}$$

In the Regge model, it is assumed that the neutral pion, the pomeron and the f_2 all contribute to leading proton production. The contributions due to the other secondary reggeons are neglected because there is no sensitivity to them in the data, and because they have been estimated to be much smaller than the contribution due to f_2 exchange [Gol97, Kaz76]. A comparison of total hadronic cross section measurements has resulted in the estimate that the flux of reggeons which have isospin equal to one (ρ and a_2) is only $\approx 3\%$ of the flux of reggeons with isospin equal to zero (ω and f_2) [Gol97]. Regge phenomenology also predicts f_2 dominance, among isoscalar trajectories in the present case, in contrast to exchange degeneracy for elastic scattering processes [Kaz76].

For leading neutrons, the isoscalar reggeons cannot contribute to the observed cross section. It is assumed that neutrons are produced by charged pion exchange only. In the limited p_T range of the data, leading neutron production due to ρ and a_2 exchanges has been estimated to be more than an order of magnitude smaller than the contribution due to pion exchange [Kop96]. Pomeron exchange also does not give a significant contribution since neutron production due to diffractive dissociation is believed to be not more than $\sim 6\%$ of the pion exchange contribution [Kop96]. The present

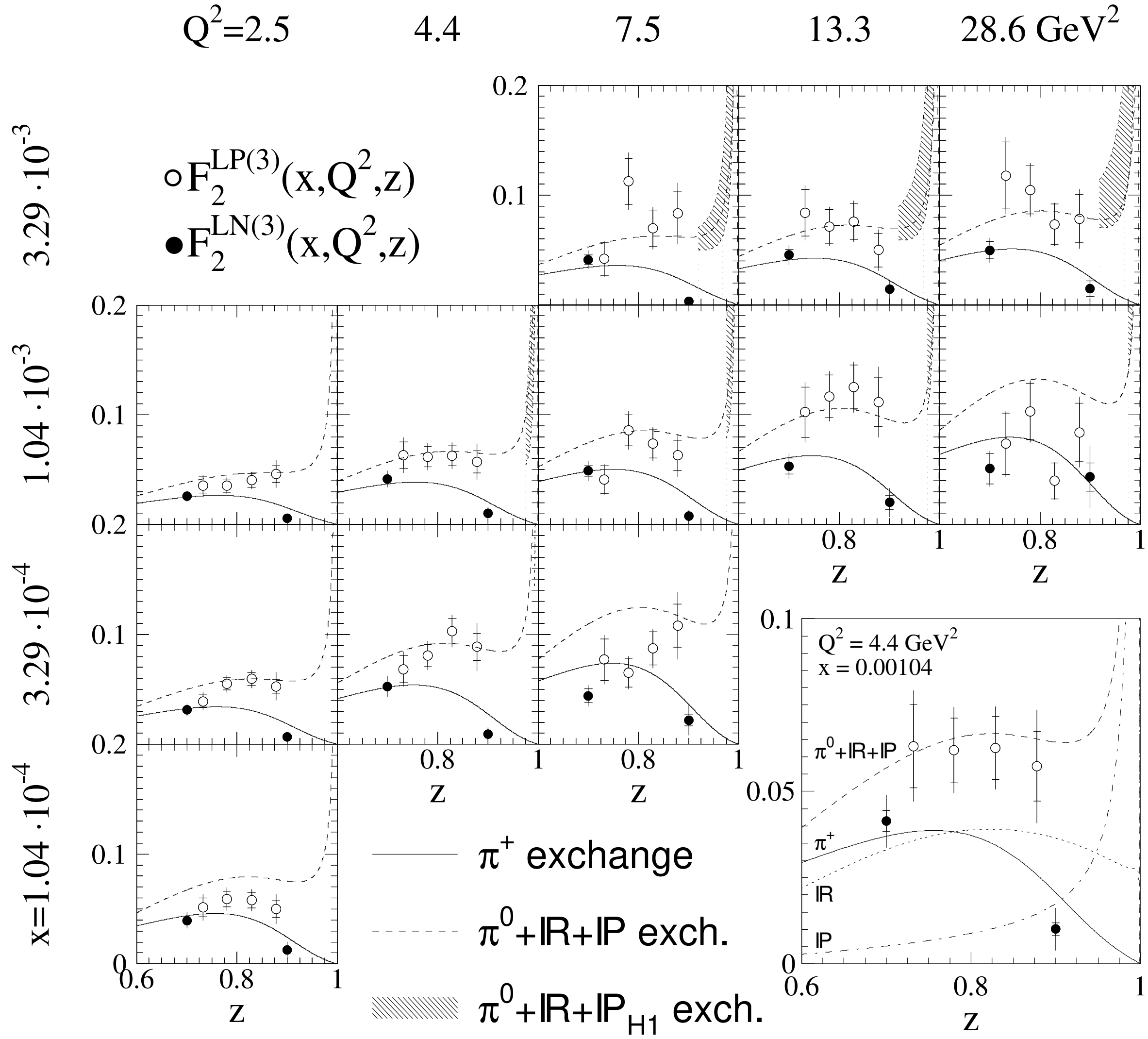

Figure 5.13: *The measured values of* $F_2^{LN(3)}$ *and* $F_2^{LP(3)}$ *with* $z \geq 0.7$ *compared to a Regge model of baryon production. The different contributions are labeled for the figure in the inset. The neutron data are described by* π^+ *exchange whereas the proton data are compared to the sum of* π^0*, pomeron and secondary reggeon* (f_2) *exchanges. The* π^0 *contribution, which is not shown, is exactly half the* π^+ *contribution. The shaded–band is explained in the text.*

data sample has been used to estimate a 2% diffractive dissociation contribution to leading neutron production by determining the fraction of events with a large rapidity gap extending into the LAr calorimeter. Additional backgrounds such as neutron production due to resonance decays have been neglected.

Figure 5.14 shows the different contributions to the production of leading neutrons and protons, which are implemented in the Regge model.

The pion, pomeron and reggeon flux factors have been determined using hadron–hadron data. The pion flux factor $f_{\pi/p}$ which has been used for neutron production is

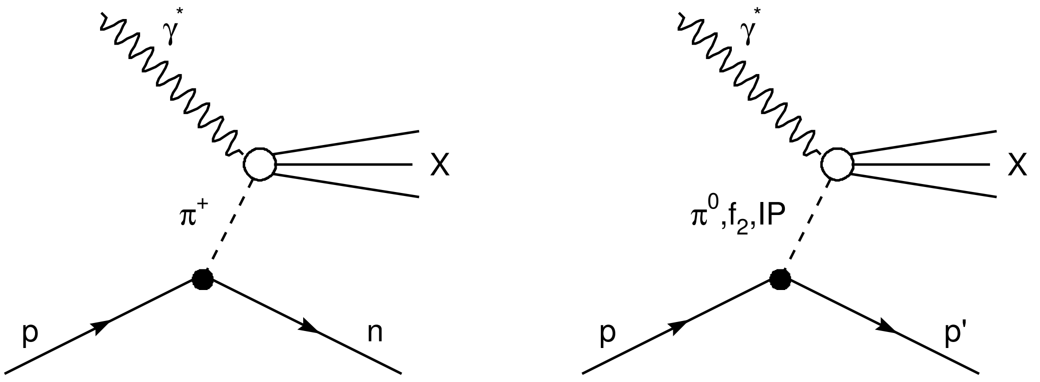

Figure 5.14: The different contributions in the Regge model of leading baryon production. Left: Neutrons are assumed to be produced by π^+ exchange only. Right: Neutral pion, f_2 and pomeron exchange contribute to leading proton production.

the same as the one used in reference [Kop96]:

$$f_{\pi/p}(z,t) = C\frac{3g^2_{p\pi N}}{16\pi^2}(1-z)^{1-2\alpha'_\pi t}\,\frac{-t}{(m_\pi^2-t)^2}\exp\left(2R_\pi^2(t-m_\pi^2)\right) \ , \tag{5.18}$$

where $g^2_{p\pi N}/(4\pi) = 13.6 \pm 0.3$ [Tim91], $\alpha'_\pi = 1\ \text{GeV}^{-2}$, $R_\pi^2 = 0.3\ \text{GeV}^{-2}$ and the square of the Clebsch–Gordon coefficient is $C = 2/3$. For proton production via π^0 exchange the same flux factor with $C = 1/3$ is used. Note that this parameterization of the pion flux factor is very similar to the one, which has been implemented in the modified RAPGAP Monte Carlo program [Hol94] (see Section 1.5.2 and 5.2).

The pomeron and reggeon flux factors are parameterized as [Szc98, Gol97]

$$f_{\mathbb{P}/p}(z,t) = \frac{54.4\,\text{GeV}^{-2}}{8\pi^2}(1-z)^{1-2\alpha_{\mathbb{P}}(t)}\exp\left(2R_{\mathbb{P}}^2 t\right) \ , \tag{5.19}$$

$$f_{\mathbb{R}/p}(z,t) = \frac{390\,\text{GeV}^{-2}}{8\pi^2}(1-z)^{1-2\alpha_{\mathbb{R}}(t)}\exp\left(2R_{\mathbb{R}}^2 t\right) \ , \tag{5.20}$$

where $\alpha_{\mathbb{P}}(t) = (1.08 + 0.25\,\text{GeV}^{-2}\,t)$ and $\alpha_{\mathbb{R}}(t) = (0.5 + 0.9\,\text{GeV}^{-2}\,t)$. The slopes are $R_{\mathbb{P}}^2 = 1.9\,\text{GeV}^{-2}$ and $R_{\mathbb{R}}^2 = 2\,\text{GeV}^{-2}$ respectively. The modulus squared of the reggeon signature factor[5], which is approximately equal to two, has been absorbed into the reggeon coupling. No reggeon–pomeron interference terms were included in the model.

The evaluation of the pion flux factor is not without some theoretical uncertainty. It has been pointed out that absorptive corrections, generated by multiple interactions,

---

[5] In reference [Szc98], equation 7 is missing the reggeon signature factor which is given in equation 5 of reference [Gol97]. The two publications also use different values of $R_{\mathbb{R}}^2$. In reference [Gol97], $R_{\mathbb{R}}^2 = 1.2\ \text{GeV}^{-2}$ which leads to a 12% difference in the values of the p_T–integrated reggeon flux factor at $z = 0.8$.

might play an important role in hadronic reactions in contrast to DIS. Since the pion flux factor which has been implemented in the model was determined using $pp \to nX$ data, it might underestimate the flux of pions in the proton for DIS reactions by up to $\approx 30\%$ [Nik97, Ale98].

The structure functions for the exchanged particles are basically unknown in the low β region, so that one has to rely on theoretical models. For the pion structure function F_2^π the GRV-LO parameterization [Glü95] was taken. The reggeon and pomeron structure functions were assumed to be proportional to the pion structure function:

$$\begin{aligned} F_2^{\mathrm{I\!R}} &= F_2^\pi \ , \\ F_2^{\mathrm{I\!P}} &= \frac{0.026}{0.12} F_2^\pi \ , \end{aligned} \tag{5.21}$$

where the latter assumption follows the arguments given in reference [Szc98]. Measurements of the diffractive structure function $F_2^{D(3)}$ [H1C95a, H1C97b, ZEU95, ZEU98] only probe the pomeron at high β ($\beta > 0.04$) and it is not possible to use these data to fix the pomeron structure function $F_2^{\mathrm{I\!P}}$ at the low β values of the semi–inclusive data ($\beta < 3 \cdot 10^{-3}$). In the small region of overlap however, the QCD fits to $F_2^{D(3)}$ [H1C97b] are consistent with the pomeron model used in the Regge model as will be discussed below.

The model gives an acceptable description of the neutron and proton data with $0.7 \leq z \leq 0.9$, in view of the fact that all particle fluxes and structure functions were taken from the literature and that no adjustment was made. The rate of leading neutron production can be described entirely by π^+ exchange. However, proton production requires contributions from both f_2 and π^0 exchange which are roughly in the ratio $2:1$ from the model.

The shaded–band in Figure 5.13 shows the prediction for $F_2^{LP(3)}$ in which the pomeron component in the Regge model was replaced by the pomeron component determined using the QCD fit to $F_2^{D(3)}$ [H1C97b]. In the QCD fit, the pomeron structure function is parameterized at a low scale and evolved to larger Q^2 using the leading order DGLAP [Gri72, Dok77, Alt77] equations. The hard–gluon leading order result which is used for $F_2^{\mathrm{I\!P}}$ (fit 3 in reference [H1C97b]) is only shown in the region in which it is valid ($3 \leq Q^2 \leq 75\,\mathrm{GeV}^2$ and $0.04 \leq \beta \leq 1.0$) and it has been interpolated from $|t| \leq 1\,\mathrm{GeV}^2$ to $p_T \leq 200\,\mathrm{MeV}$ in order to allow comparison with the leading proton data. The width of the band reflects the uncertainty in the interpolation to the different kinematic region. The pomeron flux factor used in reference [H1C97b] has been evaluated using $\alpha_{\mathrm{I\!P}}(t) = \alpha_{\mathrm{I\!P}}(0) + \alpha'_{\mathrm{I\!P}}\, t$, where $\alpha_{\mathrm{I\!P}}(0) = 1.203 \pm 0.020\,(\mathrm{stat.}) \pm 0.013\,(\mathrm{syst.})$ and $\alpha'_{\mathrm{I\!P}} = (0.26 \pm 0.26)\,\mathrm{GeV}^{-2}$. The ZEUS measurement of the slope parameter $b = (7.2 \pm 1.1\,(\mathrm{stat.})^{+0.7}_{-0.9}\,(\mathrm{syst.}))$ GeV^{-2} [ZEU98a], where $b = 2R^2_{\mathrm{I\!P}} - 2\alpha'_{\mathrm{I\!P}} \ln(1-z)$ (compare Equation 1.25), has also been used. This comparison demonstrates that the H1 measurements of the diffractive structure function $F_2^{D(3)}$ and the leading proton structure function $F_2^{LP(3)}$ can both be consistently described by Regge phenomenology.

5.8 Leading Protons and Neutrons in *pp* Scattering

It is instructive to compare the relative production cross sections for leading baryons in deep–inelastic scattering and in proton–proton scattering. In Section 3.5.1 it was mentioned, how the data on the reaction $pp \to nX$ [Fla76, Blo78] has been used by Holtmann *et al.* for the determination of the pion flux factor [Hol94, Hol96]. In addition to leading neutron production, the Bonn–Hamburg–München Collaboration studied leading proton production at the *2 m–liquid hydrogen bubble chamber* at the CERN proton synchrotron [Blo74]. The cross sections for the production of neutrons with $0\,\mathrm{GeV} \leq p_T \leq 1\,\mathrm{GeV}$ and protons with $0.2\,\mathrm{GeV} \leq p_T \leq 1\,\mathrm{GeV}$ were measured with an incident proton beam with a momentum of $p_{beam} = 12\,\mathrm{GeV}$ and $p_{beam} = 24\,\mathrm{GeV}$ [Blo74, Blo78], which corresponds to a centre–of–mass energy of $\sqrt{s} = 4.8\,\mathrm{GeV}$ and $\sqrt{s} = 6.7\,\mathrm{GeV}$ respectively.

Figure 5.15 shows a comparison of the neutron and proton data with transverse momentum of $p_T = 200\,\mathrm{MeV}$ taken at $p_{beam} = 24\,\mathrm{GeV}$. Plotted is the invariant cross section as a function of the fractional energy z. One can recognize the prominent diffractive peak at $z \approx 0.95$ in the proton data, which can be described by pomeron

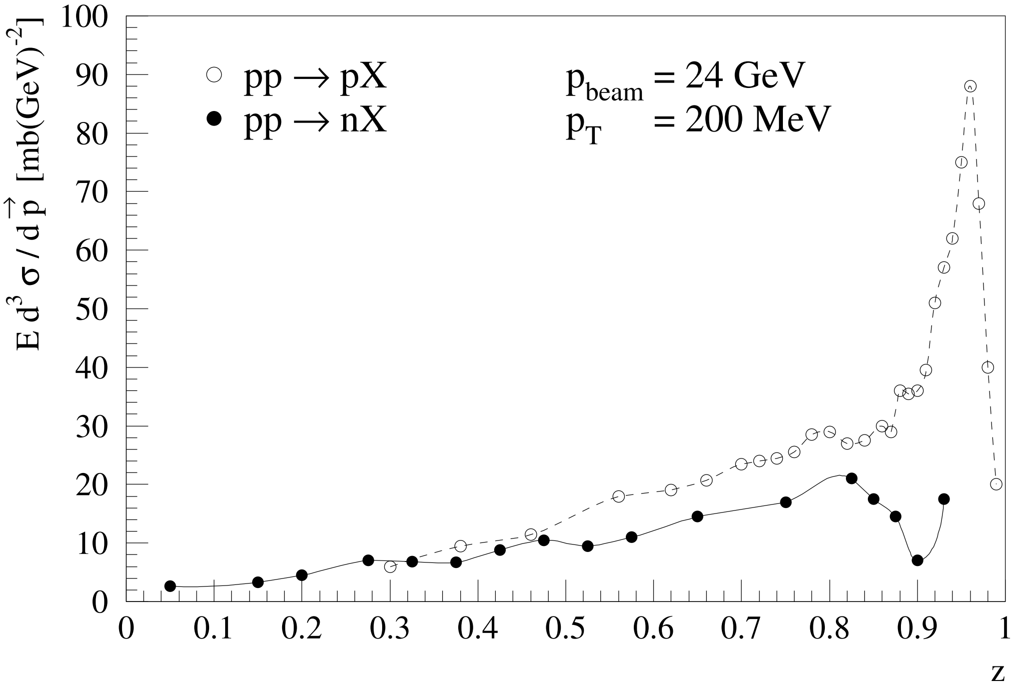

Figure 5.15: Production cross sections for protons and neutrons with $p_T = 200\,\mathrm{MeV}$ *in* pp *scattering. The data were taken at the 2 m–liquid hydrogen bubble chamber at the CERN PS with a proton beam of* $p_{beam} = 24\,\mathrm{GeV}$ *[Blo74, Blo78]. The data points, which were not published in data tables and which are not made available in the HEPDATA database [HEP98], have been transcribed from the figures in the original publications. No errors are shown.*

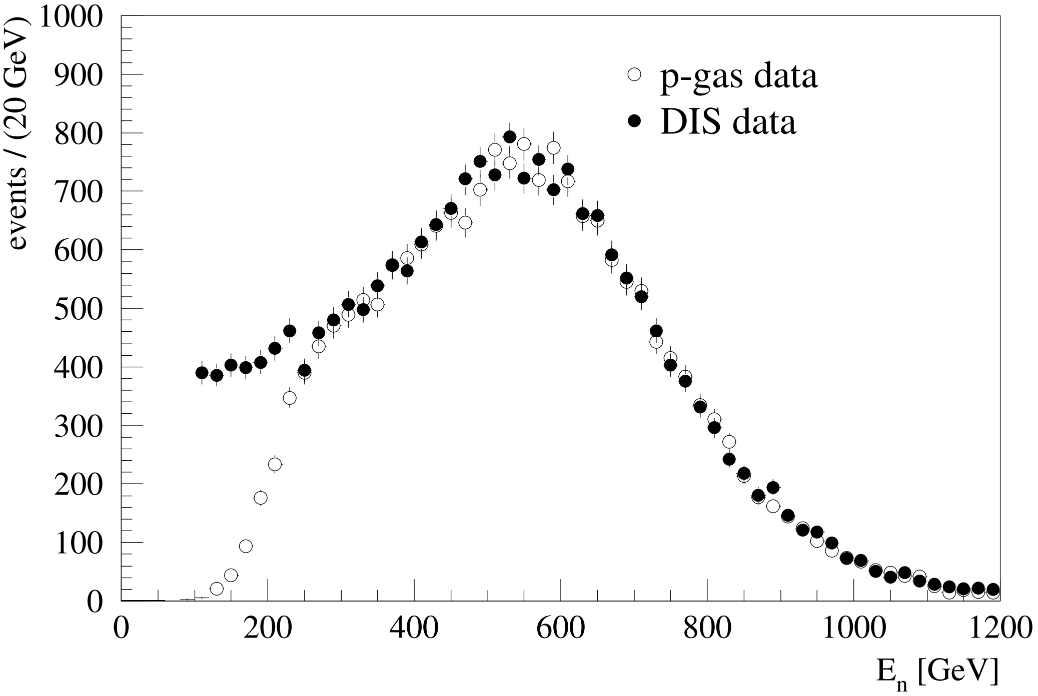

Figure 5.16: The observed neutron energy distribution in proton beam–gas interactions compared to the neutron spectrum observed in DIS. The proton beam–gas energy spectrum has not been corrected for the trigger efficiency which is less than 100% below 300 GeV. *All distributions are normalized to the number of events with* $E_n \geq 500\,\text{GeV}$.

exchange. The sharp increase in the neutron spectrum for $z > 0.9$ is due to the exclusive reaction $pp \rightarrow np\pi^+$, which can be attributed to the resonant production of $\Delta^{++}(1232)$ [Blo78]. For $z > 0.9$ the effective mass of the $p\pi^+$ system lies predominantly in the $\Delta^{++}(1232)$ resonance region. This condition in not fulfilled any more at higher centre–of–mass energies. Therefore, no increase of the neutron production cross section for $z > 0.9$ was observed at the ISR, were the data were taken at considerably higher centre–of–mass energies between 22.5 GeV and 62.7 GeV [Fla76] (compare Figure 3.12). At HERA the centre–of–mass energy of the virtual photon–proton system W is of the order of 100 GeV, depending on the specific value of x and Q^2 since $W^2 = Q^2(1-x)/x$.

In the region of $0.5 \leq z \leq 0.9$, the shape of the neutron spectrum, plotted in Figure 5.15, is consistent with pion–exchange (compare Figure 3.12). For fractional energies between ~ 0.5 and ~ 0.8 the rate of neutrons is approximately 2/3 of the proton rate. This is in agreement with the relative size of $F_2^{LN(3)}$ compared to $F_2^{LP(3)}$ at $z = 0.7$, considering that these semi–inclusive structure functions are not defined with respect to a fixed value of p_T, but parameterize the p_T integrated production cross section for $p_T \leq 200\,\text{MeV}$. This observation suggests, that for large values of z the fragmentation in the very forward region does not depend strongly on the scattering partner. This general behaviour is expected in the Regge model of leading baryon production (see Section 5.7).

At HERA it is possible to study the reactions $pp \to nX$ and $ep \to enX$ in a single experiment. Neutron production in pp scattering can be measured in interactions between the proton beam and residual gas in the beam pipe (see Section 3.5.1). Figure 5.16 shows the uncorrected neutron energy spectrum observed in proton beam–gas interactions compared to the spectrum obtained for DIS events. Above 300 GeV the two distributions agree very well in shape. This agreement supports the hypothesis that the pion flux factor is a universal property of the proton which is the same in both DIS and hadronic interactions [Sul72, Hol94]. Below 300 GeV, the sharp rise in the proton beam–gas energy spectrum is due to the trigger threshold used to obtain the data.

5.9 The Structure Function of the Pion

In Section 5.7 it was demonstrated that leading neutron production in deep–inelastic scattering with $z \geq 0.7$ is well described by pion exchange. Since the pion flux factor is known from hadron–hadron experiments, it is therefore possible to use the measurement of the semi–inclusive structure function $F_2^{LN(3)}$ to estimate for the first time the structure function of the pion at low Bjorken–x. Before the discussion of the results of this analysis, the next section summarizes briefly, what is presently known about the pion structure function.

5.9.1 Review of the Drell–Yan and Prompt–Photon Data

Our knowledge of the pion structure function comes mainly from pion–nucleon and pion–nucleus collision experiments which were done in the eighties at FERMILAB (Fermi National Accelerator Laboratory, USA) [E573-88, E615-89] and in particular at CERN [NA3-83, NA10-85, NA24-87, WA70-88]. The major reactions which were employed to study the pion structure were Drell–Yan processes and the production of prompt photons. For kinematical reasons these fixed target experiments are only sensitive to the pion structure function for Bjorken–x values of $x_\pi \gtrsim 0.2$.

The Drell–Yan process was studied at numerous experiments [E573-88, E615-89, NA3-83, NA10-85]. These experiments measured the cross section of dimuon–pair production in the continuum of the dimuon mass spectrum, outside the vector meson resonances. This process is dominated by $q\bar{q}$–annihilation and it is therefore sensitive to the valence quark density in the pion. Denoting with x_π and x_N the fractional momenta of the quark (antiquark) in the pion beam and target nucleon, the differential cross section is given in the Drell–Yan model by [Dre70, E615-89]

$$\frac{\mathrm{d}^2\sigma_{DY}}{\mathrm{d}x_\pi\,\mathrm{d}x_N} = \frac{4\pi\alpha^2}{9x_\pi x_N s} \cdot \sum_i e_i^2 \left[q_\pi^i(x_\pi)\,\bar{q}_N^i(x_N) + \bar{q}_\pi^i(x_\pi)\,q_N^i(x_N)\right] , \tag{5.22}$$

where the sum is over different quark flavours, e_i is the quark charge and q_π^i, $\bar{q}_\pi^i(x_\pi)$ and q_N^i, $\bar{q}_N^i(x_N)$ denote the quark and antiquark densities in the pion and the target nucleon respectively. Since the parton distribution functions of the nucleon are well known, Equation 5.22 allows the determination of the quark and antiquark densities of the pion. In principle the Drell–Yan data could constrain both valence and sea quark distributions, but no experimental information is existing for $x_\pi \lesssim 0.2$. Nevertheless the NA3–Collaboration published a fit to the sea quark structure function [NA3-83], which was, however, questioned [Sut92]. Since the Drell–Yan process has only a small next–to–leading–order correction due to gluons [Sut92], the data do not put any effective constraints on the shape of the gluon distribution in the pion.

In contrast to the Drell–Yan process, the gluon enters at leading order in prompt photon production, $\pi^\pm N \to \gamma X$. The cross section for prompt photon production is dominated by quark–gluon scattering, thus directly sensitive to the gluon density [Aur89]. The reaction $\pi^\pm N \to \gamma X$ has been measured by two experiments at CERN [NA24-87, WA70-88]. Again these experiments are only sensitive to the region $x_\pi \gtrsim 0.2$. In addition to the prompt photon data, also the production of J/Ψ and Υ is sensitive to the gluon contents of the interacting hadrons [NA3-83a, NA10-85a, NA10-86].

The experiments are principally not able to measure the quark or gluon distributions directly, but the measured cross sections can be used to fit the parton densities. Global fits to the data were performed by four different groups and their parameterizations for the parton distribution functions have been made available in PDFLIB [Plo93]. Lacking experimental data, the sea quark distributions have been parameterized on the basis of theoretical assumptions. The following parameterizations are existing:

- **Owens** [Owe84]: The fit is based on Drell–Yan [NA3-83, E573-88] and J/Ψ production data [NA3-83a]. The sea quark distribution at the starting scale of $Q_0^2 = 4\,\mathrm{GeV}^2$ is assumed to be proportional to $(1 - x_\pi)^5$.

- **SMRS** (Sutton, Martin, Roberts, Stirling) [Sut92]: The valence quark densities are fixed by the Drell–Yan measurement of NA10 [NA10-85], and the gluon structure function is determined using the prompt photon data of the WA70–Collaboration [WA70-88]. The sea quark distribution has been taken from Owens. The starting scale of the parameterization is $Q_0^2 = 5\,\mathrm{GeV}^2$.

- **ABFKW** (Aurenche, Baier, Fontannaz, Kienzle–Focacci, Werlen) [Aur89]: They use the prompt photon data of the NA24 and WA70 experiments [NA24-87, WA70-88] to determine the valence and gluon distribution functions. For the sea quark density the result of the NA3–Collaboration [NA3-83] was used, which is proportional to $(1 - x_\pi)^{7.5}$ at a starting scale of $Q_0^2 = 2\,\mathrm{GeV}^2$.

- **GRV** (Glück, Reya, Vogt) [Glü92]: This parameterization adopts a model, which the authors originally developed for the proton structure function [Glü90]. The valence quark distribution is taken from [Aur89] and evolved down to the starting scale of $Q_0^2 = 0.25\,\mathrm{GeV}^2$. The gluon density is assumed to be valence like at the starting scale and it is set proportional to the valence quark structure function. The sea quark density, which is assumed to vanish at the starting scale, is radiatively generated from the valence quark and gluon distributions.

5.9.2 $F_2^{LN(3)}$: Probing the Pion Structure at Low x

In the Regge model of leading baryon production (see Section 5.7) forward neutrons with $z \geq 0.7$ are produced by pion exchange only. In this region of z the semi–inclusive

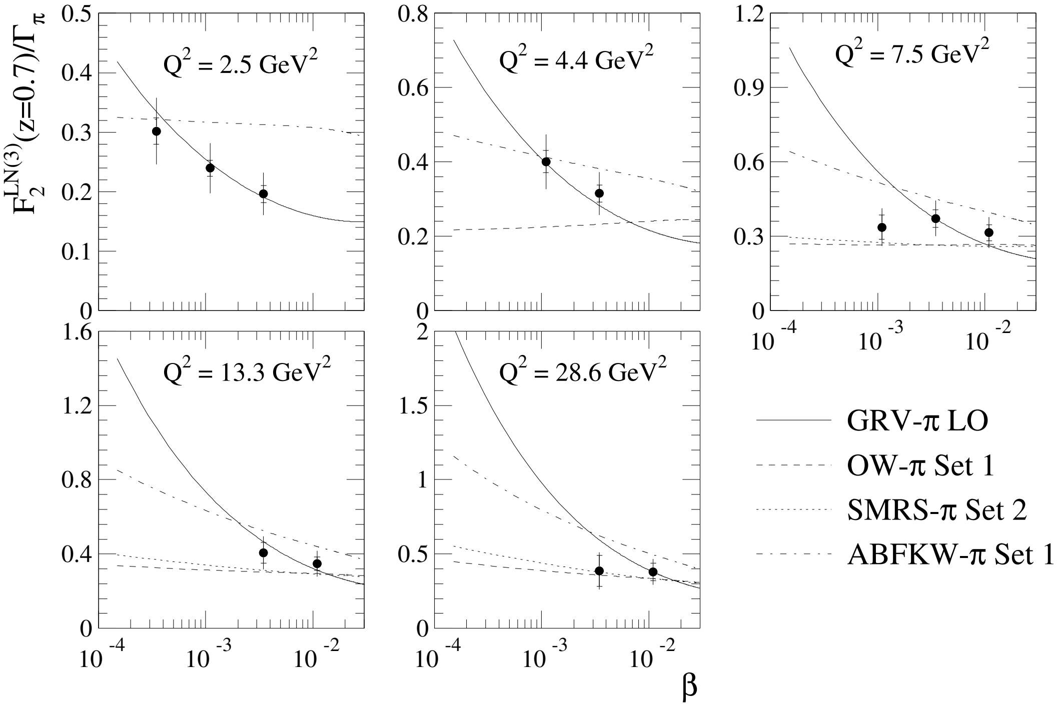

Figure 5.17: $F_2^{LN(3)}/\Gamma_\pi$ at $z = 0.7$ plotted as a function of β for fixed values of Q^2. The quantity Γ_π is the p_T integrated pion flux factor. Within the framework of the Regge model, $F_2^{LN(3)}/\Gamma_\pi$ can be interpreted as being equal to the pion structure function F_2^π. The data are compared to different parameterizations of F_2^π which are only shown above the specific starting scales Q_0^2.

structure function $F_2^{LN(3)}$ factorizes into the pion flux factor and the structure function of the pion:

$$F_2^{LN(3)}(\beta, Q^2, z) = \left(\int_{t_0}^{t_{\min}} \mathrm{d}t \, f_{\pi^+/p}(z,t) \right) \cdot F_2^\pi(\beta, Q^2) \ , \tag{5.23}$$

where the integration limits are given by Equation 5.17. The measurement of $F_2^{LN(3)}$ at $z = 0.7$ and the integral of the pion flux factor is used to estimate the pion structure function at low Bjorken–x. Assuming that the Regge model of leading neutron production is valid, the quantity $F_2^{LN(3)}/\Gamma_\pi$ can be interpreted as being equal to the structure function of the pion where:

$$\Gamma_\pi(z = 0.7) = \int_{t_0}^{t_{\min}} \mathrm{d}t \, f_{\pi^+/p}(z = 0.7, t) = 0.131 \ . \tag{5.24}$$

Figure 5.17 shows $F_2^{LN(3)}/\Gamma_\pi$ as a function of β for fixed values of Q^2. The data are compared to predictions of several parameterizations of the pion structure function [Owe84, Aur89, Sut92, Glü92, Plo93] (see Section 5.9.1). The latter are only shown in the Q^2 regions in which they are valid. The data are in good agreement with the expectations of the GRV leading order parameterization.

The parameterizations of the pion structure function are very different for $x_\pi \lesssim 0.1$. As described in the preceding section the quark and gluon distributions of the pion have previously been only constrained in the $x_\pi \gtrsim 0.2$ region using Drell–Yan data and prompt photon production data obtained by πN scattering experiments [E573-88, E615-89, NA3-83, NA10-85, NA24-87, WA70-88]. This determination using $F_2^{LN(3)}$ is the first result which constrains the pion structure function at values of x_π which are more than an order of magnitude smaller. Background contributions and possible absorptive corrections [Kop96, Nik97, Ale98] have not been taken into account. Since they are assumed to depend only on z and since all of the data are at $z = 0.7$, they are expected to only affect the absolute normalization of the result.

5.9.3 The Pion and Proton Structure Function at Low x

The cross section of electron–hadron (eh) scattering is commonly described by an inclusive structure function F_2^h. An alternative understanding is the interpretation in terms of a total $\gamma^* h$ cross section $\sigma_{tot}^{\gamma^* h}$, which can be related to the hadron structure function F_2^h through the relation [Lev97]

$$F_2^h(x, Q^2) = \frac{Q^2(1-x)}{4\pi^2\alpha} \frac{Q^2}{Q^2 + 4m_h^2 x^2} \sigma_{tot}^{\gamma^* h}(x, Q^2) \ . \tag{5.25}$$

Figure 5.18 shows the dependence of the total virtual photon–proton cross section $\sigma_{tot}^{\gamma^* p}$ on the squared $\gamma^* p$ centre–of–mass energy W^2 for fixed values of Q^2. The data points were obtained [Lev97] through Equation 5.25 from the measured F_2^p values [H1C96b, ZEU96, NMC97, ZEU97a]. Measurements of the real photoproduction cross section $\sigma_{tot}^{\gamma p}$ are also shown. For large values of W^2 the cross section rises exponentially with the centre–of–mass energy, where the exponent increases with increasing values of the photon virtuality Q^2. There is a smooth transition between the photoproduction data at $Q^2 = 0\,\mathrm{GeV}^2$ and the deep–inelastic scattering data.

Due to the hadronic fluctuations of the photon, the total photoproduction cross section $\sigma_{tot}^{\gamma p}$ behaves like a regular hadronic cross section. Total cross sections of any hadron–proton reactions are known to rise similarly with increasing centre–of–mass energy $\sqrt{s}$. The total cross section as a function of s can be parameterized in the framework of Regge phenomenology by [Don92, PDG96]

$$\sigma_{tot}^{hp}(s) = X_{\mathbb{P}} s^{\varepsilon} + Y_{\mathbb{R}} s^{-\eta} \ , \tag{5.26}$$

where $\varepsilon \approx 0.08$ and $\eta \approx 0.45$ are universal quantities[6], which are related to the intercept of the pomeron and reggeon trajectory respectively (see Section 1.3.1). The parameters $X_{\mathbb{P}}$ and $Y_{\mathbb{R}}$ give the normalizations of the two contributions depending on the specific reaction. For large values of the centre–of–mass energy ($\sqrt{s} \gtrsim 10\,\mathrm{GeV}$) the reggeon term can be neglected and the pomeron term completely dominates the total cross section.

---

[6] The reggeon intercept is experimentally not very well constrained. Here $\alpha_{\mathbb{R}}(0) = 0.55$ is used, whereas in the Regge model of leading baryon production $\alpha_{\mathbb{R}}(0) = 0.5$.

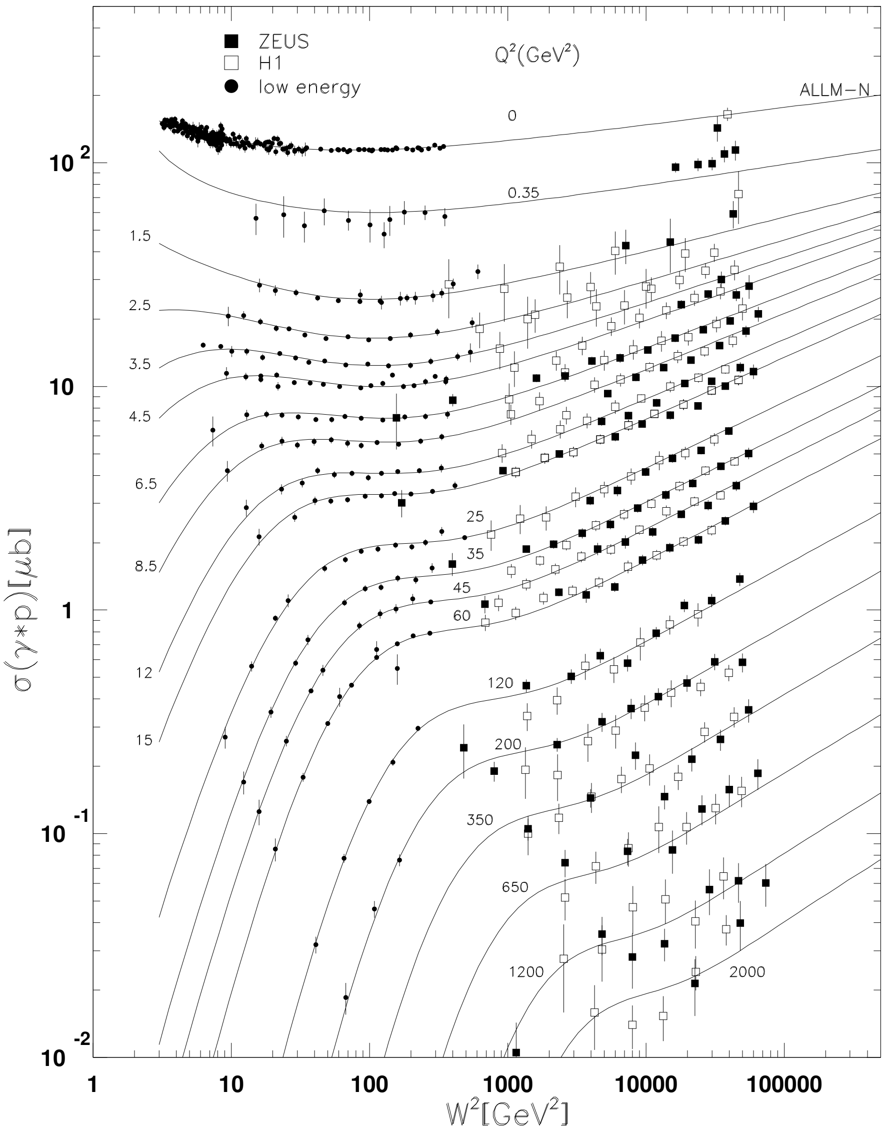

Figure 5.18: The total $\gamma^* p$ cross section as a function of W^2 for different Q^2, calculated from the F_2^p measurements [H1C96b, ZEU96, NMC97, ZEU97a]. Also shown are measurements of the total real photoproduction cross section. The superimposed lines represent the ALLM parameterization [Abr91, Abr97] (from [Lev97]).

In this region, total hadronic cross sections can also be interpreted in the framework of a geometrical model [Pov87, Hüf88, Pov90]. In this model, the total hadron–proton cross section is proportional to the square of both the proton radius and the hadron radius:

$$\sigma_{tot}^{hp} = a R_h^2 R_p^2 \ , \tag{5.27}$$

where a is an universal quantity and the squared radii increase logarithmically with increasing s, $R_h^2(s) = R_h^2(s_0)[1 + \epsilon \ln(s/s_0)]$.

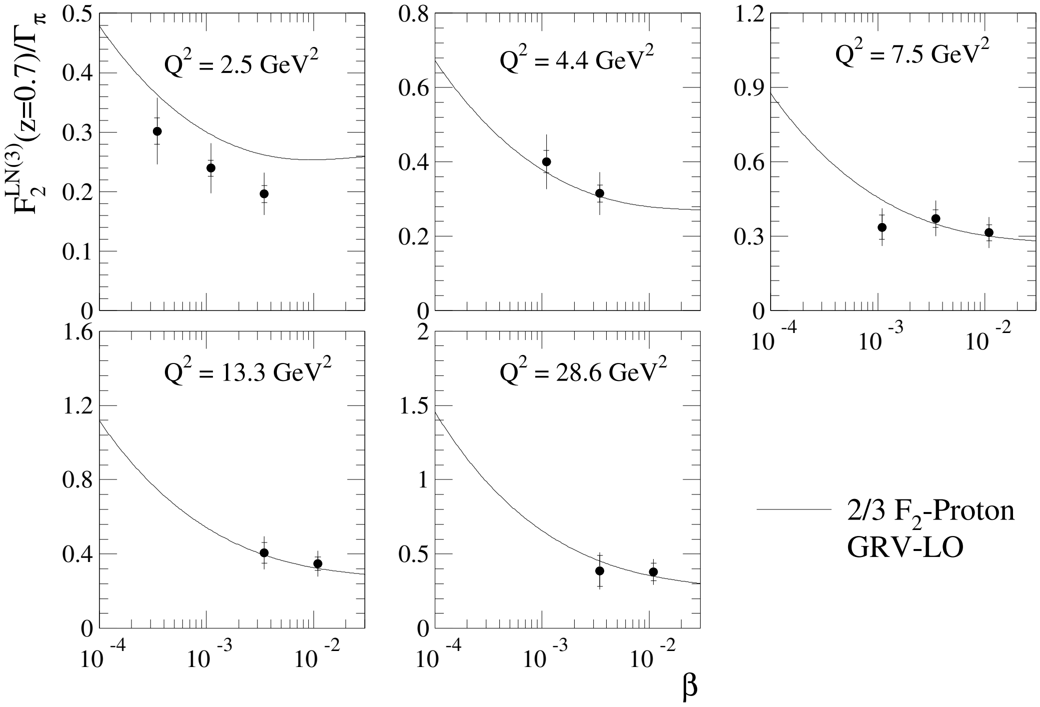

Figure 5.19: $F_2^{LN(3)}/\Gamma_\pi$ *at* $z = 0.7$ *plotted as a function of* β *for fixed values of* Q^2*. Within the framework of the Regge model,* $F_2^{LN(3)}/\Gamma_\pi$ *can be interpreted as being equal to the pion structure function* F_2^π*. The data are compared to the GRV-LO parameterization of the proton structure function, which has been scaled by* $2/3$*.*

This model can be extended to any hadron–hadron reaction. Like in the case of $\sigma_{tot}^{\gamma p}$, the total pion–photoproduction cross section $\sigma_{tot}^{\gamma\pi}$, which is practically impossible to measure directly, should have the same shape as any hadronic cross section. Thus, one can assume that $\sigma_{tot}^{\gamma\pi}$ can be expressed by Equation 5.27 and the following relation should hold for large values of W^2 and s:

$$\frac{\sigma_{tot}^{\gamma\pi}}{\sigma_{tot}^{\gamma p}} = \frac{\sigma_{tot}^{\pi p}}{\sigma_{tot}^{pp}} = \frac{R_\pi^2}{R_p^2} = 0.61 \approx \frac{2}{3} \ , \tag{5.28}$$

where for the radii the values obtained in [Pov90] have been taken. The resulting value of $\sim 2/3$ for the cross section ratio is in agreement with the naive expectation based on the number of valence quarks in the pion and proton respectively (*constituent quark model*).

Thus, the structure function of the pion at low x (which means large W^2) and in the limit of $Q^2 \to 0\,\mathrm{GeV}^2$ can be estimated by

$$F_2^\pi(x, Q^2) \approx \frac{2}{3} F_2^p(x, Q^2) \ . \tag{5.29}$$

However, for non–vanishing values of Q^2 this approximation should be worse due to the different shapes of the valence quark and gluon distributions of the pion and of the proton respectively. Because of the Q^2 evolution of the parton densities, the valence quarks and the gluons have an impact on the shape of the sea quark distributions.

Figure 5.19 shows a comparison of $F_2^{LN(3)}/\Gamma_\pi$, which can be interpreted as the structure function of the pion, and the proton structure function, which has been scaled by 2/3. The shape and magnitude of the naive expectation, based on the ratios of total hadronic cross sections, is in fair agreement with the data.

Generalizing the argument, one can assume that at low x any hadronic structure function should be similar in shape to the proton structure function.

Summary and Conclusions

In 1996 the H1 Experiment was upgraded with a forward neutron calorimeter, which gave the possibility to study leading neutron production at HERA. Neutrons, which are produced at scattering angles $\theta \lesssim 0.6\,\mathrm{mrad}$, are within the acceptance of the calorimeter.

For the first time at HERA, the triple–differential cross section $\mathrm{d}\sigma/(\mathrm{d}x\mathrm{d}Q^2\mathrm{d}z)$ for the production of leading neutrons with transverse momenta $p_T \leq 200\,\mathrm{MeV}$ has been measured in the kinematic region $2\,\mathrm{GeV}^2 \leq Q^2 \leq 50\,\mathrm{GeV}^2$, $6 \cdot 10^{-5} \leq x \leq 6 \cdot 10^{-3}$ and $0.2 \leq z \leq 1$. This measurement is parameterized in terms of a semi–inclusive structure function $F_2^{LN(3)}$ in analogy to the inclusive proton structure function.

The Lepto Monte Carlo program, which is based upon soft colour interactions and the Lund string fragmentation model, describes the magnitude and the general shape of the data over the entire z range, although it tends to underestimate the production cross section for $z \approx 0.7$.

The Rapgap Monte Carlo program, which simulates pion exchange, gives, after the modification of the implemented pion flux factor, an acceptable description of the data in the region $z \geq 0.7$. For small values of z ($z \lesssim 0.4$) pion exchange is ruled out to be the principal production mechanism. In this region additional physical processes, e. g. as simulated in the Lund string fragmentation model, dominate the observed cross section.

Scaling violations have been observed in the measured semi–inclusive structure function $F_2^{LN(3)}$, which are similar in size and shape to those seen in the GRV-LO parameterizations of the inclusive structure functions of the pion and the proton. The data is equally well described by fits assuming factorization in x, Q^2 and z or β, Q^2 and z. Since the measurement is probing only the low β region, the data have only a relatively limited sensitivity to distinguish the different factorization hypotheses. Within the accuracy of the measurement, the leading neutron structure function $F_2^{LN(3)}$ constitutes a constant fraction of the inclusive proton structure function F_2^p for fixed values of z, independent from x and Q^2 in the kinematical region covered by this analysis. In $(5.7 \pm 1.6)\%$ of all deep–inelastic events a leading neutron with $p_T \leq 200\,\mathrm{MeV}$ and $z \geq 0.2$ is produced.

The leading neutron data are compared to a similar measurement of the leading proton structure function $F_2^{LP(3)}$. The production cross section for leading protons is larger than it is for leading neutrons, which demonstrates that leading proton production cannot be dominated by pion exchange. Also the soft colour interaction model as implemented in the Lepto Monte Carlo program fails to describe the proton data since it underestimates the cross section by a factor of approximately two.

A Regge model of leading baryon production, which considers the colour neutral exchanges of pions, pomerons and reggeons, gives a fairly good description of both the neutron and proton data. The production cross section for leading neutrons with $0.7 \leq z \leq 0.9$ can be described entirely by π^+ exchange whereas the semi–inclusive cross section for protons with $0.73 < z < 0.88$ require π^0 and f_2 exchange contributions. In the model, the contribution due to f_2 exchange is approximately a factor of two greater than the contribution due to π^0 exchange.

In the framework of this Regge model, the leading neutron data have been used to estimate for the first time the structure function of the pion at low Bjorken–x, which are one to more than two orders of magnitude smaller than in previous measurements. The data are in good agreement with the GRV leading order parameterization of the pion parton distributions. The estimated pion structure function is approximately 2/3 of the proton structure function, which is expected from the relative magnitudes of the total hadronic cross sections of πp and pp scattering.

A major restriction for the accuracy of the cross section measurement, presented in this work, is given by the limited energy resolution of the Forward Neutron Calorimeter. A significant improvement is anticipated from the installation of a preshower detector in front of the FNC in 1998. The high luminosity, which was taken in 1997 and which HERA is expected to deliver in the next years, provides the possibility to extend the cross section measurement to considerably higher values of Q^2 and x. With the enlarged kinematic range, one can hope to obtain further information, which allow to better discriminate between the different production models. Measurements at $\beta > 0.2$ would provide a direct comparison of the neutron data with the pion structure function determined in pion–nucleon scattering experiments. At very large x, when the valence quark distribution in the proton is probed, the dynamics of neutron production is expected to differ significantly.

References

[Abr91] H. Abramowicz, E.M. Levin, A. Levy and U. Maor, *Phys. Lett.* **B269** (1991) 465.

[Abr97] H. Abramowicz and A. Levy, *The ALLM Parameterization of* $\sigma_{tot}^{\gamma^* p}$*: an Update*, DESY report DESY-97-251, December 1997.

[Aco90] D. Acosta et al., *Nucl. Instr. and Meth.* **A294** (1990) 193.

[Aco91] D. Acosta et al., *Nucl. Instr. Meth.* **A314** (1991) 431.

[Aco91a] D. Acosta et al., *Nucl. Instr. Meth.* **A308** (1991) 481.

[Alb81] G. Alberi and G. Goggi, *Phys. Rept.* **74** (1981) 1.

[Ale98] U. D'Alesio, H.J. Pirner and A. Schäfer, *Target Fragmentation in pp and* γp *Collisions at High–Energies*, HD–TVP–98–3, hep–ph/9806321.

[Alt77] G. Altarelli and G. Parisi, *Nucl. Phys.* **B126** (1977) 298.

[And83] B. Andersson, G. Gustafson, G. Ingelman and T. Sjöstrand, *Phys. Rept.* **97** (1983) 31.

[ASG94] Application Software Group, *GEANT Detector Description and Simulation Tool*, CERN Program Library Long Writeup W5013, October 1994.

[Aur89] P. Aurenche et al., *Phys. Lett.* **B233** (1989) 517.

[Bas95] U. Bassler and G. Bernardi, *Nucl. Instr. Meth.* **A361** (1995) 197.

[Bec95] M. Beck et al., *Proposal for a Forward Neutron Calorimeter for the H1 Experiment*, H1–PRC–95/02, 1995.

[Bec96] M. Beck et al., *Nucl. Instr. Meth.* **A381** (1996) 330.

[Ben69] J. Benecke et al. *Phys. Rev.* **188** (1969) 2159.

[Ben89] BCDMS Collaboration, A.C. Benvenuti et al., *Phys. Lett.* **B223** (1989) 485.

[Ben92] S. Bentvelsen, J. Engelen and P. Kooijman in *Proceedings of the Workshop on Physics at HERA*, Hamburg (1991), W. Buchmüller and G. Ingelman eds., DESY, Hamburg (1992), Vol. 1.

[Bet34] H. Bethe and W. Heitler, *Proc. Roy. Soc.* **A146** (1934) 83.

[Bha97] ZEUS FNC Group, S. Bhadra et al., *Nucl. Instrum. Meth.* **A394** (1997) 121.

[Bjo67] J.D. Bjorken, *Phys. Rev.* **163** (1967) 1767.

[Blo74] V. Blobel et al., *Nucl. Phys.* **B69** (1974) 454.

[Blo78] V. Blobel et al., *Nucl. Phys.* **B135** (1978) 379.

[Blo69] E.D. Bloom et al., *Phys. Rev. Lett.* **23** (1969) 930.

[Blo84] V. Blobel, *Unfolding Methods in High–Energy Physics Experiments*, DESY report 84–118 (1984); *Proceedings from the 1984 CERN School of Computing*, Aiguablava, Spain, CERN 85–02 (1985).

[Blo96] V. Blobel, *The RUN manual, Regularized Unfolding for High–Energy Physics Experiments*, OPAL Technical Note TN361, March 1996.

[Bou95] V. Boudry et al., *The Inclusive Electron Trigger for SPACAL: Design and CERN-Test Results*, Internal H1 Note, January 1995.

[Bre69] M. Breidenbach et al., *Phys. Rev. Lett.* **23** (1969) 935.

[Buc95] W. Buchmüller and A. Hebecker, *Phys. Lett.* **B355** (1995) 573.

[Bru96] P. Bruni, A. Edin and G. Ingelman, *Pompyt version 2.6 - A Monte Carlo to Simulate Diffractive Hard Scattering Processes*, unpublished program manual, September 1996, `http://www3.tsl.uu.se/thep/pompyt/`.

[Cal69] C.G. Callan and D.J. Gross, *Phys. Rev. Lett.* **4** (1969) 156.

[Cho94] T.T. Chou and C.N. Yang, *Phys. Rev.* **D50** (1994) 590.

[Col84] P.D.B. Collins and A.D. Martin, *Hadron Interactions*, Adam Hilger, 1984.

[Coo81] R.L. Cool et al., *Phys. Rev. Lett.* **47** (1981) 701.

[Cou92] A. Courau and P. Kessler, *Phys. Rev.* **D46** (1992) 117.

[Dok77] Yu.L. Dokshitser, *Sov. Phys. JETP* **46** (1977) 641.

[Don86] A. Donnachie and P.V. Landshoff, *Nucl. Phys.* **B267** (1986) 690.

[Don92] A. Donnachie and P.V. Landshoff, *Phys. Lett.* **B296** (1992) 227.

[Dre61] S.D. Drell, *Rev. Mod. Phys.* **33** (1961) 458.

[Dre70] S.D. Drell and T.M. Yan, *Phys. Rev. Lett.* **25** (1970) 316.

[E573-88] E537 Collaboration, E. Anassontzis et al., *Phys. Rev.* **D38** (1988) 1377.

[E615-89] E615 Collaboration, J.S. Conway et al., *Phys. Rev.* **D39** (1989) 92.

[E866-98] E866/NuSea Collaboration, E.A. Hawker et al., *Phys. Rev. Lett.* **80** (1998) 3715.

[E866-98a] E866/NuSea Collaboration, J.C. Peng et al., *Phys. Rev.* **D58** (1998) 92004.

[Edi96] A. Edin, G. Ingelman and J. Rathsman, *Phys. Lett.* **B366** (1996) 371.

[Edi97] A. Edin, G. Ingelman and J. Rathsman, *Z. Phys.* **C75** (1997) 57.

[Edi98] A. Edin and G. Ingelman, *Phys.Lett.* **B432** (1998) 402.

[Egl96] S. Egli, *Userguide for Program Runselect*, Internal H1 Note, December 1996.

[Fey69] R.P. Feynman, *Phys. Rev. Lett.* **23** (1969) 1415.

[Fla76] W. Flauger and F. Mönnig, *Nucl. Phys.* **B109** (1976) 347.

[Fra89] L.L. Frankfurt, L. Mankiewitz and M.I. Strikman, *Z. Phys.* **A334** (1989) 343.

[Glü90] M. Glück, E. Reya and A. Vogt, *Z. Phys.* **C48** (1990) 471.

[Glü92] M. Glück, E. Reya and A. Vogt, *Z. Phys.* **C53** (1992) 651.

[Glü95] M. Glück, E. Reya and A. Vogt, *Z. Phys.* **C67** (1995) 433.

[Gol97] K. Golec–Biernat et al., *Phys. Rev.* **D56** (1997) 3955.

[Got67] K. Gottfried, *Phys. Rev. Lett.* **18** (1967) 1174.

[Gou83] K. Goulianos, *Phys. Rept.* **101** (1983) 169.

[Gri72] V.N. Gribov and L.N. Lipatov, *Sov. J. Nucl. Phys.* **15** (1972) 438.

[H1C93] H1 Calorimeter Group, B. Andrieu et al., *Nucl. Instr. Meth.* **A336** (1993) 499.

[H1C94] H1 Collaboration, T. Ahmed et al., *Nucl. Phys.* **B429** (1994) 477.

[H1C95] H1 Collaboration, T. Ahmed et al., *Z. Phys.* **C66** (1995), 529.

[H1C95a] H1 Collaboration, T. Ahmed et al., *Phys. Lett.* **B348** (1995) 681.

[H1C95b] H1 Collaboration, T. Ahmed et al., *Nucl. Phys.* **B439** (1995) 471.

[H1C96] H1 Collaboration, *Proceedings of the International Conference on High Energy Physics*, Warsaw 1996, ICHEP96-pa17-025.

[H1C96a] H1 Collaboration, *Proceedings of the International Conference on High Energy Physics*, Warsaw 1996, ICHEP96-pa17-026.

[H1C96b] H1 Collaboration, S. Aid et al., *Nucl. Phys.* **B470** (1996) 3.

[H1C97] H1 Collaboration, I. Abt et al., *Nucl. Instr. Meth.* **A386** (1997) 310, *ibid.* 348.

[H1C97a] H1 Collaboration, C. Adloff et al., *Nucl. Phys.* **B497** (1997) 3.

[H1C97b] H1 Collaboration, C. Adloff et al., *Z. Phys.* **C76** (1997) 613.

[H1C98] H1 Collabration, C. Adloff et al. *Measurement of Leading Proton and Neutron Production in Deep Inelastic Scattering at HERA*, DESY report DESY 98-169, October 1998, accepted for publication in *Eur. Phys. J.* **C**.

[H1C98a] H1 Collabration, contributed papers 533, 534 and 535 to the *29th Intern. Conf. on High-Energy Physics*, Vancouver, Canada (1998)

[H1S96] H1 SPACAL Group, T. Nicholls et al., *Nucl. Instr. Meth.* **A374** (1996) 149.

[H1S97] H1 SPACAL Group, R.–D. Appuhn et al., *Nucl. Instr. Meth.* **A386** (1997) 397.

[HER98] HERMES Collaboration, K. Ackerstaff et al., *The Flavor Asymmetry of the Light Quark Sea from Semiinclusive Deep Inelastic Scattering*, DESY report DESY-98-078, July 1998.

[HEP98] Durham Database group (UK) and Compas group (Russia), *HEPDATA: REACTION DATA database*, regularly updated, `http://durpdg.dur.ac.uk/HEPDATA/REAC`.

[Hol94] H. Holtmann et al., *Phys. Lett.* **B338** (1994) 363.

[Hol96] H. Holtmann et al., *Nucl. Phys.* **A596** (1996) 631.

[Hol96a] H. Holtmann, N.N. Nikolaev, J. Speth and A. Szczurek, *Z. Phys.* **A353** (1996) 411.

[Hüf88] J. Hüfner and B. Povh, *Phys. Lett.* **B88** 772.

[Ing85] G. Ingelman and P.E. Schlein, *Phys. Lett.* **B152** (1985) 256.

[Ing97] G. Ingelman, A. Edin and J. Rathsman, *Comp. Phys. Comm.* **101** (1997) 108, for the program code and manual see `http://www3.tsl.uu.se/thep/lepto/`.

[Jam94] F. James, *Minuit: Function Minimization and Error Analysis, Reference Manual, Version 94.1, CERN Program Library Long Writeup D506*, 1994, unpublished, see also `http://wwwinfo.cern.ch/asdoc/minuit_html3/minmain.html`.

[Jun95] H. Jung, *Comp. Phys. Commun.* **86** (1995) 147;
H. Jung, *The RAPGAP Monte Carlo for Deep Inelastic Scattering, version 2.06/27*, unpublished program manual, May 1998, for the program code and manual see `http://www-h1.desy.de/~jung/rapgap/rapgap.html`.

[Kai79] A.B. Kaidalov, *Phys. Rept.* **50** (1979) 159.

[Kat97] J. Katzy, Ph.D. Thesis (in German), University of Heidelberg (1997).

[Kaz76] Yu. M. Kazarinov et al., *Sov. Phys. JETP* **43** (1976) 598.

[Kop96] B. Kopeliovich, B. Povh and I. Potashnikova, *Z. Phys.* **C73** (1996) 125.

[Kum98] S. Kumano, *Phys. Rep.* **303** (1998) 183; and references therein.

[Kwi92] A. Kwiatkowski, H. Spiesberger and H.-J. Möhring, *Comp. Phys. Comm.* **69** (1992) 155; *Proceedings of the Workshop on Physics at HERA*, Hamburg (1991), W. Buchmüller and G. Ingelman eds., DESY, Hamburg (1992), Vol. 3.

[Kwi93] A. Kwiatkowski, H. Spiesberger and H.-J. Möhring, *HERACLES. An event generator for ep interactions at HERA including radiative processes. Version 4.5.2.*, unpublished program manual (1993).

[Lai97] H.L. Lai et al., *Phys. Rev.* **D55** (1997) 1280.

[Lan94] P.V. Landshoff, *The two Pomerons*, hep–ph/9410250.

[Lev95] G. Levman and K. Furutani, *Virtual Pion Scattering at HERA*, DESY report DESY-95-142, July 1995.

[Lev97] A. Levy, *Low–x Physics at HERA*, DESY report DESY-97-013, Feb 1997, published in F. Lenz (ed.), *Lectures on QCD: Applications*, Springer, 1997, p. 347.

[Lis97] B. List, Ph.D. Thesis (in German), University of Hamburg (1997);
B. List (for the H1 Collaboration) in *Proceedings of the 5th International Workshop on Deep Inelastic Scattering and QCD, Chicago 1997*, J. Repond and D. Krakauer eds., American Institue of Physics, 1997, p. 520.

[Lyt97] L. Lytkin, private communication.

[Mar96] J. Marks et al., *QESCAT - Electron Identication Software in H1PHAN*, H1 Analysis Software Package, Internal Report, July 1996.

[Met98] F. Metlica, Ph.D. Thesis, University of Heidelberg (1998).

[NA3-83] NA3 Collaboration, J. Badier et al., *Z. Phys.* **C18** (1983) 281.

[NA3-83a] NA3 Collaboration, J. Badier et al., *Z. Phys.* **C20** (1983) 101.

[NA10-85] NA10 Collaboration, J. Betev et al., *Z. Phys.* **C28** (1985) 9.

[NA10-85a] NA10 Collaboration, S. Falciano et al., *Phys. Lett.* **B158** (1985) 92.

[NA10-86] NA10 Collaboration, M. Grossmann–Handschin et al., *Phys. Lett.* **B179** (1986) 170.

[NA24-87] NA24 Collaboration, C. De Marzo et al., *Phys. Rev.* **D36** (1987) 8.

[NA51-94] NA51 Collaboration, A. Baldit et al. *Phys. Lett.* **B322** (1994) 244.

[Nac90] Otto Nachtmann, *Elementary Particle Physics: Concepts and Phenomena*, Springer, 1990.

[Nik97] N.N. Nikolaev, J. Speth and B.G. Zakharov, *Absorptive Corrections to the One Pion Exchange and Measurability of the Small–x Pion Structure Function at HERA*, KFA–IKP–TH–97–17 (1997), hep–ph/9708290.

[NMC91] New Muon Collaboration, P. Amaudruz et al., *Phys. Rev. Lett.* **66** (1991) 2712.

[NMC94] New Muon Collaboration, M. Arneodo et al., *Phys. Rev.* **D50**(1994) 1.

[NMC95] New Muon Collaboration, M. Arneodo et al., *Phys. Lett.* **B364** (1995) 107.

[NMC97] New Muon Collaboration, M. Arneodo et al., *Nucl. Phys.* **B483** (1997) 3.

[Nun96] T. Nunnemann, Diploma Thesis (in German), University of Heidelberg (1996).

[Mey97] A. Meyer, Ph.D. Thesis, University of Hamburg (1997).

[Owe84] J.F. Owens, *Phys. Rev.* **D30** (1984) 943.

[PDG96] Particle Data Group, R.M. Barnett et al., *Review of Particle Properties*, *Phys. Rev.* **D54** (1996) 1.

[Per87] D.H. Perkins, *Introduction to High Energy Physics*, 3rd edition, Addison-Wesley, 1987

[Plo93] H. Plothow–Besch, *Comp. Phys. Comm.* **75** (1993) 396, for the program code and manual see `http://consult.cern.ch/writeups/pdflib/main.ascii`.

[Pom58] I.J. Pomerančuk, *Sov. Phys. JETP* **7** (1958) 499.

[Pov87] B. Povh and J. Hüfner, *Phys. Rev. Lett.* **58** (1987) 1612.

[Pov90] B. Povh and J. Hüfner, *Phys. Lett.* **B245** (1990) 653.

[Pov95] B. Povh et al., *Particles and Nuclei: An Introduction to the Physical Concepts*, Springer, 1995.

[Pum73] J. Pumplin, *Phys. Rev.* **D8** (1973) 2249.

[Prz97] M. Przybycien, A. Szczurek and G. Ingelman, *Z. Phys.* **C74** (1997) 509.

[Reg59] T. Regge, *Nuov. Cim.* **14** (1959) 951; *Nuov. Cim.* **18** (1960) 947.

[Rob90] R.G. Roberts, *The Structure of the Proton*, Cambridge University Press, 1990.

[Sch92] G.A. Schuler and H. Spiesberger in *Proceedings of the Workshop on Physics at HERA*, Hamburg (1991), W. Buchmüller and G. Ingelman eds., DESY, Hamburg (1992), Vol. 3.

[Sch94] C. V. Scheel, Ph.D. Thesis, University of Amsterdam (1994).

[Sch97] B. Schwab, Ph.D. Thesis (in German), University of Heidelberg (1997).

[Sjö94] T. Sjöstrand, *Comp. Phys. Comm.* **82** (1994) 74;
T. Sjöstrand, *Pythia 5.7 and Jetset 7.4: Physics and Manual*, Lund preprint LU-TP-95-20 and CERN preprint CERN-TH-7112-93, revised version, August 1995, for program code and manual see `http://www.thep.lu.se/tf2/staff/torbjorn/Pythia.html`;
T. Sjöstrand, *Comp. Phys. Comm.* **39** (1986) 347;
T. Sjöstrand and M. Bengtsson *Comp. Phys. Comm.* **43** (1987) 367.

[Spi92] H. Spiesberger et al., in *Proceedings of the Workshop on Physics at HERA*, Hamburg (1991), W. Buchmüller and G. Ingelman eds., DESY, Hamburg (1992), Vol. 2.

[Spi96] H. Spiesberger, *DJANGO6 version 2.4 – A Monte Carlo Generator for Deep Inelastic Lepton Proton Scattering Including QED and QCD Radiative Effects*, unpublished program manual, October 1996, `http://www.desy.de/~hspiesb/django6.html`.

[Sul72] J.D. Sullivan, *Phys. Rev.* **D5** (1972) 1732.

[Sut92] P.J. Sutton et al., *Phys. Rev.* **D45** (1992) 2349.

[Szc98] A. Szczurek, N.N. Nikolaev and J. Speth, *Phys. Lett.* **B428** (1998) 383.

[Tao96] E140X Collaboration, L.H. Tao et al., *Z. Phys.* **C70** (1996) 387.

[Tho83] A.W. Thomas, *Phys. Lett.* **B126** (1983) 97.

[Tim91] R.G.E. Timmermanns, Th.A. Rijken and J.J. de Swart, *Phys. Rev. Lett.* **67** (1991) 1074.

[Tod97] R. Todenhagen, private communication.

[WA70-88] WA70 Collaboration, M. Bonesini et al., *Z. Phys.* **C37** (1988) 535.

[WA89-87] WA89 Collaboration, Proposal to the SPSC CERN/SPSC–87/43, 1987.

[Whi92] Whitlow et al., *Phys. Lett.* **B282** (1992) 475.

[Wii92] B. Wiik in *Proceedings of the Workshop on Physics at HERA*, Hamburg (1991), W. Buchmüller and G. Ingelman eds., DESY, Hamburg (1992), Vol. 1.

[You87] S. Youssef, *Computer Physics Communications* **45** (1987) 423.

[Yu98] CCFR/NuTeV Collaboration, J. Yu et al., *Determination of* α_s *and Measurements of* $R(L)$*,* K*, and* $|V(cs)|$ *from Neutrino Nucleon DIS at CCFR.*, FERMILAB-CONF-98-304-E, October 1998, to be published in the proceedings of *29th International Conference on High-Energy Physics (ICHEP 98)*, Vancouver, Canada

[Yuk35] H. Yukawa, *Proc. Phys. Math. Soc. Jap.* **17** (1935) 48.

[ZEU93] ZEUS Collaboration, M. Derrick et al., *Phys. Lett.* **B315** (1993) 481.

[ZEU95] ZEUS Collaboration, M. Derrick et al., *Z. Phys.* **C68** (1995) 569.

[ZEU96] ZEUS Collaboration, M. Derrick et al., *Z. Phys.* **C72** (1996) 399.

[ZEU97] ZEUS Collaboration, *Properties of Events with a Leading Proton in DIS and Photoproduction at HERA*, contributed paper N-644 to the International Europhysics Conference on High Energy Physics, Jerusalem, August 1997.

[ZEU97a] ZEUS Collaboration, J. Breitweg et al., *Phys. Lett.* **B 407** (1997) 432.

[ZEU98] ZEUS Collaboration, J. Breitweg et al., *Eur. Phys. J.* **C2** (1998) 237.

[ZEU98a] ZEUS Collaboration, J. Breitweg et al., *Eur. Phys. J.* **C1** (1998) 81.

[Zol92] R. Zoller, *Z. Phys.* **C53** (1992) 443.

List of Figures

List of Tables

Acknowledgements

I am indebted to my supervisor Prof. Bogdan Povh for offering me the opportunity to work on this challenging project, for his support and his continuous interest in my work. I also thank him for making it possible to me to attend conferences and summer schools.

I would like to thank Prof. Jürgen von Krogh, for proof–reading this thesis and participating in the examination committee.

I am grateful to Doug Jansen for his valuable advice and our good teamwork. Without his substantial help, the results presented in this thesis would not have been achieved. I want to thank him for our lively discussions and for his useful suggestions after reading the manuscript.

I would like to thank Ralf Todenhagen for his never–ending assistance, in particular during the first years after I started working for the FNC as a diploma student.

Thanks to Fabio Metlica, with whom I shared the office at CERN, DESY and MPI, for his cooperation and for reading parts of the manuscript and to Leonid Lytkin for taking so much care of the FNC.

I thank Igor Konorov and Walter Brückner for putting efforts in the electronics and computing system.

I would like to thank Wieland Hoprich for careful and critical reading of the manuscript.

For the friendly and cooperative atmosphere, I would like to thank all the members of the H1 group at MPI Heidelberg, which are, besides the ones already mentioned: Michael Kreuz, Irina Potashnikova and Vitali Dodonov.

Special thanks to Benno List for valuable discussions and his fruitful cooperation, which continued even after he had left H1.

It is a pleasure to thank the members of the diffractive working group of H1, especially Paul Newman and Prof. Pierre Marage for very inspiring discussions and suggestions. I am grateful to many members of the H1 Collaboration. I would like to stress the very helpful ideas and suggestions of Prof. Rolf Felst, Prof. John Dainton and Priv.-Doz. Martin Erdmann.

For their theoretical assistance, I would like to thank Prof. Hans Jürgen Pirner, Umberto d'Alsesio and in particular Prof. Boris Kopeliovich.

Special thanks to Henning Krüger and Jürgen Simon for our joined efforts since the time we prepared for our diploma examination, and for their helping hand when I had various troubles with the computing system.

Many thanks to Oliver Thilmann for offering a "place of silence" in his office during the time I wrote up the thesis, to Phillip Geiger for his bike, which improved my mobility at DESY considerably, and to Ivo Eschrich, who frequently provided the transportation to escape the "pfälzische Küche" at MPI.

I enjoyed the stimulating and friendly atmosphere at the Max–Planck–Institute in Heidelberg. My gratitude goes to the whole group, to Priv.-Doz. Antje Brüll, Christian Busch, Christian Büscher, Uwe Dersch, Guido Dirkes, Frank Dropmann, Peter Fauland, Nicolas Keller, Heiko Neeb, Priv.-Doz. Josef Pochodzalla, Tina Schati, Claudia Schröder, Prof. Hans–Wolfgang Siebert, Erik Volk, Klaus Vorwalter, Thomas Wilhelm, Eva Wittmann and Michael Zavertyaev.